ISTANBUL TECHNICAL UNIVERSITY ★ GRADUATE SCHOOL OF SCIENCE ENGINEERING AND TECHNOLOGY

THEORETICAL AND EXPERIMENTAL INVESTIGATION OF SILICON NANOWIRE WAVEGUIDE DISPLACEMENT SENSORS

M.Sc. THESIS

Muhammet Mustafa KAYKISIZ

Department of Mechatronics Engineering

Mechatronics Engineering

NOVEMBER 2013

ISTANBUL TECHNICAL UNIVERSITY ★ GRADUATE SCHOOL OF SCIENCE ENGINEERING AND TECHNOLOGY

THEORETICAL AND EXPERIMENTAL INVESTIGATION OF SILICON NANOWIRE WAVEGUIDE DISPLACEMENT SENSORS

M.Sc. THESIS

Muhammet Mustafa KAYKISIZ
(518111051)

Department of Mechatronics Engineering

Mechatronics Engineering

Thesis Advisor: Asst. Prof. Dr. Erdal BULGAN

NOVEMBER 2013

İSTANBUL TEKNİK ÜNİVERSİTESİ ★ FEN BİLİMLERİ ENSTİTÜSÜ

EŞZAMANLI SİLİKON NANOKABLO DALGAKILAVUZU YER-DEĞİŞİM ALGILAYICILARININ KURAMSAL VE DENEYSEL OLARAK İNCELENMESİ

YÜKSEK LİSANS TEZİ

Muhammet Mustafa KAYKISIZ
(518111051)

Mekatronik Mühendisliği Anabilim Dalı

Mekatronik Mühendisliği Programı

Tez Danışmanı: Yrd. Doç. Dr. Erdal BULĞAN

KASIM 2013

Muhammet Mustafa kaykısız, a **M.Sc.** student of ITU **Graduate School of Science Engineering and Technology** student ID **518111051**, successfully defended the **thesis** entitled "**THEORETICAL AND EXPERIMENTAL INVESTIGATION OF SILICON NANOWIRE WAVEGUIDE DISPLACEMENT SENSORS**", which he prepared after fulfilling the requirements specified in the associated legislations, before the jury whose signatures are below.

Thesis Advisor :   **Asst. Prof. Dr. Erdal BULGAN**   ....
İstanbul Technical University

Jury Members :   **Prof. Dr. Ata MUGAN**   ....
Istanbul Technical University

                        Asst. Prof. Dr. M. Fazıl SERINCAN   ....
Istanbul Bilgi University

Date of Submission : 03 May 2013
Date of Defense :   **01 Dec 2013**

To my family,

FOREWORD

First of all, I would like to thank Asst. Prof. Dr. Erdal BULĞAN, for his priceless support, guidance, and tolerance within the three years along the masters study. I am very grateful to meet and work him together. I would like to acknowledge again for novel vision on engineering and academic life.

I would like to acknowledge Marie Curie International Reintegration Grants Seventh Framework Programme for the fundational support. I also would like to thank National Nanotechnology Research Center (UNAM) at Bilkent University, Turkey and Dr. Volkan OZGUZ at Nanotechnology Research and Application Center (SU-NUM) at Sabancı University, Turkey for their support during fabrication.

I also would like to thank my tiny, nano friend Irem Koca for her unlimited support and love.

I also would like to thank my roommate, researchmate and friend Shahab Bahktiari GORAJOOBI, for his support. I would like to thank my officemates and friends, Asım YILDIZ, Ayse KARAGOZ, Fatih TEMIZKAN, Unal DEGIRMENCI and Cihan TUNC for their unlimited support and love.

Finally, I would like to thank my father, mother, brothers and sisters, namely Ahmet KAYKISIZ, Oznur KAYKISIZ, Pınar KAYKISIZ, Emrah KAYKISIZ, TUGBA KAYKISIZ, Ebru KAYKISIZ, Eren KAYKISIZ, Emirhan KAYKISIZ and Arda KAYKISIZ for all their support, I love them all depth of my heart.

November 2013   Muhammet Mustafa KAYKISIZ

x

TABLE OF CONTENTS

ABBREVIATIONS

AFM	**:** Atomic Force Microscopy
BOX	**:** Buried Oxide
DC	**:** Directional Coupler
E_x	**:** Electric field of the lightwave
EFM	**:** Electromagnetic Field Modulation
EBL	**:** Electron Beam Lithography
EWR	**:** Evanescent Wave Region
FDTD	**:** Finite-Difference Time-Domain
HF	**:** Hydrofluoric Acid
InGaAs	**:** Indium Gallium Arsenide
ICP-DRIE	**:** Inductively-Coupled-Plasma Deep-Reactive-Ion-Etching
MEMS	**:** Microelectromechanical Systems
NEMS	**:** Nanoelectromechanical Systems
NIR	**:** Near Infrared
PhC	**:** Photonic Crystal
PLC	**:** Planar Lightwave Circuit
PMMA	**:** Poly(methyl methacrylate)
RF	**:** Radio Frequency
SEM	**:** Scanning Electron Microscopy
SPM	**:** Scanning Probe Microscopy
SOI	**:** Silicon-on-Insulator
TIR	**:** Total Internal Reflection
TE	**:** Transverse Electric Wave
WDM	**:** Wavelength Division Multiplexing

LIST OF TABLES

LIST OF FIGURES

THEORETICAL AND EXPERIMENTAL INVESTIGATION OF SILICON NANOWIRE WAVEGUIDE DISPLACEMENT SENSORS

SUMMARY

Efforts towards integrated optical circuits have seen significant interest for combining microelectronics and photonics in order to bring compact device sizes and volume economics. Silicon nanowire waveguides and photonic crystals are among those heavily investigated. Photonic devices with embedded Nano/Microelectromechanical Systems (NEMS/MEMS) such as an optical add-drop multiplexer deploying relative motion of silicon waveguides, nanowire waveguide ring and microdisk resonators demonstrated as narrow-band filters, optical switches utilizing silicon nanowire waveguide couplers, and an optical waveguide modulator have been reported.

Integrated photonic circuit devices with embedded NEMS/MEMS technology utilize either in-plane or out-of plane motion to accomplish their task. Characterization of such devices can be realized either under Scanning Electron Microscope (SEM) or optical microscopes. Ultimate device characterization, therefore, depends on the quality and evaluation accuracy of the series of images taken consecutively under the corresponding microscope at various actuation levels. Hence, employment of images for device motion characterization causes measurement errors from several tens to hundreds of nanometers during evaluation stage for SEM and optical microscope uses, respectively. Without proper characterization of devices where precise motion or distance in the nano/micro-system level is critical, full understanding of the studied concept, or proper operation or control of the system becomes impossible. In addition, they are usually only for testing purposes and cannot be integrated into the device level.

Targeting the aforementioned need, embedded in-plane distance/displacement sensors utilizing Bragg reflectors within an optical Fabry-Pèrot microcavity, geometrical modulation-based interferometry are reported. Performances in both approaches are highly dependent on the optical wavelengths employed, which, as a result, enforces highly accurate microfabrication or arises calibration need afterwards for proper functionality. In addition, while the former provides only 29nm measurement range, the latter requires large device footprint.

An embedded nanophotonic displacement sensing mechanism based on end-to-end waveguide coupling in the near-field will present. Numerical studies are carried out by 3D Finite-Difference Time-Domain analysis software. Displacement sensing mechanism is fabricated on a Silicon-on-Insulator wafer with 340nm-thick device silicon and 1μm-thick SiO_2 layers. The footprint of the sensing mechanism is about $32 \times 25 \mu m^2$. Theoretical and experimental results are in very good agreement with a maximum deviation of 2.77% in transmittance at 600nm displacement. The measurement sensitivity and range obtained at 1.55μm wavelength are maximum

0.29% change of light intensity per nanometer, and about 1000nm, respectively. The mechanism well-suits real-time measurements in integrated optical circuits operating with the help of embedded NEMS/MEMS actuation, various nano-scale positioning and imaging applications.

Both numerical and experimental study of two sub-nanometer mechanical tuning mechanisms of evanescent wave mode coupling in planar lightwave circuits will demostrate. The mechanisms provide tunability, device footprint, and cost advantages due to being embedded. Numerical studies are carried out by 3D Finite-Difference Time-Domain Analysis. Mechanisms are fabricated on Silicon-on-Insulator wafer with 340nm-thick device silicon and 1μm-thick SiO_2 layers. Optical response results between theoretical and experimental studies are in good agreement. Tunability of the first and second mechanisms in the mechanical excitation range of 75nm and 100nm at 1.55μm wavelength are 1.13nm and 1.19nm per percent of average light intensity change, respectively. By utilization of a proper light intensity measurement approach as it is realized in this study, one can increase tunability values even further below. Both mechanisms presented are $40\times25\mu m^2$ in footprint. The studied evanescent wave mode coupling mechanisms are well-suited for employment in PLCs where mechanical tuning with sub-nanometer or greater excitation is needed.

Also 1x2 optical switch is presented. In the liteature, using comb actuator as a mechanical motion, designed mechanisms has high sensitivity. Experimental and numerical results agree very well.

Two types of sensing mechanisms are introduced. Short-range high-sensitivity in-plane optical sensor again, but at normally-on state are being investigated in order to clarify their initial state effects on the sensing characteristics. Towards this goal, two major types of sensor approaches are studied. All sensors utilized in Chapter 3 are based on Electromagnetic Field Modulation. Sensitivities achieved in this phase are from 0.84nm down to 0.06nm per percent of light intensity within sub-100nm distances.

Low loss silicon elliptical intersection based on diffraction grating method will present at the first time. Diffraction grating is demonstrated as a numerical at sub-nanometer for optical devices. The optical performance of silicon intersection for single fold is increased from 92.14% to 98.99% without extra fabrication cost and footprint. Also, for doubly-fold intersections efficiency is powered up to 99.80%. Optical performance of optical NEMS/MEMS can be improve with presented elliptical intersections. Two new intersection could not fabricate due to used equipment.

EŞZAMANLI SİLİKON NANOKABLO DALGAKILAVUZU YER-DEĞİŞİM ALGILAYICILARININ KURAMSAL VE DENEYSEL OLARAK İNCELENMESİ

ÖZET

Birleşik optik devreler sağladığı küçük cihaz boyu ve fabrikasyon maliyeti bakımından mikro elektronik ve fotonik teknolojileri için önemlidir. Silikon nanotel dalgaklavuzları ve fotonik kristaller bu amaç doğtultusunda çok yönlü incelenmiş ve çalışılmıştır. Fotonik cihazlar gömülü nano/mikroelektromekanik sistemler (NEMS/MEMS) ile birlikte yayınlanmıştır. Bunlar silikon dalgaklavuz bazlı add-drop multiplexer, nanotel dalgaklavuz yüzükleri, silikon nanotel dalgaklavuzu temelli optik anahtarlar, optik dalgaklavuz modülatörleridir.

Birleşik optik devreler gömülü NEMS/MEMS teknolojisi ile birlikte görevlerine göreve yüzey üzeri ya da yüzeye dik olarak çalışabilir. Bu cihazların karakterizasyonları Taramalı Elektron Mikroskoplarında (SEM) veya optik mikroskoplarda yapılabilmektedir. Farklı voltaj değerleri için sırasıyla optik mikroskop altında çekilmiş foroğrafların kaliteleri optik cihazlarının karakterizasyonunun kalitesini belirlemektedir. Çekilen fotoğrafların kalitesinin yüksek olmaması ile birlikte çok yüksek kalitede mikro optik cihaz üretilmesi halinde dahi karakterizyon sorunu yaşamaktadır. Bu fotoğrafların cihazın karakterizyonunda kullanılmasında ki hata payı on nanometrelerden yüzlerce nanometreye kadar çıkabilmektedir.

Nano/Mikro optik sistemlerde hassas hareket yada uzaklık ölçmek herhangi bir düzgün karakterizasyon düzeneği olmadan kritik bir parametredir. Bu parametrenin düzgün kurulamaması halinde herhangi bir hareketi ölçmek ve kontrol etmek imkansız olmaktadır. Sonuç olarak yayınlanmış mikro cihazlar sadece test düzeneklerinde kullanılarak herhangi bir optik sisteme entegre edilememektedir.

Yukarında bahsedilen gereksinimden dolayı Fabry-Perot methodu temelli gömülü yüzey üzeri uzaklık/mesafe sensörleri çalışılmıştır. Performansının yüksek olmasıyla birlikte optik dalgaboyuna bağımlılığından dolayı çok hassas derecede mikro fabrikasyon gereksinimi vardır. Bir başka dezavantajı ise ölçüm aralığının sadece 29nm olmasıyla birlikte cihazın kapladığı alan mikro cihazlara göre büyük kalmaktadır.

Gömülü nanofotonik silikon dalgaklavuz temelli mesafe ölçümünü yakın-alan da algılayabilen mekanizma önerilecektir. Teorik çalışmaları 3 boyutlu Sınırlı-Fark Zaman-Alan analiz yazılımı ile yapılacakmıştır. Mesafe ölçücü mekanizma silikon-yalıtkan pul üzerine 340nm kalınlıklı silikon, 1µm kalınlıklı SiO_2 tabaka üzerine imal edilmiştir. Ölçüm mekanizmasının toplam cihaz alanı yaklaşık olarak $32\times25\mu m^2$ 'dır. Teorik ve deneysel sonuçlar 600nm uzaklık için birbirleri ile maksimum 2.77% sapmayla uyuşmaktadır. 1.55µm dalgaboyunda ölçüm aralığı 0.29% nanometre başına optik değişim olmakla birlikte ölçüm aralığı ise yaklaşık 1000nm'dir. Bu mekanizma entegre optik devrelerde gerçek zamanlı ölçümlerde kullanılabilecektir.

Ayrıca NEMS/MEMS methodu ile birlikte çeşitli nano boyutlu pozisyonlamada ve görüntüleme teknolojisinde kullanılabilecektir.

2 tane farklı nanometre altı fiziksel temasa dayalı görünmez dalga boyunda çalışabilen mekanik mekanizmalar nümerik ve deneysel olarak çalışılmıştır. Mekanizmalar gömülü olarak çalıştıklarından dolayı yüksek hassasiyet, küçük cihaz boyu ve düşük fabrikasyon fonksiyonelliği göstermektedir. Teorik çalışmaları 3 boyutlu Sınırlı-Fark Zaman-Alan analiz yazılımı ile yapılacakmıştır. Mesafe ölçücü mekanizma silikon-yalıtkan pul üzerine 340nm kalınlıklı silikon, 1µm kalınlıklı SiO$_2$ tabaka üzerine imal edilmiştir. Teorik ve deneysel çalışma sonuçları birbirleri ile uyuşmaktadır. Sunulan birinci ve ikinci mekanizmaların hassasiyetleri 1.55µm dalgaboyu için yaklaşık 1.13nm ve 1.19nm olarak ölçülmüştür. Sonraki uygumalar için hassasiyetleri kullanılan ışık kaynağına göre daha aşağılara çekilebilmektedir. İki cihazında toplam alanları yaklaşık 40×25µm^2 'dır. Görünmez ışık bölgesinde çalışabilen mekanizmalar düz optik devreler için nanometre altı hareket ve mesafeler için gelecek sunan bir teknoloji sunmaktadır.

Literatürde ilk defa tarak eyleyiciler kullanılarak yüksek performans ve hassasiyette çalışan mekanik sensör olacaktır. 1x2 optik anahtar farklı nanometre altı fiziksel temasa dayalı görünmez dalga boyunda çalışabilen mekanik mekanizmalar nümerik ve deneysel olarak çalışılmıştır. Mekanizmalar gömülü olarak çalıştıklarından dolayı yüksek hassasiyet, küçük cihaz boyu ve düşük fabrikasyon fonksiyonelliği göstermektedir. Teorik çalışmaları 3 boyutlu Sınırlı-Fark Zaman-Alan analiz yazılımı ile yapılacakmıştır. Mesafe ölçücü mekanizma silikon-yalıtkan pul üzerine 340nm kalınlıklı silikon, 1µm kalınlıklı SiO$_2$ tabaka üzerine imal edilmiştir. Ayrıca nümerik ve deneysel sonuçlar birbiri ile örtüşmektedir. Optik anahtarı Sonlu Elemanlar Methodu kullanarak bilgisayar ortamında modellemesi yapılmıştır. Cihazın mukavemeti, sağlamlığı, elektrostatik kuvveti, yer çekimi testi ve güvenlik katsayıları hesaplanmıştır. Optik anahtarın nümerik sonuçlara göre verimi %48.21 olup hassasiyeti 1nm civarındadır. Deneysel sonuçlar sonunda cihaz simulasyon sonuçlarından daha iyi veriler sağlamıştır. Bunun en büyük nedeni ise nümerik hesaplamalar yapılırken en küçük mesafe noktasının büyük olmasıdır. Bu değer çok küçük tutulduğunda doğru değere daha da yaklaşılabiliyor fakat bu da simülasyon süresini günlerden aylara kadar uzatmaktadır. Optik anahtar 0.077 nm hassasiyet ile çalışmaktadır. Toplam optik değişim %39 civarında olup maksimum optik performansı ise yaklaşık %59 olarak hesaplanmıştır.

İki tane farklı geometriye sahip optik anahtarlar mekanizmaları nümerik ve deneysel olarak çalışılmıştır. Kısa-mesafe yüksek-hassasiyetli yüzey üzere optik anahtarlar olmakla birlikte normal olarak açık çalışabilen mekanizmalar çalışılmıştır. Çalışılan sensörlerin çalışma presibi Elektromanyetik alan değişimine dayanmaktadır. Teorik çalışmaları 3 boyutlu Sınırlı-Fark Zaman-Alan analiz yazılımı ile yapılacakmıştır. Mesafe ölçücü mekanizma silikon-yalıtkan pul üzerine 340nm kalınlıklı silikon, 1µm kalınlıklı SiO$_2$ tabaka üzerine imal edilmiştir. Ayrıca nümerik ve deneysel sonuçlar birbiri ile örtüşmektedir. Uzaklık ölçüm sensörü Sonlu Elemanlar Methodu kullanarak bilgisayar ortamında modellemesi yapılmıştır. Cihazın mukavemeti, sağlamlığı, elektrostatik kuvveti, yer çekimi testi ve güvenlik katsayıları hesaplanmıştır. Uzaklık ölçüm sensörlerinin hassasiyetleri 100nm altı mesafeler için 0.06nm ile 0.84nm aralığındadır. Simülasyon sonuçlarına göre iki farklı yapıya sahip olup toplamda dört adet sensör imal edilmiştir. İlk üretilen cihaz 1µm radüse sahip olup yarım daire şeklinde ikinci dalgakılavuzu tarafından tahrik edilen uzaklık ölçüm cihazıdır. Nümerik sonuçlara göre beklenen hassasiyet 0.083nm olup mesafesi

108nm olarak hesaplanmıştır. Uzaklık ölçüm cihazının üretimi sonucunda elde edilen hassasiyet 0.045nm ile 0.050nm arasında değişmektedir. Hesaplanan değerden daha iyi çıkmasının ana sebebi nümerik hesaplamalarda göz önünde bulundurulan en küçük uzaklık değeridir. İkinci üretilen cihaz 2µm radüse sahip olup yarım daire şeklinde ikinci dalgakılavuzu tarafından tahrik edilen uzaklık ölçüm cihazıdır. Nümerik sonuçlara göre beklenen hassasiyet 0.082nm olup mesafesi 107nm olarak hesaplanmıştır. Uzaklık ölçüm cihazının üretimi sonucunda elde edilen hassasiyet 0.039nm olarak elde edilmiştir. Üçüncü üretilen cihaz 2µm kenar uzunluğuna sahip olup üçgen şeklinde ikinci dalgakılavuzu tarafından tahrik edilen uzaklık ölçüm cihazıdır. Nümerik sonuçlara göre beklenen hassasiyet 0.088nm olup mesafesi 112nm olarak hesaplanmıştır. Uzaklık ölçüm cihazının üretimi sonucunda elde edilen hassasiyet 0.064nm olarak elde edilmiştir. Dördüncü üretilen cihaz 3µm kenar uzunluğuna sahip olup üçgen şeklinde ikinci dalgakılavuzu tarafından tahrik edilen uzaklık ölçüm cihazıdır. Nümerik sonuçlara göre beklenen hassasiyet 0.097nm olup mesafesi 132nm olarak hesaplanmıştır. Uzaklık ölçüm cihazının üretimi sonucunda elde edilen hassasiyet 0.026nm ile 0.050 arasında değişmektedir. 0.026nm hassasiyet bu sunulan tezde ulaşılan en büyük hassasiyet değeridir. Ölçülen bu hassasiyet değerleri mekanik olarak gömülü olarak çalışabilen mikro cihazlarda teknolojisinde öncüdür.

Daha önceki bölümlerde sunulan mesafe ölçüm sensörlerin ve optik anahtarların performanslarını arttırmak üzere düşük kayıplı silikon bağlantılar sunulacaktır. Diffraction grating nanometre altı mesafede nümerik olarak literatürde ilk olarak ispat edilmiştir. Tek-katlı silikon bağlantının optik performansı %92.14'den %98.99'a çıkartılmıştır. Ayrıca çift-katlı silikon bağlantı için ise optik performans %99.80 değerine kadar yüksektilmiştir. Bu sunulan yeni silikon bağlantılar kullanılarak NEMS/MEMS teknolojisi altında sunulan optik mikro cihazlarının performanları arttırılabilecektir.

1. INTRODUCTION

1.1 Background

1.1.1 Silicon Photonics

Stemming from the microelectronics field, silicon as a semiconductor material enjoys its standard and mature microfabrication equipment and techniques available worldwide. Because of its transparency and high confinement feature owing to its high refractive index above 1.1μm wavelengths, silicon is an attractive platform for integration of microelectronics and photonics in order to bring compact device sizes and volume economics, which is called as "Silicon Photonics" [1]. Thus, research efforts towards silicon photonics have recently seen significant interest, and many research groups from the telecommunications and future all-optical computing areas are already active in the field. Silicon nanowire waveguides and photonic crystals are among the heavily investigated topics [2-13].

There are several examples indicating towards future silicon integrated optical circuits. Among all, a silicon nanowire bent waveguide with a radius as small as 0.5μm has depicted propagation loss levels less than 1dB [2], suggesting very compact integration of optical circuits on silicon using nanowire waveguides. Splitter and coupler using silicon nanowire waveguides were proposed for dividing incident lightwave [3, 4]. Complex devices such as arrayed-waveguide gratings were also reported using submicron silicon waveguides [5].

Silicon photonics devices with embedded nano/micro-electromechanical systems (NEMS/MEMS) such as a planar 2×2 optical add-drop multiplexer deploying relative motion of silicon waveguides, nanowire waveguide ring and microdisk resonators demonstrated as narrow-band filters [6], optical switches utilizing photonic crystal (PhC) line-defect waveguides [7, 8], an optical waveguide modulator [9], and most recently 1×1 and 1×2 optical switches using physical contact of silicon waveguides [10, 11] have recently been reported. Due to very high confinement of lightwave in silicon waveguides, the device sizes have shrunken by

two orders of magnitude in area compared to conventional silica-based waveguide devices. Thus, they are regarded as promising tools for very large integration of optical circuits. Silicon photonics devices with embedded NEMS/MEMS technology utilize either in-plane or out-of plane motion to accomplish their task. Characterization of such devices is realized either by actuation under optical microscope for post-micron-level motion ranges, or actuation under scanning electron microscope (SEM) for submicron-level motion ranges. Ultimate device characterization, therefore, depends on the quality and evaluation accuracy of the series of images taken consecutively under the corresponding microscope at various actuation levels. Hence, employment of images for device motion characterization causes measurement errors from several tens to hundreds of nanometers during evaluation stage for SEM and optical microscope uses, respectively. Some scientists, on the other hand, even prefer to publish the optical performance as a function of the actuation voltage or energy applied to the system alone, because of the difficult and tedious work required, and high levels of uncertainty involved.

Without proper characterization of devices where precise motion or distance in the nano/microsystem level is critical, full understanding of the studied concept, or proper operation or control of the system becomes impossible. Among many possible examples imaginable to such cases are NEMS actuated directional couplers (DCs), micro-ring and micro-disk resonators, where resonant coupling is a function of both the distance between parallel and cross waveguides, and the wavelength of the lightwave utilized. In such systems, for instance, a precise and reliable expression of the concept in consideration should be realized since wavelength sensitivities are in the nanometer levels. Currently, such levels of distances/displacements are barely measurable with external means of such techniques as atomic force microscopy (AFM), several other approaches [12, 13], which are effort-intensive. In addition, they are usually only for testing purposes and cannot be integrated into the device level.

1.1.2 Optical MEMS and Switches

Optical MEMS are miniatures devices with optical, electrical and mechanical specifications at the same time, fabricated at micro scale. There are several sub-classes for optical switching using MEMS technology which are thermo-optical, electro-optical, opto-optical and acusto-optical switches. These techniques are divided to 2 parts, 2D MEMS or digital and analog, scanning mirror or 3D MEMS technology, as shown in Fig. 1.1 [14]. Figure 1.1a illustrates the stable substrate which is movable mirrors integrated via magnetic or electrostatic forces. The input and output port can be changed with the help of mirrors as a digital or analog. Figure 1.1.2.1b depicts 2 mirrors which are selector and router with the input and output fibers. Any optical fiber can tunable to desired output port with the help of integrated movable mirrors.
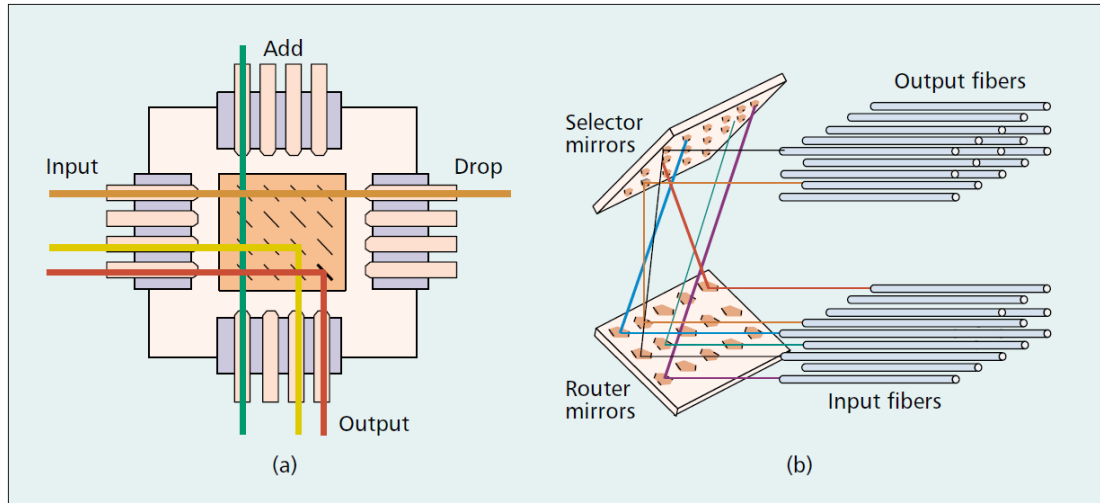
Figure 1.1: MEMS approaches for optical crossconnect switching. a) Digital or 2D MEMS technology. b) Analog, scanning mirror, or 3D technology.

Insertion loss, switching speed, crosstalk, polarization-dependent loss, wavelength dependency, bit rate and protocol transparency and operation bandwidth are the basic parameters for the performance of optical switches. Dobbelaere *et al.* were reported a mirror/gap closing electrostatic actuator, as shown in Fig. 1.2 [14]. The insertion loss is <3.1dB for 16x16 and crosstalk is ≤-50dB. The actuator switch speed is 7ms, transparency at 1.55µm is very good without any wavelength dependency.
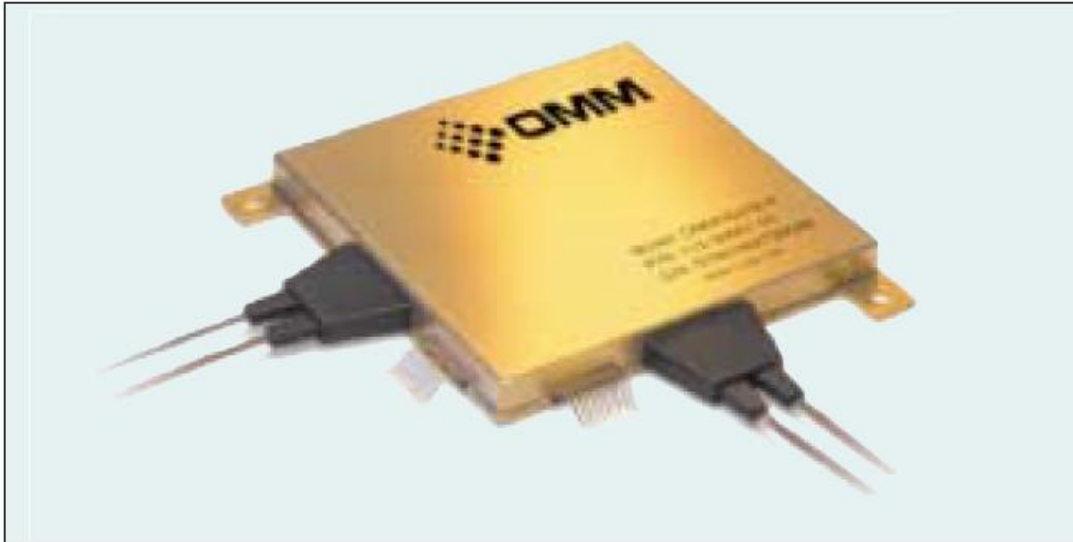
Figure 1.2: Hermetic housing with 32 fiber feed through for a 16x16 2D optical crossconnect switch.

Ollier *et al.* were presented optical MEMS devices based on moving waveguide [15]. The insertion loss is 1.5dB and 2dB, the cross talk is ≤-42dB and ≤-52dB for 1×2 and 1×8 ports, respectively. Transparency is good at 1.55μm without ant wavelength dependency.

Kaneko *et al.* were reported thermo capillarity optical switch for improvement of switching time, as seen in Fig. 1.3 [16]. The structure consists of the micro heater, refractive index matching liquid, crossing waveguide and groove. Heating the refractive index matching liquid in the groove driven due to surface tension variations. When the liquid is present at the crossing point of waveguides, the optical signals pass straight through the groove, however, when the liquid moves away from the crossing point, the signals are switched into the crossing waveguide by total internal reflection (TIR).
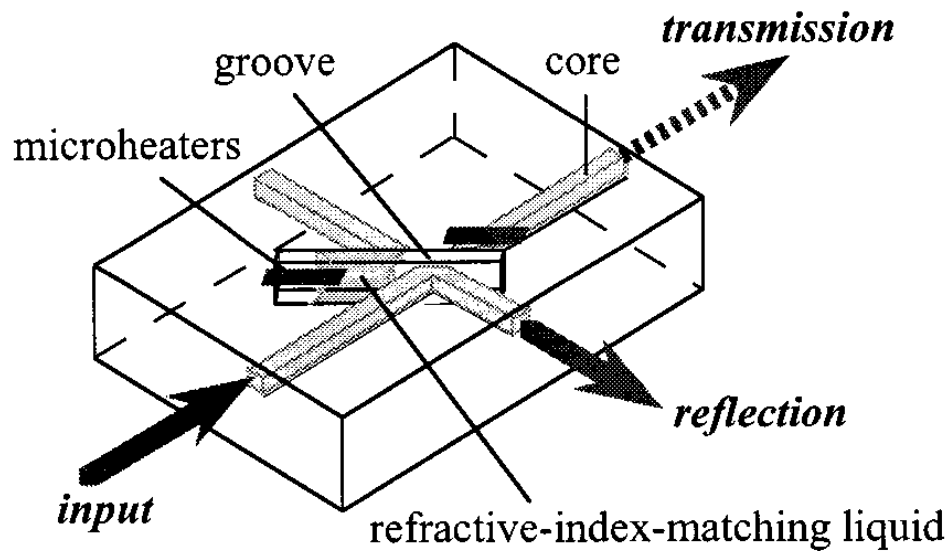
Figure 1.3: OLIVE structure.

Zandi *et al.* were demostrated in-plane SOI optical MEMS accelerometer using waveguide fabry-perot microcavity with silicon\air bragg mirrors, as seen Fig. 1.4 [17]. The sensor has a theoretical resolution limit below 1μg with a 2.5nm\g sensitivity and 400μg resolution. The sensor has also a resonance frequency of 10kHz with a cross-sensitivity.
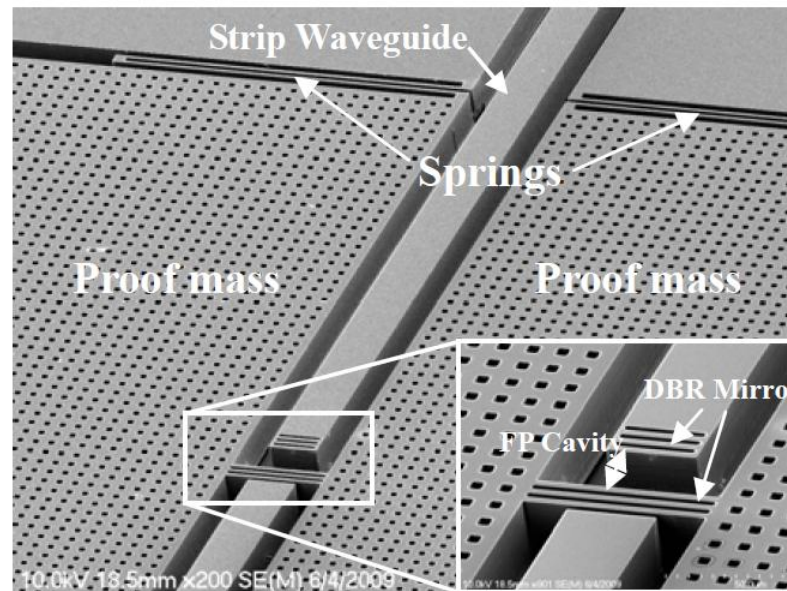
Figure 1.4: SEM photograph of the silicon microfabricated FP based accelerometer.

5

Grutter *et al.* were developed a fabrication techniques for integrating silicon optical devices and MEMS [18]. The new optical MEMS and switches can be fabricable with the help of this method. Figure 1.5 illustrates the fabricated device composed of silicon MEMS. The microdisk includes adiabatic tapering to improve phase matching with the waveguide, as seen in Fig. 1.5b.
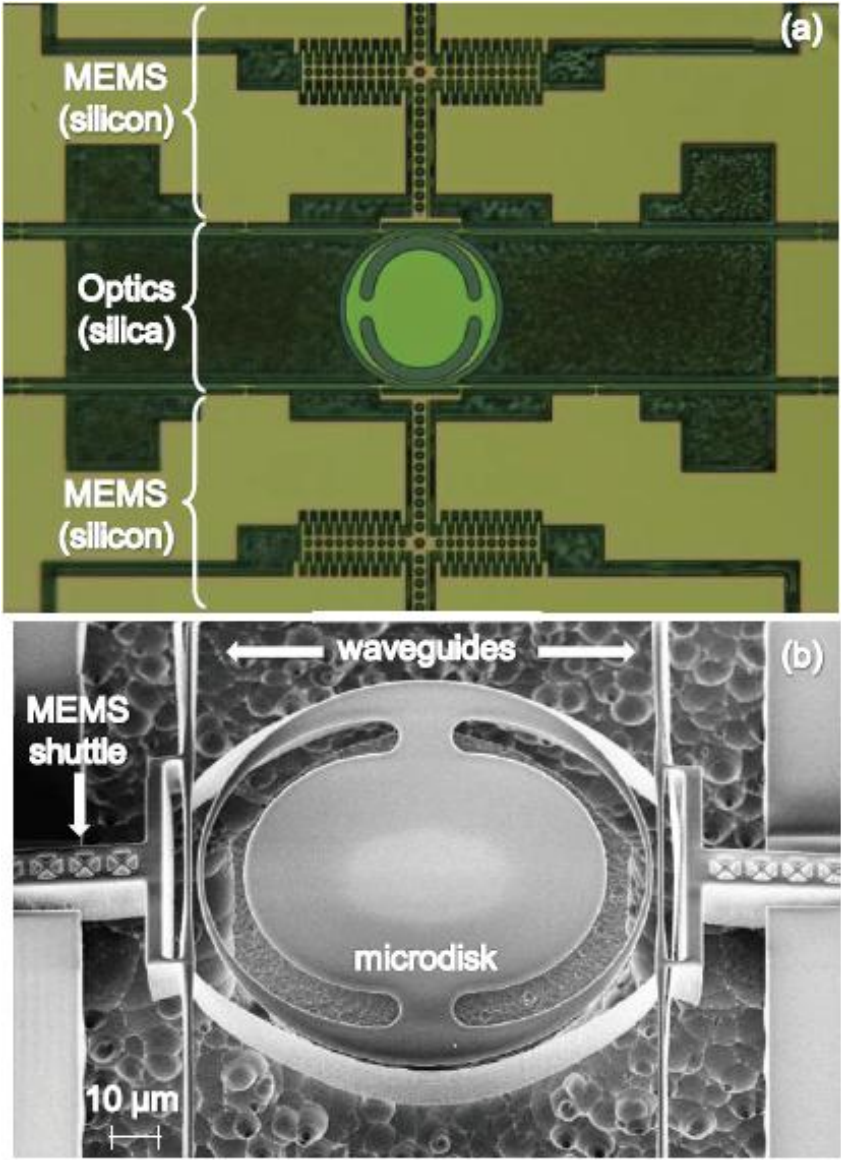
Figure 1.5: a) Fabricated device composed of integrated silica optics and silicon MEMS. b) Scanning electron micrograph of device; silica-only optical components (waveguides, microdisk) are suspended above substrate while connected to released silica-on-silicon MEMS (shuttle).

1.1.3 Displacement Sensors

Nanoscale displacement sensors have performed a substantial role in many applications such as AFM [19], Scanning Probe Microscopy (SPM) [20], data storage [21], nanopositioning [22] and optical switching [23]. Various approaches based on nanophotonic sensing of in-plane displacements have been studied.

Lin *et al.,* for instance, reported a mechanism based on the evanescent coupling of guided resonance as shown in Fig. 1.6 [24] . The mechanism eliminated the requirement of long propagation distance and high reflectivity in Fabry-Perot cavity based structures to achieve high sensitivity. The minimum detectable displacement and shear stress have been demonstrated to be 10nm and 0.33Pa, respectively. The sensitivity of displacement and shear stress sensing are of 0.1249nm/nm (wavelength shift/floating element displacement) and 6.825nm/Pa (wavelength shift/shear stress), respectively.
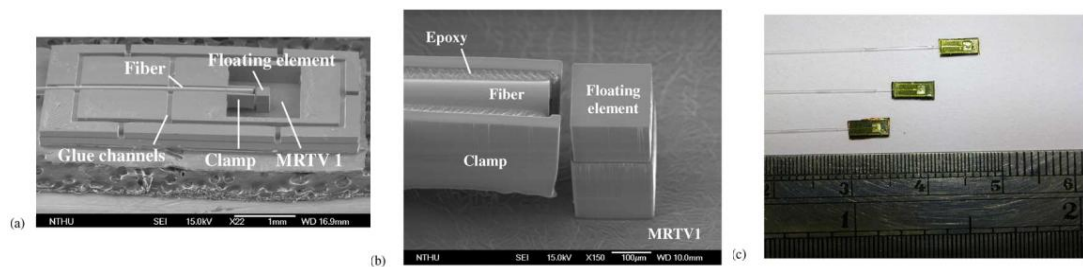
Figure 1.6: a) SEM picture of the fabricated second-generation sensor before packaging. b) Close-up of the clamp structure, fiber and floating element. c) The packaged devices.

Displacement sensing via line-defect resonant cavity in PhC has been another approach presented [25]. Figure 1.7 depicts the presented sensor. The sensor can measure the distance to an external reflective mirror. The measurement resolution is as high as 0.01µm. The sensor is only $0.8 \times 0.75 \text{mm}^2$.
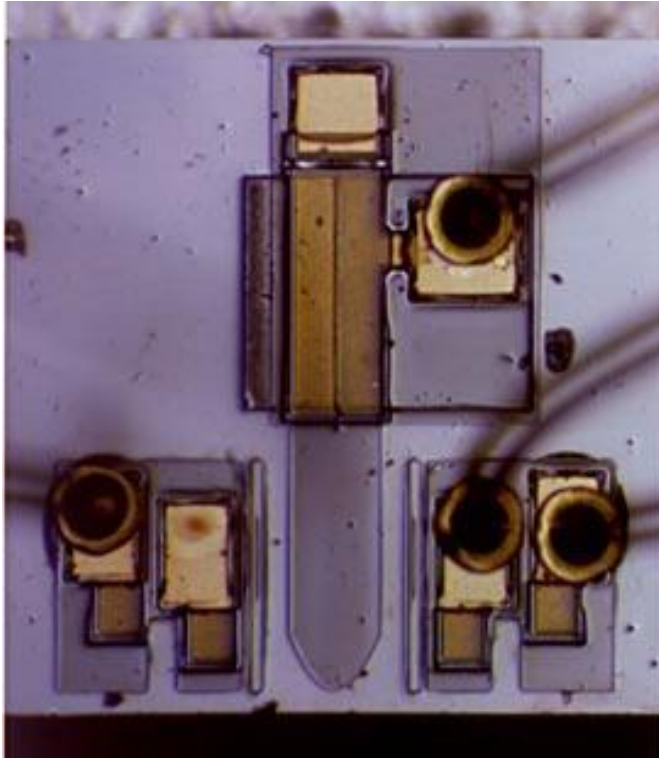
Figure 1.7: Integrated optical micro-displacement sensor.

A recent approach reported has deployed end-to-end waveguide coupling for optical switching in the near-field region. The device employed subwavelength-scale displacements to adjust optical power coupled between submicron silicon waveguide tip ends. Thus, in this thesis, an approach to enhance end-toend waveguide coupling. The expected features are high sensitivity, subwavelength measurement range, wavelength-insensitivity and small device footprint will propose.

1.2 Approach

In this thesis, has recently developed an approach using physical contact of silicon nanowire waveguides for optical switching. The demonstrated switch changed its state by in-plane displacement of a movable elliptical waveguide generated by a NEMS actuator. The technique provides sensitivity even to submicron distance/displacement levels and is applicable to various wavelengths. Later, both the theoretical and experimental research was carried to determine the effects of the waveguide tip geometry and relative positioning of the input and output waveguides on the optical characteristics of the waveguide connections. Although these efforts were towards realizing optical switches using physical contact, same approach can

well be employed as an optical distance/displacement sensor in demanding silicon photonics devices as an embedded tool, and in acoustical, flow, mechanical displacement sensing.

In this thesis also, for the first time, a technique that will equip researchers and engineers with guidelines for a standard and customizable optical measurement technique for embedded synchronous submicron distance/displacement sensors covering slow to very high frequencies will propose. The technique utilizes change of optical transmittance in the evanescent wave region (EWR) and coupling in the near-field between silicon nanowire waveguides as a function of the distance they are apart. The technique is also extendable to post-micron level displacement ranges and various wavelengths by proper selection of the waveguide and buffer materials.

Conceptually, input, movable and output waveguides all with subwavelength-scale tip geometries are utilized in the verification of the nanophotonic enhanced end-to-end waveguide coupling. The movable waveguide is connected to the source of the motion, which, here, is imitated by an embedded electrostatic comb actuator. Initially, the movable waveguide is offset by an air gap both from the input and output waveguides in order to prevent lightwave coupling between waveguide ends. Applying a bias voltage between the fixed and moving combs starts translational displacement of the movable waveguide causing smaller air gaps. The air gap and displacement in this concept are terms that complement to a constant sum equal to the initial air gap. Hence, as displacement increases, air gap will decrease in the same rate. At smaller air gap or higher displacement values, as a result, the lightwave can propagate proportionally from the input to the output waveguide. The optical loss that may occur due to the mismatch of the optical modes at the end-coupled waveguides can be controlled by the geometry of the waveguide ends and the air gap. Hence, the proposed mechanism can be exploited and optimized to measure the displacements with high sensitivity at the nanoscale.

1.3 Dissertation Outline

Chapter 1 first introduces the review of the prior research conducted on silicon photonics, optical MEMS and switch, A review of silicon displacement sensors is presented. Approach utilized in this thesis is also given in this chapter.

Chapter 2 presents an embedded nanophotonic displacement sensing mechanism based on end-to-end waveguide coupling in the near-field. Numerical studies are carried out by 3D Finite-Difference Time-Domain analysis software. Displacement sensing mechanism is fabricated on a Silicon-on-Insulator wafer with 340nm-thick device silicon and 1μm-thick SiO_2 layers. The mechanism well-suits real-time measurements in integrated optical circuits operating with the help of embedded NEMS/MEMS actuation, various nano-scale positioning and imaging applications.

Chapter 3 presents both numerical and experimental study of two sub-nanometer mechanical tuning mechanisms of evanescent wave mode coupling in planar lightwave circuits. The mechanisms provide tunability, device footprint, and cost advantages due to being embedded. Numerical studies are carried out and are fabricated on Silicon-on-Insulator wafer with 340nm-thick device silicon and 1μm-thick SiO_2 layers. The studied evanescent wave mode coupling mechanisms are well-suited for employment in PLCs where mechanical tuning with sub-nanometer or greater excitation is needed.

Chapter 4 presents 1x2 optical switch. Numerical studies are carried out by 3D Finite-Difference Time-Domain software. The experimental results shows that the optical performance of the output is around 59% well agreed with the theoretically results. Optical switch can present the concept works very high sensitivity which is 0.078nm per percent of the light intensity. Experimental and numerical spectral response results of the 1x2 optical switch are studied. The optical switch has a optical pick around 1.58μm wavelength.

Chapter 5 presents normally-on short-range high-sensitivity physical contact optical switches. Numerical studies are carried out by 3D Finite-Difference Time-Domain software. High-sensitivity and short-range four different optical switched is studied numerically. The numerical results proved that sensitivities of the optical switches around 1nm even smaller.

Chapter 6 presents low loss silicon intersection based on diffraction grating. A novel silicon elliptical intersection is studied to improve the optical performances. Diffraction grating technology is utilized at sub-nanometer devices at the first time.

Chapter 7 summarizes overall conclusions achieved throughout the duration of this thesis dissertation study.

2. EMBEDDED NANOPHOTONIC DISPLACEMENT SENSING USING END-TO-END WAVEGUIDE COUPLING

2.1 Introduction

Efforts towards integrated optical circuits have seen significant interest for combining microelectronics and photonics in order to bring compact device sizes and volume economics [1]. Silicon nanowire waveguides and photonic crystals are among those heavily investigated [4, 26]. Photonic devices with embedded NEMS/MEMS such as an optical add-drop multiplexer deploying relative motion of silicon waveguides [27], nanowire waveguide ring and microdisk resonators demonstrated as narrow-band filters [28, 29], optical switches utilizing silicon nanowire waveguide couplers [6, 30], and an optical waveguide modulator [26] have been reported.

Integrated photonic circuit devices with embedded NEMS/MEMS technology utilize either in-plane or out-of plane motion to accomplish their task. Characterization of such devices can be realized either under SEMs or optical microscopes. Ultimate device characterization, therefore, depends on the quality and evaluation accuracy of the series of images taken consecutively under the corresponding microscope at various actuation levels. Hence, employment of images for device motion characterization causes measurement errors from several tens to hundreds of nanometers during evaluation stage for SEM and optical microscope uses, respectively. Without proper characterization of devices where precise motion or distance in the nano/micro-system level is critical, full understanding of the studied concept, or proper operation or control of the system becomes impossible. In addition, they are usually only for testing purposes and cannot be integrated into the device level.

Targeting the aforementioned need, embedded in-plane distance/displacement sensors utilizing Bragg reflectors within an optical Fabry-Pèrot microcavity [31], geometrical modulation-based interferometry [32] are reported.

13

Performances in both approaches are highly dependent on the optical wavelengths employed, which, as a result, enforces highly accurate microfabrication or arises calibration need afterwards for proper functionality. In addition, while the former provides only 29nm measurement range, the latter requires large device footprint. In this chapter, we propose an alternative mechanism for embedded in-plane displacement sensing based on end-to-end waveguide coupling. The obtained advantages are high displacement-sensitivity, subwavelength measurement range, high wavelength-insensitivity and small device footprint.

2.2 Structure and Principle

Figure 2.1 illustrates schematic structure of the proposed approach. Conceptually, input, movable and output waveguides all with subwavelength-scale tip geometries are utilized in the verification of the nanophotonic end-to-end waveguide coupling. The movable waveguide is connected to the source of the motion, which, here, is imitated by an embedded electrostatic comb actuator. Initially, the movable waveguide is offset by an air gap both from the input and output waveguides in order to prevent lightwave coupling between waveguide ends. Applying a bias voltage between the fixed and moving combs starts translational displacement of the movable waveguide causing smaller air gaps. The air gap and displacement in this concept are terms that complement to a constant sum equal to the initial air gap. Hence, as displacement increases, air gap will decrease in the same rate.

At smaller air gap or higher displacement values, as a result, the lightwave can propagate proportionally from the input to the output waveguide. The optical loss that may occur due to the mismatch of the optical modes at the end-coupled waveguides [33] can be controlled by the geometry of the waveguide ends and the air gap. Hence, the proposed mechanism can be exploited and optimized to measure the displacements at the nanoscale with high sensitivity.
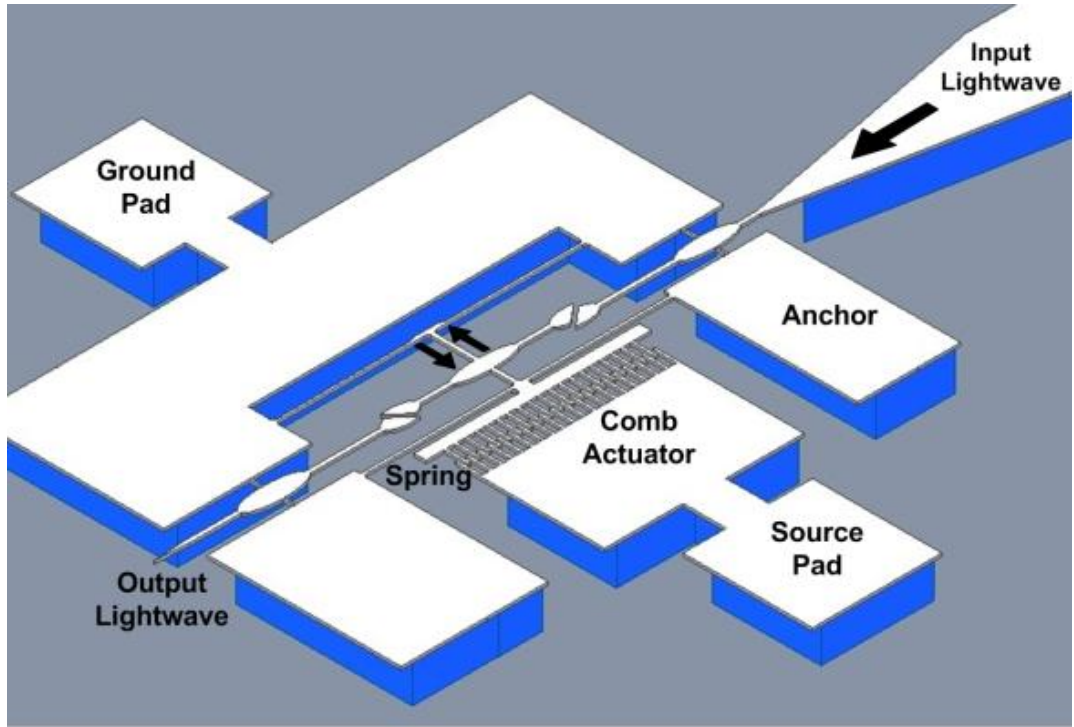
Figure 2.1: Schematic structure of the proposed nanophotonic displacement
sensing mechanism.

2.3 Numerical Study

Displacement sensing mechanism simulations are numerically conducted in 3D
Finite-Difference Time-Domain (FDTD) Analysis software, namely FullWAVE of
RSoft Inc. Refractive indices of silicon, SiO_2, and air are 3.46, 1.47, and 1,
respectively. For single-mode transverse wave polarized light (TE) at 1.55μm
wavelength, waveguide width and thickness are 500nm and 260nm, respectively.
Incident TE polarized electric field is perpendicular to the device layer. Thickness of
SiO_2 must at least be 1μm in order to keep optical propagation loss in the waveguides
less than 0.001dB/cm. SiO_2 as the bottom cladding is designed as 2μm and upper
cladding is air material. The grid size is selected to be 25nm, since, for reliable
calculation, it must be smaller than one tenth of the smallest dimension in the model.

2.3.1 Effects of relative waveguide positions and tip angle

Elliptical tip geometry, which is 1.5μm-wide, 7.2μm-long, and 260nm-thick, is
designed to facilitate the physical contact of waveguides to maximize optical
transmission and contrast, thereby, increasing the measurement sensitivity to

acceptable levels. Figure 2.2 illustrates two possible relative waveguide positions for a waveguide tip pair designed and simulated. Both design have the tip angle of θ. While the first as in Fig. 2.2a, a distance perpendicular to light propagation direction, D, in Fig. 2.2b, a distance along the propagation direction, L, is left.
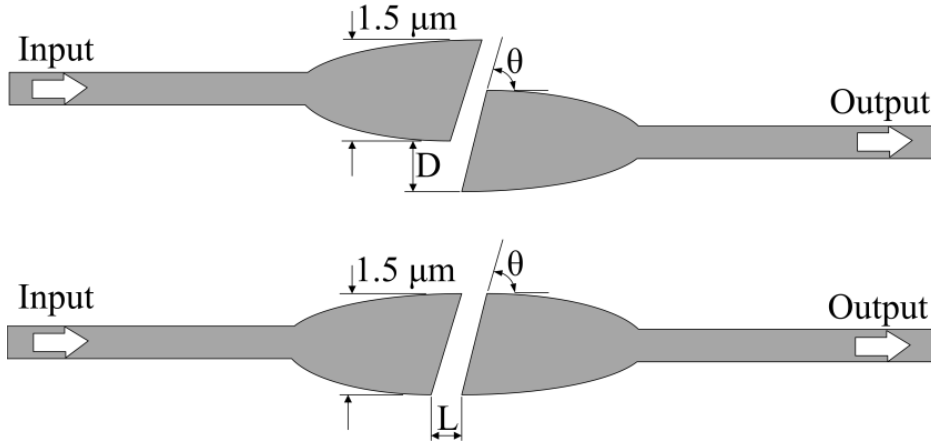
Figure 2.2: Two possible relative waveguide positions. a) Perpendicular to light propagation direction. b) Along the propagation direction.

The relations between Brewster's angle, θ_B, angle of incidence, θ_1, angle of refraction, θ_2, refractive index of air, n_1, refractive index of silicon n_2 are given in equations (2.1), (2.2) and (2.3). When incident angle, θ_1, is equal to the Brewster's angle, θ_B, no light gets back-reflected. From the Snell's Law, critical angle for silicon/air pair is approximately 16.3°. Brewster's angle is the complement of critical angle, which corresponds to 73.7° for silicon/air pair. In this phase, three tips with an angle above the Brewster's and two below are investigated in order to understand the effect of tip angle in the elliptical geometry. To be specific, tip angles of 65°, 70°, 74°, 80°, and 85° are simulated.

$$\theta_1 + \theta_2 = 90° \tag{2.1}$$

$$n_1 . \sin \theta_1 = n_2 . \sin \theta_2 \tag{2.2}$$

$$\theta_B = arc\ tan \frac{n_2}{n_1} \tag{2.3}$$

First, optical performance of structures shown in Fig. 2.2a is studied at 100nm, 200nm, 400nm, and 600nm distances. Figure 2.3 depicts typical cases where the behavior of the lightwave and, hence, optical performance changes.

16

As seen in Fig. 2.3a, transmittance is 91.31% at a tip angle of 74º when the distance between the waveguides is zero. When the distance for the same geometry is increased to 600nm, transmittance decreases down to 11.12% as illustrated in Fig. 2.3b. Transmittance with tip angles above the Brewster's is observed to be greater. At a distance of 100nm at 74º tip angle, transmittance increases to 97.31% as it can be seen in Fig. 2.3c. Transmittance calculated at 100nm distance is greater than that at 0nm, because the tip satisfies the Brewster's angle. However, for tip angles below the Brewster's angle, yields high loss as in the tip with 65º even at 100nm distance as shown in Fig. 2.3d.
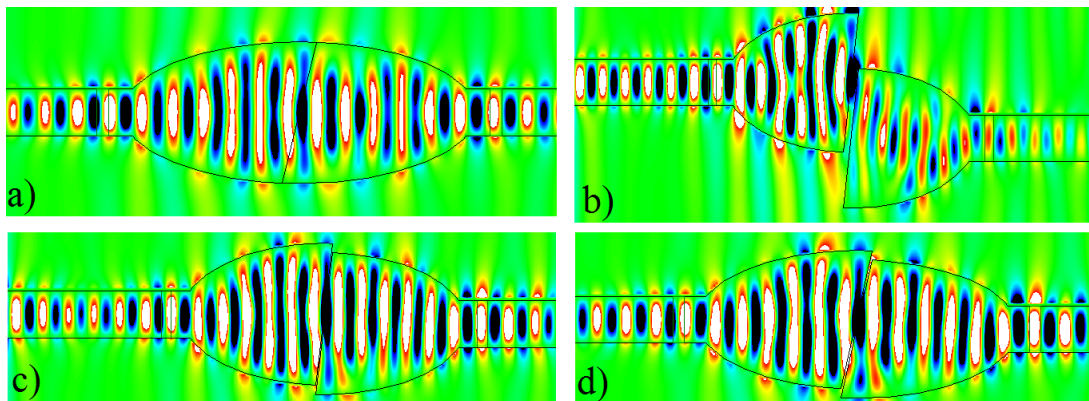
Figure 2.3: Electric field (E_x) of the lightwave. a) At 0 nm at 74º, b) at 600 nm at 74º, c) at 100 nm at 74º, d) at 100 nm at 65º.

Figure 2.4 shows the complete set of results obtained including those presented in Fig. 2.3 in the numerical study. It is understood that the larger tip angle, the higher transmittance. 85º tip angle, for example, is suitable for large-range displacement sensors because transmittances are high above 90% at both 0nm and 200nm distances, and also because transmittance is still high about 35% at even 600nm, offering even larger distances for measurement. 65º tip angle, on the other hand, seems to be useful for short-range high-sensitivity sensors rather than large-range low-sensitivity ones due to sudden decline between 0nm and 300nm distances. Hence, tip angles above the Brewster's such as 74º, 80º and 85º seem to be suitable as normally-off large-range low-sensitivity sensors. When micro/nano-fabrication constraints are considered, tip angles above the Brewster's and below approximately 80º are expected to be the most appropriate.

17
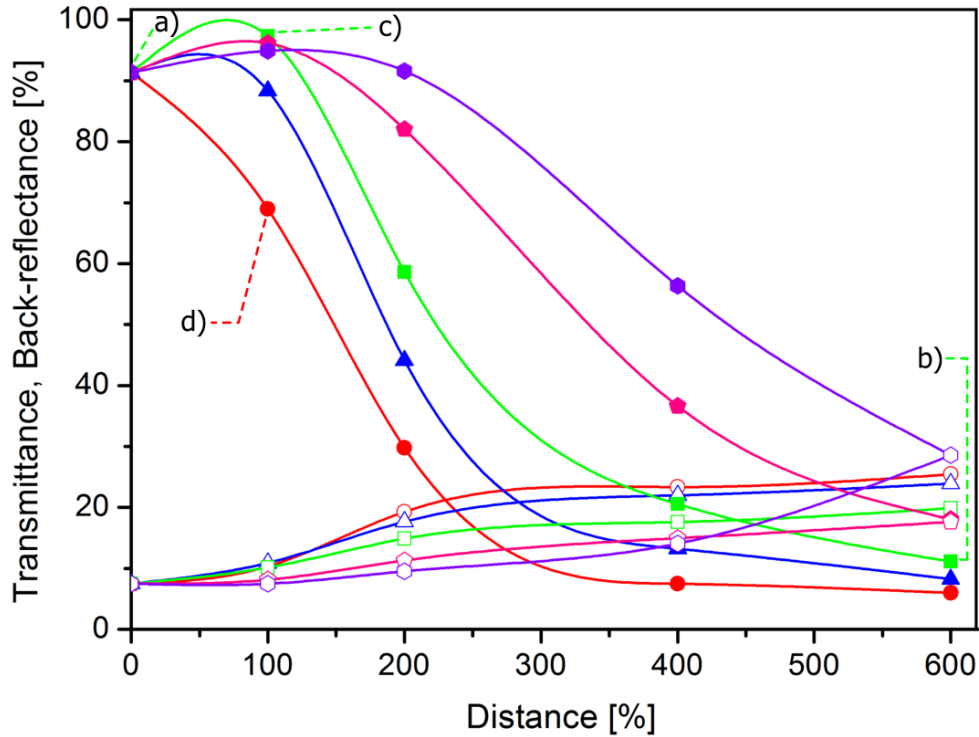
Figure 2.4: Simulated transmittance and back-reflectance as a function of distance, D, at the tip angles, θ, of 65º, 70º, 74º, 80º, and 85º.

Optical performance of structures as illustrated in Fig. 2.2b are studied at 100nm, 200nm, 400nm, and 600nm distances, results of which are given in Fig. 2.5. Results again point that the smaller the tip angle, the smaller the transmittance. Results of the study also indicate that regardless the tip angle is above or below the Brewster's, the sensor will be highly prone to fabrication errors within sub-100nm distances, where surface roughness also fall into, owing to significant loss calculated numerically. Thus, measurement sensitivities from 0nm to 100nm will be far below acceptable levels. Hence, sensor structures positioned as in Fig. 2.2b cannot be utilized in realization of large-range low-sensitivity measurements.

18
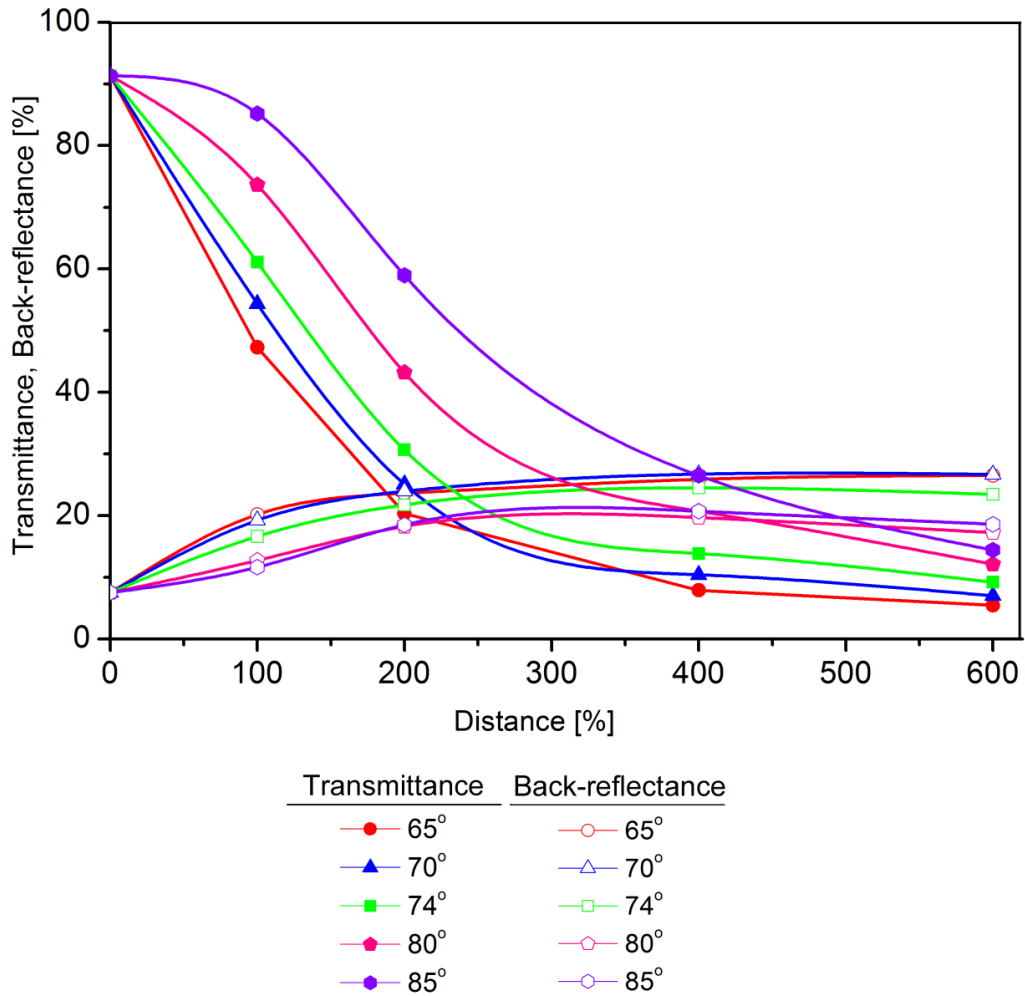
Figure 2.5: Simulated transmittance and back-reflectance as a function of distance, L, at the tip angles, θ, of 65º, 70º, 74º, 80º, and 85º.

2.3.2. Effect of elliptical tip geometry length

After the effects of relative waveguide positions and tip angle on optical character is understood, elliptical tip geometries with different lengths are investigated. The aforementioned studies employed a length of 7.2µm in the elliptical geometry. Below elliptical tip geometries with lengths of 4.8µm, 6.0µm, 8.4µm, 9.6µm, 10.8µm and 12.0µm are conducted to figure out their effect. Results are as discussed below. Transmittance and back-reflectance as a function of distance, D, at the tip angles, θ, of 65º, 70º, 74º, 80º, and 85º for 4.8 µm length and 1.5µm width of elliptical geometry at 100nm, 200nm, 400nm, and 600nm distances are simulated. Results are given in Fig. 2.6. As it will be mentioned in the following parts of this report in the details of the sensor fabrication process, in the worst case, a maximum of 100nm air gap (distance) can be achieved on the physically-contacting sidewalls

19

of sensor tip geometries due to the microfabrication limits. The highest transmittance will be seen at this small distance within 100nm, where the possible highest contrast in transmittance will be attained for large-range sensors. Hence, elliptical geometries with 74º and 80º tip angles are the best candidates towards realization of large-range low-sensitivity sensors. The contrast values for these elliptical geometries are calculated to be 84.64% and 86.96% causing measurement ranges of 690nm and 674nm, respectively. Optical performances at the aforementioned geometries change from 88.37% to 3.7% and from 94.43% to 12.46% at 100 nm and 600nm displacement values, corresponding to sensitivities of about 5.90nm and 5.74nm per percent of light intensity, again respectively.
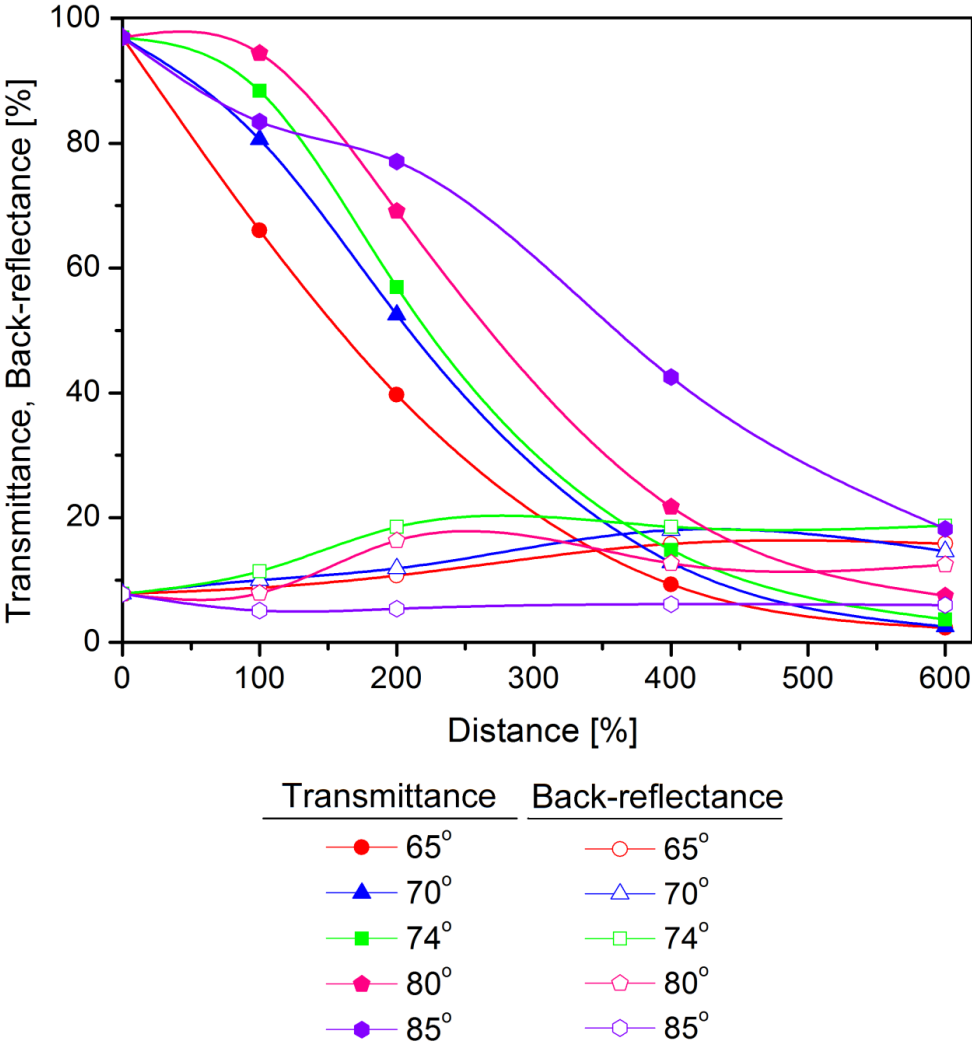
Figure 2.6: Calculated transmittance and back-reflectance as a function of distance, D, for 4.8μm length of elliptical geometry.

Next, transmittance and back-reflectance as a function of distance, D, at the tip angles, θ, of 65º, 70º, 74º, 80º, and 85º as studied for 4.8µm, but this time for 6.0µm length and 1.5µm width of elliptical geometry at 100nm, 200nm, 400nm, and 600nm distances are numerically studied. Results are given in Fig. 2.7. At this step, change in contrast caused by fabrication errors for elliptical sensor geometries with 74º, 80º, and 85º tip angles will be useful. The contrast values for these elliptical geometries are calculated to be 76.29%, 70.52% and 58.15% causing measurement ranges of 755nm, 809nm and 959nm, respectively. Optical performances at the aforementioned geometries change from 81.29% to 5.00%, from 84.69% to 14.17%, and from 85.23% to 27.08% at 100nm and 600nm displacement values, corresponding to sensitivities of about 6.55nm, 7.09nm, and 8.59nm per percent of light intensity, respectively.
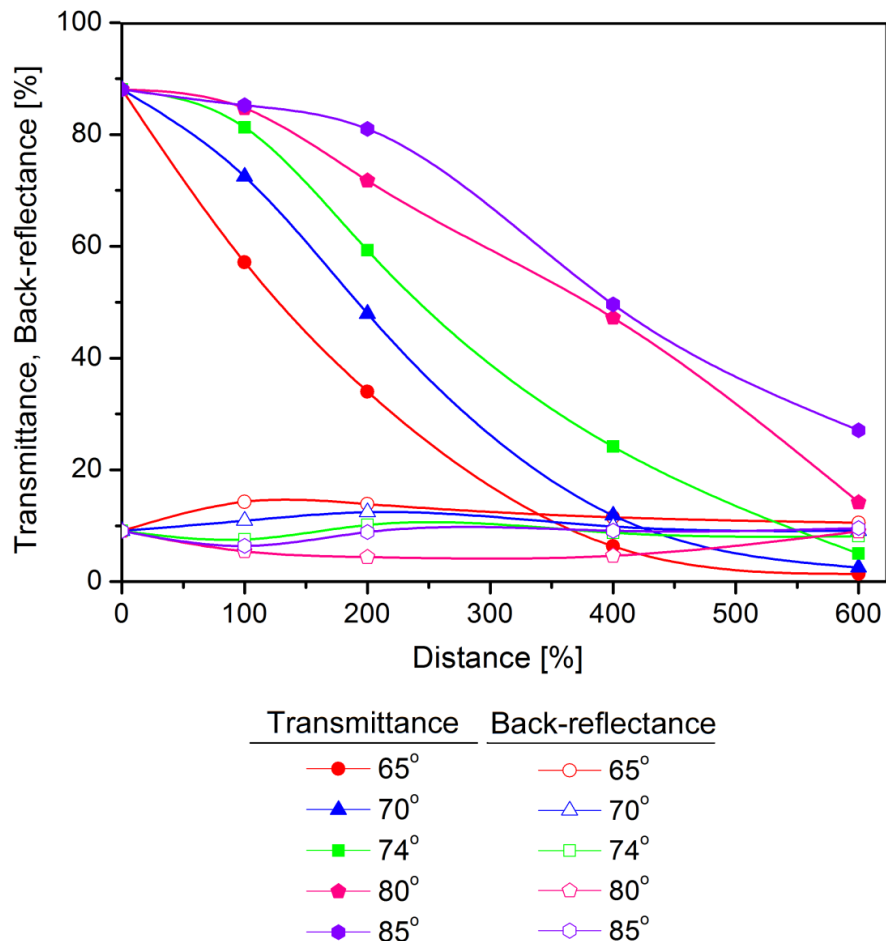
Figure 2.7: Calculated transmittance and back-reflectance as a function of distance, D, for 6.0µm length of elliptical geometry.

Later, transmittance and back-reflectance again for the same elliptical geometry, but with a length of 8.4μm are numerically calculated. Results are given in Fig. 2.8 8.4μm is understood to be the most appropriate length for large-range displacement sensors because not only high contrast values at all studied tip angles of 65º, 70º, 74º, 80º, and 85º are achieved, but also highest contrast values when compared to results of other studied elliptical geometry lengths are obtained. Measurement ranges of respective 722nm, 732nm, 799nm, 911nm, and 1017nm are observed. FDTD analysis showed that the studied elliptical geometries yielded corresponding sensitivities of about 6.22nm, 6.32nm, 6.99nm, 8.11nm, and 9.17nm per percent of light intensity.
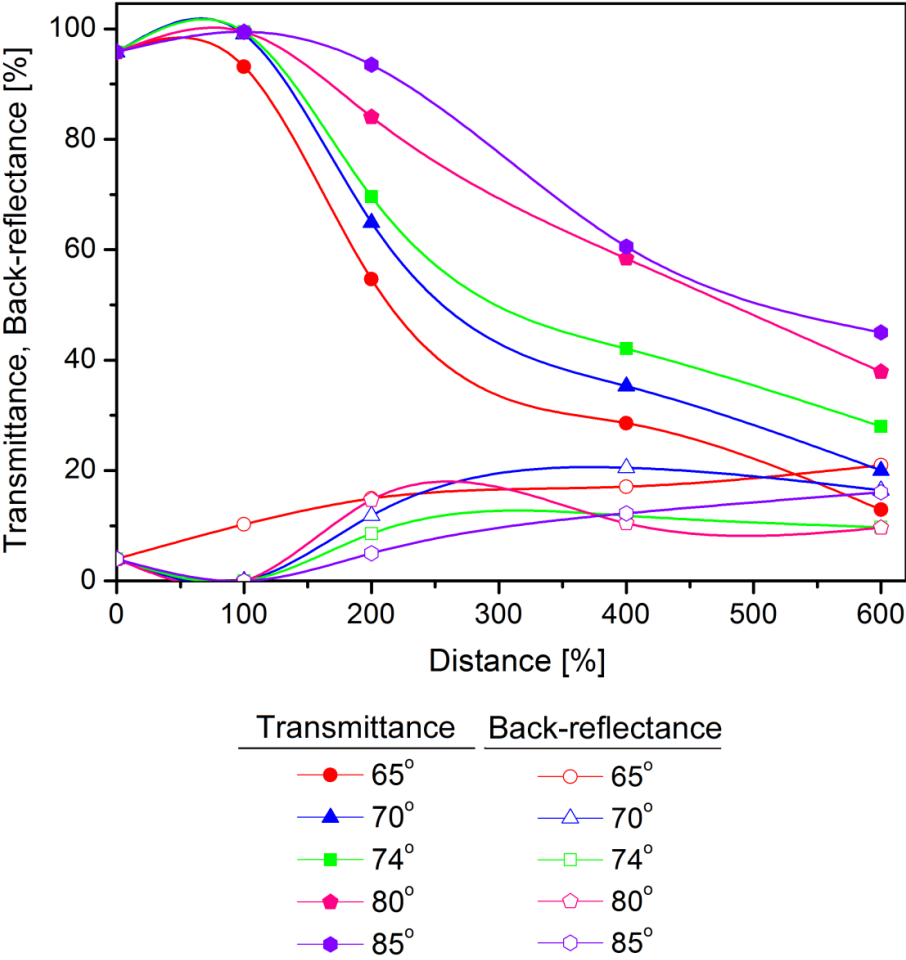
Figure 2.8: Calculated transmittance and back-reflectance as a function of distance, D, at the tip angles, θ, of 65º, 70º, 74º, 80º, and 85º for 8.4μm length of elliptical geometry.

Next, transmittance and back-reflectance for the same elliptical geometry, but with a length of 9.6µm are studied. Results are given in Fig. 2.9. Contrasts in transmittance for sensors with 65º, 70º, and 74º tip angles at 100nm and 600nm are appropriate in large-range measurements. Respective measurement sensitivities are calculated to be 6.90nm, 8.20nm, and 8.02nm per percent of light intensity. Sensors with 80º and 85º tip angles are understood to be suitable in measurements in the range from 200nm to 600nm, suggesting non-contact large-range sensors eliminating fabrication errors by nature. Numerically analysis in the latter case showed that the studied elliptical geometries yielded corresponding sensitivities of about 6.76nm and 9.06nm per percent of light intensity.
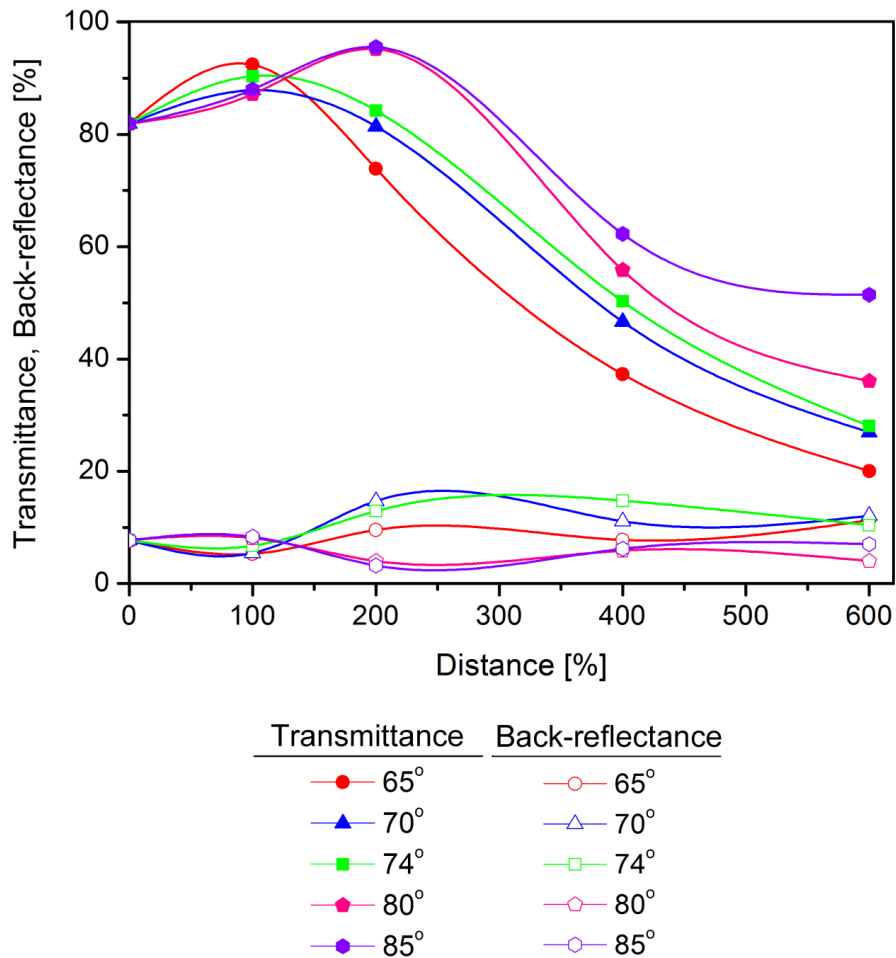
Figure 2.9: Calculated transmittance and back-reflectance as a function of distance, D, at the tip angles, θ, of 65º, 70º, 74º, 80º, and 85º for 9.6µm length of elliptical geometry.

Next, transmittance and back-reflectance for the same elliptical geometry, but with a length of 10.8 μm are studied. Results are given in Fig. 2.10. Elliptical geometries with 65º, 70º, and 74º tip angles are obtained to be suitable for short-range sensors owing to their rapid decrease from 0nm to 600nm distances range. Those with 80º and 85º tip angles, on the other hand, are appropriate for large-range low-sensitivity displacement sensors, yielding transmittance contrasts of 74.47% and 70.62% causing measurement ranges of 771nm and 808nm, respectively. Optical performances change from 92.44% to 17.97% and from 92.49% to 21.87% at 100nm and 600nm displacement values, corresponding to sensitivities of about 6.71nm and 7.08nm per percent of light intensity.
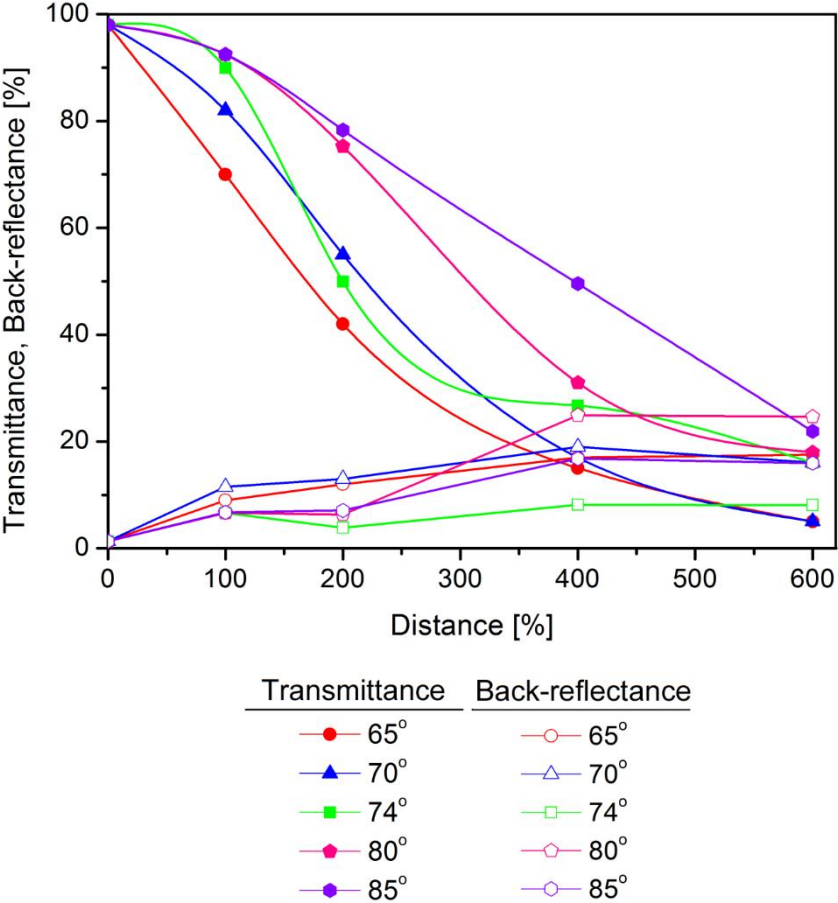
Figure 2.10: Calculated transmittance and back-reflectance as a function of distance, D, at the tip angles, θ, of 65º, 70º, 74º, 80º, and 85º for 10.8μm length of elliptical geometry.

Last, transmittance and back-reflectance for the elliptical geometry with a length of 12.0μm are calculated. Results are given in Fig. 2.11. Contrasts in transmittance for sensors with 80º and 85º tip angles at 100nm and 600nm are appropriate in large-range measurements. The contrast values for these elliptical geometries are calculated to be 63.81% and 51.97% causing measurement ranges of 883nm and 1062nm, respectively. Numerically study showed that the elliptical geometries yielded respective sensitivities of about 7.83nm and 9.62nm per percent of light intensity.
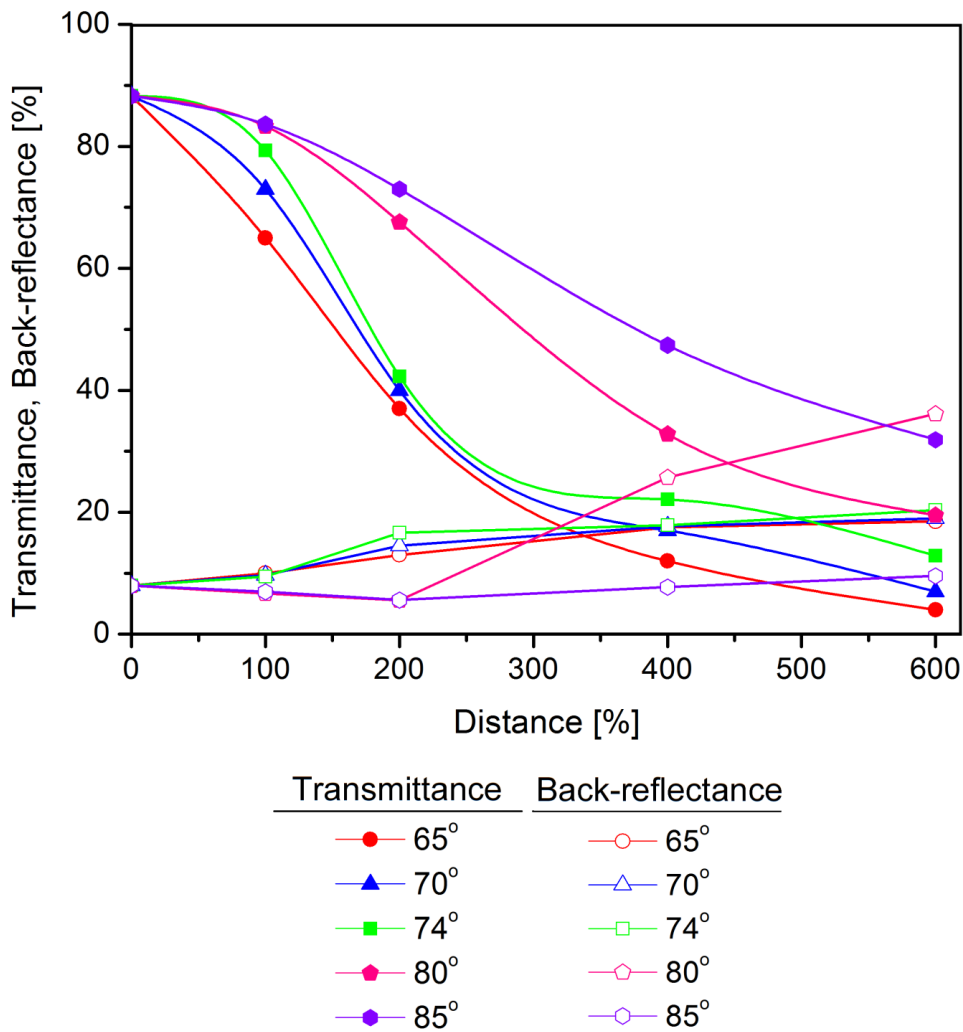
Figure 2.11: Calculated transmittance and back-reflectance as a function of distance, D, at the tip angles, θ, of 65º, 70º, 74º, 80º, and 85º for 12.0μm length of elliptical geometry.

Numerous models suitable for large-range low-sensitivity sensors are obtained. Studies demonstrated that length of elliptical tip geometry affects optical characteristics. In all tip lengths, higher contrasts in transmittance are achieved for tip angles above the Brewster's, whereas smaller values are observed in smaller tip angles than the Brewster's for the same length. In this phase, 22 different sensor designs are learned to be suitable for realization of the large-range displacement sensors. For a tip length of 4.8μm, tip angles of 74º and 80º, for 6.0μm, 74º, 80º and 85º, for 7.2μm, 74º, 80º and 85º, for 8.4μm, 65º, 70º 74º, 80º and 85º, for 9.6μm, 65º, 70º 74º, 80º and 85º, for 10.8μm, 80º and 85º, and for 12.0μm, 80º and 85º are understood to be appropriate. Among all suitable sensors, the highest sensitivity per percent of light intensity is calculated to be at 74º tip angle for 3.6μm tip length and 1.5μm tip width is selected.

Optical character of waveguide ends is numerically studied in the displacement range of 0nm to 1000nm at every 100nm. Results are as depicted in Fig. 2.12. Insets in the figure present the electrical field distribution instances obtained at the end-to-end coupled waveguides at displacement values of 400nm, 600nm and 800nm. While the transmittance is only 11.12%, for example, at 400nm, it experiences sharp increase up to 92.24% at 900nm yielding high optical contrast in subwavelength displacements. An average sensitivity of about 0.16% change of light intensity per nanometer contrast between 400nm and 900nm is obtained. A total effective range of 0nm to 1000nm is theoretically achieved. Calculations show that use of enlarged waveguide-end widths and angles at the optimal length for 1.55μm wavelength helps enhance optical mode overlap in end-to-end waveguide coupling.
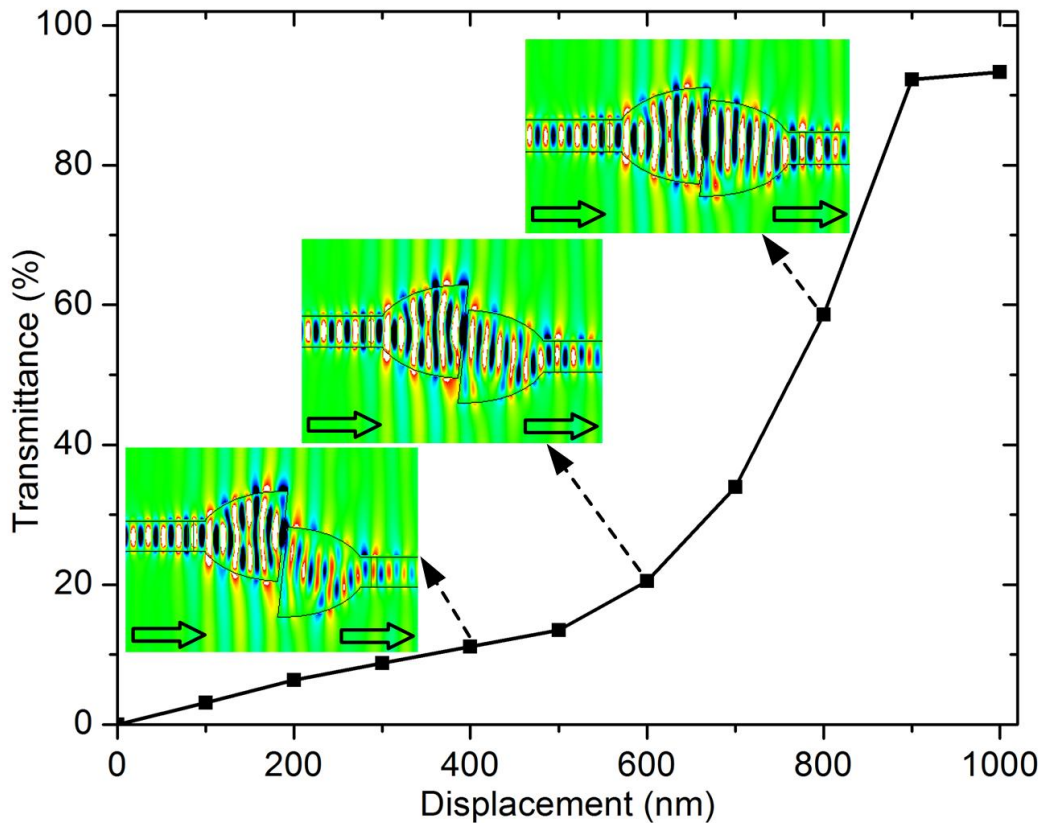
Figure 2.12: Calculated optical transmittance of waveguide ends as a function of the displacement range of 0nm to 1000nm. Discrete markers and solid line depict the numerical results and the regressed curve, respectively. Insets illustrate electrical field distributions for end-to-end coupled waveguides at displacement values of 400nm, 600nm and 800nm.

2.4 Design of Actuator as the Source of Motion

Actuators as the source of motion can be embedded in order to experimentally verify optical characteristics of sensors as a function of distance. Electrostatic comb-drive actuation is a common mechanism in MEMS [34]. Such comb-drives can be actuated in in-plane or out-of plane modes. In the sensors under consideration, in-plane actuation mode will be utilized. Figure 2.13 depicts the schematic view of integrated sensor-actuator design in mind.
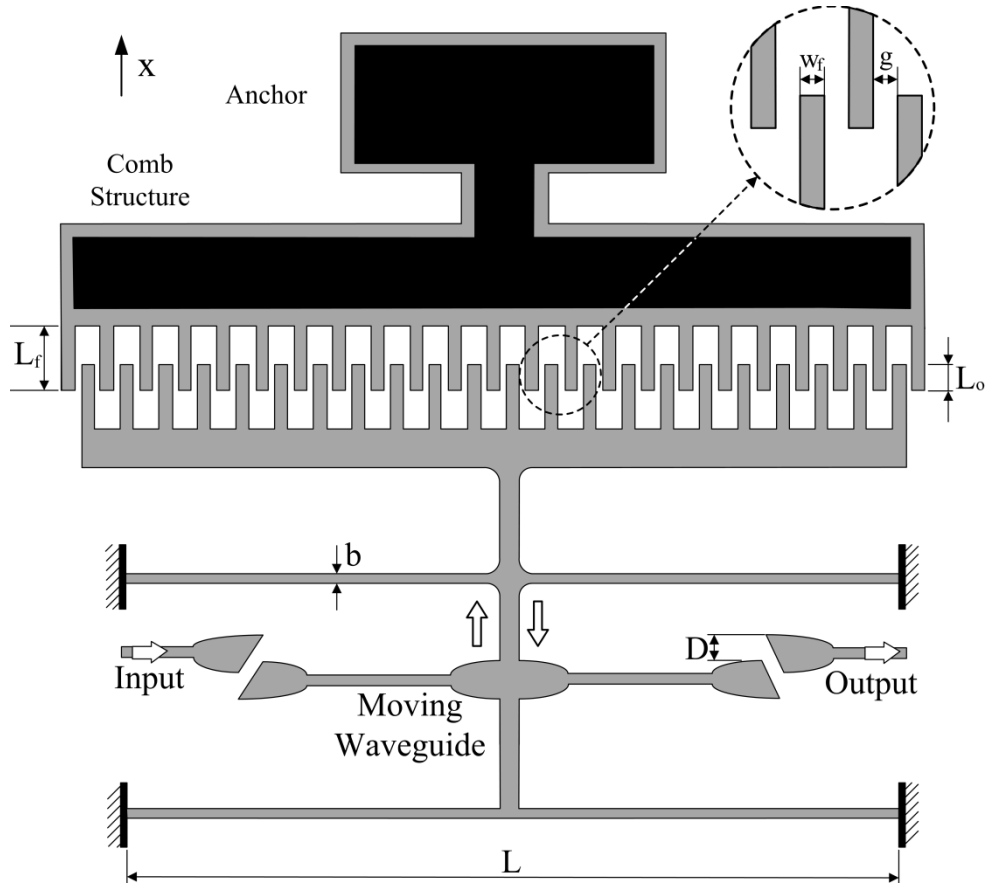
Figure 2.13: Schematic diagram of electrostatic comb-drive actuator.

In this particular design, total electrostatic force, F_x, moment of inertia, I_x, maximum stable deflection, δ_x, spring coefficient, K_x, all along x direction are as given in equations (2.4), (2.5), (2.6) and (2.7) below.

$$F_x = \frac{n.\varepsilon.t.V^2}{2g} \qquad\qquad (2.4)$$

$$I_x = \frac{b.t^3}{12} \qquad\qquad (2.5)$$

$$\delta_x = \frac{n.\varepsilon.V^2.L^3}{16.E.g.b^3} \qquad\qquad (2.6)$$

$$K_x = \frac{2.E.h.b^3}{l^3} \qquad\qquad (2.7)$$

In this particular design, n is the number of finger pairs in the comb actuator, g is the gap between stationary and moving comb finger pairs, w_f is finger width, t is finger thickness, L_f is finger length, L_0 is initial finger overlap, b is spring beam width, h is spring beam thickness, L is spring beam length, E is Young's Modulus for single crystalline silicon, ε is permittivity of air, and V is applied DC bias voltage. Values of the parameters listed above are provided in Table 2.1.

Table 2.1. Specification of the comb-drive actuator.

Symbol	Name	Value
n	Finger Pairs	37
g	Finger Spacing	0.30μm
w_f	Finger Width	0.20μm
t	Finger Thickness	0.26μm
L_f	Finger Length	2.00μm
L_o	Finger Overlap	0.30μm
b	Spring Width	0.25μm
h	Spring Thickness	0.26μm
L	Spring Length	35.88μm
E	Young's Modulus	185GPa
ε	Permittivity	1.885E-4
V	Bias Voltage	0-55.8V

In order to achieve 1.7μm displacement range, D, at approximately 55.8V DC for covering any possible distance under investigation of sensors, a set of two double-clamped flexures with an equivalent spring coefficient of 0.52N/m is designed. The calculated distance versus bias voltage curve is depicted in Fig. 2.14.
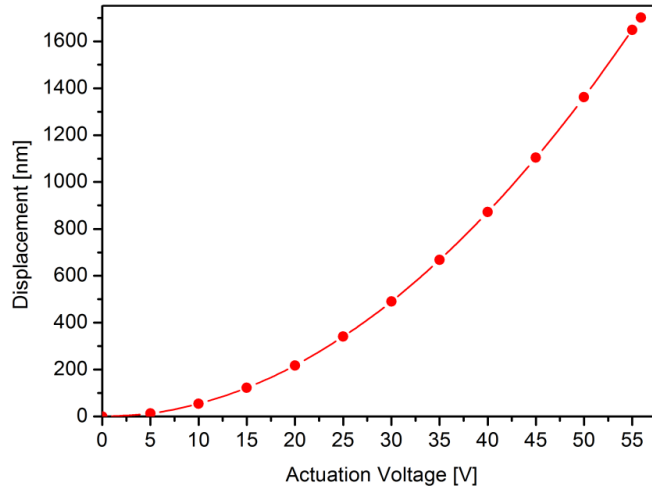
Figure 2.14: Calculated displacements for various voltages for the actuator.

2.5 Experimental Study

Displacement sensing mechanism is fabricated on a Silicon-on-Insulator (SOI) wafer with 340nm-thick device silicon and 1μm-thick SiO_2 layers. Process plan is illustrated in Fig. 2.15.
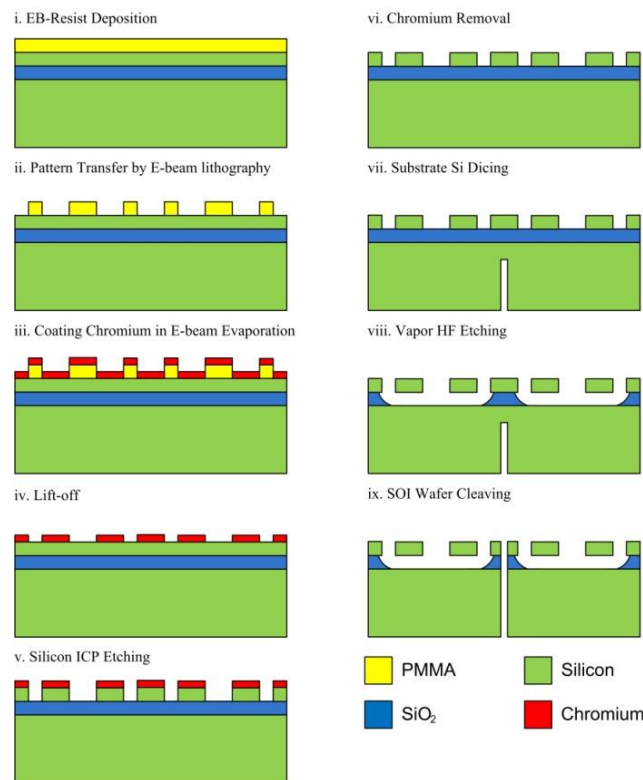
Figure 2.15: Process plan of the displacement sensing mechanisms.

First, device silicon layer is spin-coated by 120nm-thick positive electron beam resist, namely Poly(methyl methacrylate) (PMMA 950K, Microchem Co., USA). Then, sensing structure geometries are patterned using Electron Beam Lithography (EBL, FEI Nova NanoSEM 600 with integrated Raith ElphyPlus, FEI Co., USA, Raith Co., Germany, respectively). Stitching of subfields $50\times50\mu m^2$ in size is employed during EBL. The recipe of large and small pattern features utilized in the electron beam lithography processes are given in Table 2.2.

Table 2.2. Electron beam lithography parameters.

Electron Beam Resist Patterning Recipe			
Positive resist Deposition of Small Features	Prebake/Postbake	180ºC	2min
	Spin coat	750 rpm	10sec
		1500rpm	1min
	Resist Thickness	100nm	
Patterning Small Features	Acceleration Voltage	30kV	
	Beam Current	69pA	
	Step Size along x, y	10nm	
	Exposure Density	$240\mu C/cm^2$	
	Write Field Size	$50\mu m \times 50\mu m$	
Development	Developing by 1:3 MIBK:IPA	25ºC	50sec
	Rinsing by IPA	25ºC	20sec
	Postbake	100ºC	1min
Positive resist Deposition of Large Features	Prebake/ Postbake	180ºC	
	Spin Coat	800rpm	10sec
		1700rpm	1min
	Resist Thickness	80nm	
Patterning Large Features	Acceleration Voltage	10kV	
	Beam Current	2.58nA	
	Step Size along x, y	500nm	
	Exposure Density	$100\mu C/cm^2$	
	Write Field Size	$1000\mu m \times 1000\mu m$	
Development	Developing by 1:3 MIBK:IPA	25ºC	50sec
	Rinsing by IPA	25ºC	20sec
	Postbake	100ºC	1min

Next, 50nm-thick chromium layer is deposited at 3nm/min deposition rate by Electron Beam Evaporation (PVD Vapor 4S E-Beam, Vaksis Co., Turkey) as a hard-mask protecting the device structures underneath. Metallization parameters of chromium layer are selected to ensure minimum deposition rate in order to minimize roughness of window sidewalls [35]. Lift-off process is realized to define windows. Parameters utilized in both evaporation steps are as presented in Table 2.3.

Table 2.3. Electron beam evaporation parameters.

Chromium Deposition for Lift-off		
Small Features		
Preparation	Chamber Vacuum	4×10^{-6} Torr
	Chromium Density	7.19g.cm^{-3}
	K Factor	100
	Temperature	20ºC
Deposition	Voltage	35kV
	Current Beam	25mA
	Rate	0.03nm/s
	Thickness	50nm
Drying	Dry N_2 Gas	1min
Large Features		
Preparation	Chamber Vacuum	5×10^{-6} Torr
	Chromium Density	7.19g.cm^{-3}
	K Factor	100
	Temperature	20ºC
Deposition	Voltage	50kV
	Current Beam	25mA
	Rate	0.06nm/s
	Thickness	30nm
Drying	Dry N_2 Gas	1min

Later, device silicon layer is dry etched fully through windows via Inductively-Coupled-Plasma Deep-Reactive-Ion-Etching (ICP-DRIE) (LPX SR-Cl, STS Co., UK) using SF_6 and O_2 gases as activation and passivation gases, respectively, at the slowest possible rate of 34.34nm/min in order to minimize the sidewall roughness of the optical sensing structures [36]. Table 2.4 lists the parameters utilized in the ICP-DRIE process.

Table 2.4. ICP-DRIE parameters.

Silicon DRIE Recipes		
Recipe	I	II
Number of Cycles	25	
Passivation Time	6 sec	
Etch Time	5 sec	
Chamber Vacuum	8×10^{-3} Torr	10×10^{-3} Torr
SF_6/O_2 Flow Rates	20/50 sccm	
RF Platen Power @ Etch/Passivation	600/20 W	300/10 W
RF Generator Power @ Etch/Passivation		

Figure 2.16 depicts SEM images taken for devices etched using Recipe 1 and 2. Ionization energy affects etch rate and smoothness of sidewalls. In Recipe 1, silicon sidewalls are over etched causing large scallops as seen in Figs. 2.16a and 2.16b. Figure 2.16c shows that due to high etch rate, the straight waveguide is damaged and lifted off the Buried Oxide (BOX) layer. In Recipe 2, where Radio Frequency (RF) platen and generator powers at etch and passivation steps are optimized, however, silicon sidewalls are smooth as seen in Figs. 2.16d and 2.16e with scallops of around 20nm. Properly fabricated straight waveguide as a result of use of Recipe 2 is as shown in Fig 2.16f.
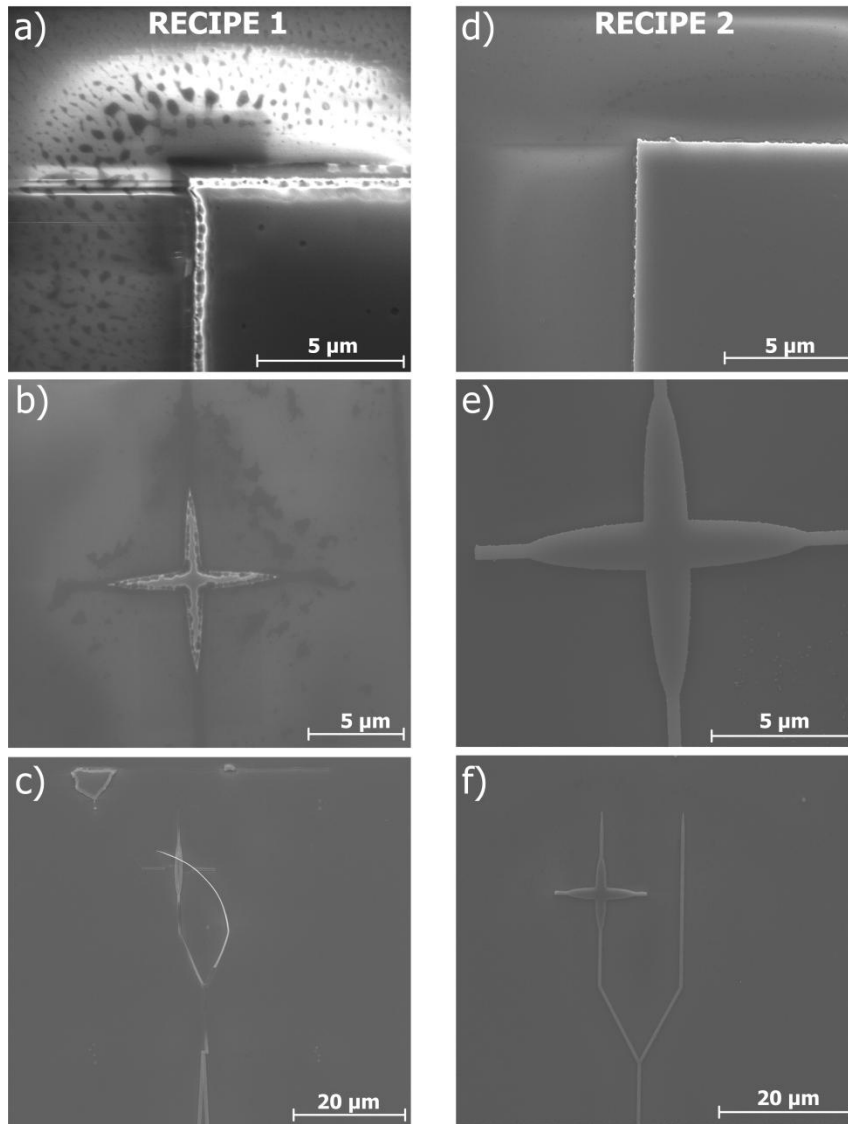
Figure 2.16: Comparison of a failed and succeeded ICP-DRIE recipes. a) Silicon sidewalls with large scallops. b) Overetched elliptical geometry. c) Lifted off straight waveguide. d) Smooth silicon sidewalls, e) Smooth elliptical geometry. f) Smooth straight waveguide.

Vapor Hydrofluoric Acid (HF) Etching Setup is used for device release by etching SiO_2 as the last step of microfabrication of displacement sensing mechanism [37]. Etch rate is dependent on wafer temperature. Thus, wafer temperature is being controlled during the etching process. 3D solid model of the assembled setup is as illustrated in Figs. 2.17.
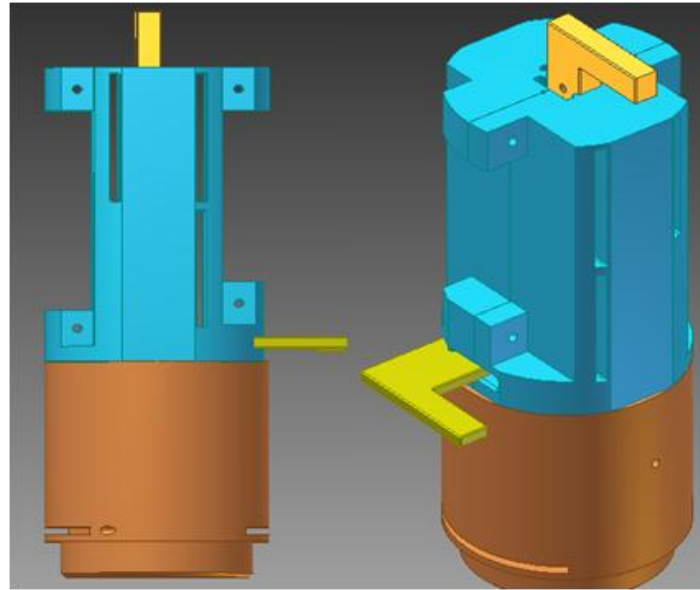
Figure 2.17: 3D model of Vapor HF Setup.

Bottom of the Vapor HF Setup is a container for liquid hydrofluoric acid. The container has an input and an output, which direct vapor HF from its source to the wafer being etched with the help of nitrogen gas at a flow rate of 10ml/min. A flow meter with a manual valve is deployed to observe and control flow rate of nitrogen gas. The main body of etching is designed as the assembly of four components, front body, container, rear body, gate, and wafer holder as illustrated in Figs. 2.18. While front and rear body form the etch channel into which the wafer will be placed, gate and wafer holder are used to start and stop HF etching, and to mount wafer into etch channel.
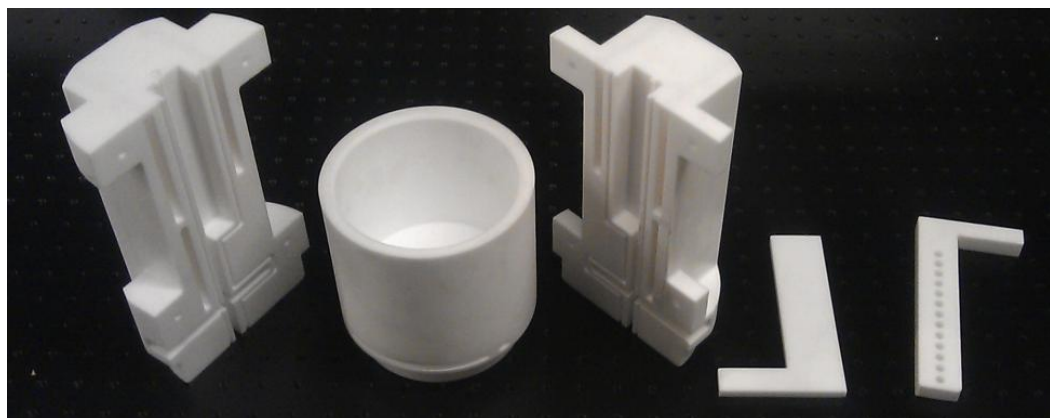
Figure 2.18: Front body, container, rear body, gate and wafer holder in order.

Suspended parts of the displacement sensing mechanism are released in a home-made Vapor HF Etching Setup in order to prevent device stiction to the substrate. Device release is accomplished at a wafer temperature of 65°C, yielding an isotropic etch rate of 40nm/min, for 25mins.

Figure 2.19 illustrates SEM micrographs of the sensing mechanism fabricated. As can be seen in Fig. 2.19a, the footprint of the sensing mechanism is about $85 \times 50 \mu m^2$. Despite proximity effect, fabrication of springs as the highest aspect ratio pattern with a value of 160:1 (length/width) is completed. Furthermore, being critical for effective coupling, waveguide-end geometries are properly fabricated as designed. SEM images of both springs and waveguide ends are illustrated in Fig. 2.19b. Since the device footprint is greater than subfield size, stitching accuracies in EBL are improved up approximately to 500nm and 200nm along lightwave propagation and its transverse directions, respectively, with the help of patch insertions at subfield boundaries where at least two patterns have to be continuous for device functionality. The input and output waveguides to and from the mechanism are suspended in air by 250nm-wide supports physically connected to anchors. Optical leakage from the waveguides through the supports is eliminated by utilization of elliptical intersections [38]. As demonstrated in Fig. 2.19c and 2.19d, physical supports are properly released such that out-of-plane tilting owing to residual internal stress of SOI at both the input and output waveguides is invisible. Since, otherwise, it would have caused remarkable deterioration in the quality of end-to-end waveguide coupling. The output waveguide of the mechanism is tapered off at 5° so as to minimize lightwave back-reflection for reliable output light intensity measurements. In mechanical surface profiling, sidewall roughness of approximately 9nm is measured. A typical SEM image illustrating sidewall roughness is as seen in Fig. 2.19e.
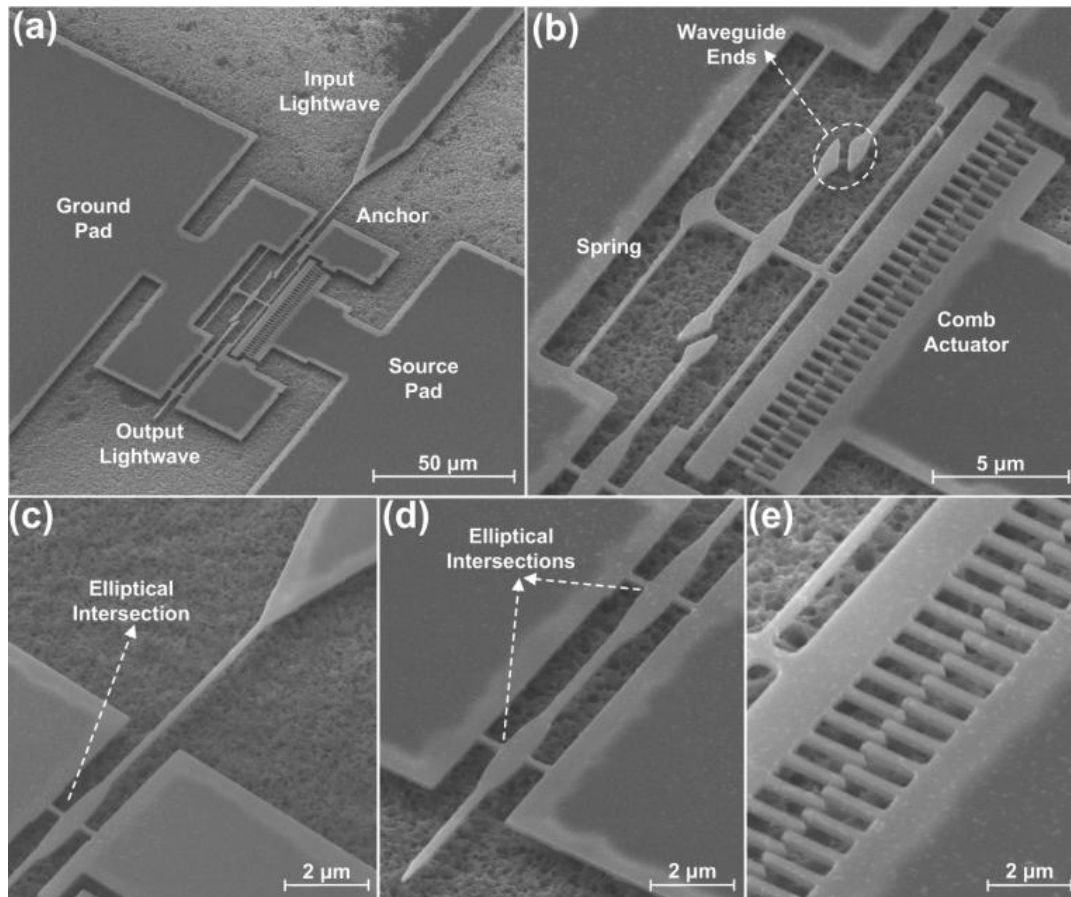
Figure 2.19: a) SEM images of the fabricated mechanism together with the actuator and contact pads. b) End-to-end waveguide coupling pairs and high aspect-ratio springs. c) Properly released 12μm-wide input waveguide with 10°-taper. d) 5°-tapered output waveguide suspended in air with the help of optical intersections in elliptical shape. e) A set of comb actuator fingers and a spring with smooth sidewalls after dry etching.

2.6 Characterization

Both mechanical and optical characterization of the sensing mechanism for experimental verification is conducted. In the mechanical characterization, displacement values during electrostatic actuation are calculated accurately by counting pixels between two reference points on the waveguide ends under an optical microscope with a mounted digital camera, and comparing the counted pixels to a sufficiently long reference entity whose length is known from SEM measurements as seen in Fig. 2.20.
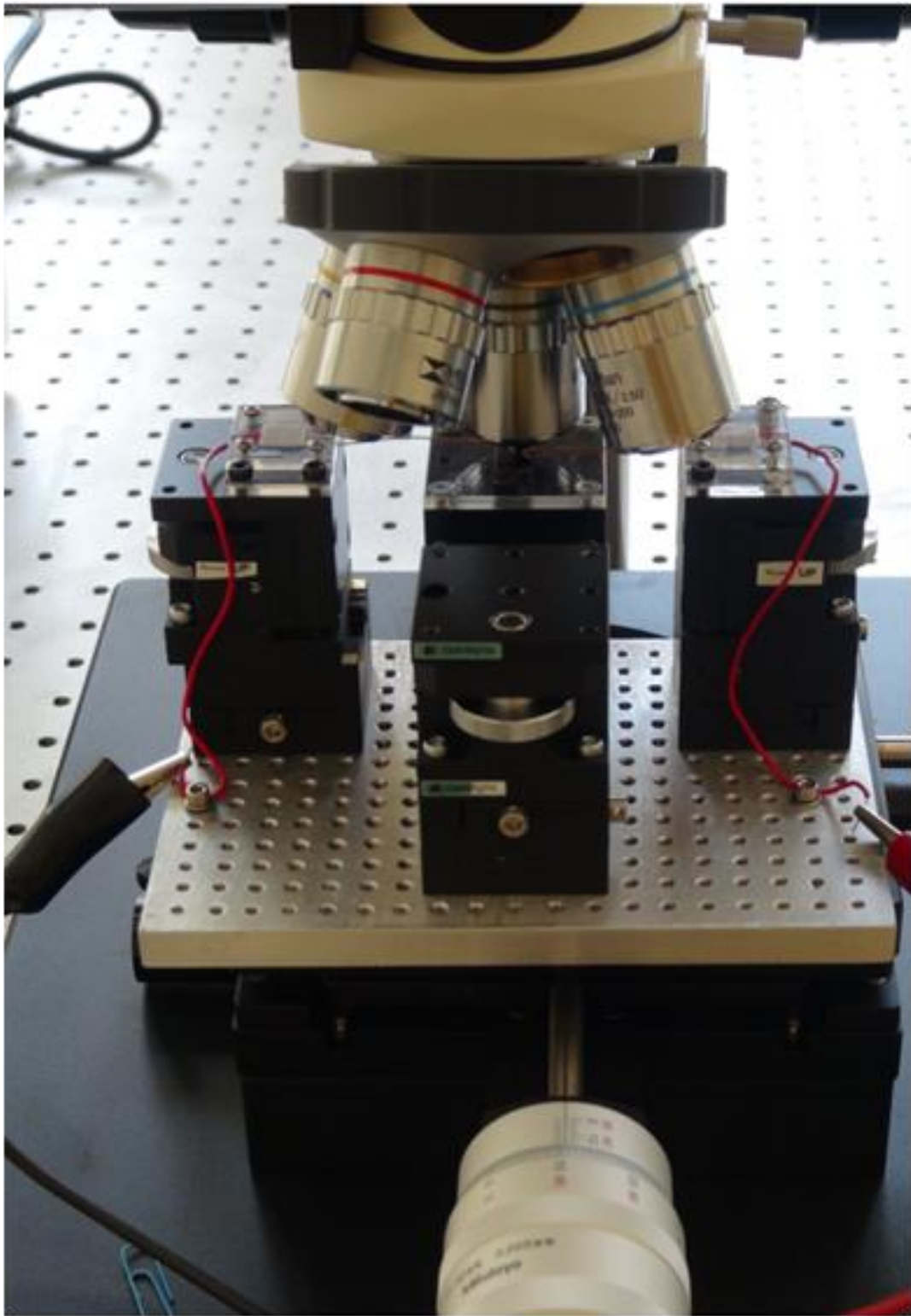
Figure 2.20: The mechanical characterization setup under the optical microscopy with positive and ground probes connected to sample holder.

In the optical characterization, a tunable solid-state Near Infrared (NIR) laser is used to excite the mechanism as shown in Fig. 2.21. Lightwave from the laser is coupled to a 12μm-wide waveguide at the input via a lensed single mode fiber. Then, the launched lightwave is offset sufficiently far by two 90°-bend waveguides in order to move SiO_2-coupled light away from the sensing region for background noise reduction. Lightwave propagating in 12μm-wide waveguide is narrowed down to 500nm-wide waveguide with the help of 10°-taper in order for nanophotonic displacement sensing in the near-field. Light experiences end-to-end coupling between input-movable and movable-output waveguide pairs. Uncoupled lightwave, on the other hand, is scattered in to the space at the air gap, and is detected by a NIR-sensitive Indium Gallium Arsenide (InGaAs) camera from top. Images obtained from the camera are processed in custom software for intensity calculation of scattered light spots. The software deploys pixel by pixel integration of light intensity on the NIR images. Total intensity values are then normalized on the fact that, because of conservation of energy, summation of scattered lights from the input, movable and output waveguides remain constant.
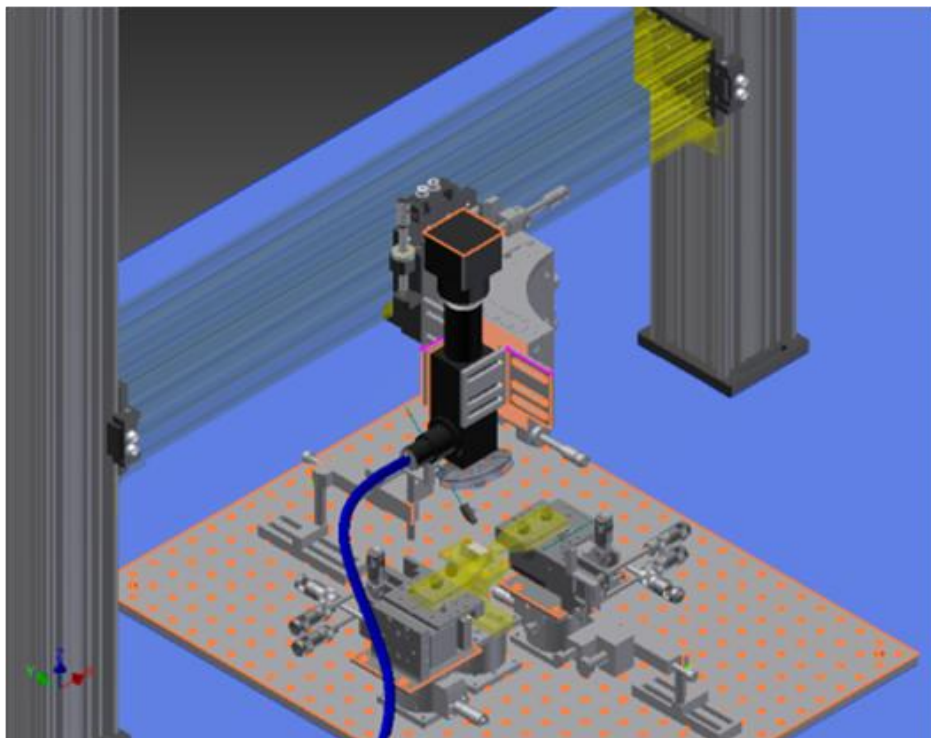
Figure 2.21: 3D model of optical characterization setup under the NIR camera with sample micro-positioner.

2.7 Results

Figure 2.22a depicts experimental characterization results of the sensing mechanism at 1.55μm wavelength along with their numerical counterparts in the range of 0nm to 1000nm at every 100nm. Experimental results agree well with the numerical ones with a maximum deviation of 2.77%. Insets of Fig. 2.22a illustrate the NIR images used to characterize the sensing performance at 0nm, 800nm and 1000nm displacements, denoted by *i*, *ii* and *iii*, respectively. Points 1, 2 and 3 in the insets represent the first waveguide-ends pair, the second waveguide-ends pair, and tapered output waveguide, respectively. Initially, a displacement value of 0nm is considered, where the movable waveguide is 1000nm apart from both the input and output waveguides. Because of large air gap between coupling waveguides, no light is able to propagate through the movable waveguide to the output. However, for instance, after 800nm of displacement, the output light intensity increases up to 56.23%. As the motion continues, finally, the air gap gets completely closed at 1000nm of displacement, which causes a boost in the optical output up to 92.12%. As a result, an effective measurement range between 0nm and 1000nm is achieved. Due to exponential nature of lightwave coupling in the near-field region, measurement sensitivity indeed varies with the particular displacement. For the proposed particular mechanism, the highest measurement sensitivity values take place approximately between 700-900nm displacement range with an average of 0.29% change of light intensity per nanometer. Displacement values in the non-700-900nm range are also measurable, nevertheless, sensitivities will be relatively smaller. Fig. 2.22b, on the other hand, illustrates the experimental spectral response obtained in the 1.52-1.60μm band for various displacements. Results show that as the displacement increases, wavelength dependency does so as well. However, it never exceeds 10%, indicating weak correlation. In addition, regardless the displacement, wavelength-independency is observed in the 1.550-1.565μm band.
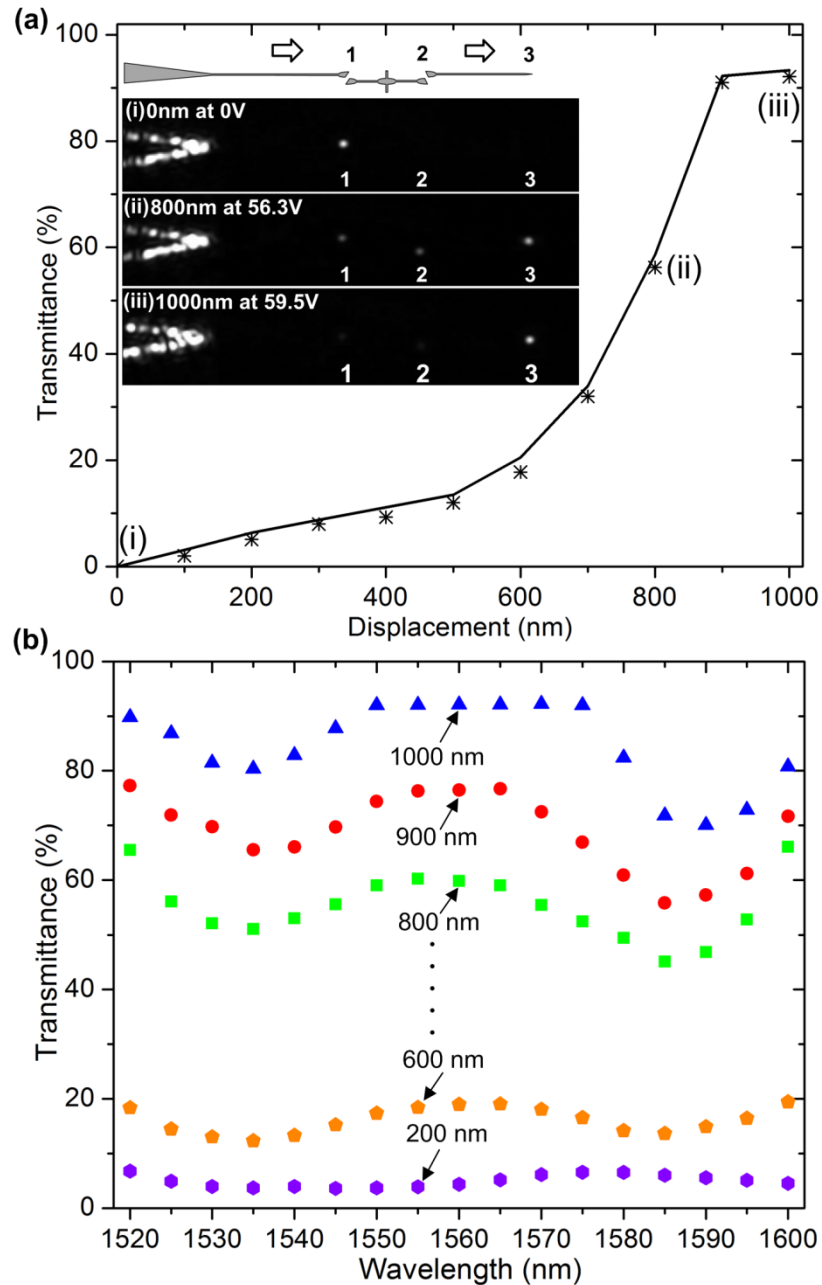
Figure 2.22: a) Experimental characterization results of the mechanism at 1550nm wavelength together with their theoretical counterparts in the range of 0nm to 1000nm. Insets illustrate the NIR micrographs shot at displacement values of 0nm, 800nm and 1000nm. b) Experimental spectral response obtained in the 1520-1600nm band at various displacements. Discrete markers and solid line depict the experimental results and curve regressed to the numerical results, respectively.

2.8 Summary

An embedded nanophotonic displacement sensing mechanism using end-to-end waveguide coupling in the near-field region is simulated, fabricated and characterized. The approach is capable of yielding high displacement-sensitivity, subwavelength measurement range, high wavelength-insensitivity and small footprint. Specifically, respective values of maximum 0.29% change of light intensity per nanometer, about 1000nm, and $85\times50\mu m^2$ in area including the motion source are achieved both numerically and experimentally at 1.55μm wavelength. The studied mechanism has weak dependency on wavelength in the range of 1.52-1.60μm providing wide bandwidth. It is well-suited for real-time displacement and distance measurements in integrated optical circuits operating with the help of embedded NEMS/MEMS actuation. The mechanism is estimated to find use also in various nano-scale positioning and imaging applications.

3. SUB-NANOMETER MECHANICAL TUNING OF EVANESCENT WAVE MODE COUPLING IN PLANAR LIGHTWAVE CIRCUITS

3.1 Introduction

Planar Lightwave Circuits (PLCs) technology is promising since being capable of replacing a set of conventional optical components in an integrated fashion over a monolithic layer, which in return provides footprint, speed and cost advantages. Signal routing in such circuits amongst components is an indispensable function for which various methods have already been investigated [39, 40]. Bulgan *et al.* have fabricated submicron silicon waveguide optical switch driven by electrostatic comb actuator on SOI as well [10]. This unique method has utilized mechanical tuning of evanescent wave mode coupling at 1550nm wavelength. In this approach, due to high dependency on fabrication and actuation errors, only 27.40% mode coupling between input/movable and movable/output waveguide pairs was achieved. In order to enhance such low level of mode coupling for effective routing, various waveguide tip-end sizes at the contact surfaces were studied numerically using FDTD [11]. The outcome of the study has shown that enlarged tip geometries allow higher levels of mode coupling. Effect of tip angle has also been investigated, and the results have indicated that optical performance increases when ends with angles greater than the Brewster's are employed [41]. As a result, an embedded sensing mechanism for mechanical excitations based on the nanophotonic effect called end-to-end waveguide coupling in the near-field has recently been presented [42]. The measurement sensitivity and range obtained at 1550nm wavelength were 3.44nm per percent of light intensity change as local maximum, and about 1000nm, respectively.

In this chapter, we report two superior mechanisms with mechanical tuning capability down to sub-nanometer values. Mechanisms presented herein are both based on the evanescent wave mode coupling. This highly-efficient approach is intended to equip scientists and engineers in NEMS and nanoscale devices with a technique that can generate high-intensity-contrast at ultra-short mechanical excitation strokes within PLCs.

3.2 Structure And Principle
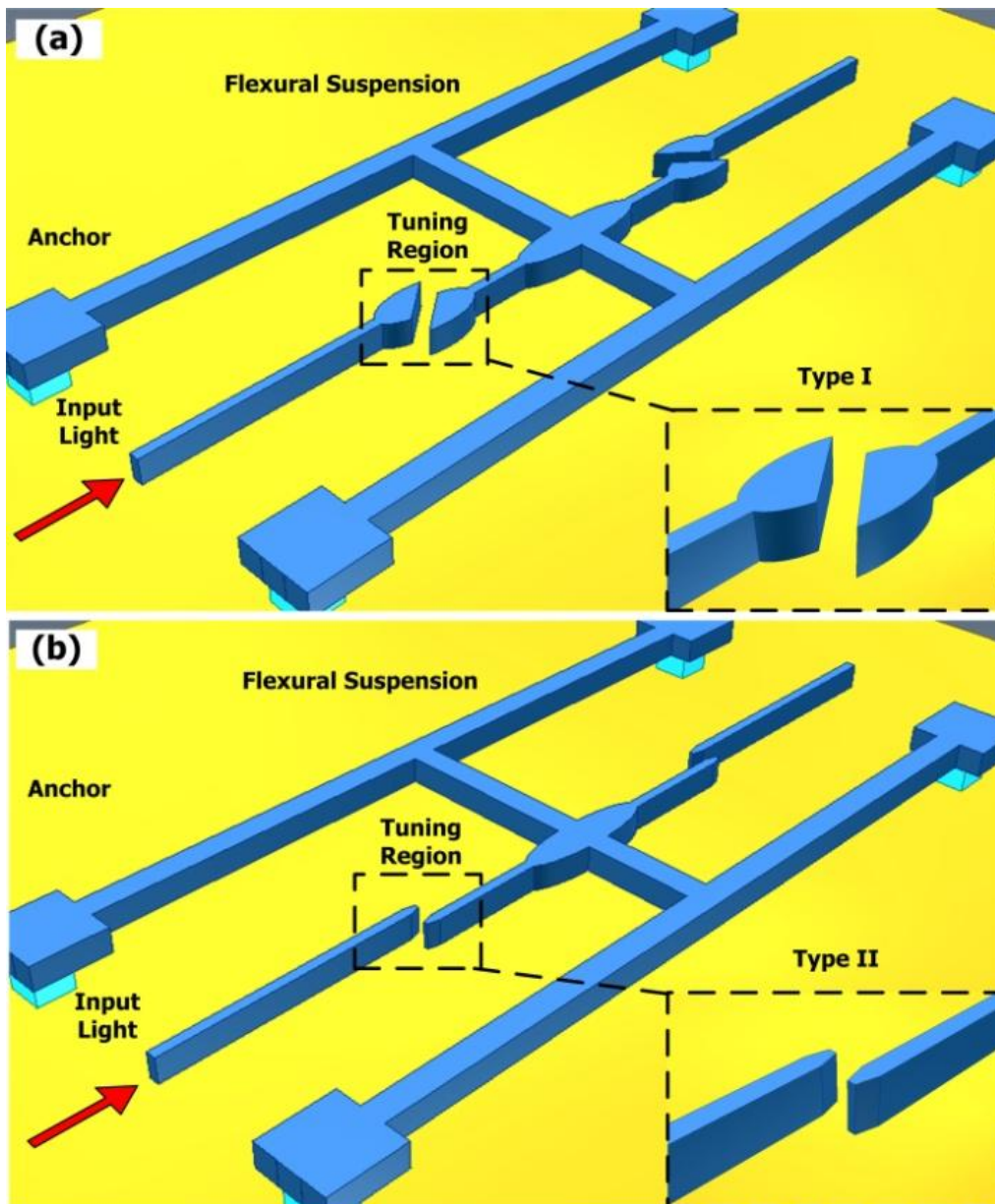
Figure 3.1: Schematic views of the mode coupling mechanisms for sub-nanometer mechanical tuning. Insets depict close-up views of tuning regions. a) First mechanism with elliptical tuning region, Type I. b) Second mechanism with trapezodial tuning region, Type II.

Fig. 3.1 illustrates the schematic views of the mechanically tunable evanescent wave mode coupling mechanisms. Both consist of subwavelength-scale input and output, and a tuning waveguide controlling mode coupling in between. The tuning waveguide is suspended via two doubly-clamped flexure sets in air for mechanical excitability.

First mechanism, as shown in Fig. 3.1a, referred to as type I, is based on an elliptical waveguide employed to couple lightwave over large contact surfaces between input and output. Whereas, second mechanism, as seen in Fig. 3.1b, referred to as type II, is based on trapezoidal waveguide deployed to couple lightwave through relatively small contact surfaces. In both mechanisms, input/tuning and tuning/output end-to-end pairs have initial offsets inhibiting the lightwave propagation. As tuning waveguide is excited mechanically towards both the input and output, mode coupling in the evanescent wave region will experience increase, which enables tunability.

3.3 Numerical Study

First, detailed numerical investigation of the mechanisms is conducted in 3D FDTD Analysis software. TE-polarized light is single-mode at 1.55μm wavelength. Incident TE polarized electric field is perpendicular to the device layer. Refractive indices of silicon, SiO_2, and air are 3.46, 1.47, and 1, respectively. Bottom and upper claddings are 2μm-thick SiO_2 and 1μm-thick air, respectively, in order to keep optical propagation loss low in the waveguides [1]. In order to satisfy numerical stability conditions for reliable calculation, mesh size values in the numerical studies are 25nm and 20nm for the first and second mechanisms, respectively. Dimensions in the first mechanism are respectively 500nm, 340nm, 1.5μm and 4.8μm as widths and thicknesses of straight waveguides, and as widths and lengths of the elliptical regions where critical mode coupling occurs. Dimensions in the second mechanism, on the other hand, are 600nm, 340nm, 100nm and 10.5° as waveguide widths, thicknesses, end-sizes and angles, respectively.

3.3.1. Effects of tip-end size and tip angle of Type I

Elliptical tip geometry is 1.5μm-wide, 4.8μm-long, and 260nm-thick. Various tip angles of 10º, 20º, 30º, 40º, 50º, 60º, 70º, and 80º are studied for mechanical excitation values of 25nm, 50nm, 75nm, 100nm, 200nm, 300nm, and 600nm. Results are shown in Figs. 3.2 and 3.3.

Data depicted in Fig. 3.2 suggest that the smaller the tip angle, the higher the tunability. While at 40º tip angle, for example, the tunability is 1.24nm per percent of light intensity, it is expected to be less than 1.24nm per percent of light intensity for elliptical tips with angles smaller than 40º. However, such geometries, as it can be

seen from the A-A inset in Fig. 2.2, again because of the very same reason, are highly dependent on gaps left between contact-tips owing to their sidewall surface roughness.
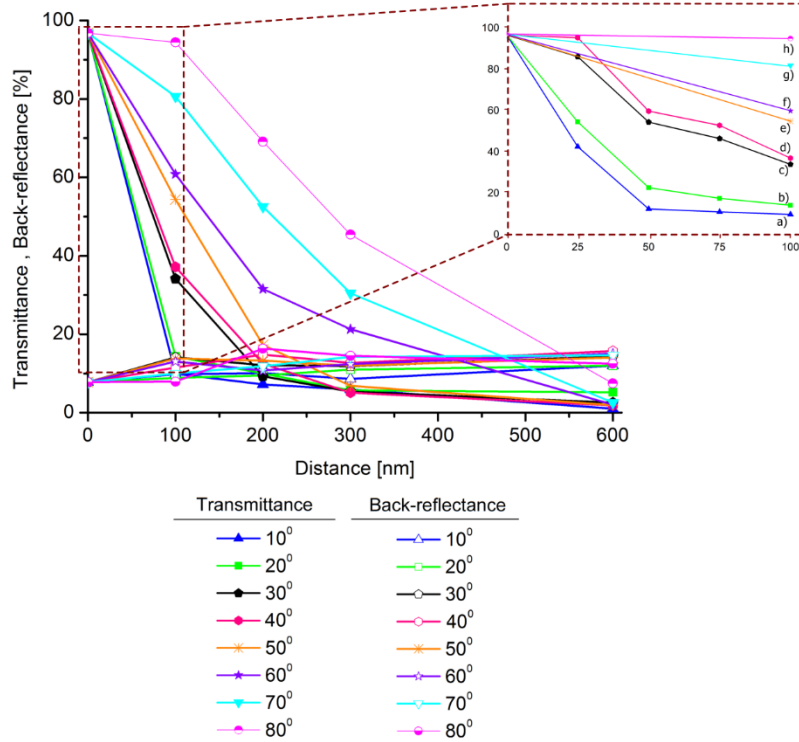
Figure 3.2: Calculated transmittance and back-reflectance as a function of distance, D, at the tip angles, θ, of 6.3º, 10º, 20º, 30º, 40º, 50º, 60º, 70º, and 80º for 4.8μm-long and 1.5μm-wide elliptical tip geometry.

Figure 3.3 illustrates special points in Fig. 3.2 at 100nm for various tip angles to understand behavior of the lightwave as it experiences tip geometry of type I. The reason why 100nm distances are particularly looked in detail is because fabrication errors are estimated to be within this distance range. High optical response above 100nm is desirable in achieving high-contrast, thereby, high-tunability sub-nanometer mechanical tuning mechanisms. As seen in Figs. 3.3a and 3.3b, at tips with 10º and 20º angles, about 15% of lightwave almost does not propagate to the output. Nevertheless, an acceptably high level, about 40%, of lightwave reaches to the output tip angles from, say, around 30º up to 40º, as presented in Figs. 3.3c and 3.3d. As of tip geometries with approximately 50º tip angle and above up to around

60º, a strong portion, about 60%, of lightwave is able to propagate to the output, as depicted in Figs. 3.3e and 3.3f, suggesting the last suitable candidate below the Brewster's angle towards realization of high-tunability mechanical tuning mechanism. Tips with angles above 60º even when they are below the Brewster's such as 70º and those above the Brewster's are understood to be inappropriate for high-tunability mechanical tuning mechanisms since most of the light above 80% is able to reach to the output causing very low contrast in optical response.
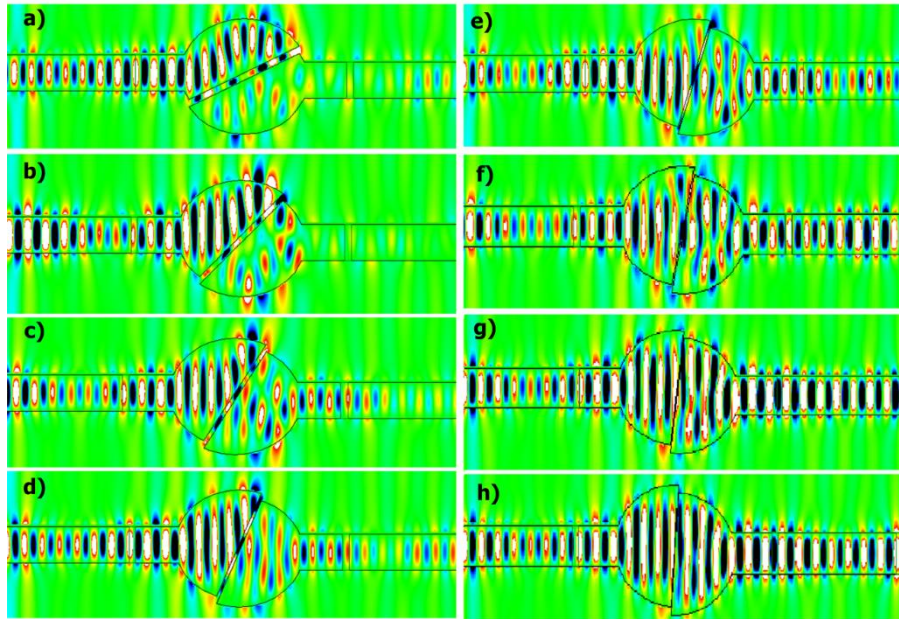
Figure 3.3: Electric field (Ex) at 100nm distance as a function of tip angles at. a) 10º. b) 20º. c) 30º. d) 40º. e) 50º. f) 60º. g) 70º. h) 80º.

Numerical analysis results showed that at elliptical tips with a length of 4.8μm, for tip angles of below 10º, 20º, 30º to 40º, and 50º measurement tunabilities of 1.10nm, 1.24nm, 3.05nm, 4.6nm, and 5.74nm per percent of light intensity at measurement ranges of 135nm, 149nm, 325nm, 485nm, and 674nm, respectively, are observed. Since the surface sidewall roughness are expected to be minimized down to about 20nm total in the tips by precise fabrication, elliptical geometries with the angles in the range from 30º up to 40º will provide the optimal solution for the highest-tunability in type I.

3.3.2. Effects of tip-end size and tip angle of Type II

Optical performance of type I structure is studied at 25nm, 50nm, 75nm and 100nm distances, whose results are shown in Figs. 3.4 through 3.6. First, for the tip angle of

8.5º, effect of tip-end sizes is investigated. Results are as provided in Fig. 3.4. When tip-end size is reduced from 200nm to 100nm, optical response gets increased from 85.62% to 96.49% at 25nm distance, reducing fabrication imperfection dependency. Furthermore, for distances in the range of 25nm to 100nm, the contrast in optical response also increases causing increase in tunability as well. Insets in Fig. 3.4 illustrate propagation of lightwave at specific points. Optical performance for the mechanically tunable evanescent mode coupling mechanisms with 100nm tip-end size at 8.5º tip angle change from 96.49% to 28.72% between 25nm and 100nm mechanical excitation values, respectively, corresponding to a tunability of about 1.10nm per percent of light intensity.
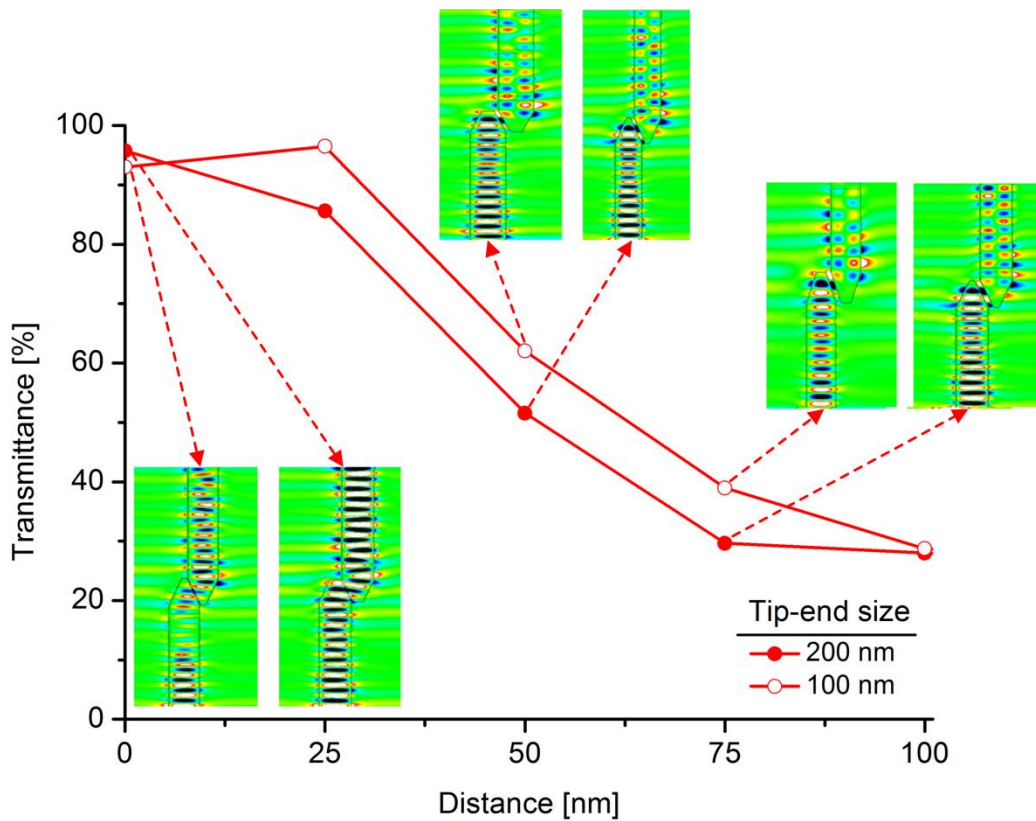
Figure 3.4: Optical response at the tip angle θ of 8.5º for tip-end sizes.

Next, for the tip angle of 9.5º, effect of tip-end sizes is studied. Results are as depicted in Fig. 2.3.2.2. When tip-end size is reduced from 200nm to 100nm, optical response gets increased from 84.89% to 97.36% at 25nm distance, reducing fabrication imperfection dependency. Furthermore, for distances in the range of

25nm to 100nm, the contrast in transmittance also increases causing increase in measurement tunability as well. Insets in Figure 3.5 illustrate propagation of lightwave at particular points. Optical performance for the mechanically tunable evanescent mode coupling mechanisms with 100nm tip-end size at 9.5º tip angle change from 97.36% to 25.99% between 25nm and 100nm mechanical excitation values, respectively, corresponding to a tunability of about 1.05nm per percent of light intensity.
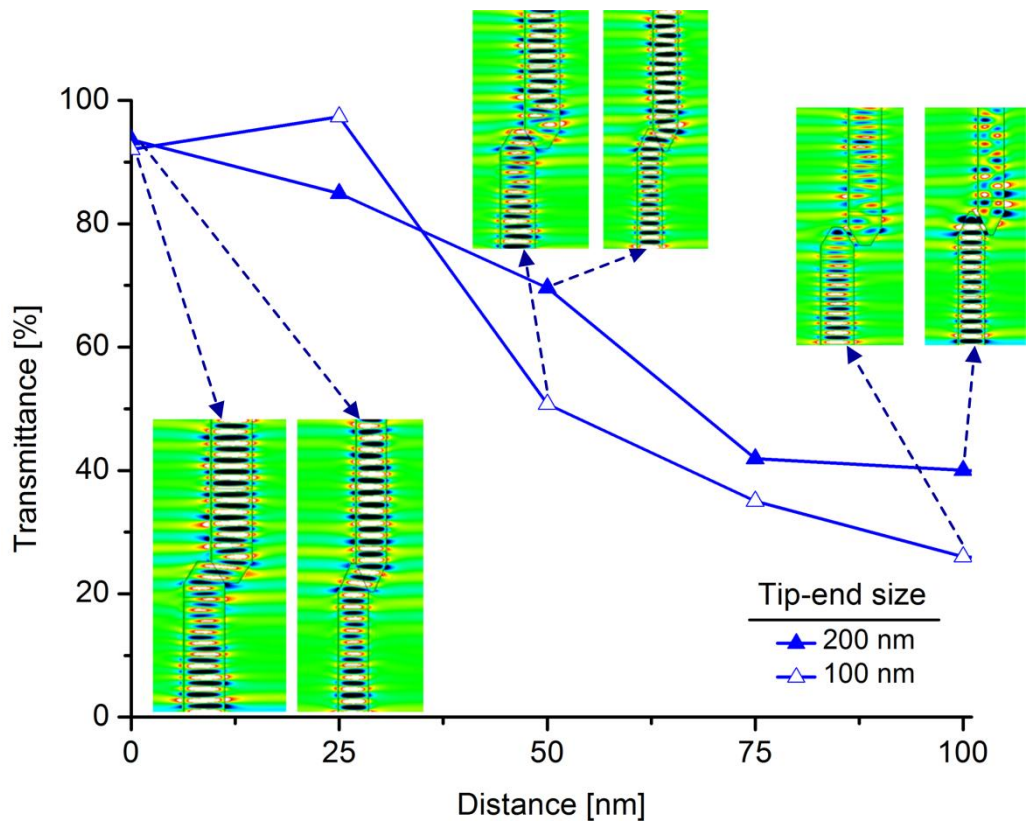
Figure 3.5: Optical response at the tip angle θ of 9.5º for tip-end sizes.

Last, for the tip angle of 10.5º, effect of tip-end sizes is studied. Results are as depicted in Fig. 3.5. When tip-end size is reduced from 200nm to 100nm, transmittance gets increased from 88.25% to 93.14% at 25nm distance, reducing fabrication imperfection dependency.

Furthermore, for distances in the range of 25nm to 100nm, the contrast in optical response also increases causing increase in measurement tunability as well. Insets in Figure 3.6 illustrate propagation of lightwave at particular points. Optical

performance for the mechanically tunable evanescent mode coupling mechanisms with 100 nm tip-end size at 10.5º tip angle change from 93.14% to 25.93% between 25nm and 100nm mechanical excitation values, respectively, corresponding to a tunability of about 1.11nm per percent of light intensity.
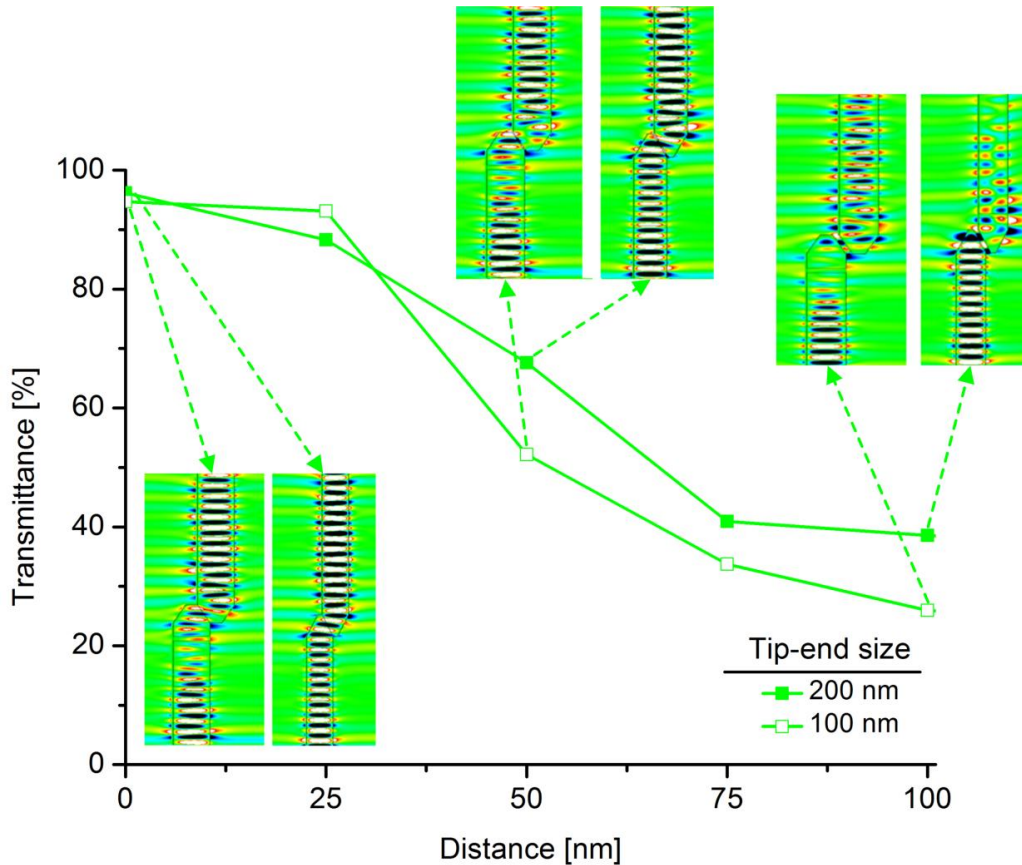
Figure 3.6: Optical response at the tip angle θ of 10.5º for tip-end sizes.

Figure 3.7 illustrates the numerical study results obtained at 25nm and 150nm mechanical excitation values so as to perceive evanescent wave behavior as it experiences type I and type II mechanisms. As illustrated in insets *i* and *iii* of Fig. 3.7, mode couplings at 25nm are 7.52% and 13.92% for type I and type II, in order. When the mechanical excitation is increased to 150nm, as depicted in insets ii and iv of Fig. 3.7, coupled evanescent waves are tuned to 92.23% and 96.17% for type I and type II, respectively.

As a result, the tunability and range values for type I and type II mechanisms are calculated to be about 1.47nm and 1.51nm per percent of light intensity change, and 150nm range, from 0nm to 150nm, respectively.
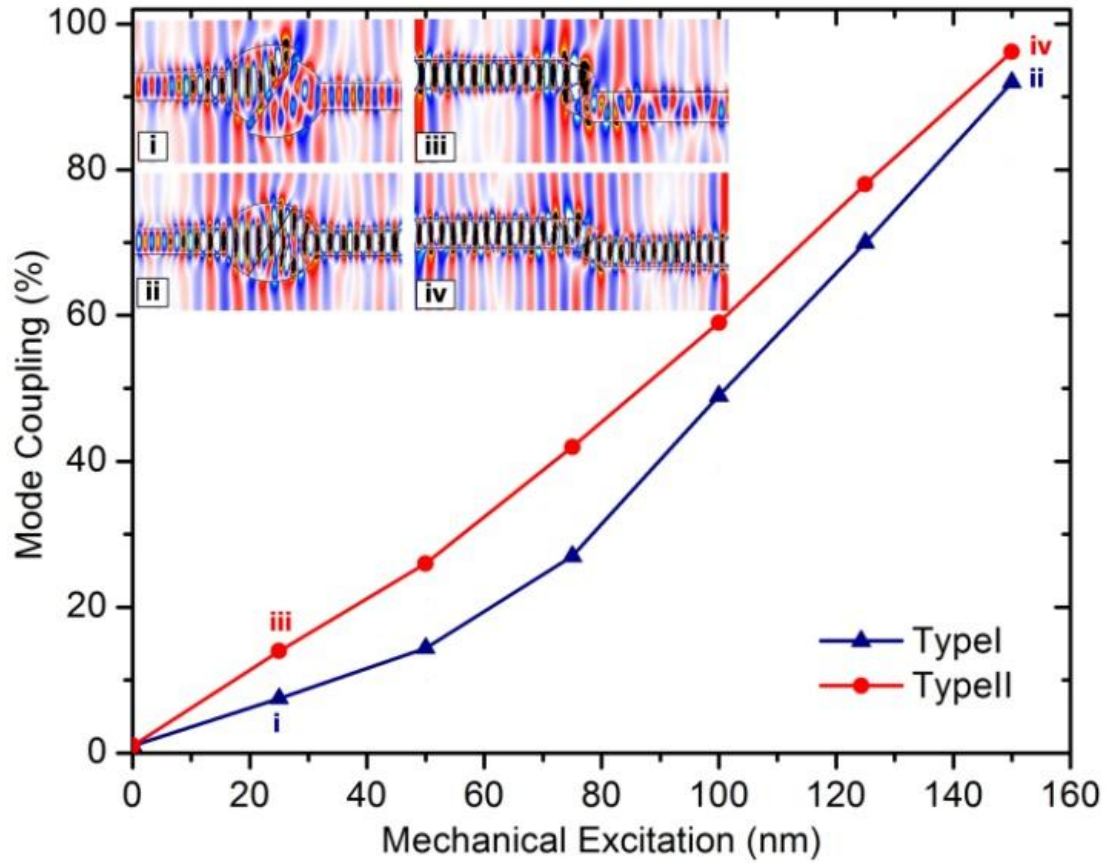
Figure 3.7: Calculation results for mode coupling in Type I and Type II tuning mechanisms as a function of the mechanical excitation from 0nm to 150nm. Insets depict electrical field distributions for both elliptical and trapezoidal coupling regions at 25nm and 150nm mechanical excitations, respectively.

3.4 Experimental Study

Mechanically tunable evanescent mode coupling mechanisms are fabricated on an SOI wafer with 340nm-thick device silicon and 1μm-thick SiO_2 layer. Both mechanisms share the same process plan and recipes. First, 120nm-thick PMMA as positive electron beam resist is spin coated as seen Fig. 3.8a. Then, features are patterned using EBL as shown in Fig. 3.8b and 3.8c.
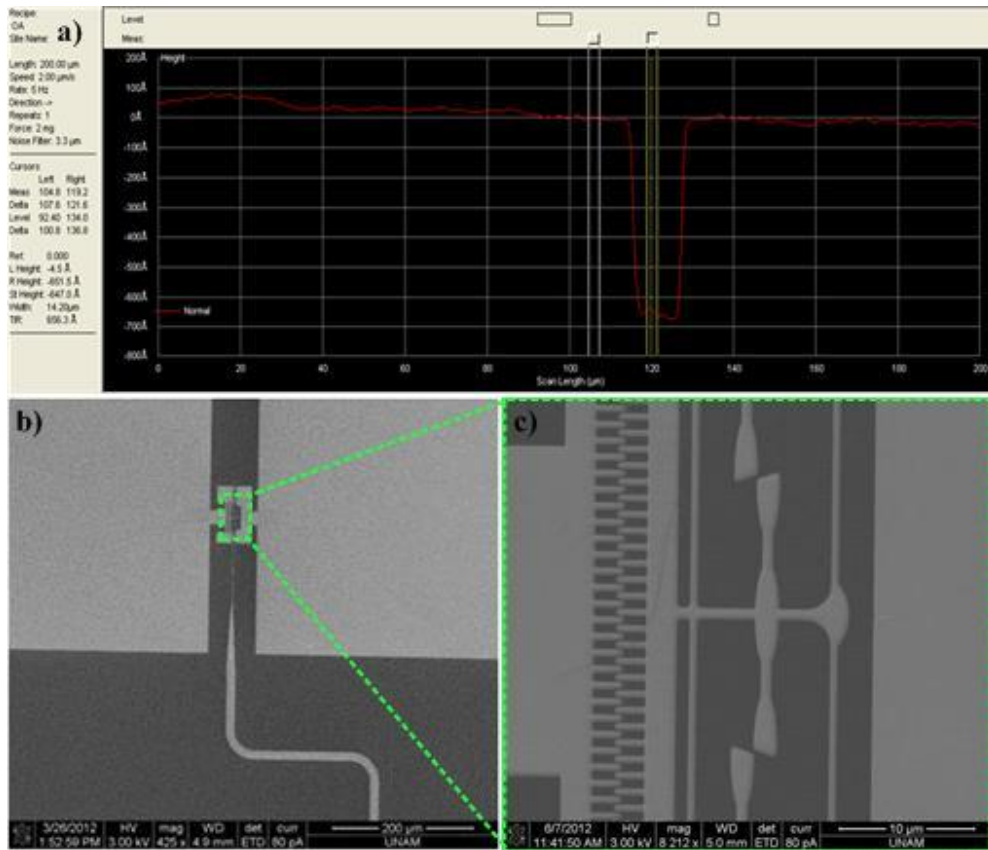
Figure 3.8: a) Thickness of positive resist under the surface profilometer. b) Exposed results of the mechanisms with ground, source pads and input waveguide after the EBL. c) Mechanically tunable evanescent mode coupling.

Next, 50nm-thick chromium is deposited on top of the device by electron beam evaporation with 3nm/min deposition rate as shown in Fig. 3.9. Deposition rate is kept as small as possible to ensure minimum roughness of waveguide sidewalls. The remaining PMMA is lifted off from the wafer surface as seen in Fig. 3.10.
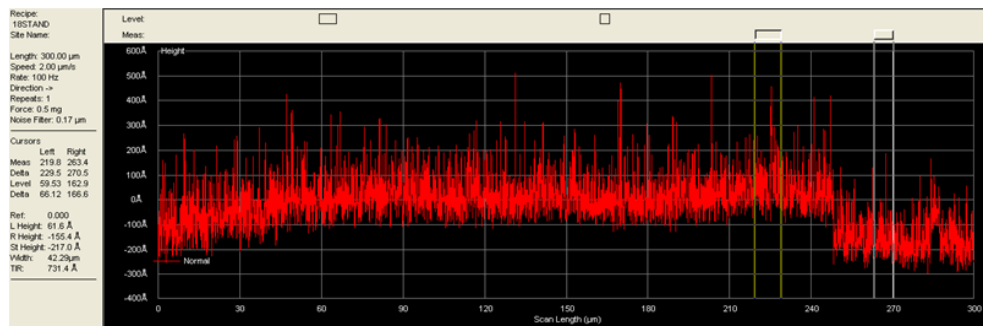
Figure 3.9: Thickness of the chromium layer after evaporation process.

52
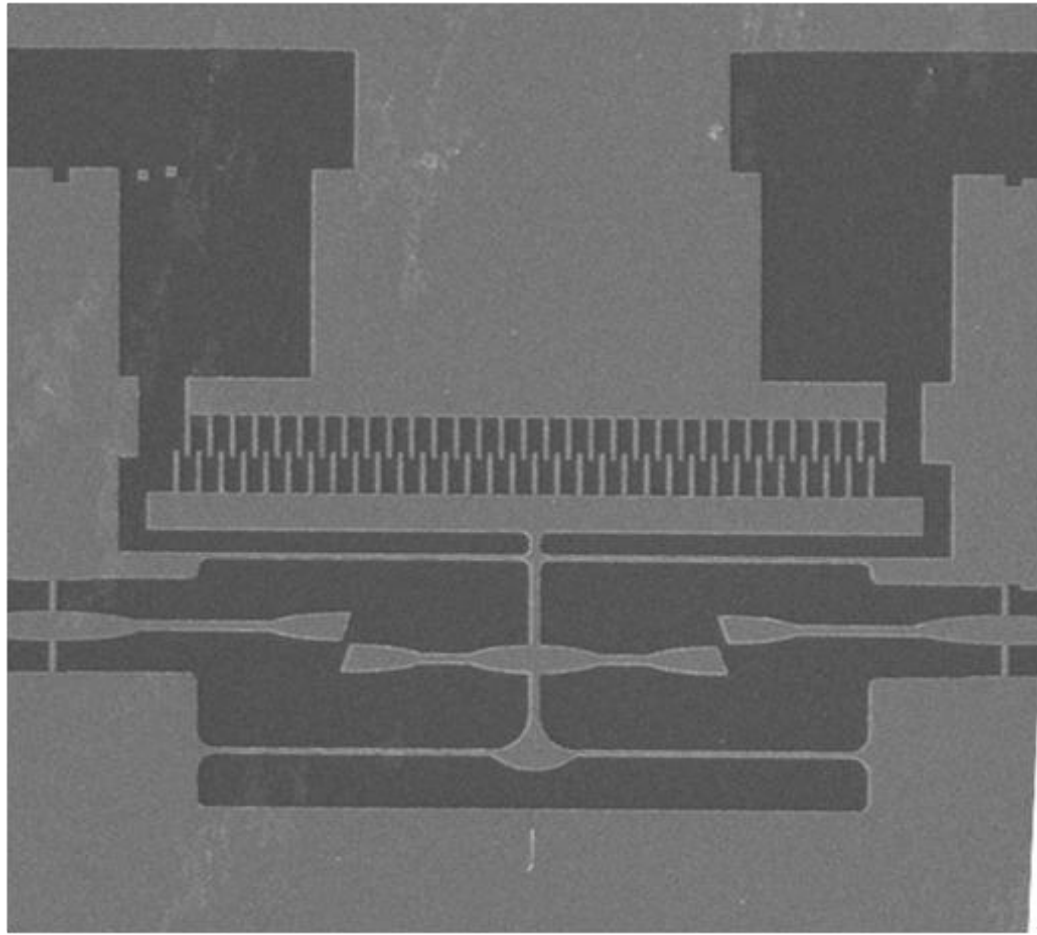
Figure 3.10: The lift-off of the mechanism after metal evaporation process. The darker windows depicts silicon layer and the brighter windows depicts chromium layer as a hard mask.

Then, the device silicon layer is dry etched in ICP-DRIE with 34.34nm/min etch rate using SF_6 and O_2 gases as activation and passivation gases, respectively. Various recipe parameters is utilized to optimize the etch rate. In each recipe, cycle number of activation and passivation is changed to understand the effect to etched amount of the silicon. 20, 40, 80 and 100 number of cycle is utilized in the a, b, c, and d recipes in order. As a results, 101nm, 122nm, 238nm and 351nm etched silicon are achieved. Figure 3.11 shows the thickness of the etched silicon under the surface profilometer after the ICP-DRIE process from a to d recipes, respectively.
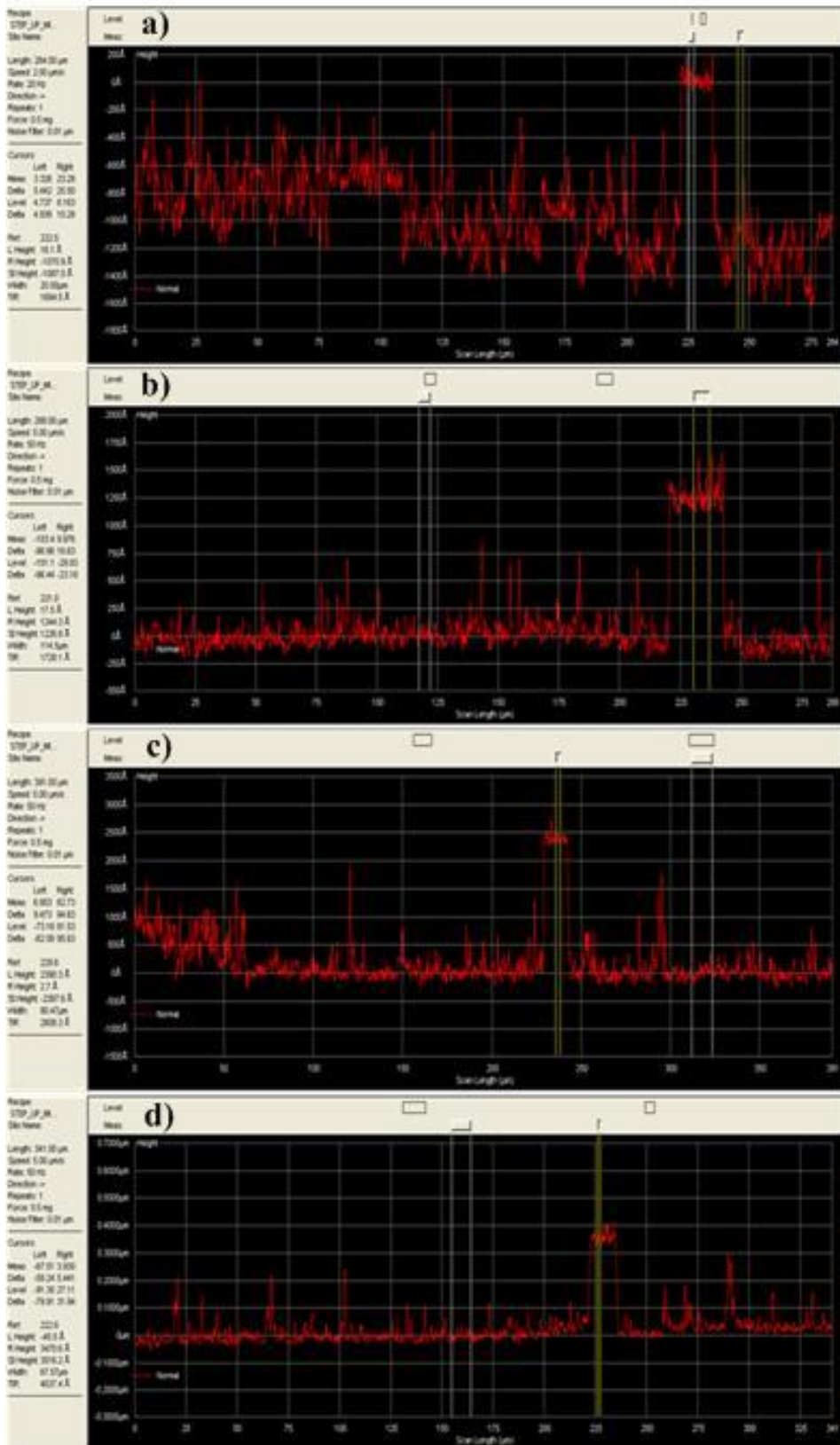
Figure 3.11: Recipes of ICP-DRIE process with various cycle number.

Finally, evanescent wave mode coupling mechanisms are released at 65° wafer temperature with 40nm/min etch rate in a home-made Vapor HF Etching setup in order to prevent the device silicon layer stick to substrate. At the start-up the setup, to initialize the all system, parameters in the Table 3.1 should be enter.

Table 3.1. The parameters of Vapor HF Setup.

	Kp	Ki	Kd	Control Period (sec)	Target Temp. (°C)	Max. Temp. (°C)	Stable Temp. (°C)	Time (min)
HF Acid	5	40	8	20	60	69	61	30
SOI Sample	1	40	8	20	50	63	50	28

Time control is significant parameter for fabrication without any problem at the Vapor HF process. When the time is so short, cannot release the SiO_2 properly and the process should start again. When the time is so long, all suspended devices brakes and stick to substrate because of the SiO_2 release. Figure 3.12 shows that different times of Vapor HF process belongs to over and normal etch in order.
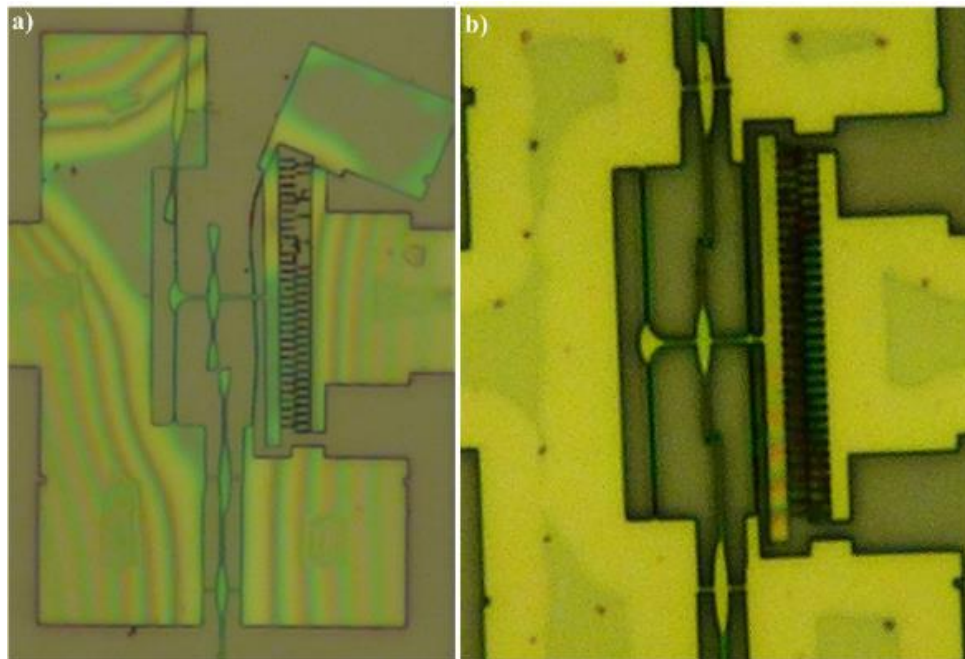
Figure 3.12: Different etch times at Vapor HF Setup. a) Over etch. b) Normal etch.

Fig. 3.13 illustrates SEM micrographs of the fabricated mechanisms on SOI. 300nm mechanical excitation at approximately 32V DC between the input/tuning and tuning/output waveguides under investigation, comb actuator with 32 finger pairs which are 200nm-wide, 2μm-long are properly designed and fabricated to verify performances of tuning mechanisms. The initial overlap in each finger pair utilized is 100nm. Footprints of the actuator for both mechanisms are $32.3 \times 8 \mu m^2$. A set of two doubly-clamped flexures with an equivalent spring coefficient of 0.52N/m are employed to suspend in both mechanisms. Flexural suspensions are properly released such that out-of-plane tilting owing to residual internal stress release at both the input and output waveguides are observed to be negligible, since otherwise this would have caused significant deterioration in mode coupling.
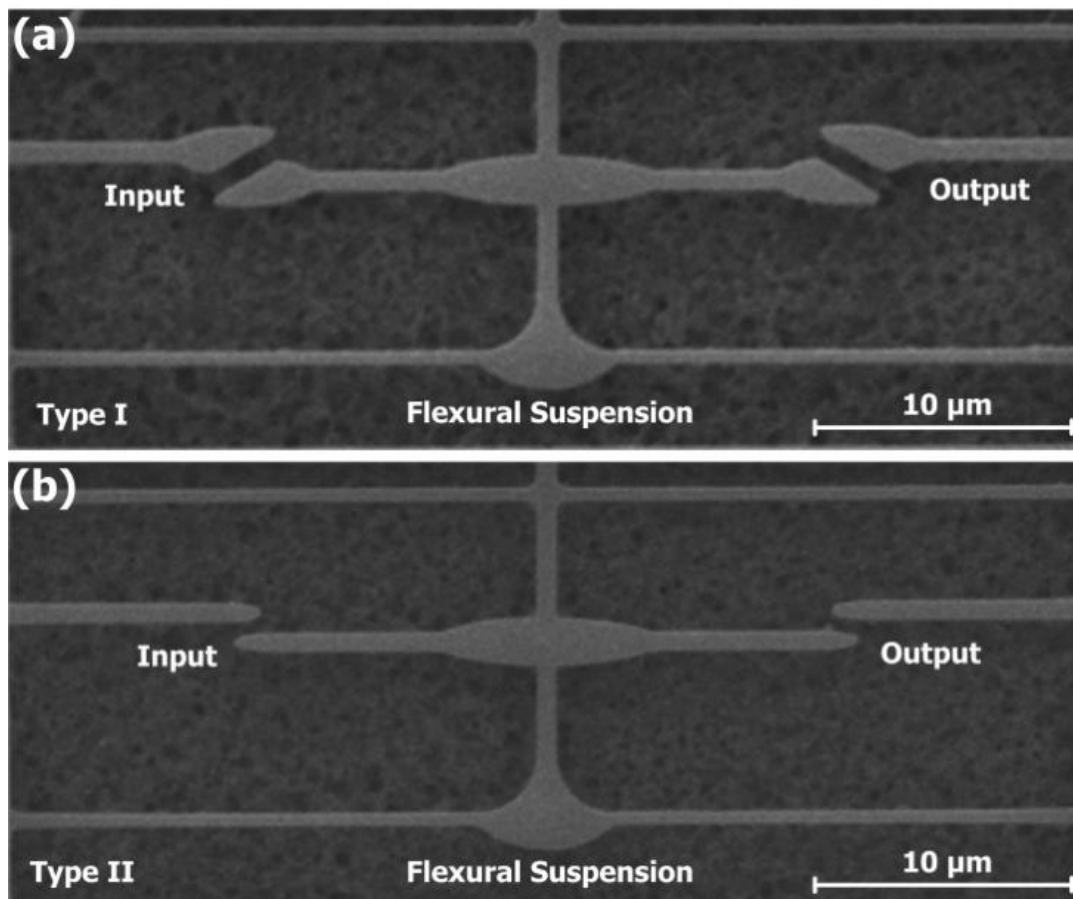
Figure 3.13: SEM images of the fabricated mechanical tuning mechanisms and doubly-clamped flexure sets for evanescent wave mode coupling. a) The elliptical region. b) The trapezodial region.

Also, 200:1 aspect ratio of the suspensions are fabricated despite proximity effect. As can be seen in Fig. 3.13a and 3.13b, each tuning mechanism alone excluding the actuator is about $45 \times 25 \mu m^2$. Surface roughness of the mechanisms is measured under the stylus surface profiler as 9nm, a sufficiently small value to achieve negligible optical propagation loss in the mechanisms. Tip of the output waveguide is tapered off 5° so as to minimize lightwave back-reflection.

3.5 Characterization

Excitation levels during actuation by the comb drive in mechanical characterization are calculated by counting pixels between two reference points under an optical microscope with a mounted high-definition digital camera. Counted pixels are compared to a sufficiently long reference entity whose length is known from SEM measurements. An accuracy of approximately 12nm is obtained in the mechanical excitation.
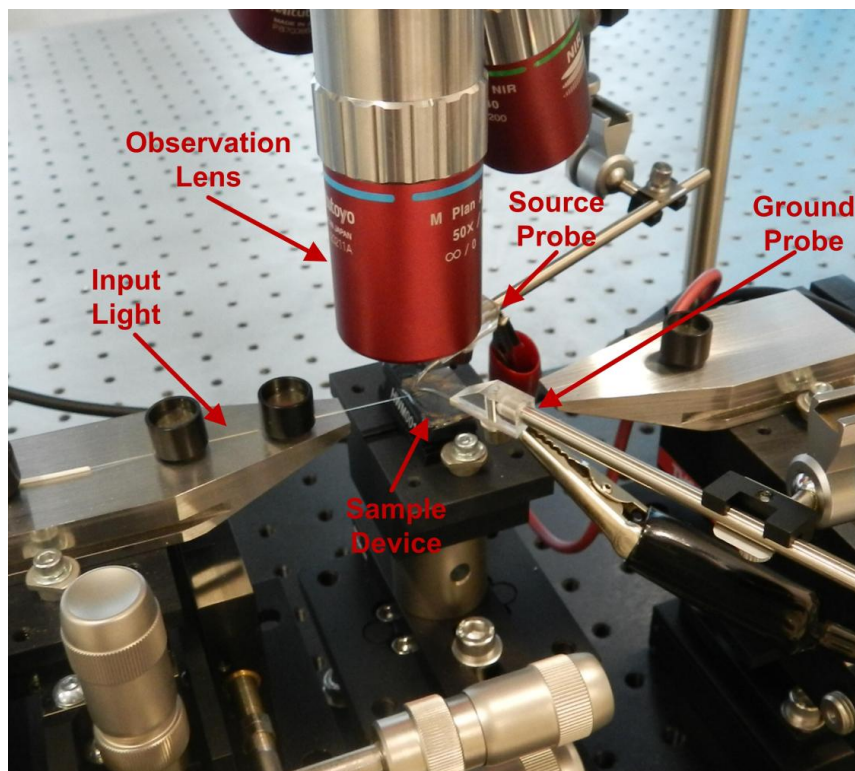
Figure 3.14: Characterization system under the NIR camera connected to source and ground probes and light propagate in optical fiber.

In the optical characterization of samples, a tunable solid-state NIR laser is used to excite the mechanism. Lightwave from the laser is coupled to a 12μm-wide waveguide at the input via a lensed single mode fiber. Then, the launched lightwave is offset sufficiently far by two 90°-bend waveguides in order to move SiO_2-coupled light away from the tuning regions for background noise reduction. Lightwave propagating in 12μm-wide waveguide is narrowed down to sub-micron waveguide with the help of 20°-tapers. Optical response characterization is based on the fact that any uncoupled optical signal in the sub-nanometer mechanical tuning mechanisms gets scattered into the space, and is detected by a NIR-sensitive InGaAs camera from top, as seen in Fig. 3.15. Exact values are achieved in home-made image processing software by integrating each pixel's brightness at scattered light spots of input/tuning, tuning/output and 5°-tapered output waveguide tips. At 150nm initial offset, where whole input lightwave gets scattered from the input waveguide into air, total brightness of the input light spot calculated corresponds to 100% of the light intensity launched. On the other hand, as the mechanisms get excited to a value below 150nm, evanescent wave starts coupling to accomplish tuning functionalities as a result of which scattering simultaneously weakens. The optical performance of both mechanisms are measured at various mechanical excitations. Provided that the energy is conserved, summation of lightwave scattered at all tips in a mechanism at all excitations remains constant. Figure 3.15 illustrate the mechanical in the left, optical characterization setup in the right in order.
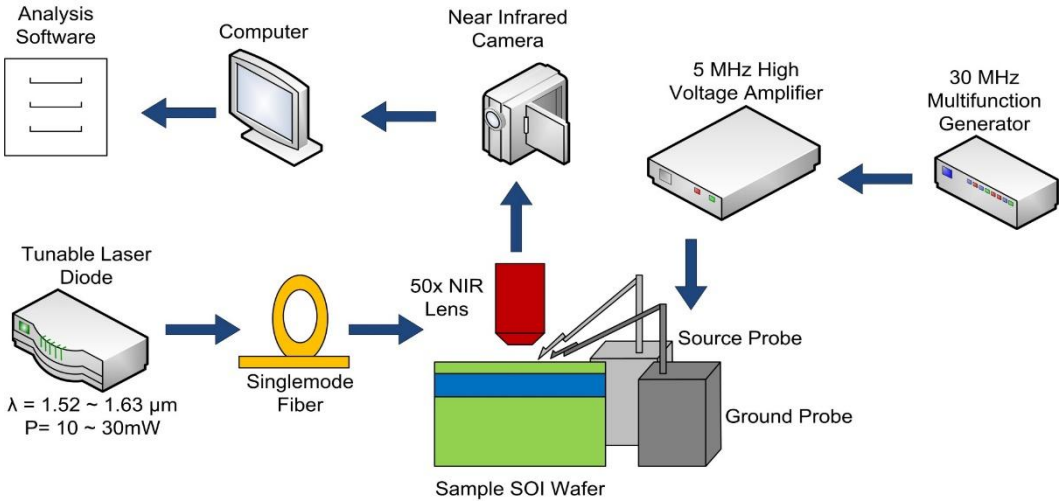
Figure 3.15: Mechanical and optical characterization setup.

3.6 Results

Experimental results of the mechanical and optical characterization for the mechanisms are as shown in Fig. 3.16. While *i* and *ii* in the left column of Fig. 3.16 illustrate representative results of low-coupling and high-coupling cases for type I tuning mechanism at 25nm and 150nm excitation levels in order, *iii* and *iv* depict their counterparts for type II in the same order. Spots 1, 2 and 3 in Fig. 3.16 show input/tuning and tuning/output regions, and tapered tip of output waveguide, respectively. As seen in NIR optical images in the right column of Fig. 3.16, as excitation levels increase, coupling in the tuning regions increases causing stronger light intensities at the tip of output waveguides shown by spots numbered 3. When the mechanical excitation, for instance, is increased from 25nm to 150nm, evanescent wave mode coupling from input to output in type I mechanism increases from 5.26% to 81.34%, respectively, corresponding to about 1.63nm per percent of average light intensity change. Corresponding values in the same excitation range in type II mechanism are from 9.82% to 90.37%, and about 1.55nm per percent of average light intensity change.
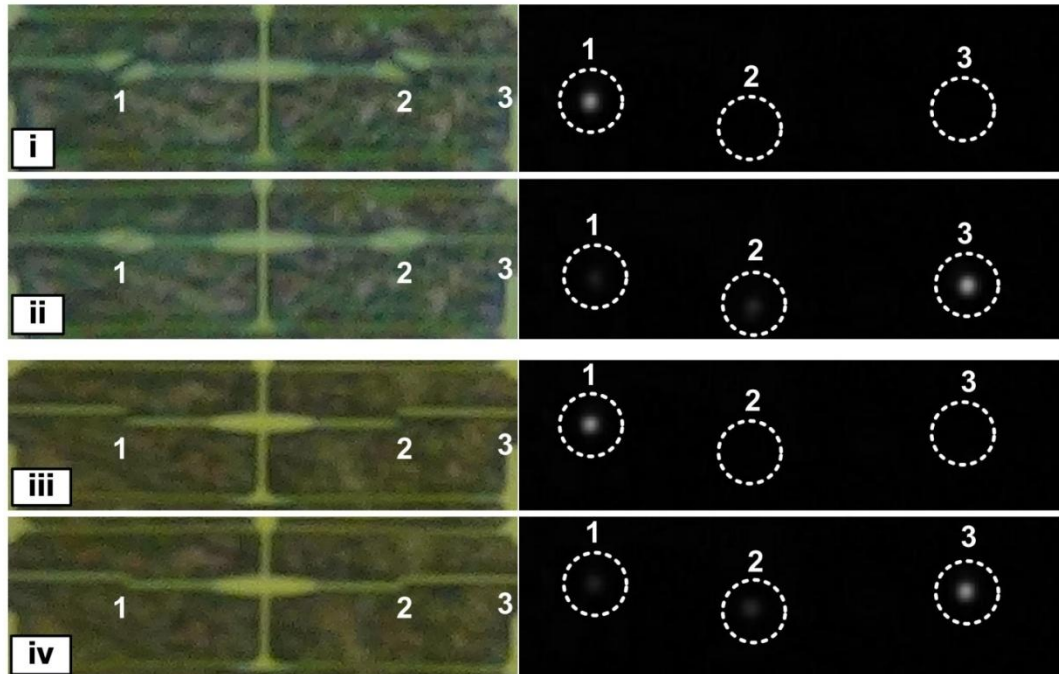
Figure 3.16: Representative result images of low-coupling and high-coupling cases under both optical microscopy and NIR camera.

Figure 3.17 depicts theoretical and experimental optical response in the excitation range from 0nm to 150nm every 25nm, including *i*, *ii*, *iii* and *iv* as given in Fig. 3.16, for both tuning mechanisms. Numerical and experimental results are in good agreement with a maximum deviation of %9.12 and %4.23 in type I and II mechanisms, respectively. The deviation is attributed to surface roughness in the waveguide sidewalls at the tuning regions indispensable during ICP-DRIE process. As size of tuning region increases, similar to the case for type I when compared to type II mechanism, total amount of rough surfaces that lightwave will experience during evanescent wave coupling increases causing degradation in optical response. Tunability of the mechanisms in the 75nm and 100nm excitation range reaches up to 1.13nm and 1.19nm per percent of average light intensity change in order. Even though tunability values defined so far are provided on a basis of per percent of average light intensity change, the measurement approach deployed in this study indeed enabled a minimum tunability of 0.0452m and 0.0476nm per measurable 0.04% of average light intensity change.
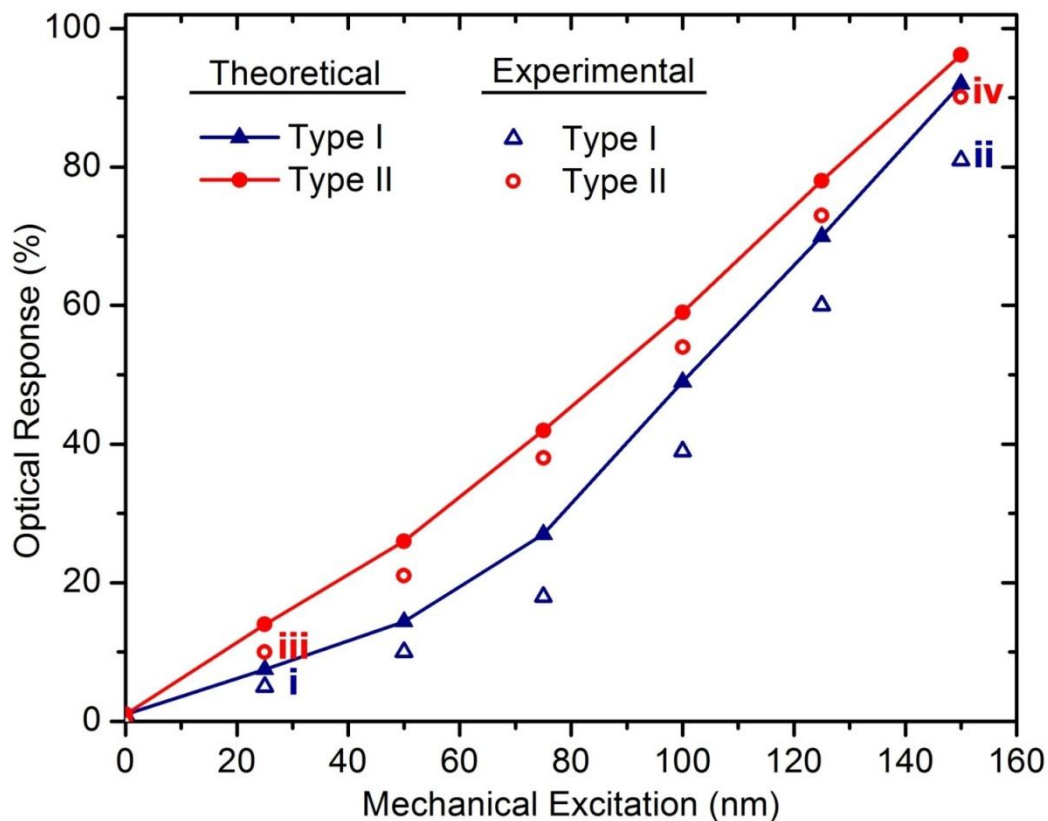
Figure 3.17: Theoretical and experimental results together for optical response in Type I and Type II tuning mechanisms as a function of the mechanical excitation from 0nm to 150nm.

60

3.7 Summary

In conclusion, design, microfabrication and characterization of two mechanical tuning mechanisms for evanescent wave mode coupling in PLCs with sub-nanometer sensitivity values are completed. Since the presented mechanisms are embedded, they depicted improvements already in tunability and device footprint, and a future cost advantage is expected in case of their use in mass production. Numerical and experimental results in optical response are in good agreement with a maximum deviation of 9.12% and 4.23% in the first and the second mechanisms, respectively. Tunability of the mechanisms in the 75nm and 100nm excitation range at 1.55µm wavelength are 1.13nm and 1.19nm per percent of average light intensity change in order. By utilization of a proper light intensity measurement approach as it is realized in this study, one can increase tunability even further below the aforementioned values. Both mechanisms presented are $40{\times}25\mu m^2$ in footprint. The smaller the surface area in the tuning region where evanescent wave mode coupling takes places, the higher coupling contrast is understood. The studied evanescent wave mode coupling mechanisms are well-suited for employment in PLCs where mechanical tuning with sub-nanometer or greater excitation is needed.

4. 1x2 SHORT-RANGE HIGH-SENSITIVITY PHYSICAL CONTACT OPTICAL SWITCH

4.1 Introduction

After fabricating various displacement sensors time to model 1x2 optical switch design. The list of parameters for such a switch design includes width of bent radius, distance between waveguides, contact length, device silicon thickness, waveguide-end and tip angle. The preliminary numerical study in FDTD analysis, for 600nm waveguide width, 10.5° tip angle and 340nm device silicon thickness, 100nm waveguide-end and 1200nm radius of the waveguides, for example, has shown 83.15% optical transmittance on the second waveguide at 150nm, 22.51% optical transmittance on the first waveguide at 0nm distance.
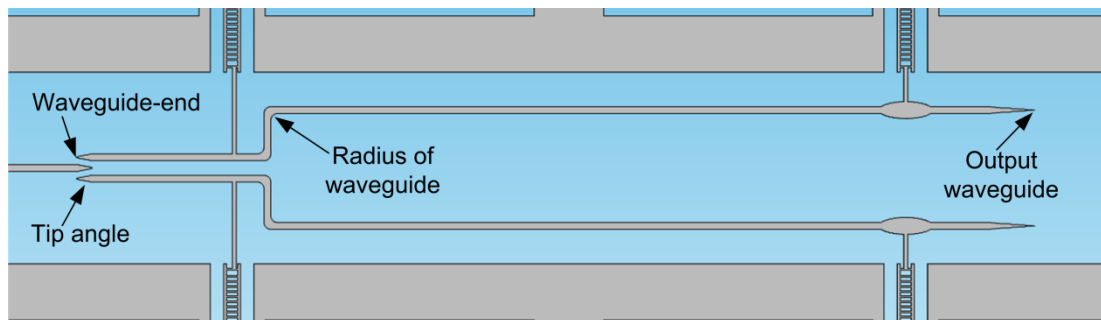
Figure 4.1: Schematic view of the 1x2 optical switch waveguide mechanism.

The 1x2 optical switch mechanism consist of the four different actuator systems. Each side only holds the one side to eliminate the collapse and sticks to ground level. Different shapes are used in the actuator springs to decrease the mass when the electrostatic force generates. The initial air gap between the input waveguides are 350nm. And each side can control itself and separate the light to spot 2.
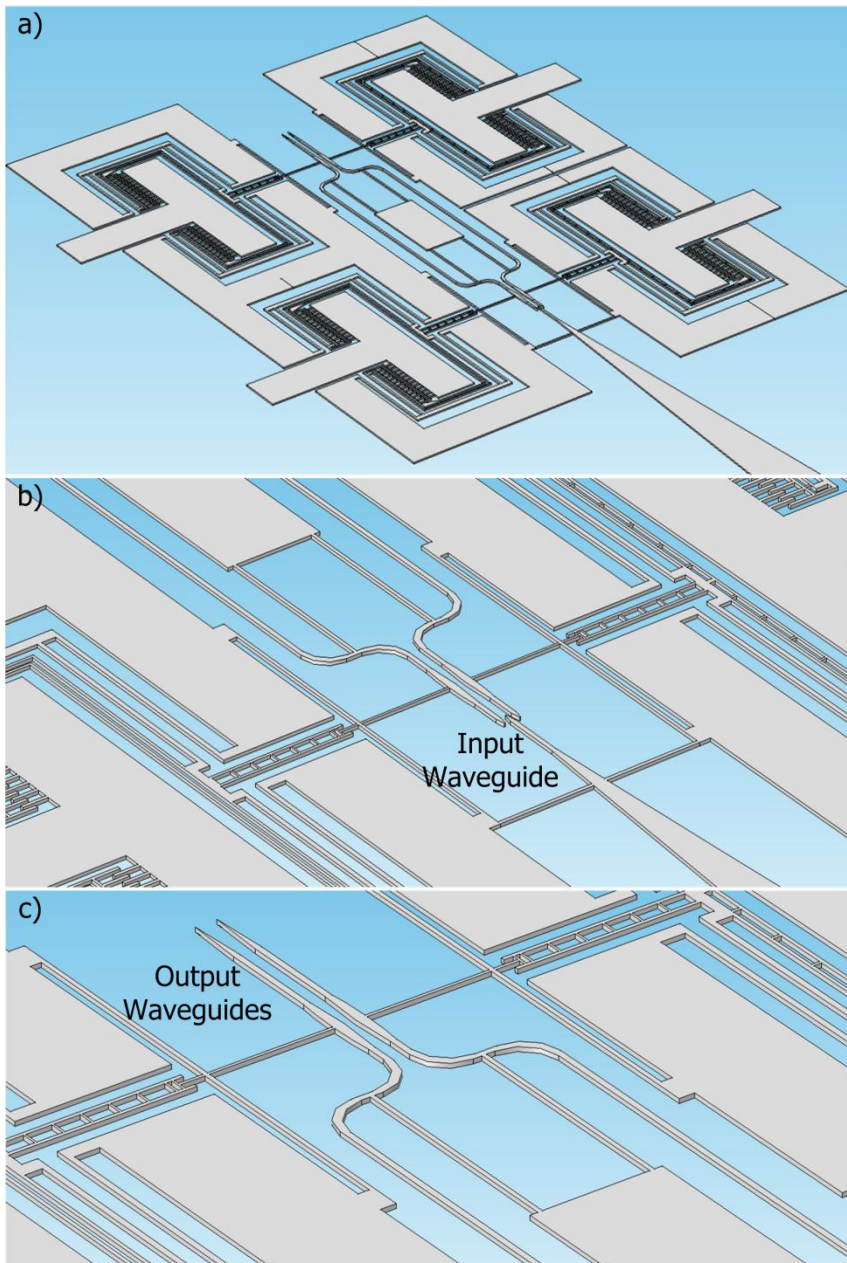
Figure 4.2: Schematic view of the all mechanism. a) Each actuator hold the single waveguide and each side control the one separation waveguide line. b) Input waveguide and separated two other transfer waveguide. c) Output waveguides of the optical switch hold by elliptical intersections.

4.2 Numerical Study in FDTD

Various radius of 600nm, 800nm, 1000nm, 1200nm, 1400nm, 1800nm and 2400nm, at the distances of 0nm, 25nm, 50nm, 75nm, 100nm and 150nm are simulated. Outcomes of the calculation in FDTD are provided and discussed with the following diagrams.
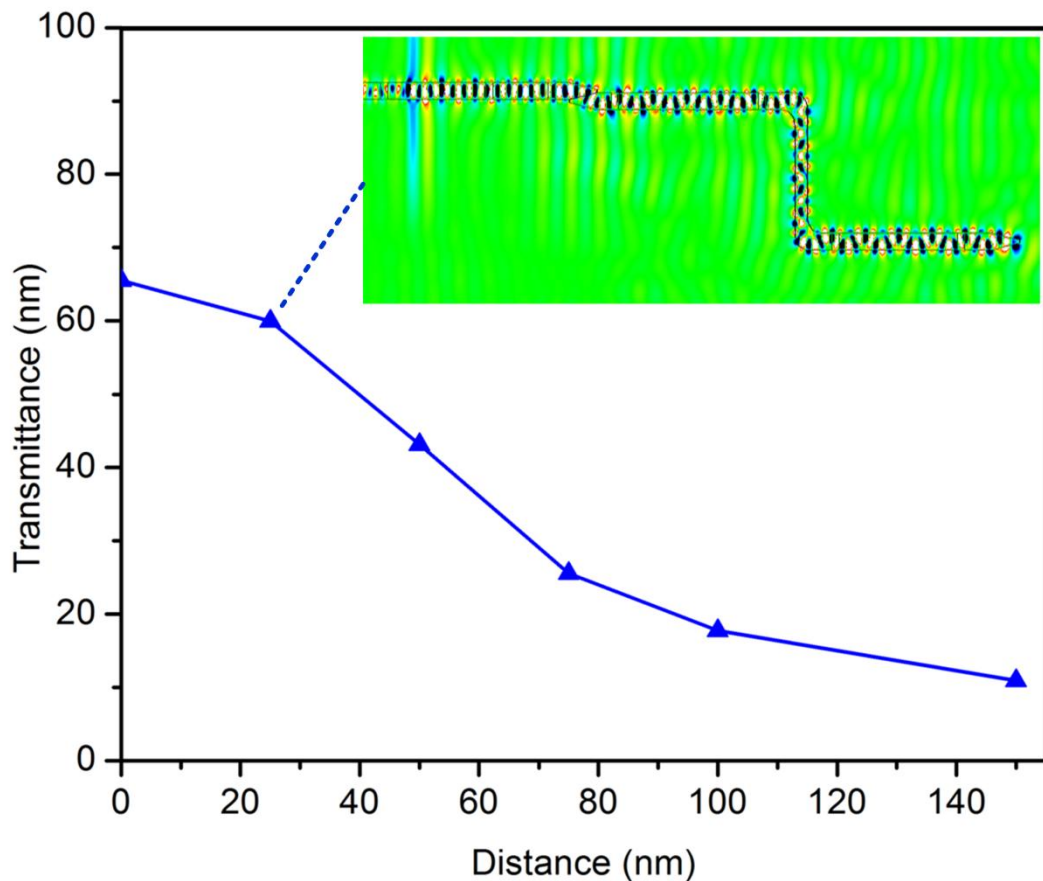
Figure 4.3: Optical performance of the switch as a function of radius 600nm.

First, optical performance of optical switch is obtained as a function of distance from 0nm to 150nm. Figure 4.3 illustrates electrical field distribution of 25nm specific point of structure. For the 600nm radius of waveguide, the total contrast change is 54.42% in the mechanism during 150nm displacement. The maximum transmittance is observed around 65.50%. The disadvantage of the this value for the mechanism increase the total loss besides that advantage is finger print is small.
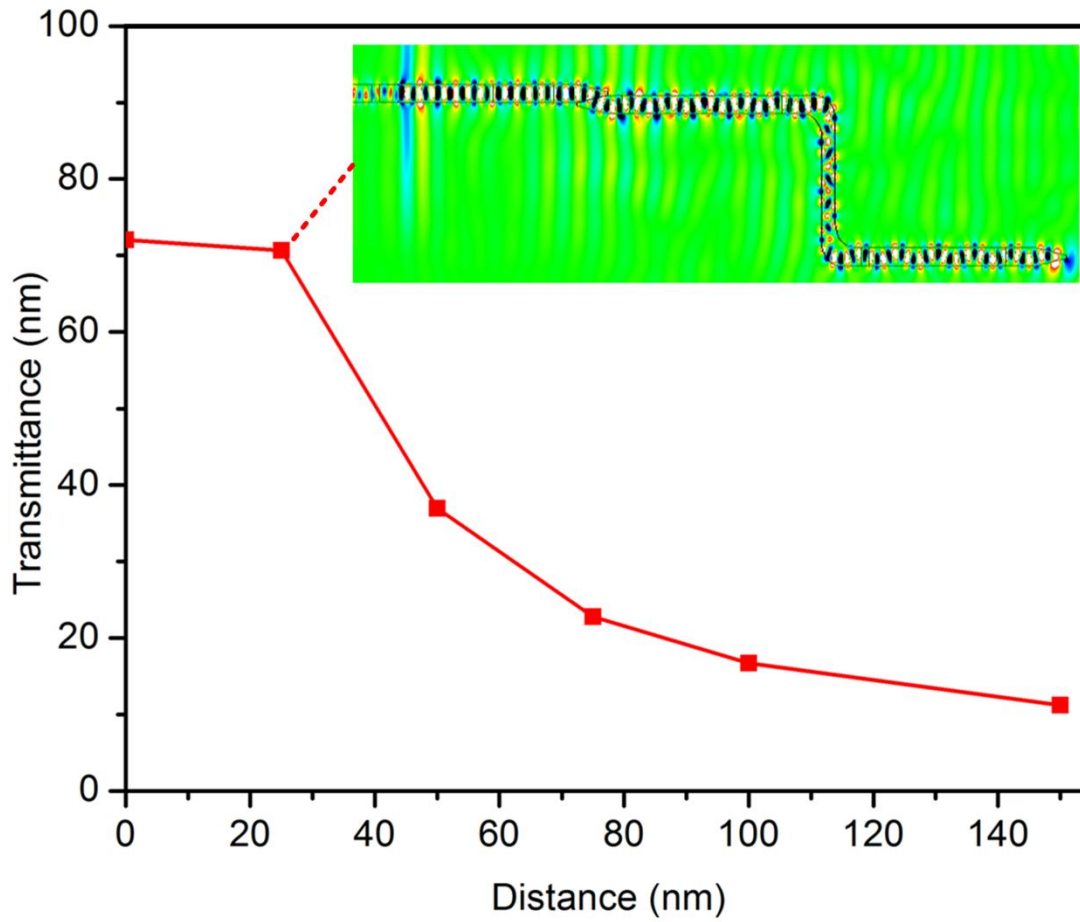
Figure 4.4: Optical performance of the switch as a function of radius 800nm.

Second, transmittance of the mechanism is utilized as a function of the displacement. For the 800nm radius of waveguide, the total contrast changes is 54.42% in the mechanism during 150nm displacement. Figure 4.4 illustrates electrical field distribution of 25nm. The maximum transmittance is increased to 72.05% according to 600nm radius value. When the air gap between two input waveguides is close, light only experienced 72.05% at the output of the waveguide and total contrast changes is 60.83% of the mechanism.
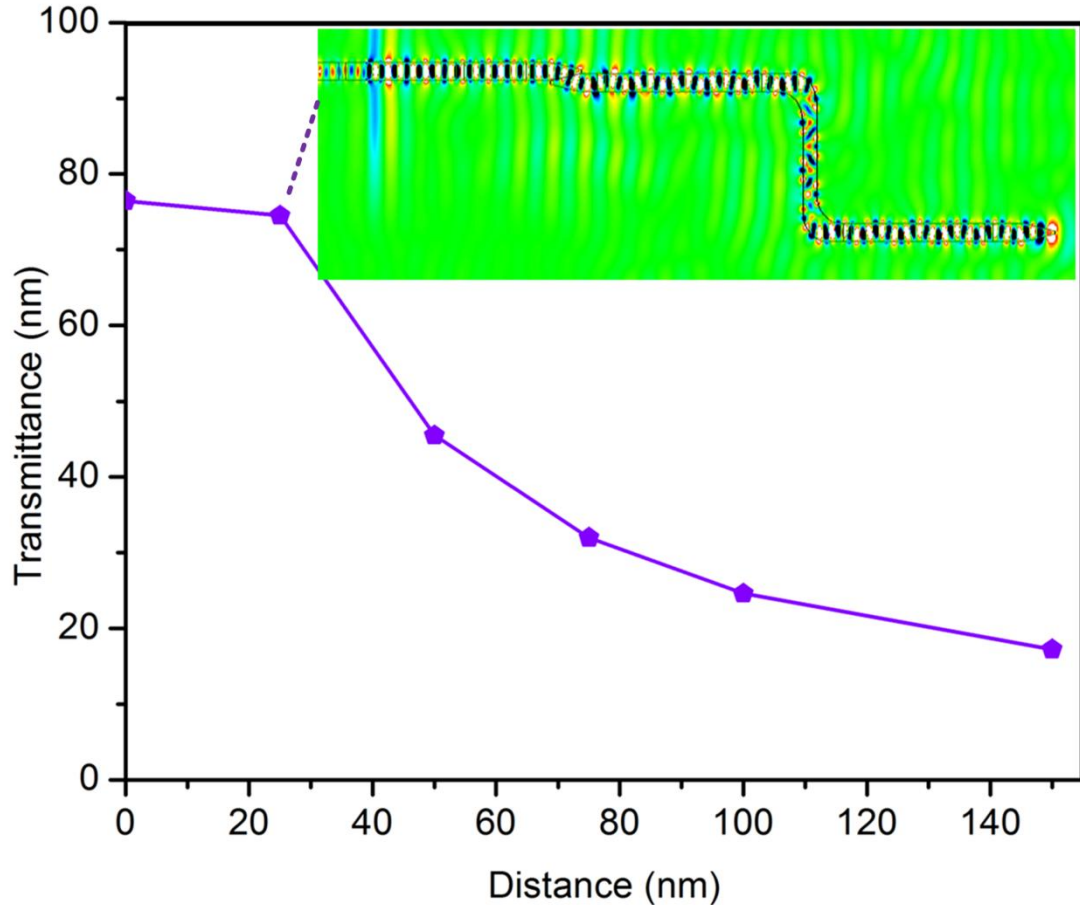
Figure 4.5: Optical performance of the switch as a function of radius 1000nm.

Next, transmittance again for the same, but with a radius of 1000nm are numerically calculated. Results are given in Fig. 4.5. For the 1000nm radius, total contrast is measured as a 59.23%. The maximum optical performance of the structure is increased to 76.46% according to previous radii values. The loss of the optical flow is decreased, as shown in electrical field distribution of 25nm in the Fig. 4.5.

Last, optical performance is calculated as a numerical for the 1200nm and various radii values, as shown in Fig. 4.6. The total performance is increased from 65.50% to 83.15% for the 1200nm. The outcome of the effect of the radius is understood. The high radius waveguide, the less optical loss. Several radii are calculated until 5µm with the 400nm and 600nm step by step. After 2400nm radius, the total optical performance are saturated. All radii values are calculated and for the fabrication 2400nm radius is selected, as depicted Fig. 4.7.
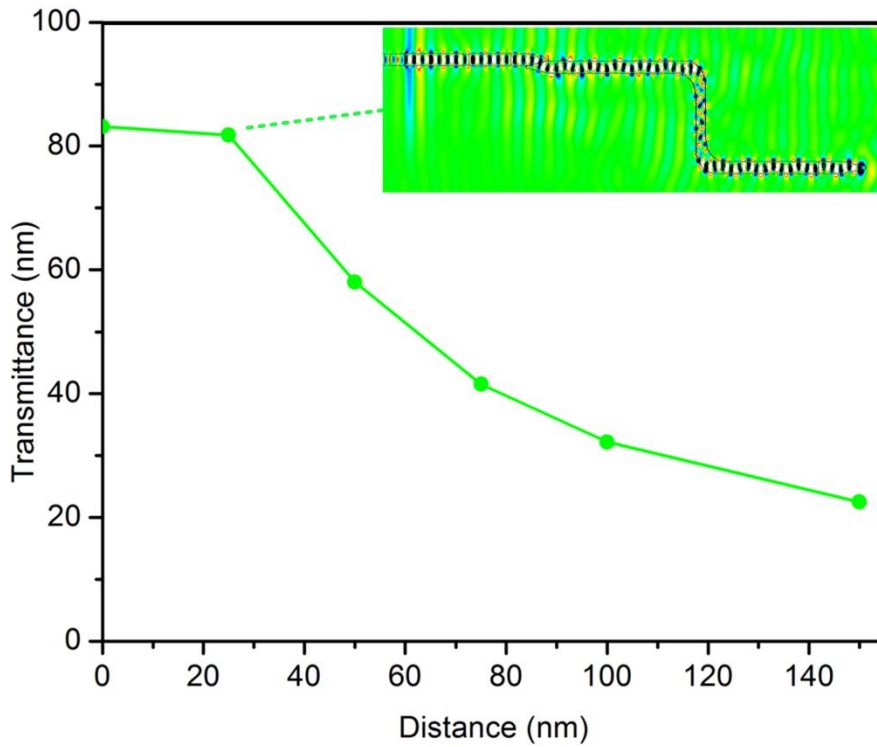
Figure 4.6: Optical performance of the switch as a function of radius 1200nm.
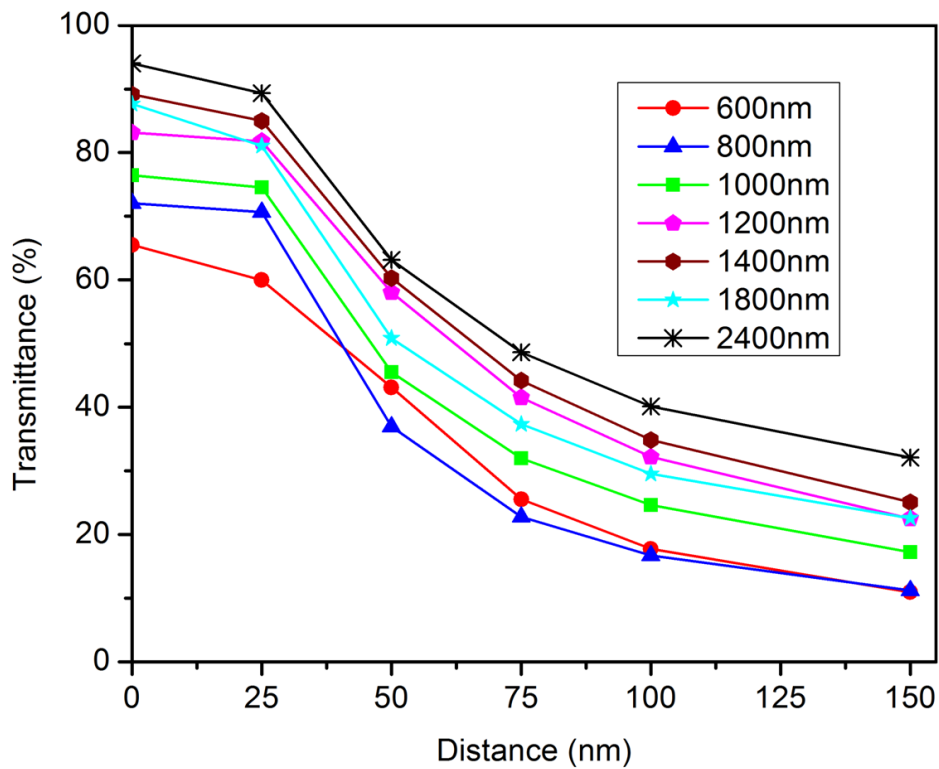
Figure 4.7: Optical performance of the switch as a function of mentioned values.

4.3 Finite Element Method Calculation

Figure 4.8 shows that mechanical analysis results before the experimental study. Electrostatic force is calculated for the 350nm displacement. When the DC voltage is apply to source pad because of the electrostatic force actuators which is contacted with ground path moves to down. Figure 4.8a depicts during the displacement under voltage for the all mechanism. Pair actuators with the gravity force can hold the separated waveguides, as depicted Fig. 4.8b. When the DC voltage is applied to the actuator there will be some rotation between the positive and negative actuation and creates the short circuit during the characterization. This problem is solved using Finite Element software. The air gap is fully closed between input waveguide, no bending and touching each other.
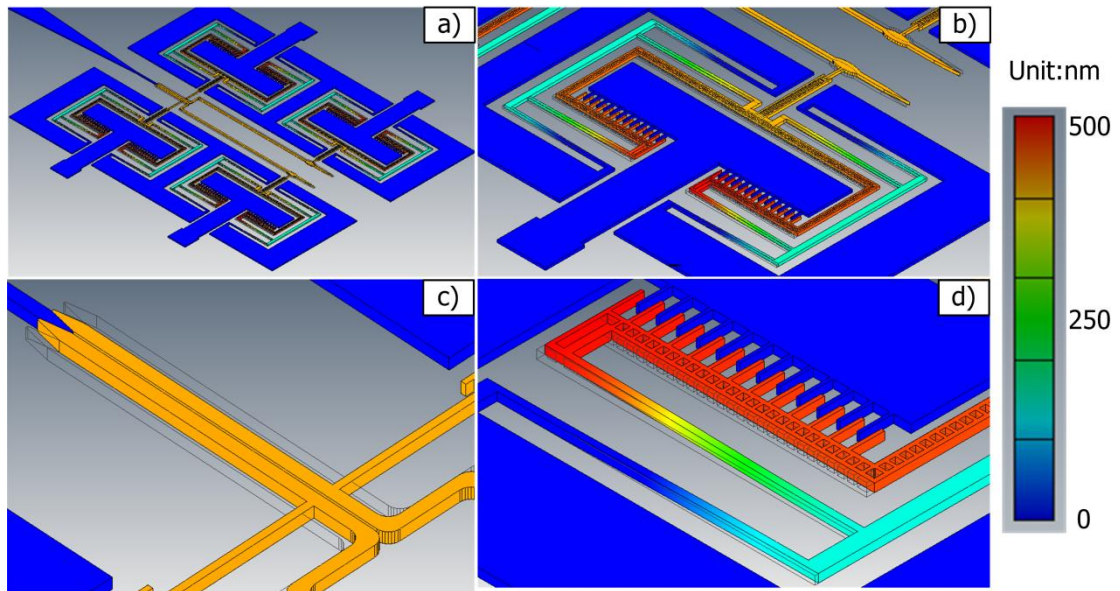
Figure 4.8: a) Numerical results for the 1x2 optical switch. b) Zoom-in to one single actuator. c) Displacement of the one side of the actuator no flips. d) Air gap fully closed between input waveguides via DC voltage.

4.4 Design of Actuator as the Source of Motion

In this particular design, n is the number of finger pairs in the comb actuator, g is the gap between stationary and moving comb finger pairs, w_f is finger width, t is finger thickness, L_f is finger length, L_0 is initial finger overlap, b is spring beam width, h is spring beam thickness, L is total spring beam length, E is Young's Modulus for single crystalline silicon, ε is permittivity of air, and V is applied DC bias voltage. Values of the parameters listed above are provided in Table 4.1.

Table 4.1. Parameters of the Comb Actuator

Symbol	Name	Value
n	Finger Pairs	24
g	Finger Spacing	0.17µm
w_f	Finger Width	0.30µm
t	Finger Thickness	0.34µm
L_f	Finger Length	2.00µm
L_o	Finger Overlap	0.50µm
b	Spring Width	0.36µm
h	Spring Thickness	0.34µm
L	Total Spring Length	33µm
E	Young's Modulus	185GPa
ε	Permittivity	1.885E-4
V	Bias Voltage	0-65V

For the given parameters, in order to achieve 350nm displacement range, D, at approximately 65V DC for covering any possible distance under investigation of sensor is designed. The calculated distance versus bias voltage curve is depicted in Fig. 4.9.
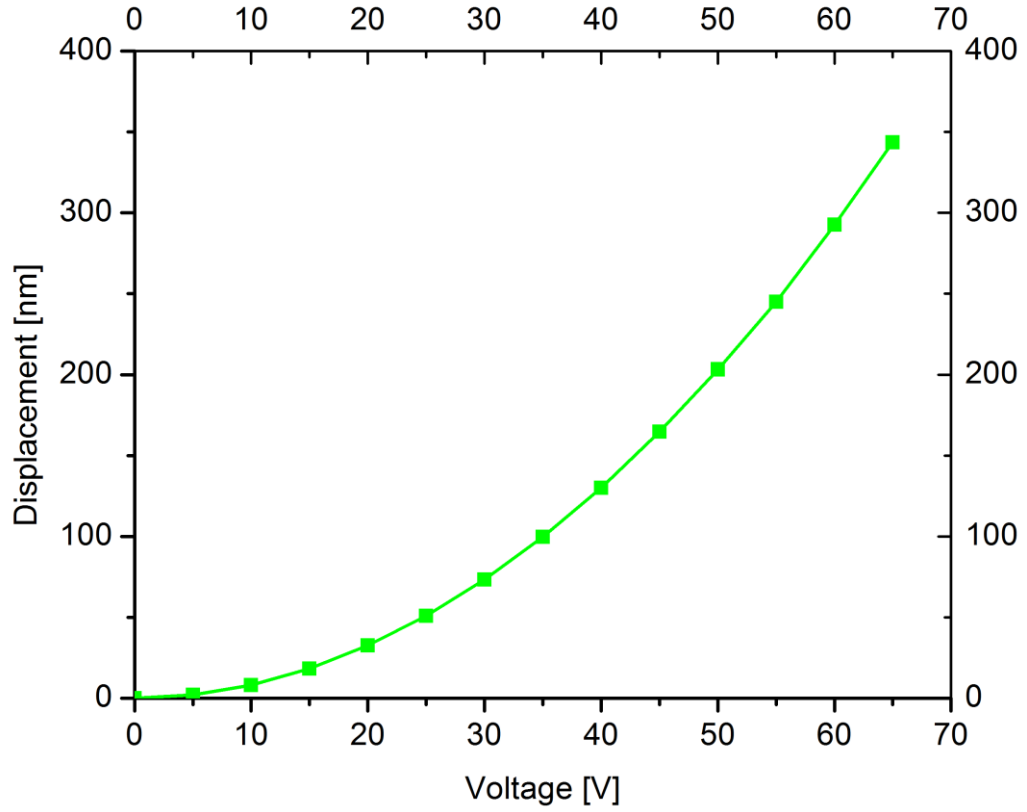
Figure 4.9: Calculated displacements for various voltages for the actuator.

In the comb drive, the model solves the electrostatic equation is as given in equation (4.4.1) below.

$$-\nabla.\left(\varepsilon\nabla V\right) = 0 \qquad \textbf{(4.4.1)}$$

The electrostatic force density is in equation (4.4.2) below.

$$F_{es} = \frac{\varepsilon E^2}{2} \qquad \textbf{(4.4.2)}$$

W_e is in the Electrostatics application mode, where D is the electric displacement, where Ω is the resistance, and E is the electric field is as given in equation (4.4.3) below.

$$W_e = \int_{\Omega} (\mathbf{D}.\mathbf{E}).\,d\Omega \qquad \textbf{(4.4.3)}$$

71

4.5 Fabrication

The 1x2 optical switch is fabricated on an SOI wafer. First, 100nm-thick 495K C2 in Chlorobenzene based PMMA is spin-coated. Then, structure geometries are patterned. Proximity effect is enabled in the software for small and big patterns. Table 4.2 shows the electron beam lithography parameters. Next, 30nm-thick chromium layer is deposited as a hard-mask by thermal evaporation. Table 4.3 shows the chromium deposition parameters.

Table 4.2. Patterning recipe

Patterning recipe			
PMMA C2	Prebake	180 °C	2 min
	Spin coating resist	1000rpm	2 secs
		4000rpm	45 secs
	Postbake	180°C	60 min
	Resist thickness	100nm	
Patterning in Vistec 2000	Voltage	100kv	
	Beam current	80pA	
	Step size x, y	2nm	
	Exposure Density	$800\mu C/cm^2$	
	Write Field	$260x260\mu m^2$	
Developing	Developing by 1:3 MIBK:IPA	25°C	40 secs
	Rinsing by IPA	25°C	20 secs
	Bake	120°C	5 min

Then, lift-off process is realized to define windows. Because of the take long time for the Chlorobenzene based PMMA of lift-off process, acetone should heat up on the hot plate around 60C°. Later, device silicon layer is dry etched fully through windows via ICP-DRIE using SF_6 and C_4F_8 gases is given in Table 4.4. The roughness of the sidewalls are critical issue. The etch ratio of the silicon in ICP-DRIE should stay under <2nm/sec. The etch rate is used 1.23nm/sec. Chromium layer is removed by Chromium liquid etchant (CR-7S, CYANTEK Co.) at ultrasonic cleaner, for 2mins after silicon etching process.

Table 4.3. Chromium Deposition

Chromium Coating			
Chromium Aligment	Chamber Vacuum	4×10^{-6}Torr
	Chromium Density	7.19g.cm^{-3}
	K factor	127
	Energy of first ionisation	2987kJ.mol^{-1}
	Tempature	45°C
Deposition	Voltage	4.2V
	Beam Current	2.1A
	Rate	0.3nm/s
	Thickness	30nm
Drying	Dry N_2 gas	

Table 4.4. Silicon Etching at ICP-DRIE

Silicon DRIE Recipe	
Number of Cycles	55
Passivation Time	7sec
Etch Time	5sec
Chamber Vacuum	10×10^{-3}Torr
SF_6/C_4F_8 Flow Rates	7/20sccm
RF Platen Power @ Etch/Passivation	900/20W
RF Generator Power @ Etch/Passivation	

Then, all structure is fabricated 2×2cm^2 SOI wafer and separated via Dicing saw to different parts at 3mm/sec speed with 400µm depth as depicted in Fig. 4.10. Home-made Vapor HF Etching Setup is uncontrollable during the process. Even for the same recipe, results of the etching is different. Updated Vapor HF Etching Setup is designed and modeled according to what we have as a part of old system. Finally, suspended parts of the optical switch are released in a Vapor HF Etching Setup, as shown in Fig. 4.11.
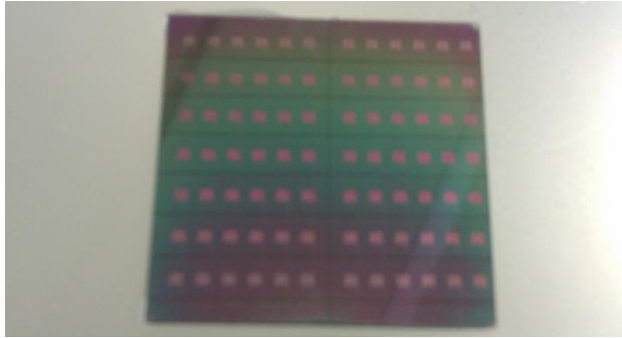
Figure 4.10: Separated wafer separated via Dicing saw.

Figure 4.11: Updated Vapor HF Etching Setup for the suspension.

Vapor HF Setup recipe is given in Table 4.5. Device release is accomplished at a wafer temperature of wafer is 50°C, corresponding to 35°C the SOI sample, yielding an isotropic etch rate of 200nm/min, for 10mins. 40 minutes should wait to set the stable temperature. The temperature should increase step by step to desired value.

Table 4.5. Vapor HF Recipe

	Volume (ml)	Etch Ratio (µm)	Stable Temp. (°C)	Time (min)
HF Acid	40	-	30	10
SOI Sample	-	2	35	-

The 1x2 optical switch is fabricated on an SOI wafer with 340nm silicon thickness as shown in Fig. 4.12. Figure 4.12a shows that four actuators are fabricated very well with the radius, input, output waveguide, springs, comb actuators. supported input and output waveguide with the springs after Vapor HF Etching process as seen in Fig. 4.12b and 12c in order.
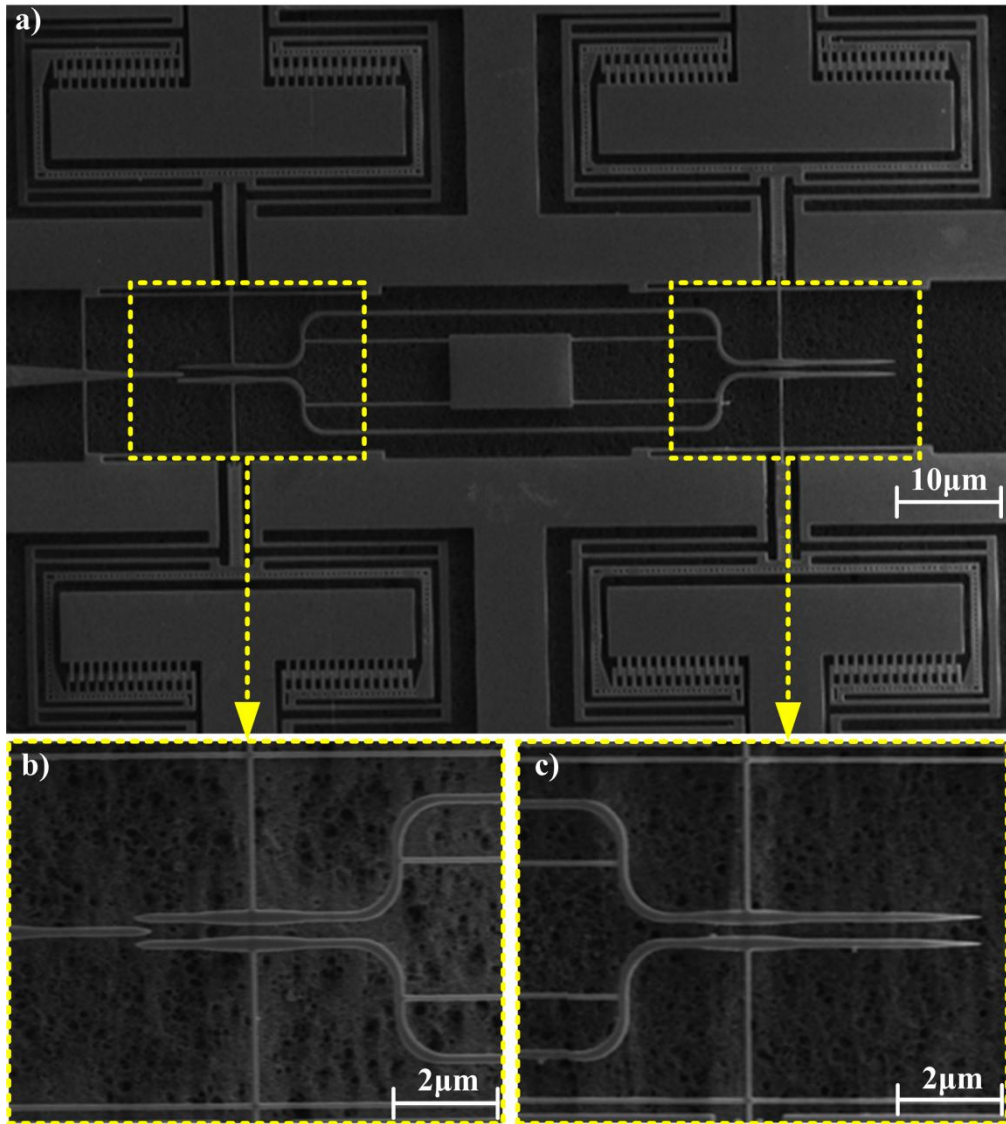
Figure 4.12: a) SEM image of the 1x2 optical switch. b) Supported input
waveguides. c) Supported output waveguides.

4.6 Characterization

First of all, under mechanical characterization setup displacement is tested between
waveguides via DC volt. According to design dimension of comb actuator,
electrostatic force is calculated which is 65V. 350nm is the displacement between
waveguides. Increasing the voltage effects the decreasing the air gap between
waveguides 0 and 65V, respectively from Fig.4.13a to Fig. 4.13b.
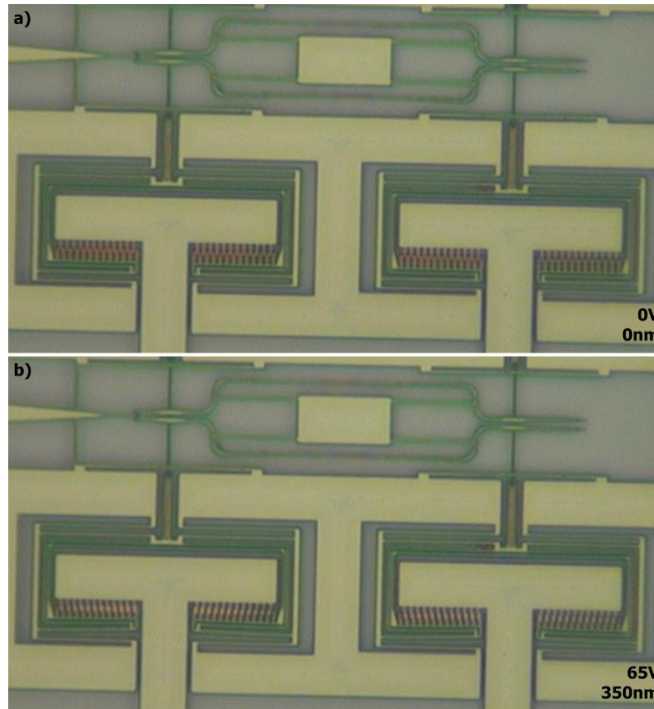
Figure 4.13: 1x2 optical switch under from off-state to on-state, respectively.

For the 350nm displacement to give motion to actuators, sawtooth voltage mode is used with several seconds at 65V as shown in Fig. 4.14a. Figure 4.14b shows that image of the osiloscope result during mechanical excitation.
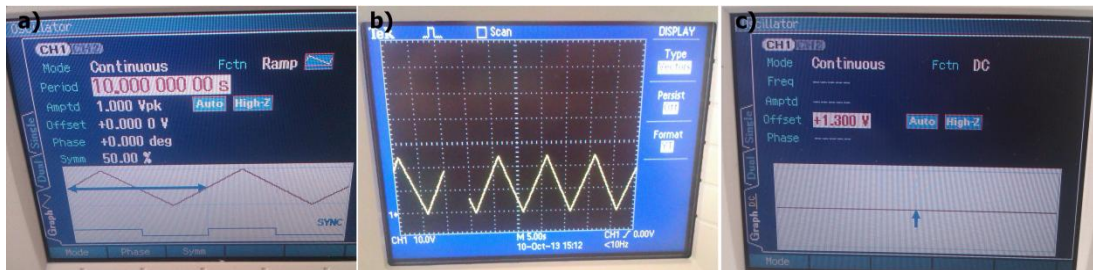
Figure 4.14: a) Sawtooth voltage mode parameters. b) Image of the osiloscope result during mechanical excitation. c) Wave form as a DC voltage during mechanical excitation.

The thing is when the sinusoidal voltage use, comb actuators moves x direction and bend to ground. It means that comb actuators bend to ground and touch the straight waveguide, go to up and come to first situation. At sawtooth voltage modes, actuator moves directly to straight waveguide without any other action. The pertentage is used 50% and period used between 1 and 10 seconds. Figure 4.14c depicts wave form as a DC voltage during mechanical excitation.

Figure 4.15 shows that the mechanical and optical characterization results under 0 and 65V, respectively. Under the 0V DC the displacement between waveguides 350nm and transmittance at the output 1 and output 2 are 0, as can seen in Fig. 4.15b. When the 65 V applied to the comb actuators for the bottom part, they work simultaneous each other and moves the input and output waveguides at the same time which is 350nm, transmittance at the output 2 is around 59% and output 1 is 0, as can seen in Fig. 4.15d. When the 65 V applied to the comb actuators for the upper part, they work simultaneous each other and moves the input and output waveguides at the same time which is 350nm, transmittance at the output 1 is around 59% and output 2 is 0, as can seen in Fig. 4.15f. The experimental and theoritically results agree with each other at about 9% deviation.
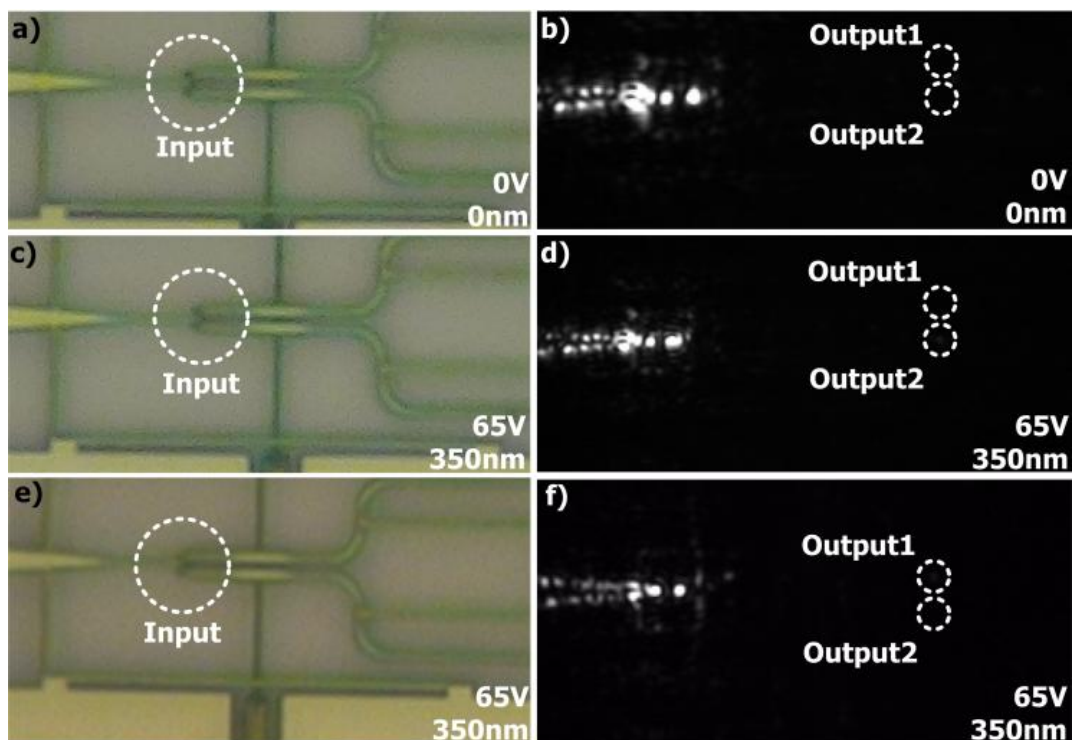
Figure 4.15: a) 350nm separation between input waveguides. b) Transmission at both output is 0. c) Bottom input waveguide is closed when there is 350nm separation between upper input waveguide. d) Transmission is around 59% and 0 at output 2 and output 1 in order. e) Upper input waveguide is closed when there is 350nm separation between bottom input waveguide. f) Transmission is around 59% and 0 at output 1 and output 2 in order.

4.7 Results

During optical characterization, with the several DC and sawtooth voltage, video is recorded via NIR camera. Optical performance is calculated with the MATLAB code by video which is recorded. Thousand points of each devices are measured and controlled the stabilization and cycle numbers. Code is given below.

```
% clear all
close all
clc

video1 = mmreader('video12.avi');   % reading video
video_frm = read(video1);                   % video between the
defined fram
video_frm_lum =  video_frm(:,:,1,:);
imshow(video_frm(:,:,2,200))

%input coordinates
frameY = 325:1:352;
frameX = 266:1:289;

%output coordinates
% frameY = 484:1:512;
% frameX = 266:1:291;

Output = (video_frm_lum(frameX,frameY,:,:));

intensity_time = [];
for i=1:size(Output,4)
    temp1 = sum(sum(Output(:,:,1,i)));
    intensity_time = [intensity_time temp1];
end

data_range = 1:i;
intensity_time =
intensity_time(data_range)/max(intensity_time(data_range));
frame_time = 1:size(intensity_time,2);

range = 450;

figure
plot(range*((frame_time/size(frame_time,2)).^2),smooth(((inten
sity_time))),'r-s'); %
range*((frame_time/size(frame_time,2)).^2)
hold on
plot(range*((frame_time/size(frame_time,2)).^2),xx,'b-s');
```

In the mechanical characterization setup optimum voltage is measured by checking the videos there is connection between waveguides. If the moving waveguide touch the fixed waveguide, optical performances reaches to maximum. However, under over-voltage, waveguides are bent under compulsion and give rise to optical loss, as shown in insets of the Fig. 4.16. Insets of Fig. 4.16a and Fig. 4.16b depicts the optical performance changing at the over voltage value. The optical losses and sudden drops can be seen. Over voltage causes buckling problem in the waveguides. Insets of Fig. 4.16c and Fig. 4.16d shows the sudden optical losses at the maximum performance point under over-voltage. Using optimum voltage value gives the maximum optical performance such as shown in inset of Fig. 4.16e. The optimum voltage value can be selected under mechanical characterization setup to prevent the optical performance losses.
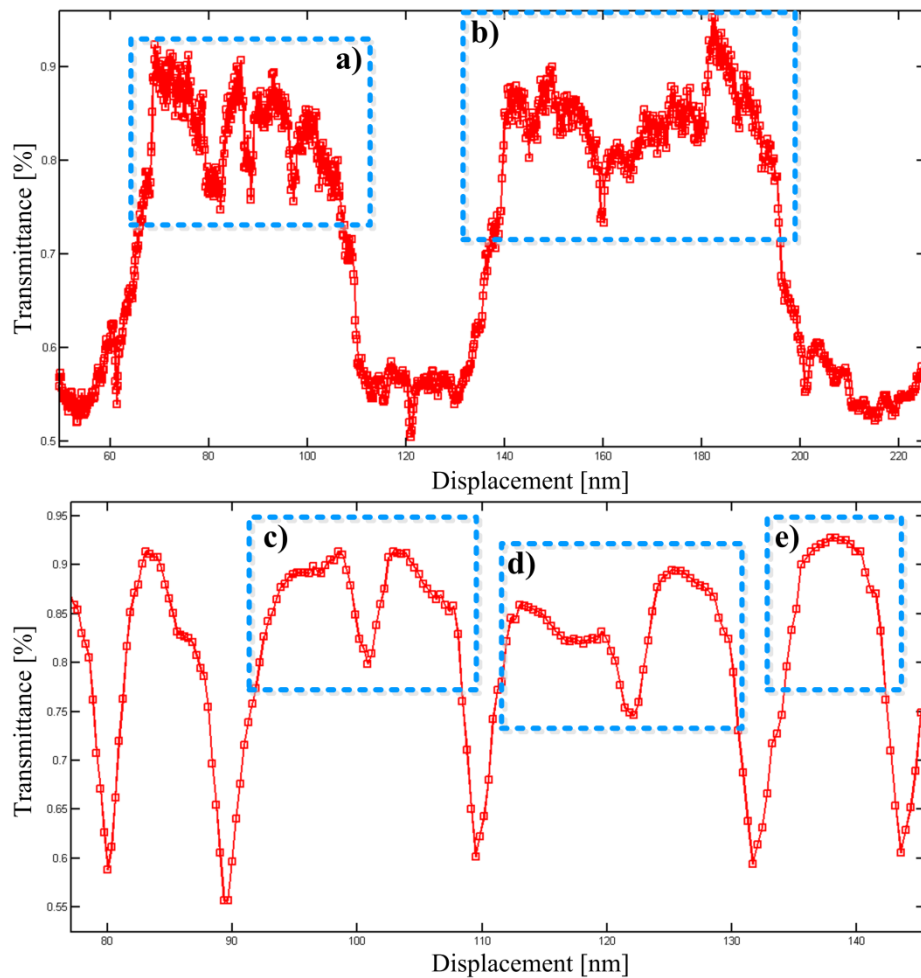
Figure 4.16: Experimental results of the optical switch under over-voltage values.
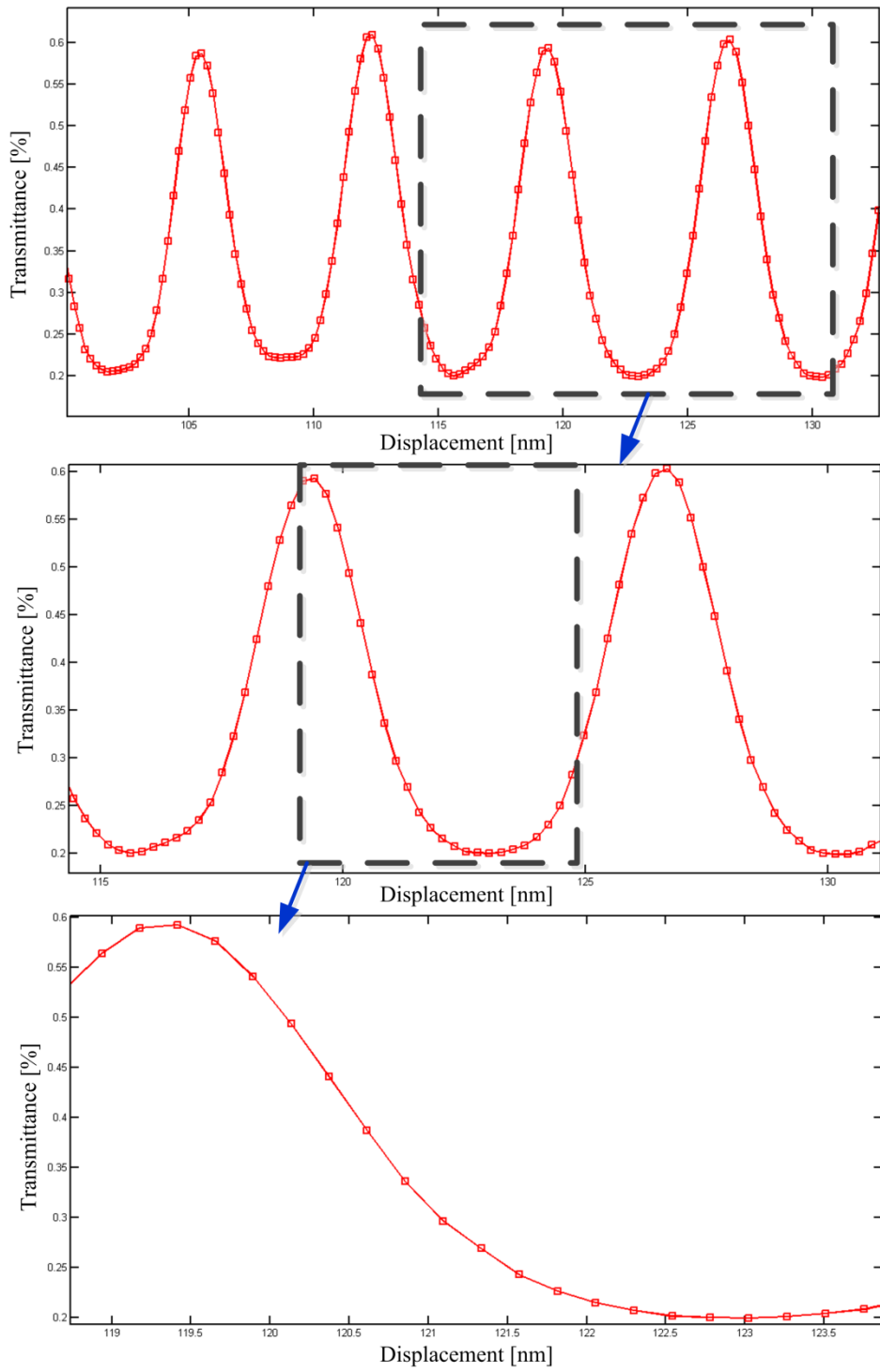
Figure 4.17: Experimental results of the 1x2 optical switch.

According to simulation results optical performance at the single output waveguide 48.21%. Totally of the output waveguides are 96.42% which is the performance of the separating the output of light of spot 2. Under the optical characterization, optical results are recorded and tested with MATLAB code. Total optical contrast is around 39%. The experimental results shows that the optical performance of the output is around 59% well agreed with the theoretically results. Even experimental results are better than simulation results because of the FDTD mesh size parameter. Figure 4.17 shows that four different peaks of the fabricated devices. The reason why this mismatch is bigger than the previous optical mechanisms because of the used springs to hold the waveguide to avoid the bending and touching the bottom silicon layer. 12 extra springs are used to hold the waveguide and effects the performance but at least can present the concept works very high sensitivity which is 0.078nm per percent of the light intensity. Figure 4.18 shows experimental and numerical spectral response results of the 1x2 optical switch. The optical switch has a optical peak around 1.58μm wavelength.
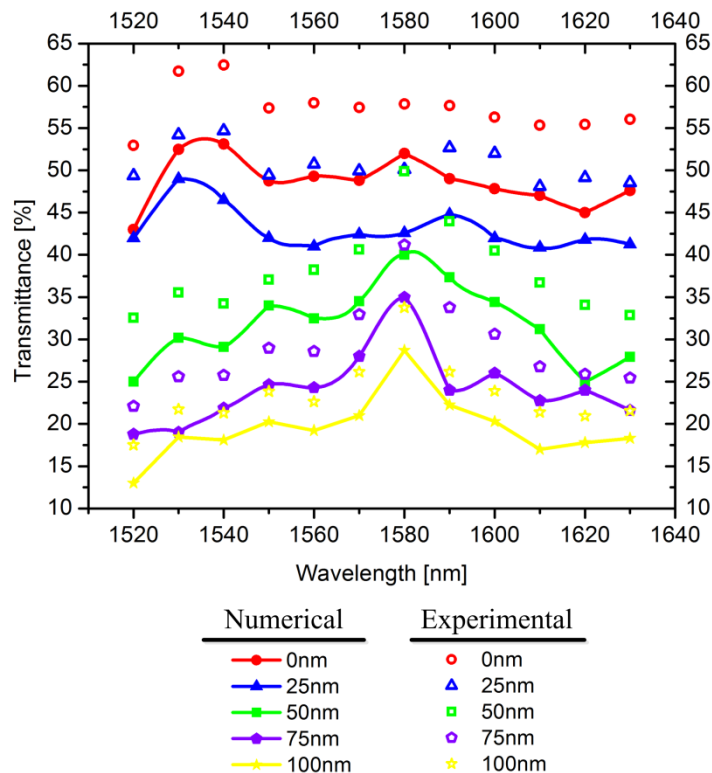
Figure 4.18: Numerical and experimental spectral response obtained in the 1520-1630nm band at various displacements.

4.8 Summary

1x2 optical switch is designed and fabricated. The experimental results shows that the optical contrast is around 39% well agreed with the theoretically results. The experimental results shows that the optical performance of the output is around 59% well agreed with the theoretically results. 12 extra springs are used to hold the waveguide and effects the performance but at least can present the concept works very high sensitivity which is 0.078nm per percent of the light intensity. Experimental and numerical spectral response results of the 1x2 optical switch are studied. The optical switch has a optical peak around 1.58μm wavelength.

5. NORMALLY-ON SHORT-RANGE HIGH-SENSITIVITY PHYSICAL CONTACT OPTICAL DISPLACEMENT SENSORS

In Chapter 2,3 and Chapter 4, normally-off displacement sensing mechanisms with large-range low-sensitivity and short-range high-tunability characteristics are studied. In this chapter, on the other hand, short-range high-sensitivity in-plane optical sensor, but at normally-on state are being investigated in order to clarify their initial state effects on the sensing characteristics. Towards this goal, three major types of sensor approaches are currently being investigated as presented below. All sensors utilized in Chapter 5 are based on Electromagnetic Field Modulation (EFM).

5.1 Introduction

Utilization of telecommunication networks between geographically dispersed users has increased over the last two decades, which in return created the need for high data transfer rates. Towards this demand, Wavelength Division Multiplexing (WDM) systems are introduced on the optical fibers. Optical switches play an important role on the WDM based telecommunication network performances along the path of optical signal. Various technologies are currently employed in optical switching such as liquid crystal [43], thermo-optic [44], electro-holographic [45], acousto-optic [46], semiconductor optical amplifiers [47], and MEMS [11]. Optical switches with MEMS are preferred mainly owing to their low cost and high extinction ratio.

Bulgan *et al.* have fabricated submicron silicon waveguide optical switch driven by electrostatic comb actuator on SOI [10]. The switch consists of input and output waveguides, and a movable waveguide. Light cannot propagate from the input to the output when the two are apart above a wavelength distance. When air gap between the input and the output is closed, light propagates from the input to the output. Due to high sensitivity of the switch to fabrication and actuation errors, only 52.34% transmittance between input/movable and movable/output waveguide pairs was achieved.

Encountered fabrication and actuation errors were reported to remain in sub-100nm range. Later, waveguide tip geometry is understood to have an effect on optical performance. In this letter, numerical study of MEMS-driven normally-on ultra-sensitivity physical contact optical switch is presented.

5.2 Principle of Optical Displacement Sensor, Type I

As shown in Fig. 5.1b, the optical sensor structure is composed of a straight and half-circled waveguides. The list of parameters for such a sensor design includes radius of the circled waveguide, distance between the two waveguides, and thickness of device silicon layer. The preliminary numerical study in FDTD analysis, for 500nm waveguide width, 2µm radius and 260nm silicon thickness, for example, has shown 97.73% optical transmittance, an extinction down to 6.81% between 25nm and 100nm displacement values, respectively. This initial result suggests ultra-sensitivite measurement capability in short ranges.
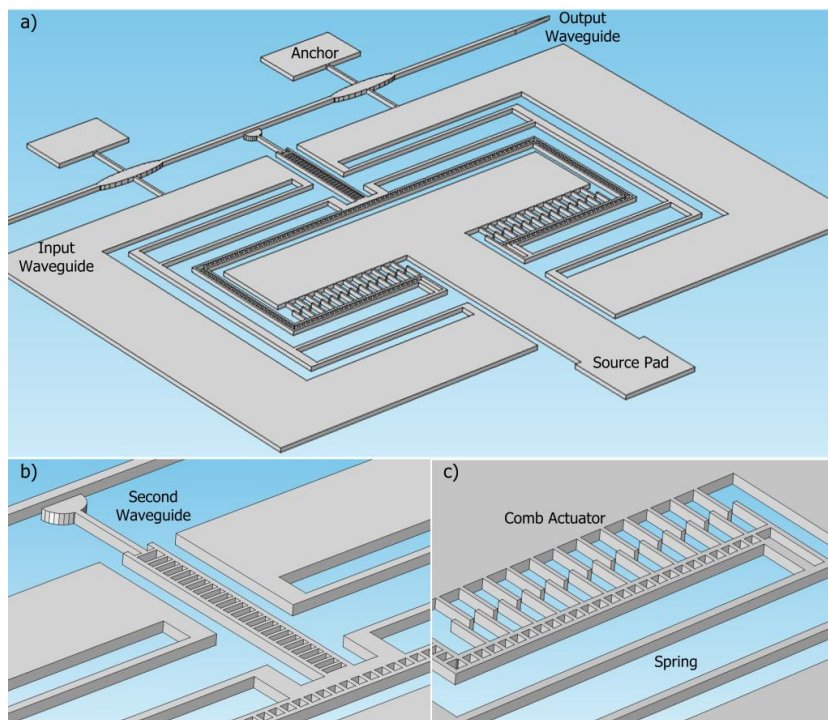
Figure 5.1: a) Schematic view of Type I tip geometry for normally-on short-range ultra-sensitivite optical displacement sensor. b) Second waveguide and straight waveguide. c) Spring and finger structure of the comb actuator.

5.3 Numerical Study in FDTD

Various radius of 0.5µm, 1µm, 2µm, 4µm, 6µm, 8µm, and 10µm, at the distances of 0nm, 25nm, 50nm, 75nm, 100nm, 300nm, and 600nm are simulated. Outcomes of the calculation in FDTD are provided and discussed in the following sections of this chapter.

5.3.1 Effect of circled waveguide radius

First, optical performance of optical sensor is obtained as a function of distance from 0nm to 100nm. Figure 5.2 illustrates electrical field distribution at 0nm and 100nm specific points of optical sensor. When the air gap between straight and half-circled waveguide is closed, light experiences only 3.97% at the output of the waveguide, as shown in the left inset. When the air gap is 100nm far away from the straight waveguide, transmittance power is up to 92.12%, as seen in the right inset. As a result of use of 2µm radius in the half-circled waveguide, sensitivity of the optical sensor is 0.083nm per percent of light intensity change about 108nm displacement range.
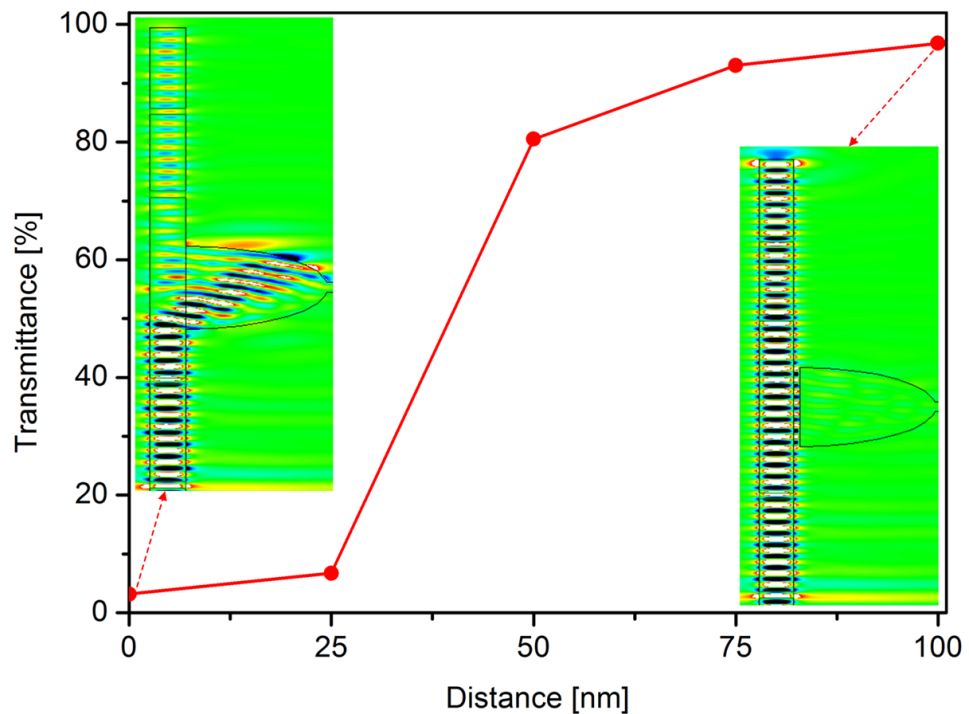
Figure 5.2: Transmittance at the circled-waveguide radius, R, of 2µm.

Then, transmittance of optical sensor is obtained as a function of distance from 0nm to 100nm for 3μm radius. Figure 5.3 illustrates electrical field distribution of 0nm and 100nm specific points. When the air gap between straight and half-circled waveguide is closed, light experiences only 4.12%, as shown in the left inset. When the air gap is 100nm far away from straight waveguide, transmittance power reaches up to 94.21% at the output of the waveguide, as seen in the right inset. As a result of 3μm radius of half-circled waveguide, sensitivity of the optical sensor 0.082nm per percent of light intensity change about 107nm range is provided. Transmittance and sensitivity of the optical sensor is increased just changing the radius from 2μm to 3μm.
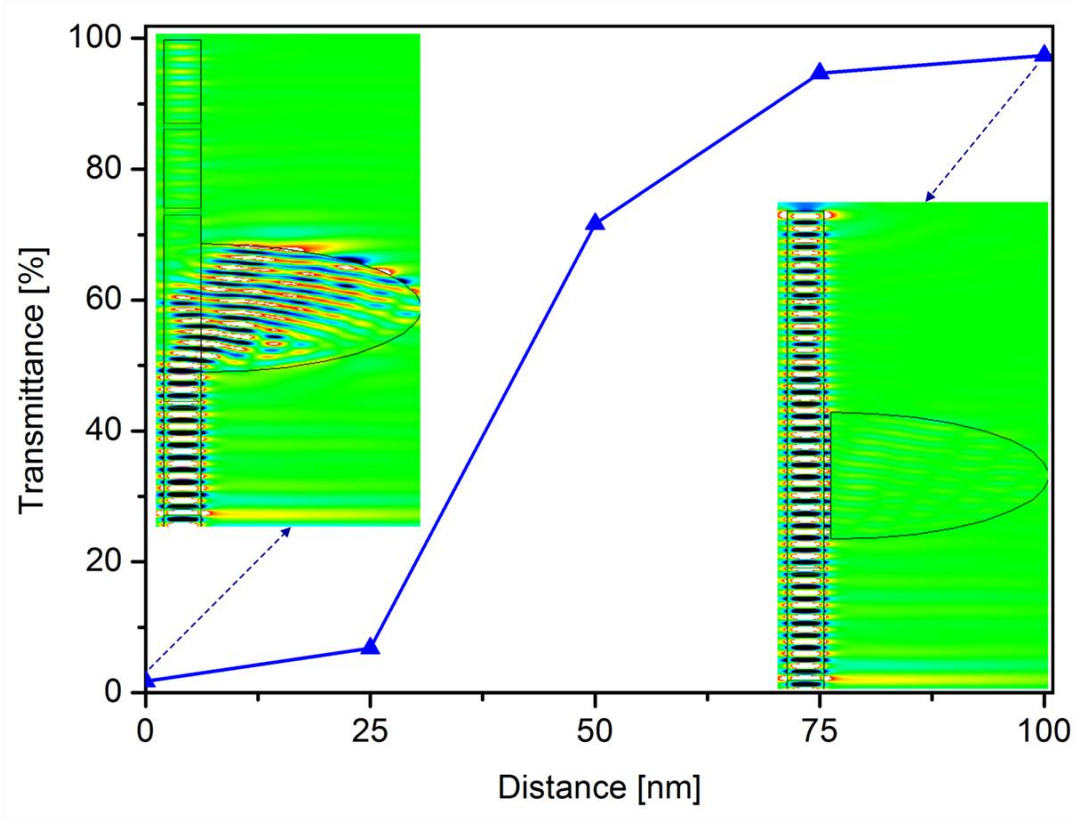
Figure 5.3: Transmittance at the circled-waveguide radius, R, of 3μm.

Next, transmittance is calculated as a function of distance from 0nm to 100nm for 4µm radius. Figure 5.4 illustrates electrical field distribution of 0nm and 100nm specific points. Optical displacement sensor performance is 5.27%, the air gap between straight and half-circled waveguide is 0nm, as shown in the left inset. Optical displacement sensor performance increases 95.12%, air gap is 100nm, as seen in the right inset. 4µm radius of half-circled waveguide, sensitivity of the sensor 0.080nm per percent of light intensity change about 105nm range is provided.
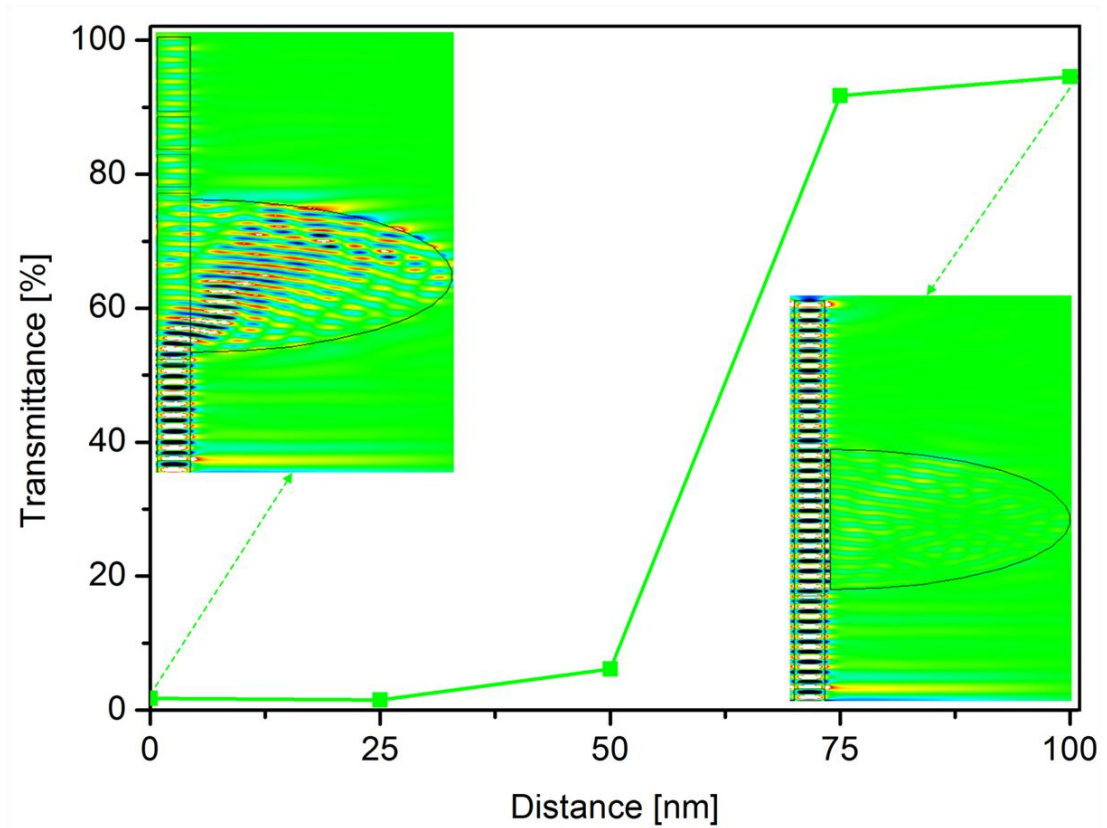
Figure 5.4: Transmittance at the circled-waveguide radius, R, of 4µm.

Last, optical performance of sensor is obtained as a function of distance from 0nm to 100nm. Figure 5.5 illustrates electrical field distribution of 0nm and 100nm specific points. When the air gap is closed, light experiences only 3.97%, as shown in the left inset. When the air gap is 100nm, transmittance power reaches up to 92.12%, as seen in the right inset. As a result of 5µm radius of half-circled waveguide, sensitivity of the sensor 0.079nm per percent of light intensity change about 104nm range is provided. The numerical results shows that the bigger radius, the higher sensitivity. And also, as the radius of the circled waveguide increases, range of the optical sensor decreases.
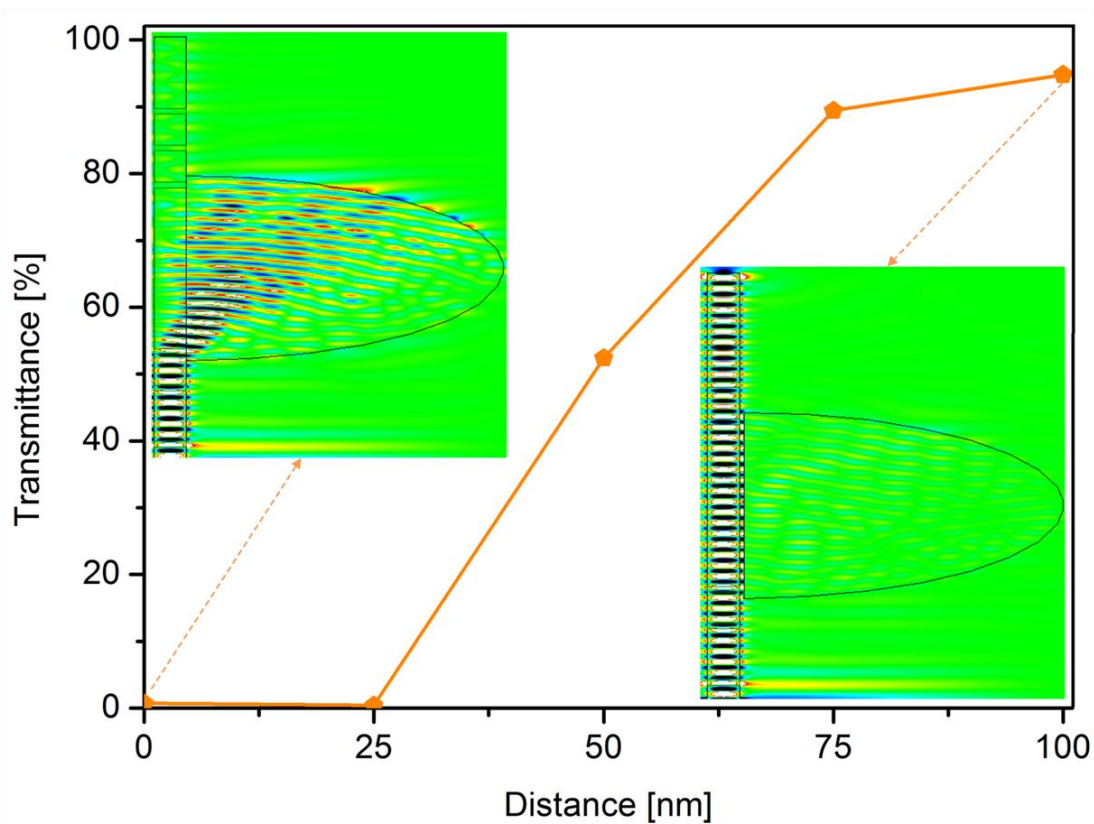
Figure 5.5: Transmittance at the circled-waveguide radius, R, of 5µm.

Optical performance of Type I optical sensor structure of this phase is studied at 25nm, 50nm, 75nm, 100nm, 300nm and 600nm distances, whose results are as shown in Figs. 5.5 and 5.6. First, effect of the radius of circled-waveguide at 2µm, 3µm, 4µm, and 5µm is investigated. Results are as provided in Fig. 5.6. Transmittance of such sensors is numerically observed to be significantly changing within sub-100nm distances. When radius of circled-waveguide decreases, sensitivity increases, however, relative change between various circled-waveguides are not

significantly large. Optical transmittance when a radius of 2μm, for example, is used in the circled-waveguide changes from 97.73% to 6.81% between 25nm and 100nm displacement values, respectively, corresponding to a sensitivity of about 0.83nm per percent of light intensity.
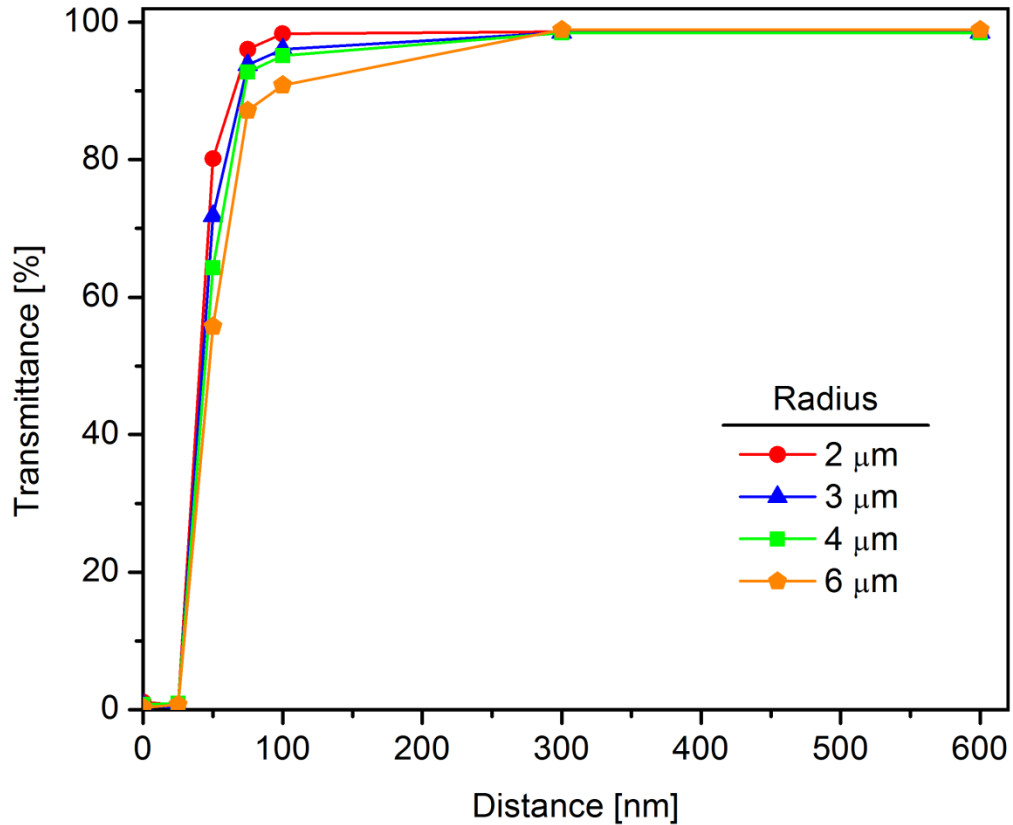
Figure 5.6: Transmittance at the circled radii, R, of 2μm, 3μm, 4μm, and 5μm.

After the effect of circled-waveguide radius on optical character is understood, range of radius is enlarged for further clarification. Such radius, R, as 0.5μm, 1μm, 2μm, 3μm, 4μm, 6μm, 8μm, and 10μm for distances of 0 to 100nm are studied, and the results are illustrated in Fig. 5.7. For all radius, high transmission contrast is obtained between distances, D, of 25nm and 50nm. Optimum radius towards short-range high-sensitivity measurement is selected to be 2μm. Optical performances for all studied sensors are showed that sensitivities around 1nm are achievable as they have been aimed.
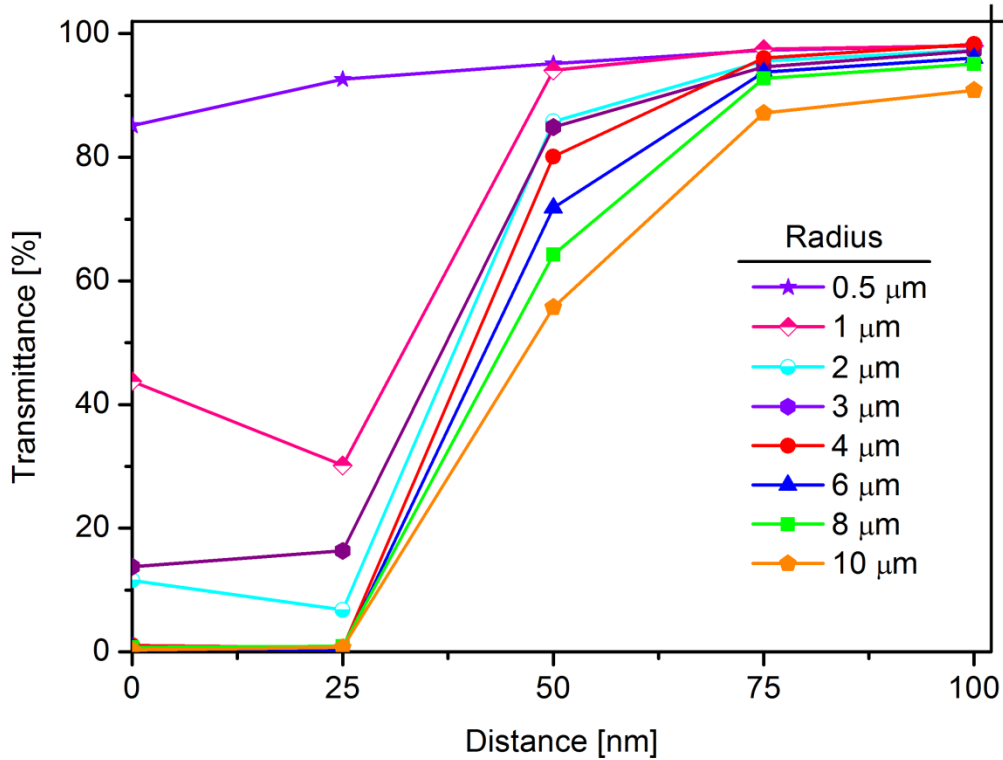
Figure 5.7: Calculated transmittance at the circled-waveguide radii, R, of 0.5µm, 1µm, 2µm, 3µm, 4µm, 6µm, 8µm, and 10µm.

5.4 Finite Element Method Calculation

The optical sensor structure is calculated via Finite Element Method Software to eliminate the design problems. The mechanism is modeled as a 3D model in the software. It is good to notice the problems before the fabrication progress to prevent the device cost and time consumption.

Figure 5.8 shows mechanical analysis results before the experimental study. Electrostatic force is calculated for the 600nm displacement. When the DC voltage is applied to source pad, because of the electrostatic force, actuator contacted to ground pad moves to down. Figure 5.8a depicts the displacement under voltage. Even the internal stress of the optical sensor is calculated, as shown in Fig. 5.8b. During the waveguide's motion, springs can carry the force against bending. At experimental characterization, springs can be broken. Figure 5.8c illustrate the safety factor of the designed structure which is understood to be sufficiently well.
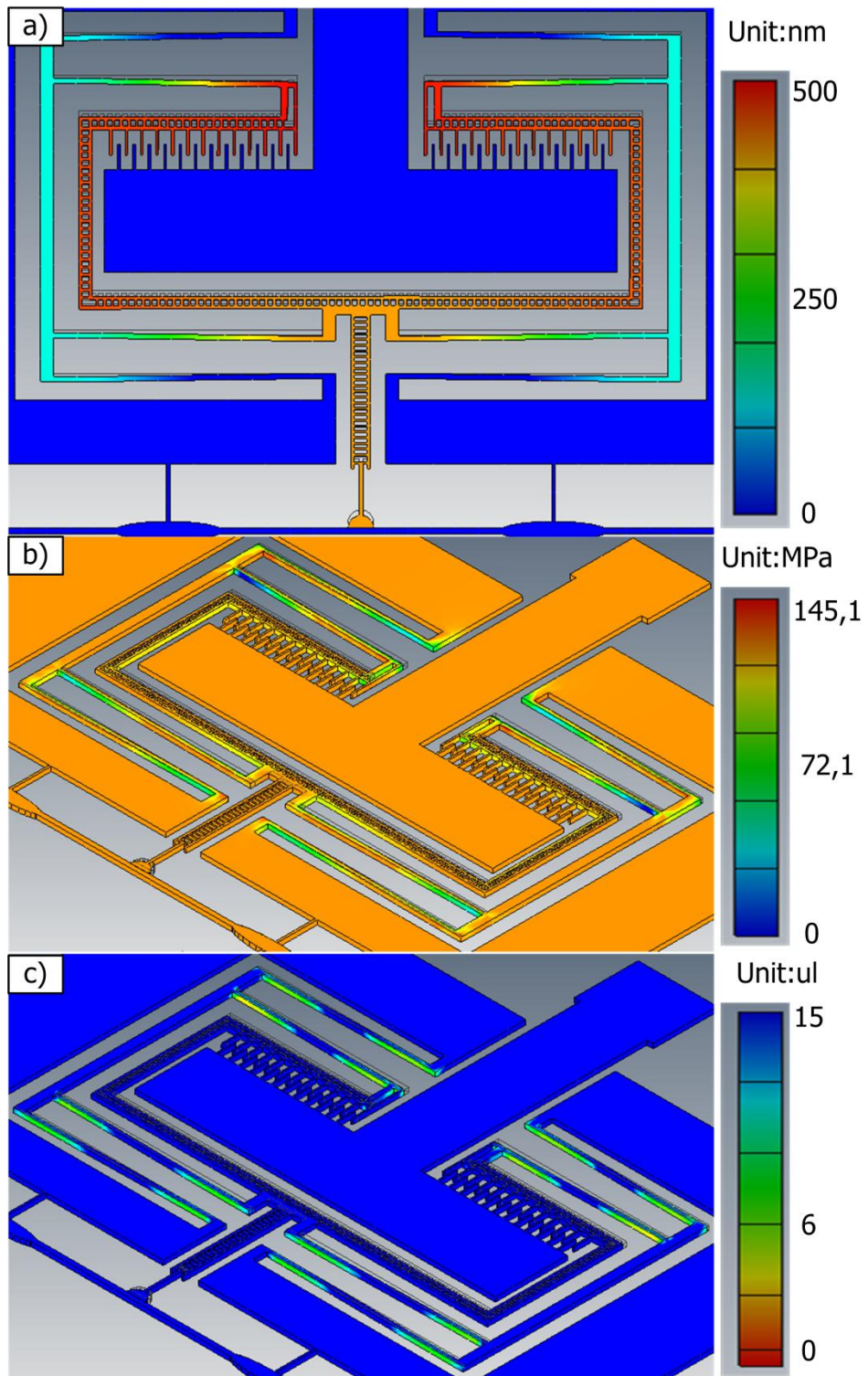
Figure 5.8: Numerical calculation results of the mechanism. a) Displacement. b) Stress. c) Safety factor.

5.5 Design of Actuator as the Source of Motion

In this particular design, n is the number of finger pairs in the comb actuator, g is the gap between stationary and moving comb finger pairs, w_f is finger width, t is finger thickness, L_f is finger length, L_0 is initial finger overlap, b is spring beam width, h is spring beam thickness, L is total spring beam length, E is Young's Modulus for single crystalline silicon, ε is permittivity of air, and V is applied DC bias voltage. Values of the parameters listed above are provided in Table 5.1.

Table 5.1. Parameters of the Comb Actuator

Symbol	Name	Value
n	Finger Pairs	28
g	Finger Spacing	0.20μm
w_f	Finger Width	0.30μm
t	Finger Thickness	0.34μm
L_f	Finger Length	2.40μm
L_o	Finger Overlap	0.40μm
b	Spring Width	0.31μm
h	Spring Thickness	0.34μm
L	Total Spring Length	35.30μm
E	Young's Modulus	185GPa
ε	Permittivity	1.885E-4
V	Bias Voltage	0-45V

For the given parameters, in order to achieve 450nm displacement range, D, at approximately 55V DC for covering any possible distance under investigation of sensor is designed. The calculated distance versus bias voltage curve is depicted in Fig. 5.9.
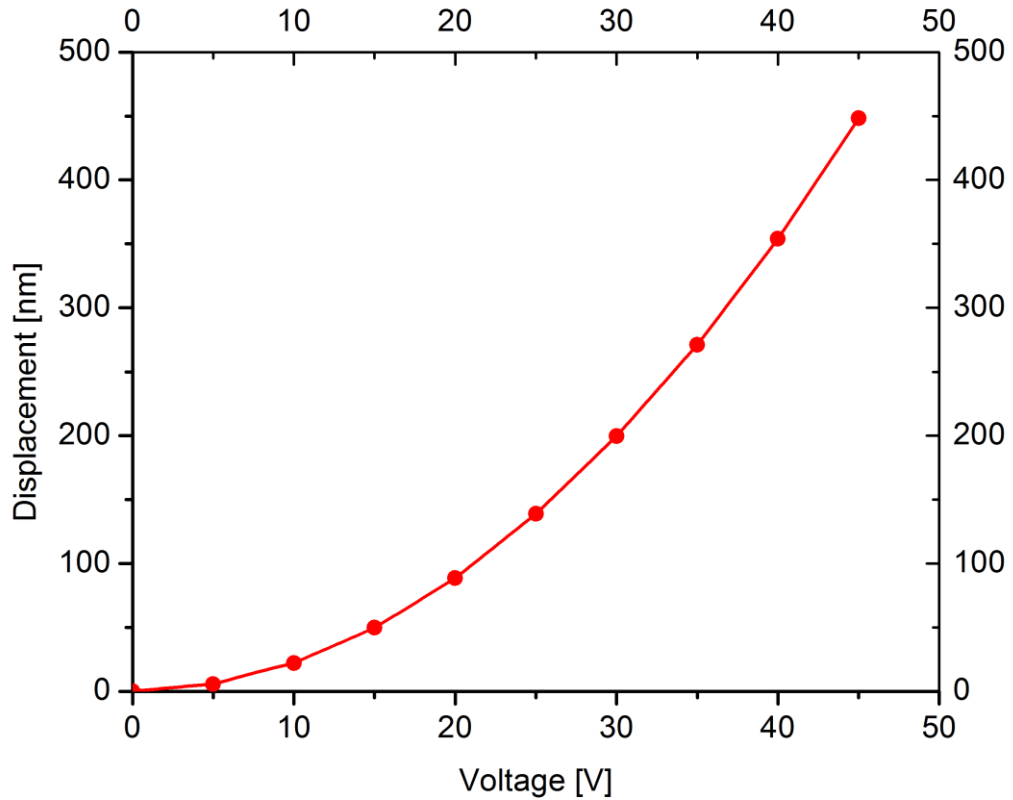
Figure 5.9: Calculated displacements for various voltages for the actuator.

5.6 Fabrication

The optical sensor is fabricated on a SOI wafer with the same progress of optical switch abovementioned. Figure 5.10 illustrates micrographs of the optical switch mechanism fabricated. As can be seen in Fig. 5.10a, the total footprint including the source and ground path is about $1 \times 2 mm^2$. Figure 5.10c depicts comb actuator, springs, input and second waveguide, elliptical intersection of the optical switch mechanism. The output waveguide of the mechanism is tapered off at 5° so as to minimize lightwave back-reflection for reliable output light intensity measurements.
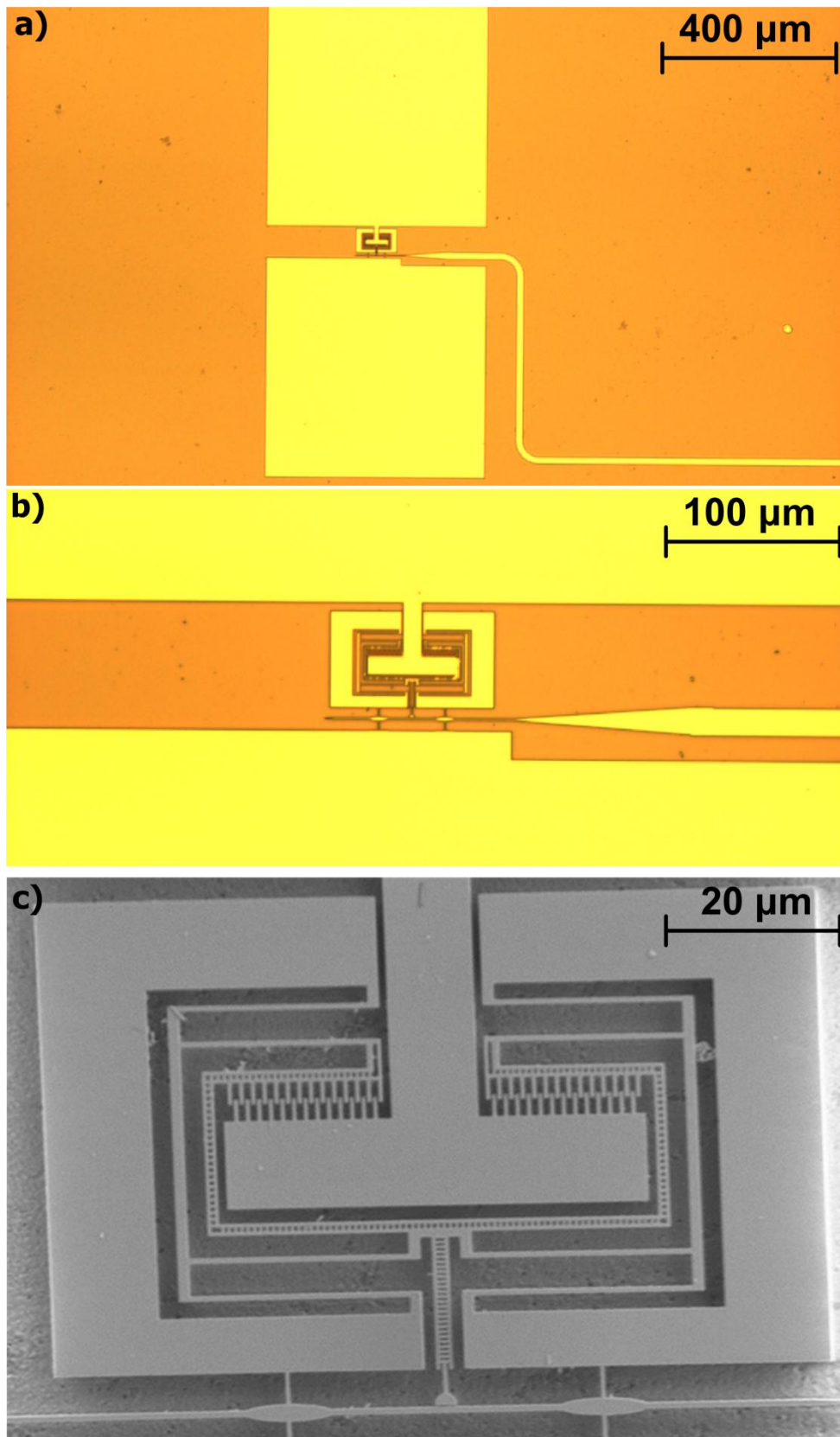
Figure 5.10: Micrographs of the optical sensing mechanism under optical microscopy. a) 10x lens. b) 20x lens. c) SEM image of the sensor.

5.7 Characterization

First of all, under mechanical characterization setup displacement is tested between second and straight waveguide via DC volt. According to design dimension of comb actuator, electrostatic force is calculated. 450nm is the displacement between waveguides.
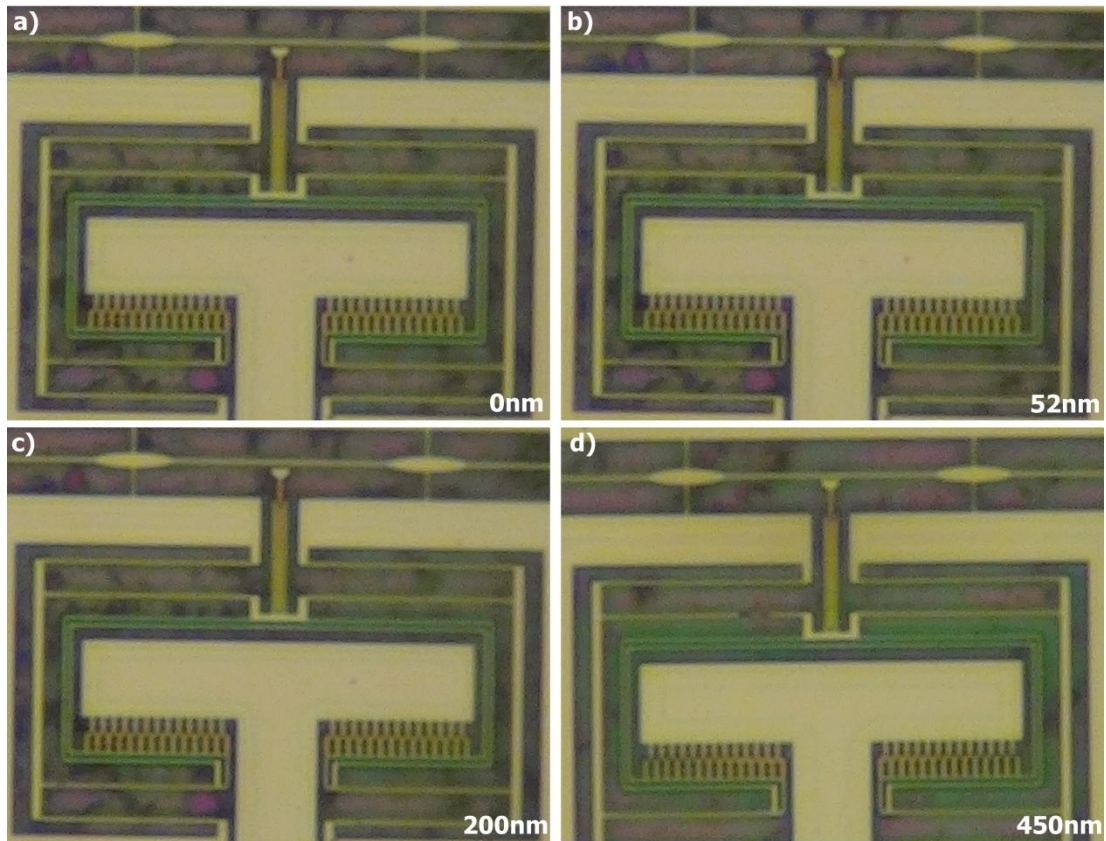
Figure 5.11: Optical sensor under several displacements.

Second, under optical characterization sensor is tested. Figure 5.12a shows that first spot and second spot as 1, 2 initials. Lightwave follow the straight waveguide until output in the 2 spot, as depicted that in Fig. 5.12b. Applying DC 15V, closes the waveguide air gap and light can penetrate to the second waveguide in the 1 spot in the Fig. 5.12c. For the fully closed the air gap, DC 45V applied to the comb actuator and 450nm displacement is moved. Figure 5.12d illustrated the light is performed in the 1 spot according to output waveguide in the switch.
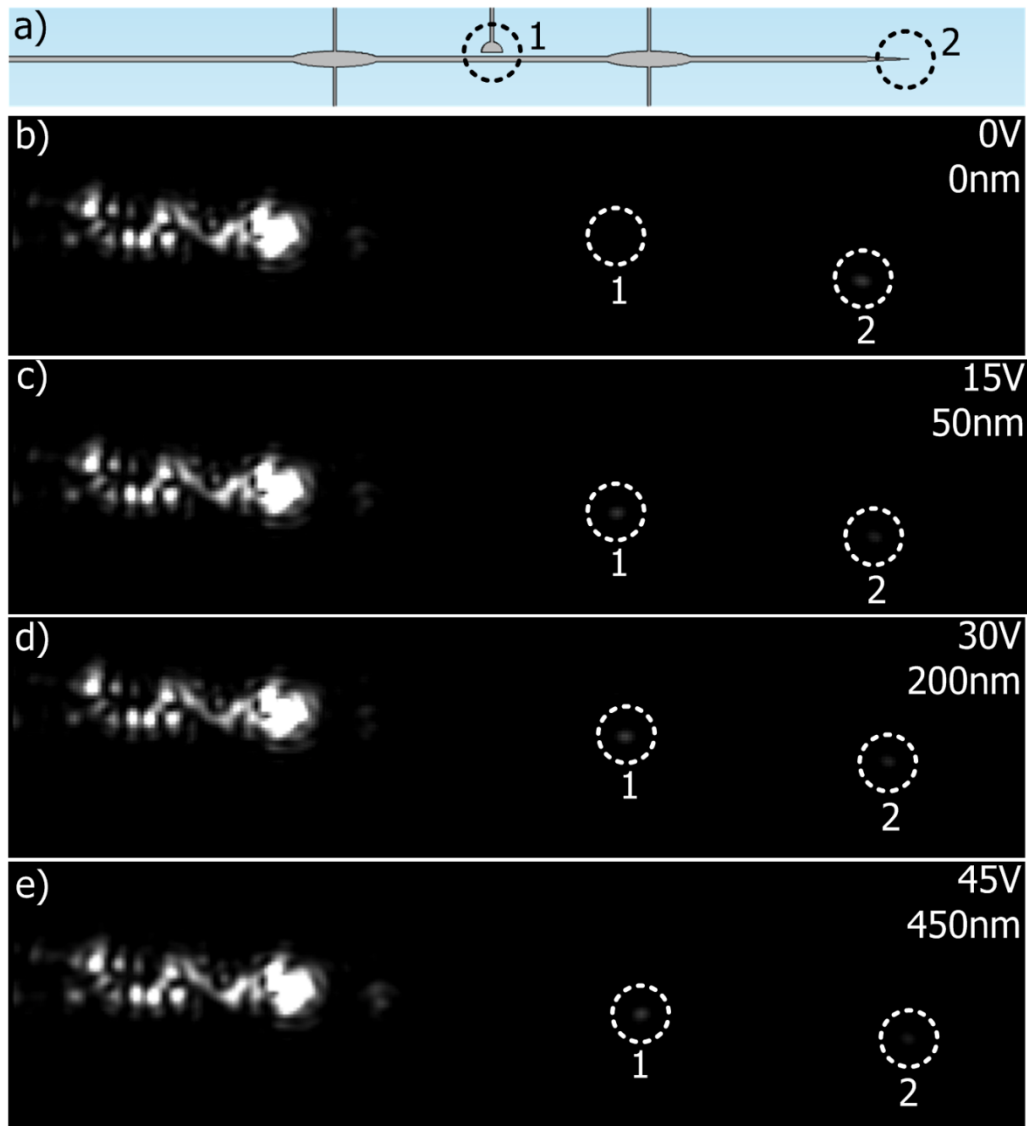
Figure 5.12: Representative result images 0, 15, 30 and 45V cases under NIR camera.

5.8 Results

Two optical sensor are fabricated which have different dimension second waveguide tips are 1µm and 2µm. 1µm optical switch is high perform according to 2µm because of the radius mass of the second waveguide to minimize the bending of the springs. During optical characterization, with the several DC volt, video is recorded via NIR camera. Optical performance is calculated with the MATLAB code by video which is recorded. Thousand points of each devices are measured and controlled the stabilization and cycle numbers. At the beginning of the study, the sensitivity is calculated about 0.083nm according to simulation results for the 1µm.
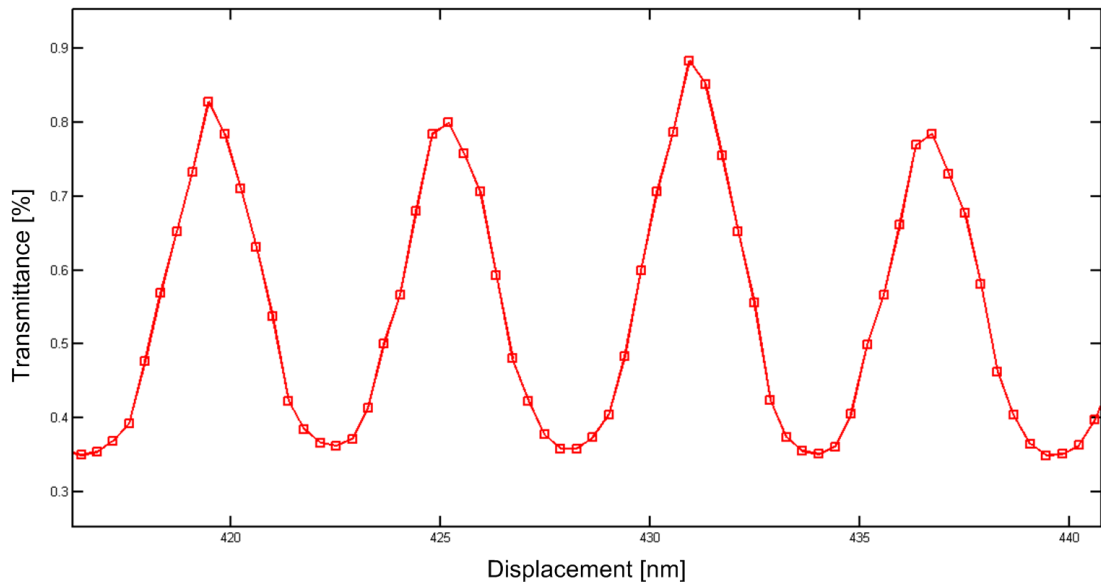
Figure 5.13: Optical results with the MATLAB code of the switch with a periodicity of 5nm.

Figure 5.13 shows that experimental performance of the switch with 4 cycle at every 5nm step at the output waveguide. The sensitivity is calculated between 0.045nm and 0.050nm per percent of the light intensity. The stability is performed several hours under the 45V and after several hours later same sensitivity is achieved. The experimental result belongs to 2µm radius of the second waveguide.
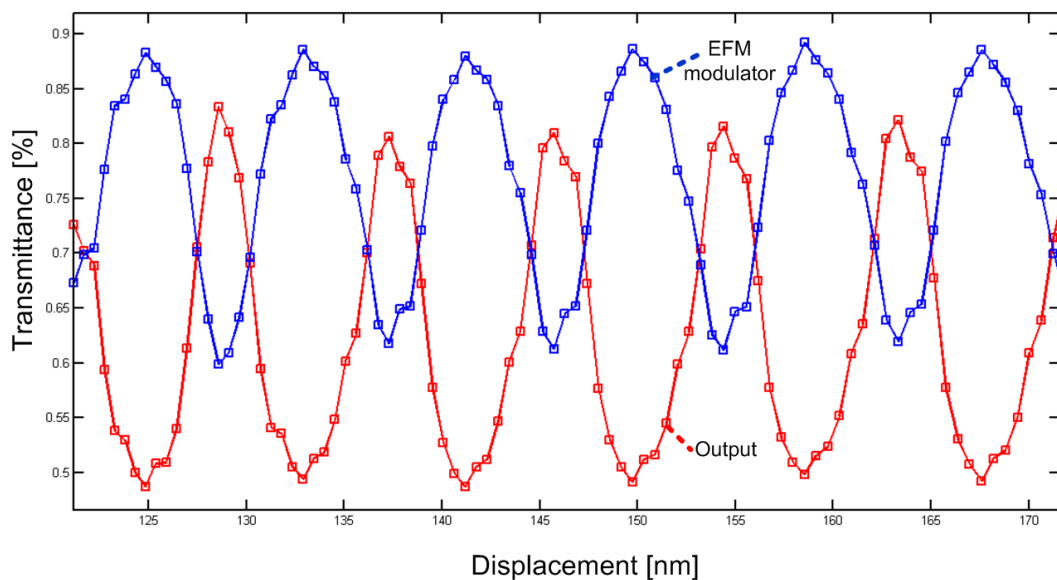
Figure 5.14: Input and output waveguide experimental results with several cycle.

Figure 5.14 shows experimental results of the input and output waveguide spots of the optical sensor. The contrast is about 30% between on and off-state between 25nm and 30nm. This value totally gives 60% optical performance change. The reason why it is not around 50% like Fig. 5.11 for the same device because of the voltage value. If the step time keep very small, the performance can decrease. The optimum time should be found for the different dimension switches.
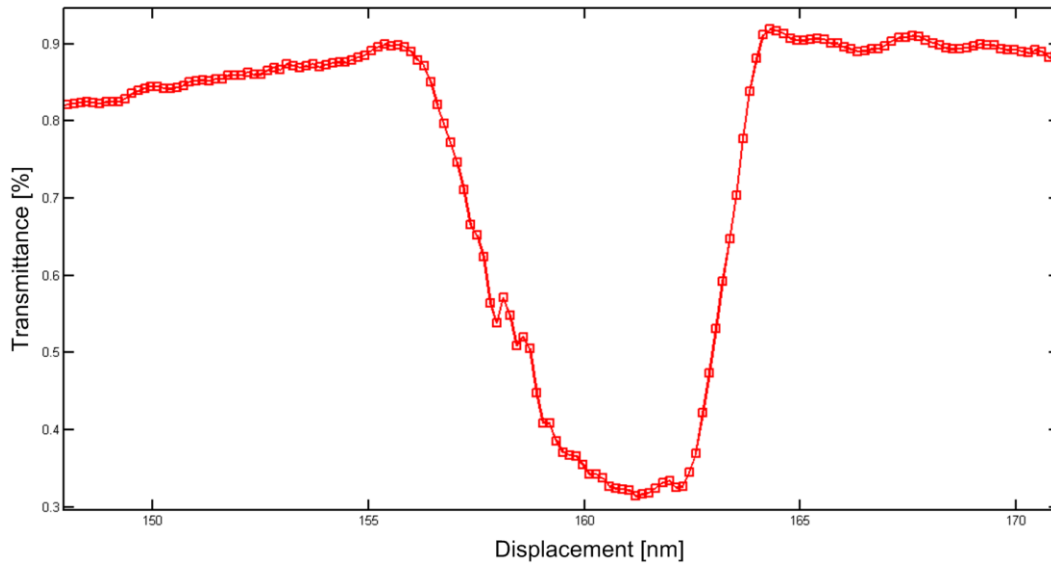
Figure 5.15: Experimental results of the output when 2μm radius sensor.

Figure 5.15 depicted that experimental results of the 2µm radius. Outcome of the MATLAB code, 61% optical contrast is performed at only 2.4nm. The sensitivity is calculated 0.039nm per percent light intensity. The measured sensitivity is higher than simulation results. The main reason is mesh size in the FDTD simulation. Mesh size is maximum used 15nm. The higher mesh size, the longer time and bigger memory space. According to design, optimum mesh size should be selected. The lower mesh size achieve close deviation with the experimental study. The second reason roughness of the sidewalls of the optical switch is close to perfect. The estimation is designed for each sidewall 10nm but according to AFM images looks like 1nm. In the AFM, high aspect ratio tip is used to measure the roughness of the sidewalls. Keeping the chromium coating deposition rate and etch ratio of the silicon very low, achieving the perfect vertical sidewalls of the micro devices. The sensitivity is the highest value as a mechanical measurement in the literature until now.
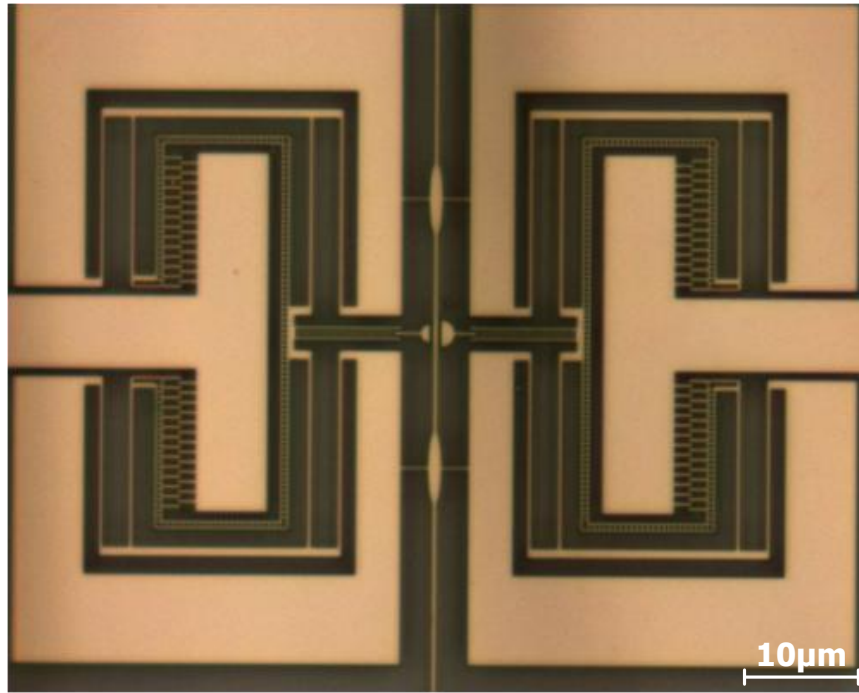
Figure 5.16: Two attachment second waveguide have different radius to same straight input waveguide.

Figure 5.16 illustrate the one design of the optical sensor. Two second waveguide is attached to the single straight waveguide so the input parameters for the light keep stable and understand the only dimension of the second waveguides and compare the results.

5.9 Principle of Optical Displacement Sensor, Type II

As shown in Fig. 5.17, the optical sensor structure is composed of a straight and triangle waveguides. The list of parameters for such a sensor design includes length of edge of the triangular-waveguide, a, distance between waveguides, D, and device silicon thickness. The preliminary numerical study in FDTD analysis for 500nm waveguide width, 10µm edge size, a, and 340nm silicon thickness values, for example, has shown 60.11% optical transmittance, an extinction ratio down to 0.73% between 25nm and 30nm displacement values, D, respectively. Such a typical value suggests high-sensitivity measurement capability in short displacement ranges.
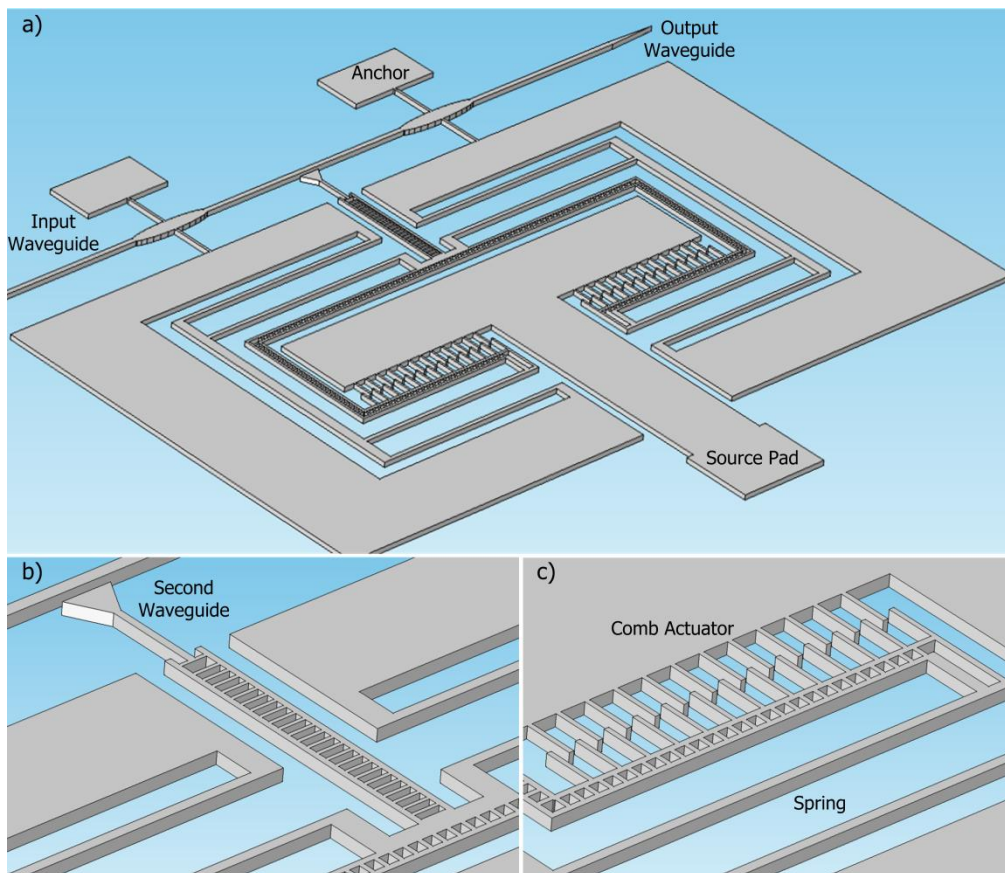
Figure 5.17: a) Schematic view of Type II tip geometry for normally-on short-range high-sensitivity optical sensor. b) Second waveguide which penetrate the light. c) Springs for the suspension of the optical sensor.

5.10 Numerical Study in FDTD

Various triangular-waveguide edge sizes of 2µm, 3µm, 4µm, 6µm, 8µm, and 10µm, at the distances of 0nm, 25nm, 30nm, 35nm, 40nm, 45nm, 50nm, 75nm, 100nm, 300nm, and 600nm are simulated. Outcomes of the calculation in FDTD are provided and discussed in detail below.

5.10.1 Effect of edge size of triangular waveguide

Optical performance of Type II optical sensor structure is studied at 0nm, 25nm, 30nm, 35nm, 40nm, 45nm, 50nm, 75nm, 100nm, 300nm, and 600nm distances, for an edge length, a, 10µm, whose results are shown in Fig. 5.19. Insets in Fig. 5.19 illustrate propagation of lightwave at the junction of the two waveguides. Optical performance for this optical switch candidate with 10µm edge of triangular-waveguide, for instance, is obtained to change from 0.73% to 60.11% between 25nm and 30nm displacement values, respectively, corresponding to a sensitivity of 0.084nm per percent of light intensity.
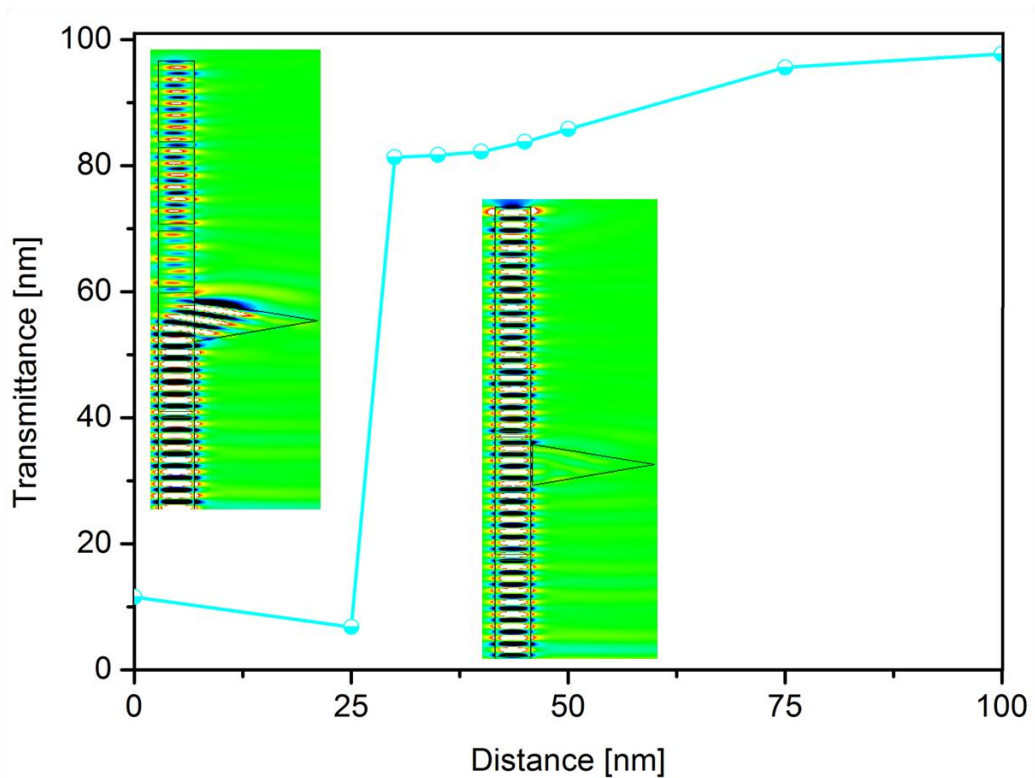
Figure 5.18: Transmittance for triangular-waveguide edge length, a, of 2µm.
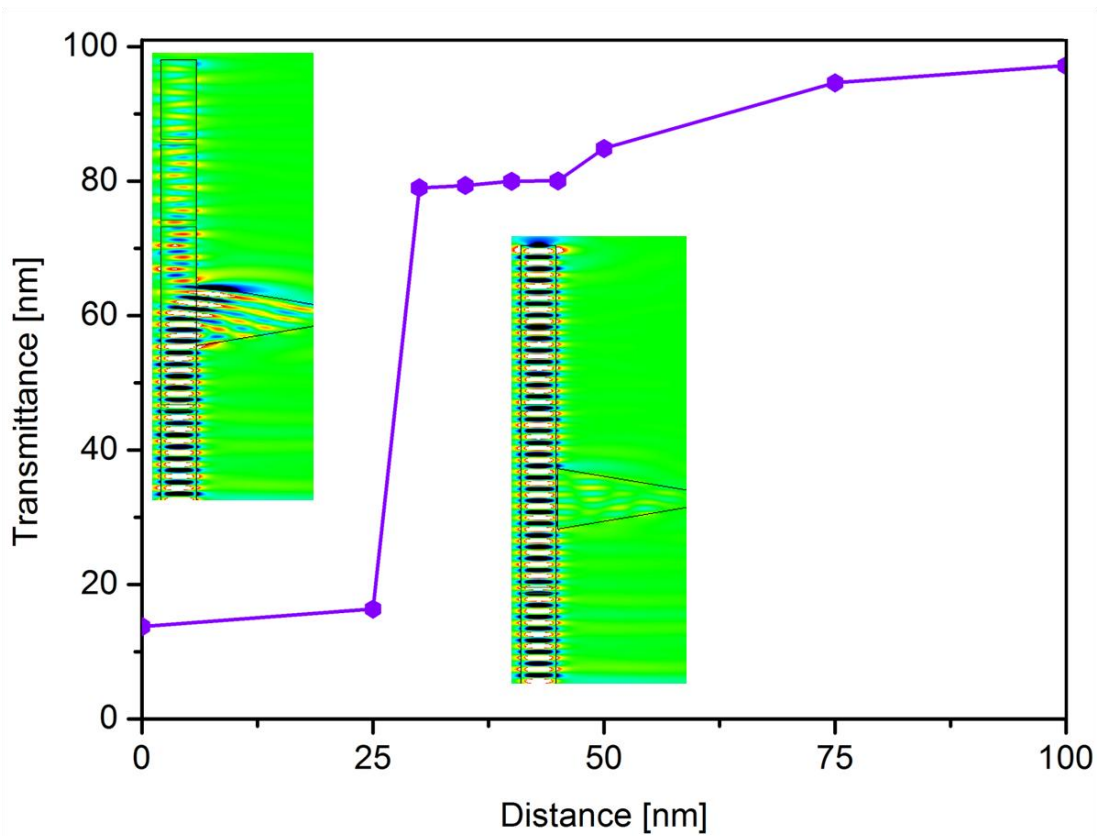
Figure 5.19: Transmittance for triangular-waveguide edge length, a, of 3μm.
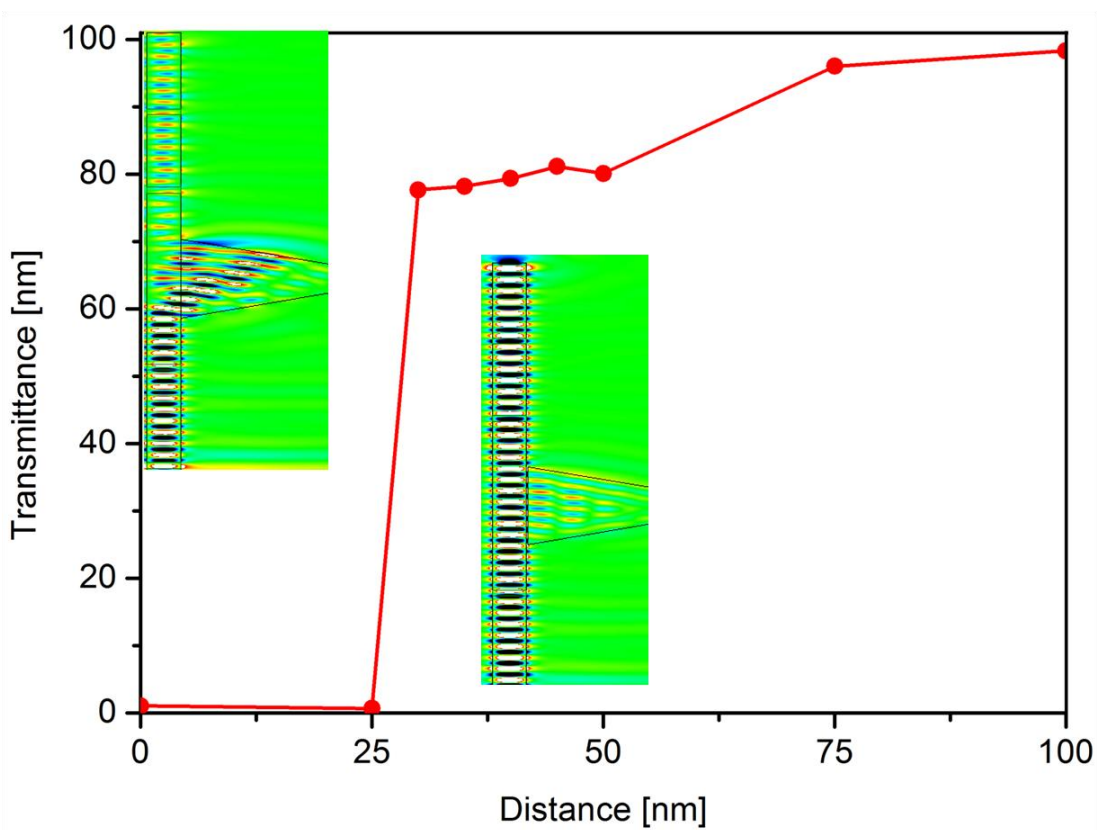
Figure 5.20: Transmittance for triangular-waveguide edge length, a, of 4μm.
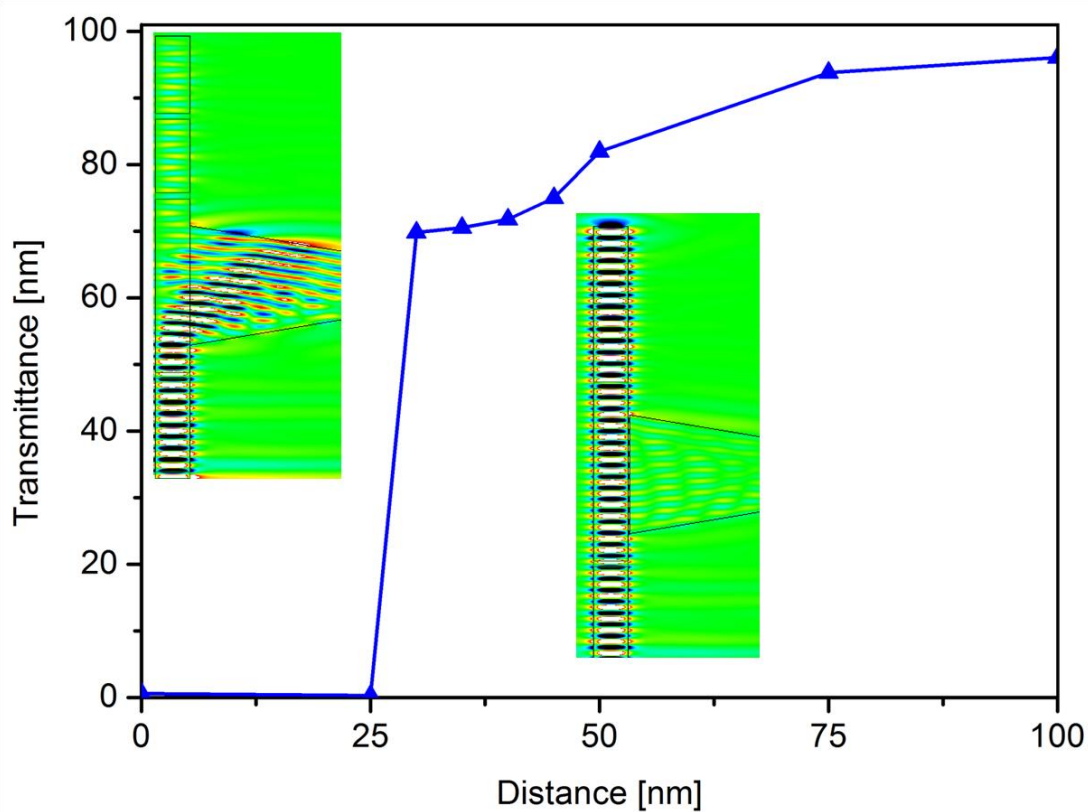
Figure 5.21: Transmittance for triangular-waveguide edge length, a, of 6μm.
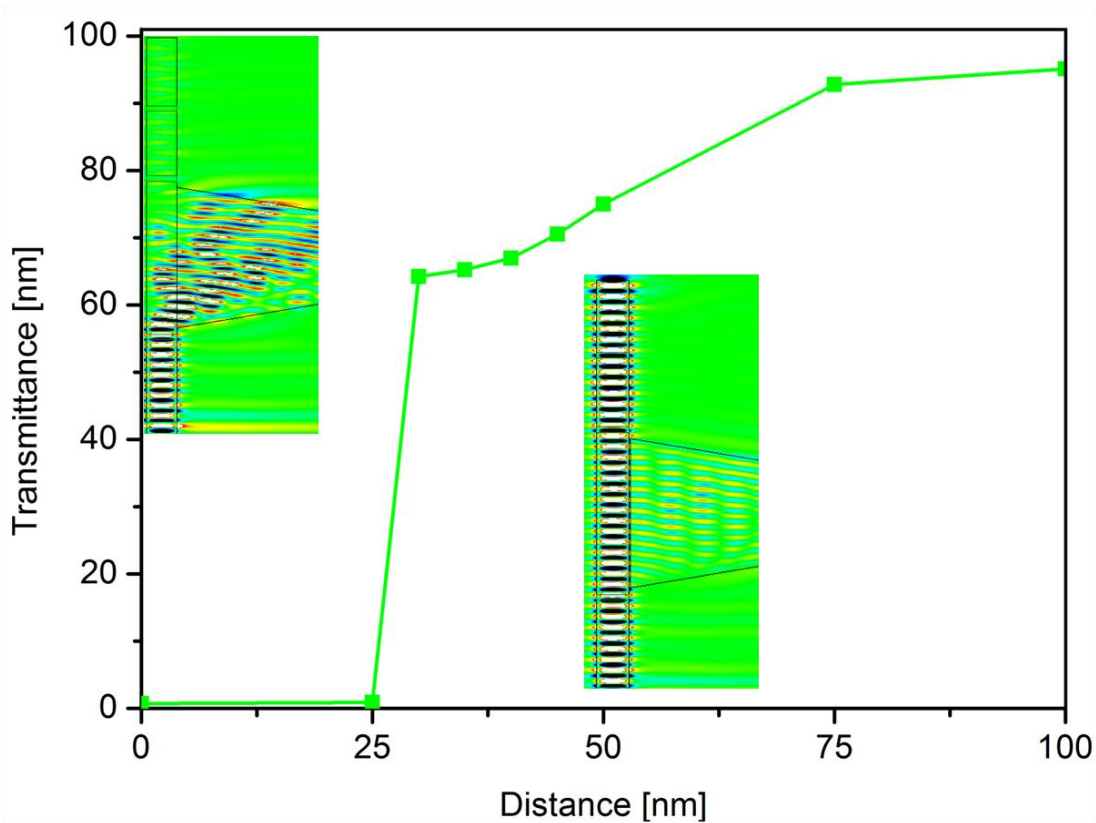
Figure 5.22: Transmittance for triangular-waveguide edge length, a, of 8μm.
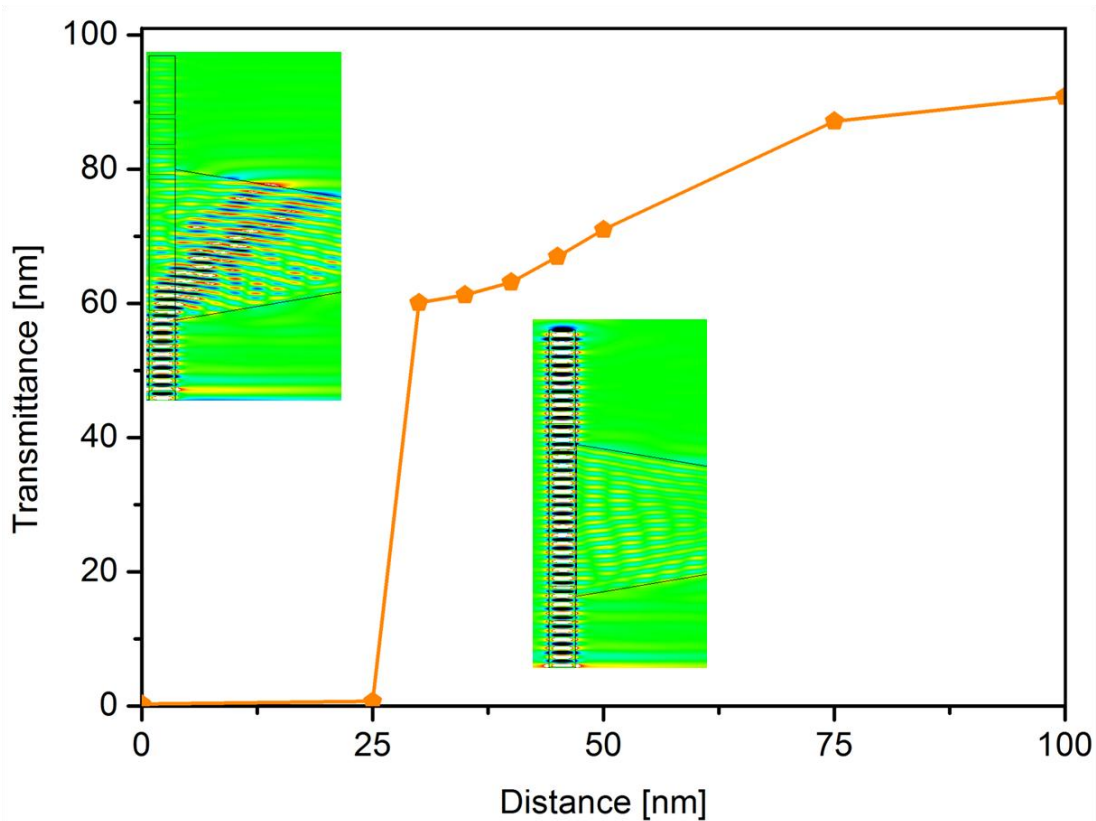
Figure 5.23: Transmittance for triangular-waveguide edge length, a, of 10µm.

After the effect of triangular-waveguide edge length on optical characteristic is understood, range of edge length, a, is enlarged for further clarification. Such lengths, a, as 2µm, 3µm, 4µm, 6µm, 8µm, and 10µm for distances from 0 to 100nm are studied, and the results are illustrated in Fig. 5.24. For all edge lengths, high transmission contrast is obtained between distances, D, of 25nm and 30nm. As the size of triangular-waveguide's edge decreases, sensor's sensitivity increases. Maximum sensitivity, 0.064nm per percent of light intensity, towards short-range high-sensitivity measurement in Type II optical sensor is selected to be at a of 2µm. Optical performances for all studied sensors are showed that sensitivities around 1nm are achievable as they have been aimed.
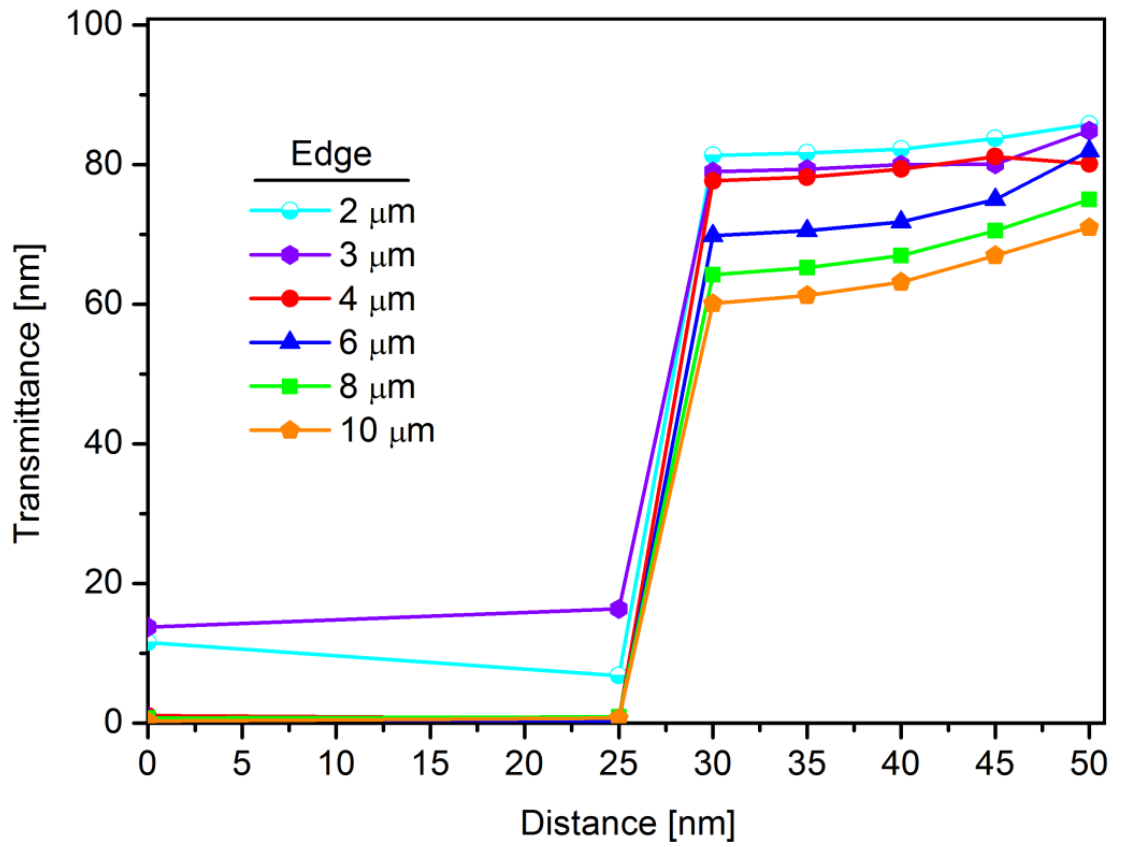
Figure 5.24: Calculated transmittance at the triangular-waveguide edge length, a, of 2µm, 3µm, 4µm, 6µm, 8µm, and 10µm.

5.11 Finite Element Method Calculation

Figure 5.25 shows mechanical analysis results before the experimental study. Electrostatic force is calculated for the 450nm displacement. When the DC voltage is apply to source pad because of the electrostatic force actuator which is contacted with ground path moves down. Figure 5.25a depicts during the displacement under voltage. Even the internal stress of the optical sensor is calculated, as shown in Fig. 5.25b. At the moves of the waveguide, springs can resist the force for the bending. At experimental characterization, springs can broken. Figure 5.25c illustrate the safety factor of the designed structure and it is very well.
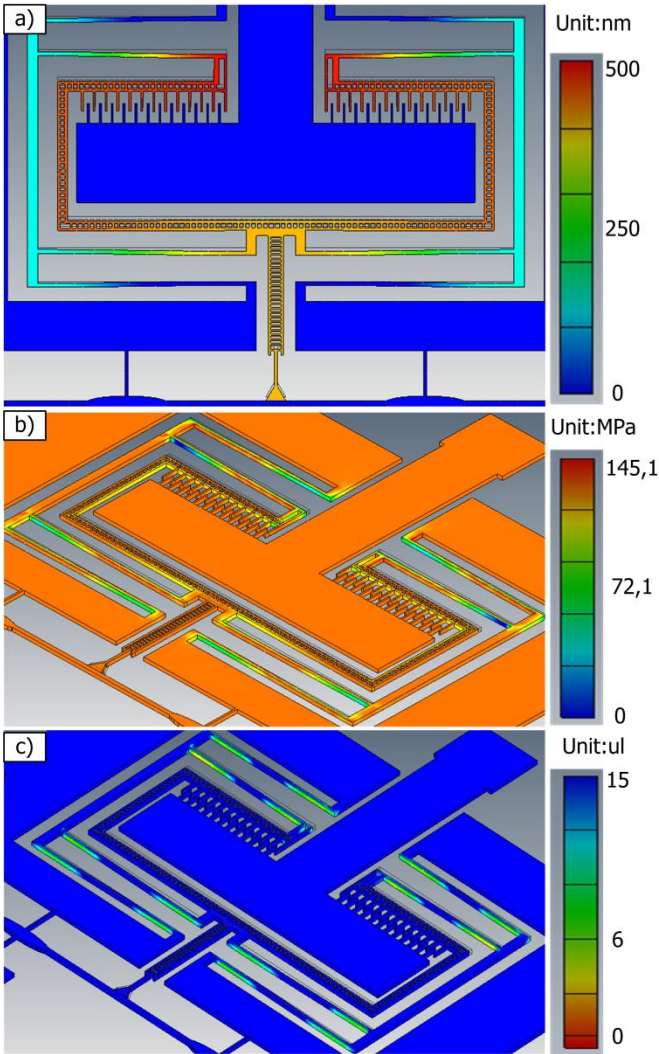
Figure 5.25: Numerical results of the optical switch via FEM. a) Displacement. b) Stress of the structure. c) Safety factor of the mechanism.

5.12 Design of Actuator as the Source of Motion

In this particular design, n is the number of finger pairs in the comb actuator, g is the gap between stationary and moving comb finger pairs, w_f is finger width, t is finger thickness, L_f is finger length, L_0 is initial finger overlap, b is spring beam width, h is spring beam thickness, L is total spring beam length, E is Young's Modulus for single crystalline silicon, ε is permittivity of air, and V is applied DC bias voltage. Values of the parameters listed above are provided in Table 5.2.

Table 5.2. Parameters of the Comb Actuator

Symbol	Name	Value
n	Finger Pairs	28
g	Finger Spacing	0.20μm
w_f	Finger Width	0.30μm
t	Finger Thickness	0.34μm
L_f	Finger Length	2.40μm
L_o	Finger Overlap	0.25μm
b	Spring Width	0.27μm
h	Spring Thickness	0.34μm
L	Total Spring Length	35.30μm
E	Young's Modulus	185GPa
ε	Permittivity	1.885E-4
V	Bias Voltage	0-55V

For the given parameters, in order to achieve 450nm displacement range, D, at approximately 55V DC for covering any possible distance under investigation of sensor is designed. The calculated distance versus bias voltage curve is depicted in Fig. 5.26.
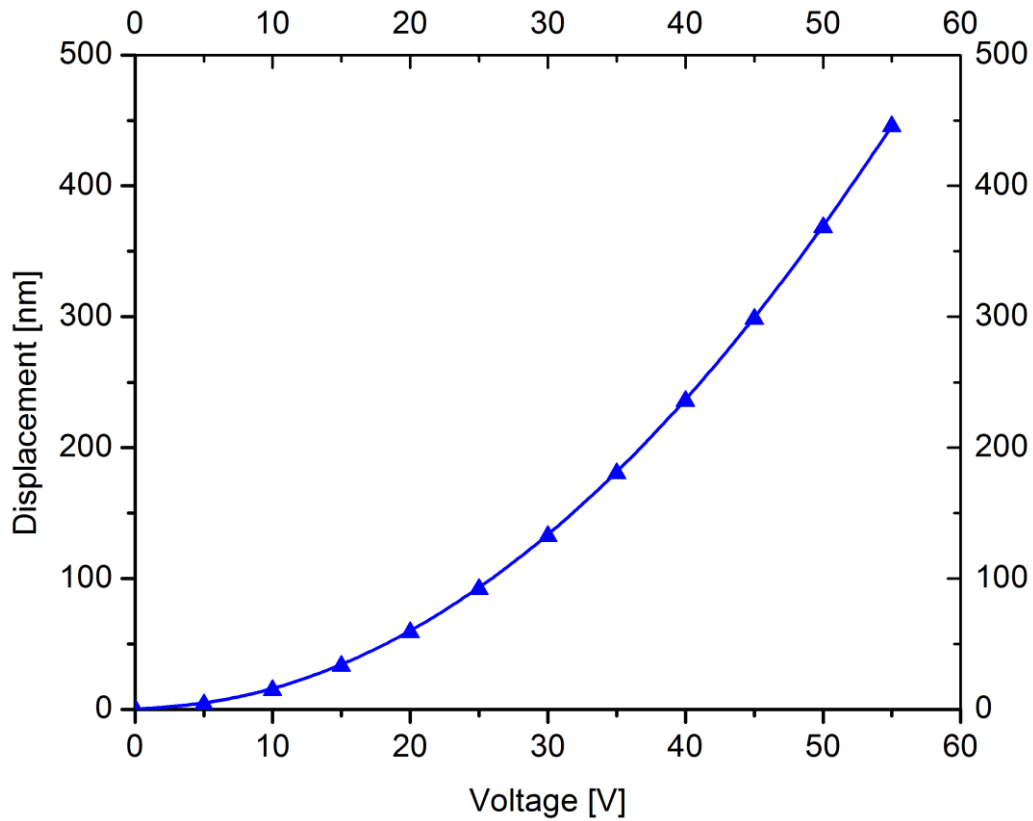
Figure 5.26: Calculated displacements for various voltages for the actuator.

5.13 Fabrication

The fabrication process is same abovementioned in Chapter 4.5 with the optical switch. All structure is fabricated $2x2cm^2$ SOI wafer and separated via Dicing saw to different parts. Figure 5.27 shows the fabricated optical sensor under SEM. Because of the low coating ratio and etch ratio, roughness is below 5nm. The roughness is measured under AFM with the high aspect ratio tip from the sidewalls. Elliptical intersection, straight, second, input and output waveguide, springs and actuator is fabricated very well.
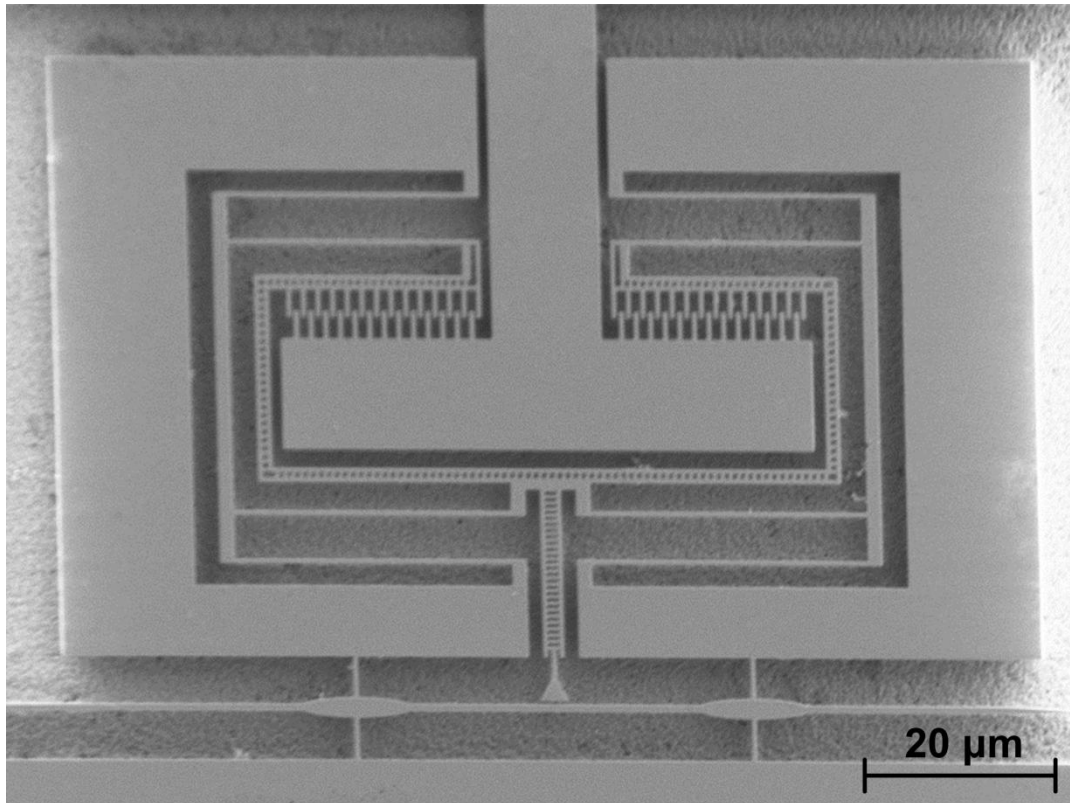
Figure 5.27: SEM image of the optical sensor mechanism.

5.14 Characterization

The mechanical characterization setup is as mentioned in Chapter 2 and 3 of this thesis report. 450nm displacement between the waveguide is enough to disturb the lightwave from the straight waveguide under DC 55V. The thing is the temperature of the wafer, HF ratio, water ratio of the solution, HF temperature and process time effects the structure mechanism bending and sticking the ground during the Vapor HF Etching Setup. If there is any bend in the structure, any actuator part go down and impossible to create any electrostatic force. Actuator pairs should stay at the same level when the HF process is finished. Figure 5.28 illustrates the optical sensor under different DC voltage values.
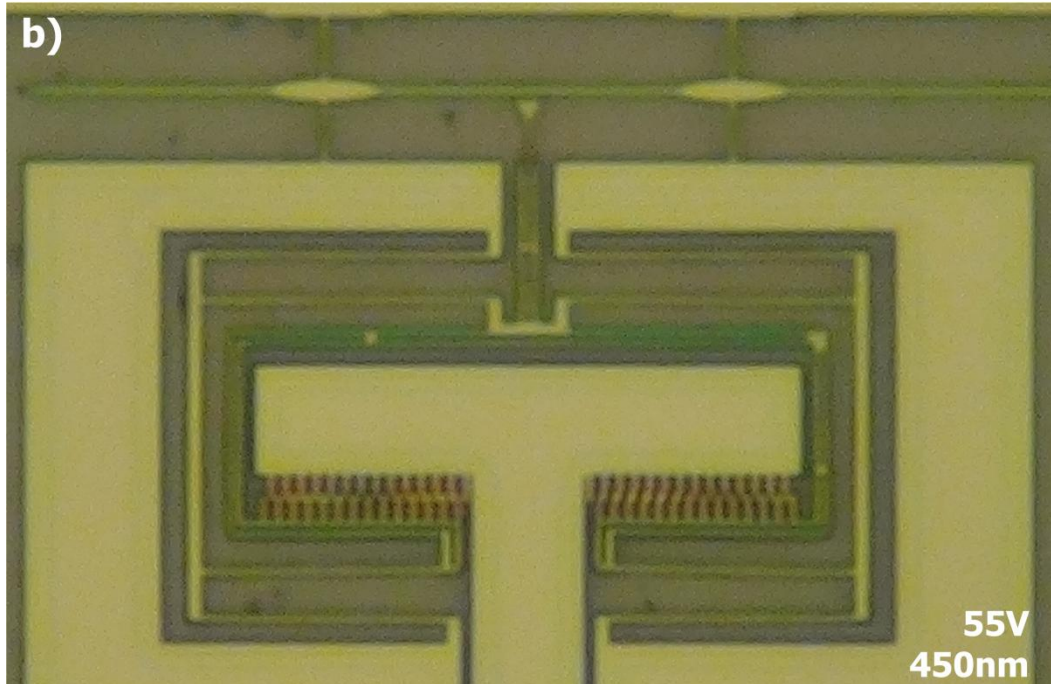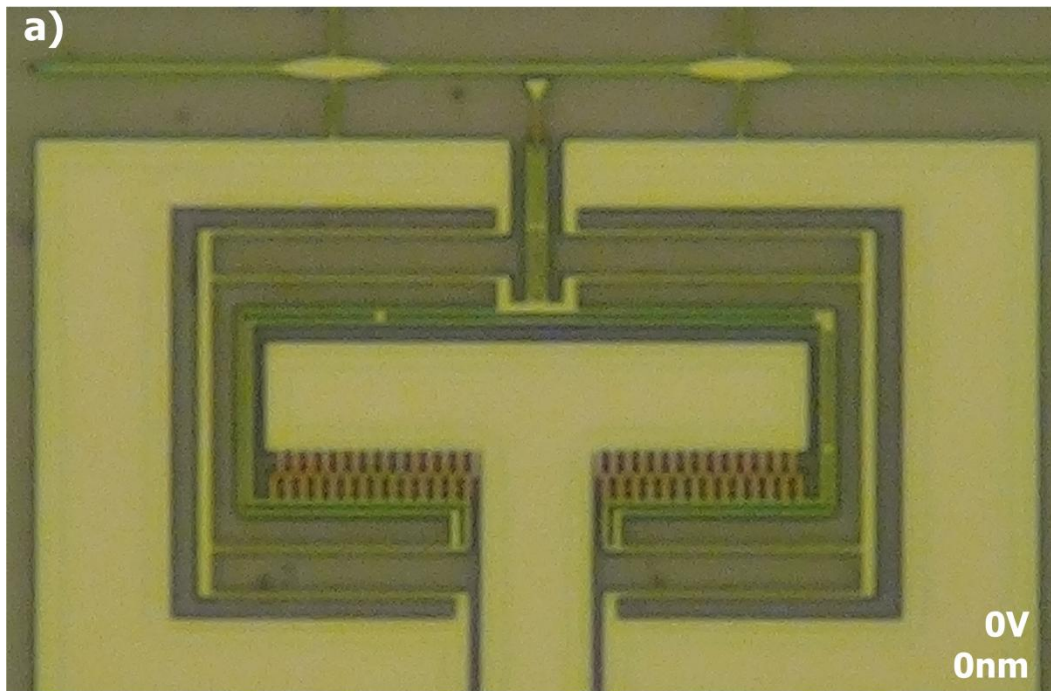
Figure 5.28: Optical switch under DC Voltage. a) 0V DC at 0nm. b) 55V DC at 450nm.

Optical characterization of the fabricated mechanism is tested for the optical performance to match the theoretical and experimental results. The optical setup is mentioned same with the Chapter 2 and 3 of this thesis report. First of all, when the 1.55µm wavelength, TE mode and 4.8 mW light is coupled to the 12µm input waveguide, shrinks with the tapered waveguide and follows to the mechanism. First spot is the part of the second waveguide touches the straight waveguide. The second spot is the 5° tapered waveguide which is output of the mechanism. When the DC voltage apply to the comb actuator of the mechanism, air gap between waveguide closes and light can block via second waveguide. The air gap is fully closed under 55V light cannot perform to output. The optical performance of the sensor is changed from around 60% to 10% at only 5nm displacement. Figure 5.29 depicts optical results of the mechanism with the 0, 20, 25, 30, 35, 40, 45, 50 and 55V values.
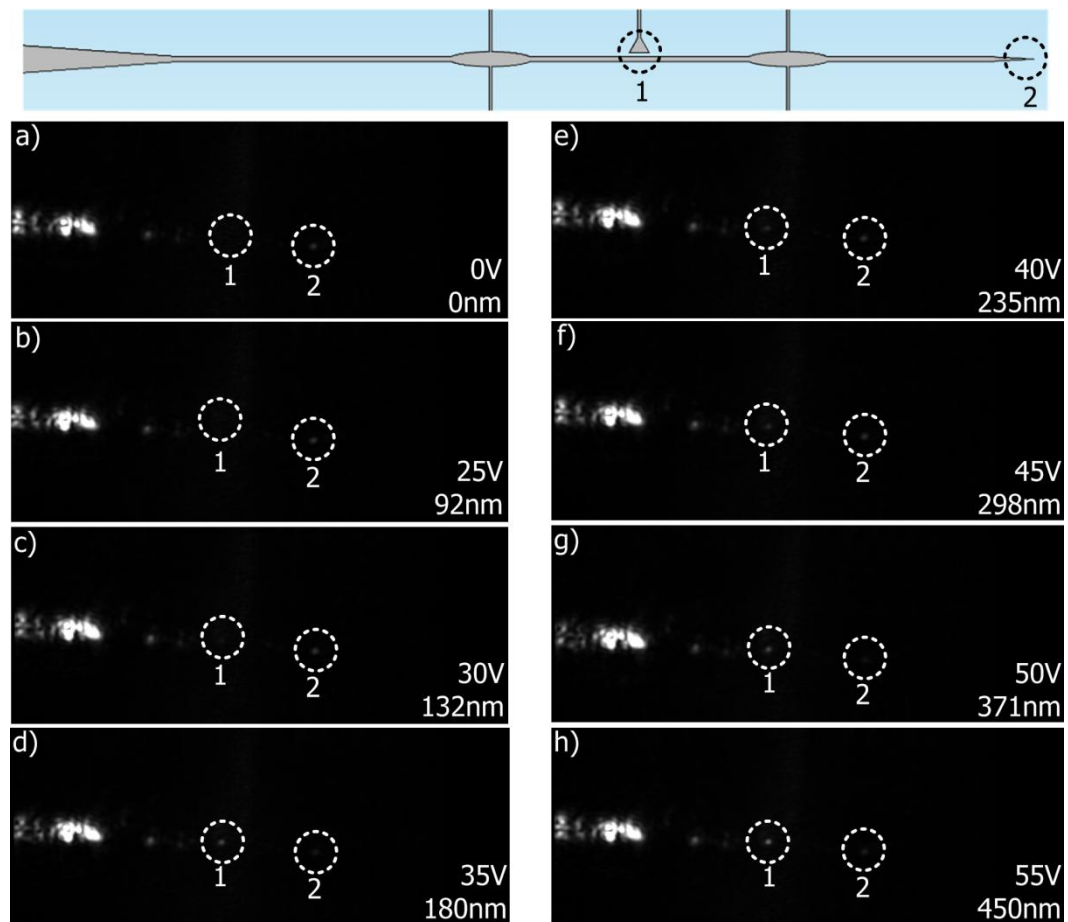
Figure 5.29: Optical performance of the fabricated mechanism with several voltage values.

5.15 Results

Two optical sensors are fabricated which have different dimension second waveguide tips are 2µm and 3µm. 2µm optical sensor is high perform according to 3µm because of the edge mass of the second waveguide to minimize the bending of the springs. Optical performance is calculated with the MATLAB code by video is recorded via NIR camera. At the beginning of the study, the sensitivity is calculated about 0.064nm according to simulation results for the 2µm.
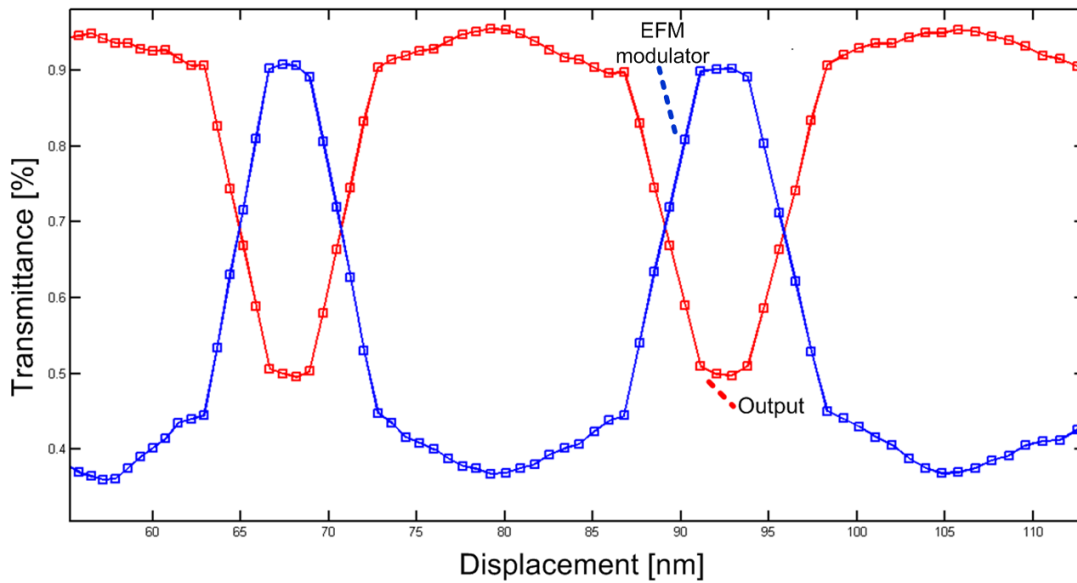
Figure 5.30: Experimental results of the optical sensor for the 2µm edge with input and output waveguides at two steps.

Figure 5.30 depicted that results of the optical sensor at optical performance. During the transmittance increases at input, decreases at output waveguide at the same value. The sensitivity is measured between minimum and maximum points 0.077nm and 0.5nm per percent of the light intensity. The minimum sensitivity value closes to FDTD results. The experimental and simulation results mismatch is only 12.03% at the picometer level which is very well. The reason of the mismatch belongs to mesh size of the simulation study. Actually, the numerical study with smaller mesh size closes to experimental result with high errors. The measurement is calculated hundred points with the different voltage and displacement and result kept same.
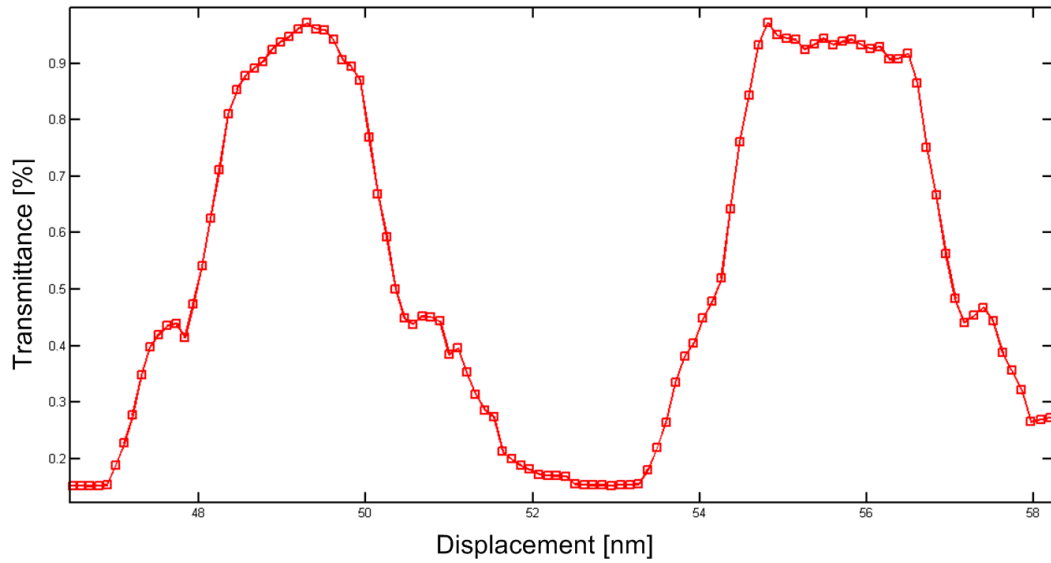
Figure 5.31: Experimental results of the optical sensor for the 3µm edge with input and output waveguide at two step.

The experimental results belongs to 3µm edge second waveguide. The sensitivity is much more better than simulation results. The reason is as aforementioned in the 5.8 Results section. The minimum and maximum sensitivity is 0.026nm and 0.050nm per percent of the light intensity as shown in Fig. 5.31. These values are very well according to literature. Figure 5.32 shows that two attachment second waveguide for the comparison.
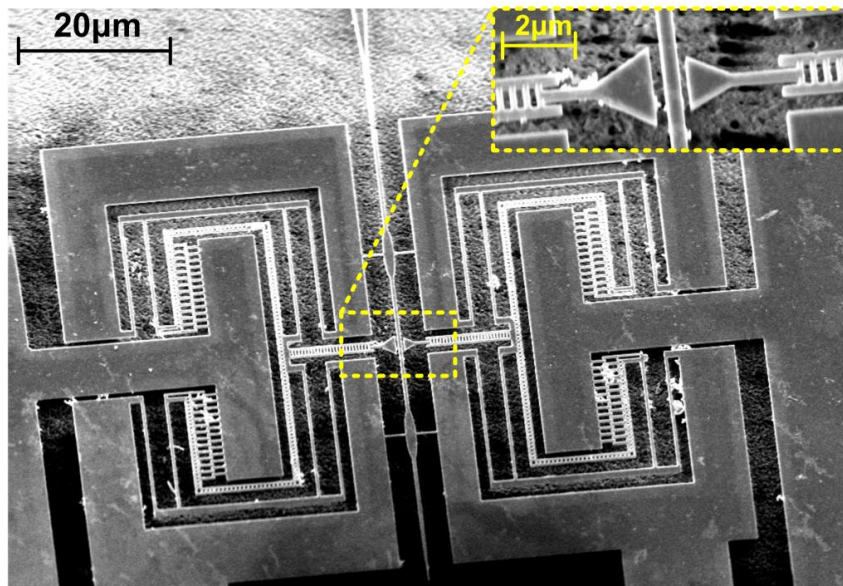
Figure 5.32: SEM images of two attachment second to single straight waveguide.

5.16. Summary

Chapter 5 presents two types of sensing mechanisms are introduced and fabricated in chapter. Short-range high-sensitivity in-plane optical sensor again, but at normally-on state are being investigated in order to clarify their initial state effects on the sensing characteristics. Towards this goal, two major types of sensor approaches are studied. All sensors utilized in Chapter 5 are based on EFM. Sensitivities achieved in this phase are from 0.084nm down to 0.06nm per percent of light intensity within sub-100nm distances. For the half-circled waveguide optical sensor, two different second waveguide is fabricated. The sensitivity is measured 0.045nm and 0.039nm per percent of the light intensity 1μm and 2μm radius, respectively. These values are very well in the mechanical tuning at the optical performance at switching in the literature. For the triangular-waveguide optical sensor, two different second waveguide is fabricated which are 2μm and 3μm. The sensitivity is measured as a experimental 0.077 and 0.026nm per percent of the light intensity.

6. LOW-LOSS SILICON INTERSECTION BASED ON DIFFRACTION GRATING

6.1 Introduction

For high-density photonic integrated circuits, low-loss and low-crosstalk intersection of waveguides is a basic but important component. Optical intersections be classified relative to each other which are photonic crystals, refractive index engineering and diffraction grating. There are common parameters used in each of these areas which are transmittance, easy of microfabrication, footprint and wavelength-dependence. Several paper published about the optical intersections used only two method of physical concept utilized which are PhC and refractive index engineering. There are advantages and disadvantages of physical concept methods which are PhC, refractive Index engineering and diffraction grating. Optical intersections of PhC has low transmittance and fabricate to hard compare to other methods and wavelength sensitivity is narrow bandwidth [48]. Chen *et al.* were reported low-loss multimode-interference-based crossings for silicon wire waveguides, as shown in Fig. 6.1 [49]. The optical performance of silicon wire waveguide 95.49% and wavelength dependency on between 1.52-1.58µm.
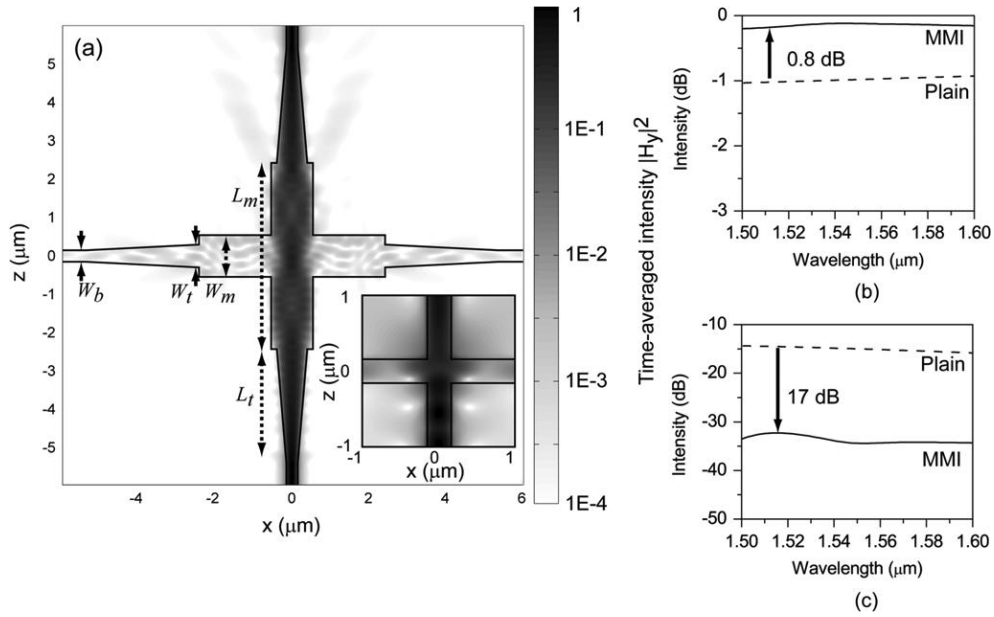
Figure 6.1: FDTD-simulated time-averaged H_j^2 pattern in an MMI crossing. Inset shows the simulated time-averaged H_j^2 pattern in a plain crossing with waveguide width of 0.3µm [49].

Bogaerts *et al.* were presented low-loss, low-cross-talk crossings for silicon-on-insulator nanophotonic waveguides, as seen in Fig. 6.2 [38]. The optical performance is 96.80% and wavelength dependency on between 1.53-1.57µm.
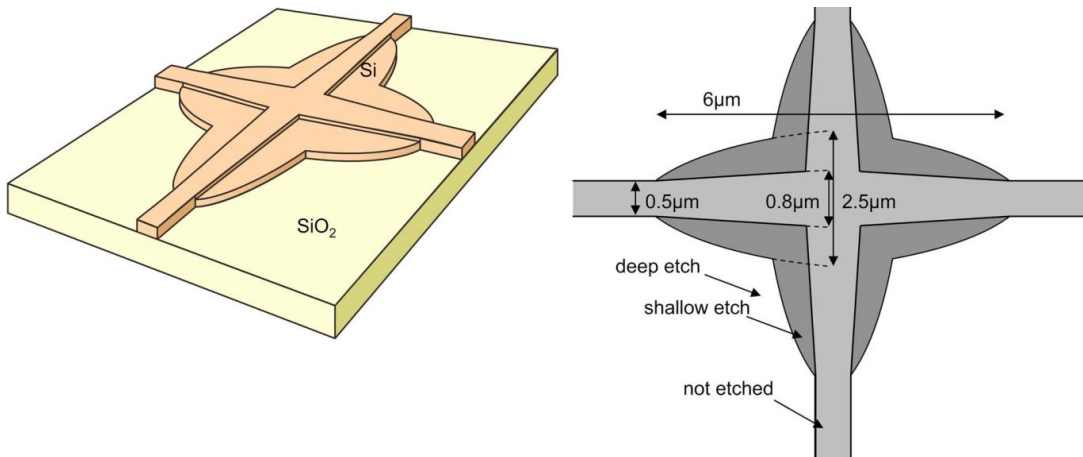
Figure 6.2: Waveguide crossing with a double etch [31].

Fukazawa *et al.* were reported low loss intersection of Si photonic wire waveguides as seen in Fig. 6.3 [32]. The transmittance of the structure is less than 0.1dB at a wavelength of 1.55µm.
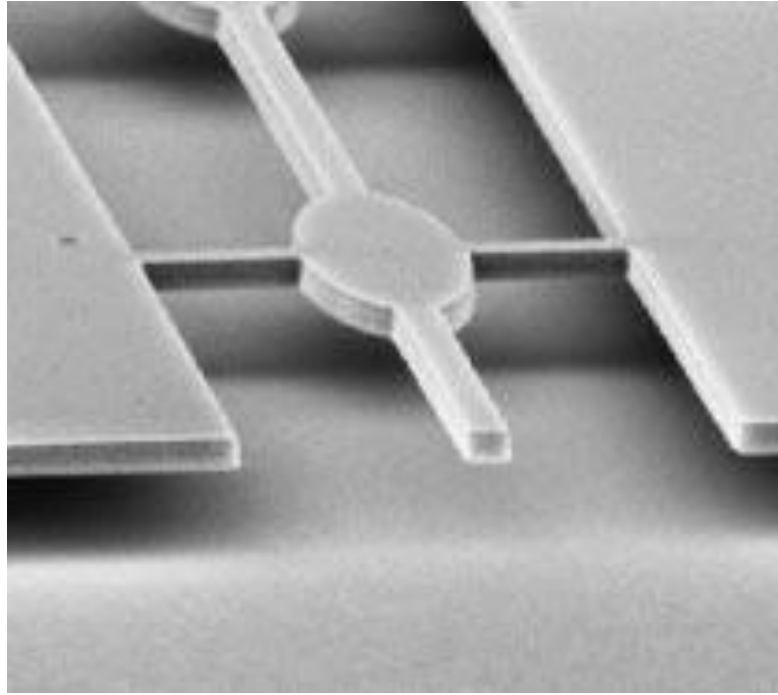
Figure 6.3 : Experimental results for SOI type and air-bridge-type waveguides.

Refractive Index engineering methods has high transmittance but less than diffraction grating method, fabrication is more easy than diffraction grating [38, 48-50]. Elliptical Intersections are utilizing to suspend the waveguides in the air with the help of springs for the displacement sensor and optical switch mechanisms. Optical performance is optimized just changing the length and width of the elliptical shape numerically. The highest transmittance of the elliptical intersection provides around 96% efficiency. This value of the intersection is decreasing the total optical performance of the structures and it is the main reason of deviation between theoretical and experimental results. In this chapter, we propose new elliptical intersection geometry based on diffraction grating with ultra high optical response.

6.2 Structure

The new elliptical intersection mechanism based on the diffraction grating method. The structure consists of separated waveguide with 50nm bridge width and 50nm air gaps. Figure 6.4 illustrate the diffraction grating on the intersection. The optical performance of intersection decreases because of lightwave penetrates in the middle of the fold to outside. However, in the proposed structure, bridges system shrink the

light to middle like biconvex lens and at the output spread the light previous situation.
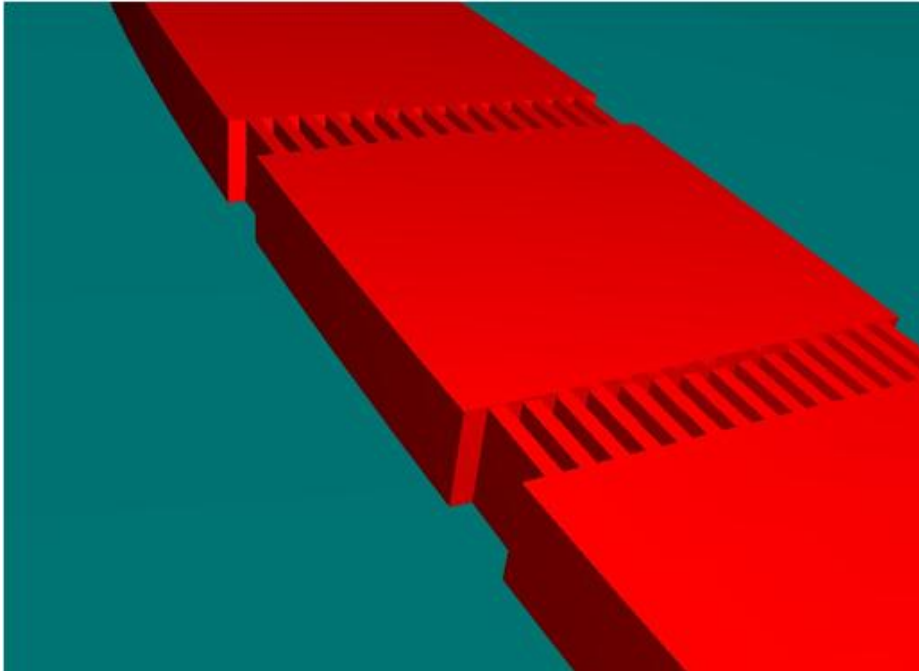
Figure 6.4: Schematic view of elliptical intersection based on diffraction grating.

6.3 Numerical study

Simulations of the tip geometries for the optical switch are numerically conducted in 3D FDTD analysis. For single-mode TE-polarized light at 1.55μm wavelength, waveguide width and thickness are 500nm and 260nm, respectively. Elliptical tip geometry is 1.5μm-wide, 7.2μm-long, and 260nm-thick. Refractive indices of silicon, SiO_2, and air are 3.46, 1.47, and 1, respectively.

6.3.1 Effect of air gap and bridge structure

First of all, 250nm air gap is utilized between the waveguides to increase the transmittance. Figure 6.5a illustrate the intersection with air gap. The total optical performance of this intersection is around 25%. Next, there are various bridges is used to close the air gap with 70nm width silicon and transmittance increased to 60.53%, as seen in Fig. 6.5b. total 11 bridges is fitted to the model with 70nm width.
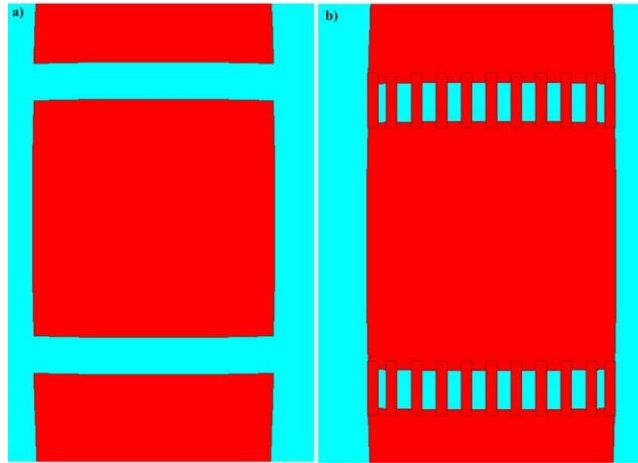
Figure 6.5: a) 250nm air gap between waveguides. b) 70nm width of bridge structure with the same value of air gap.

The width of the bridges are decreased to 60nm and 50nm values to increase the number of the bridges. at the same time, the air gap between bridges are also equal to width. When the width is decreased to 60nm, the transmittance is increased to 68.53% as shown in Fig. 6.6a. the total number of bridges are also increased to 13. Transmittance is powered up to 75.55% with the 50nm width bridges, as shown in Fig. 6.6b. Electric field distribution of 50nm bridge is illustrated in Fig. 6.6c. The first part of the bridge structure collect the light to middle of intersection. The second part convert the light normal working like a lens.
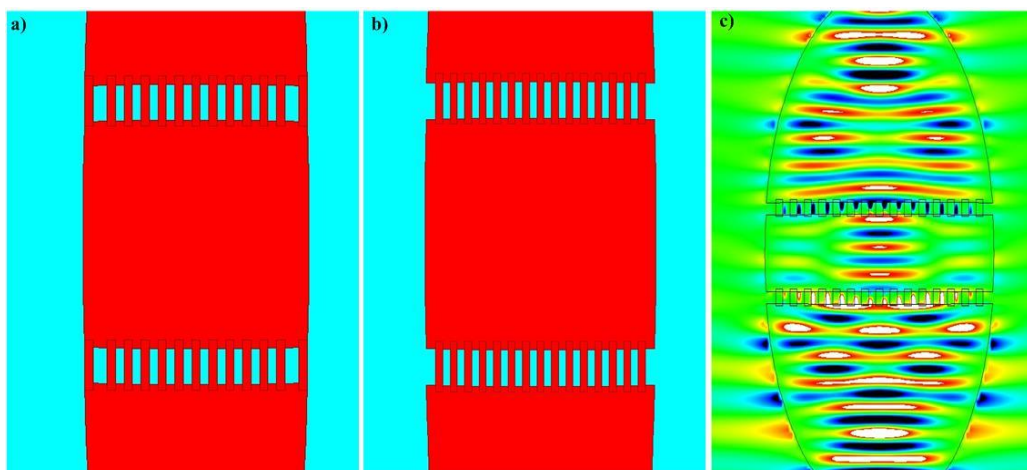
Figure 6.6: a) 60nm width of bridge structure with the same value of air gap. b) 50nm width of bridge structure. c) Lightwave in the intersection with diffraction grating.

119

Optical performance for elliptical intersection with 250nm air gap between waveguides is optimized from 25.00% to 75.55% via diffraction grating method, as shown in Fig. 6.7. The more bridge, the higher transmittance. At the same time, the air gap and width of bridge are significant parameters to optimize the performance. In the following models, if the air gap between waveguide change, optical performance of intersection change. Help of the this method, the normal intersection performance can be powered up.
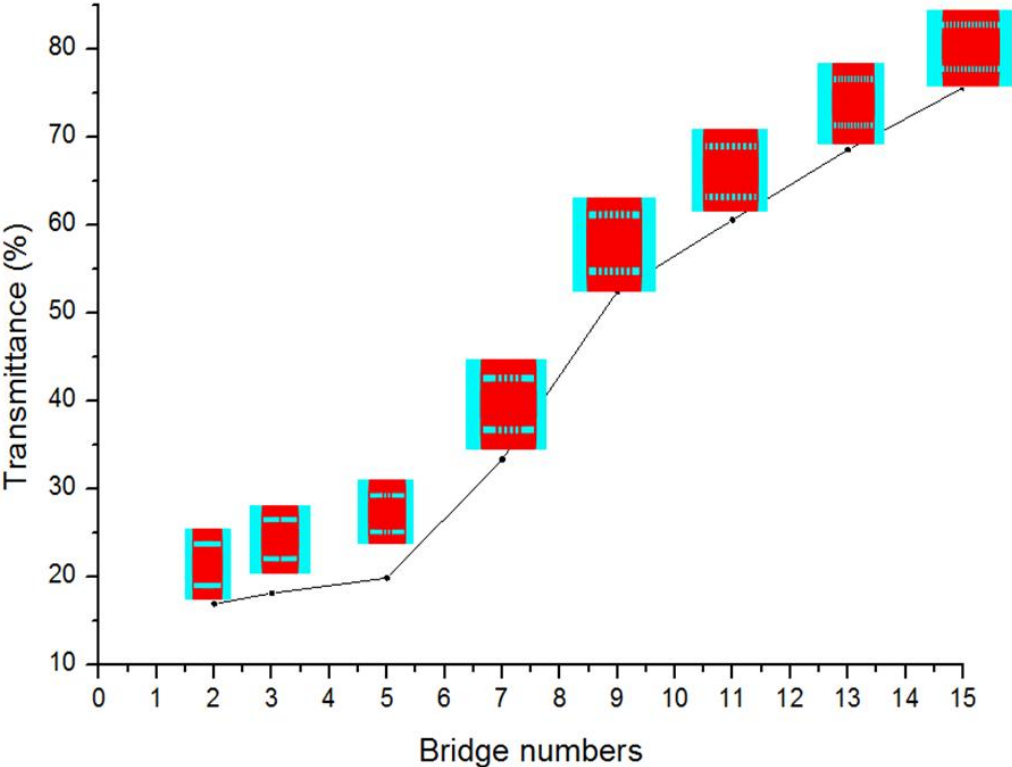
Figure 6.7: Transmittance of elliptical intersection with diffraction grating as a function of bridge number and width.

6.3.2 Effect of air gaps

First, air gap between waveguides is decreased from 250nm to 100nm and air gap between bridges to 100nm to understand the effects the result. The optical performance of the intersection is increased to 91.75%. To optimize the transmittance bridge air gap is decreased 10nm steps with the constant 100nm waveguide air gap. In the 90 nm bridge air gap, the transmittance is powered up to 92.48%. At the same time, the number of bridges is indeed increase, while decreases the bridge air gap. Next, transmittance is decreased to 90.97% for 80nm bridge air

gap. Next, transmittance is 94.85% for 70nm bridge air gap. The bridge air gap decreased until 50nm for microfabrication limits. As a result, for 100nm waveguide air gap, 50nm bridge width and 50nm bridge air gap, transmittance is powered up to 98.99%. Figure 6.8 illustrates the electric light distribution in the diffraction grating. In the middle of the intersection, bridge structure helps the increase to efficiency.
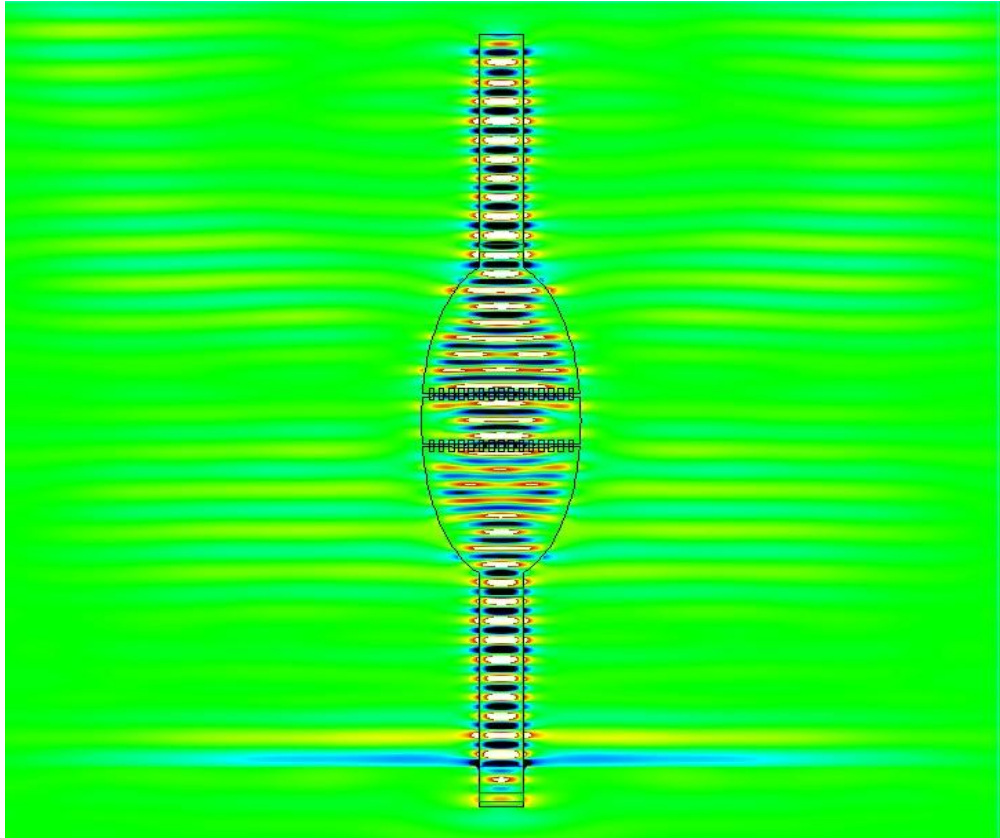
Figure 6.8: Lightwave in the bridge structures in the silicon intersection.

Optical performance of the elliptical intersection is increased via air gaps and bridge structure, as shown in Fig. 6.9. Transmittance of 100nm waveguide air gap without any bridges structure was 61.21%. Utilization of the bridge structure optical performance increased up to 98.99%. At the same time, bridge air gap also decreased to understand the effect. 50nm width and 50nm air gap is optimum values considering to microfabrication limits. In the following models, asymmetric models is studied in the diffraction grating with the bridge structure.
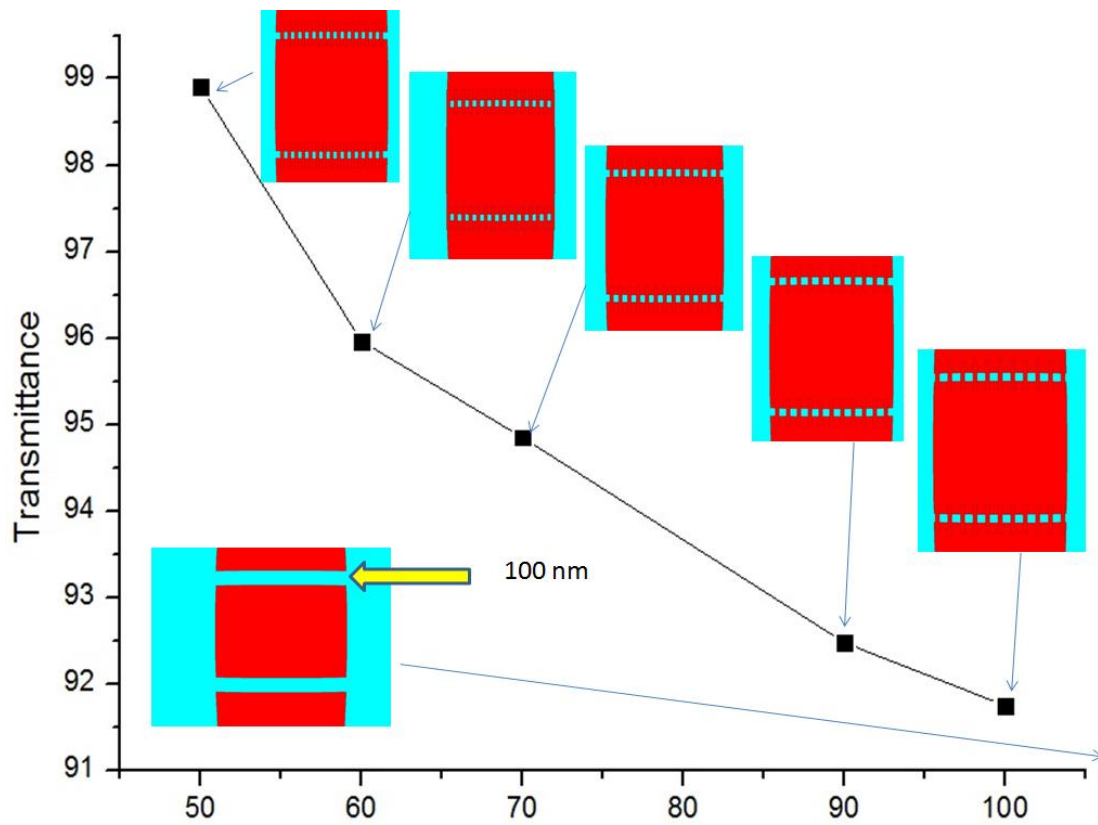
Figure 6.9: Transmittance of bridge structure of elliptical intersection as a function of air gap.

6.3.3 Effect of asymmetric model

In the asymmetric model at the middle bridge air gap constant and the others increased to outside 20nm by 20nm, as seen in Fig. 6.10a. Transmittance is decreased from 98.99% to 90.30%. Figure 6.10b illustrate the structure same model but increasing 10nm by 10nm and transmittance is decreased from 98.99% to 93.46%. However, two model optical performance is higher than standard elliptical intersection with same parameters.
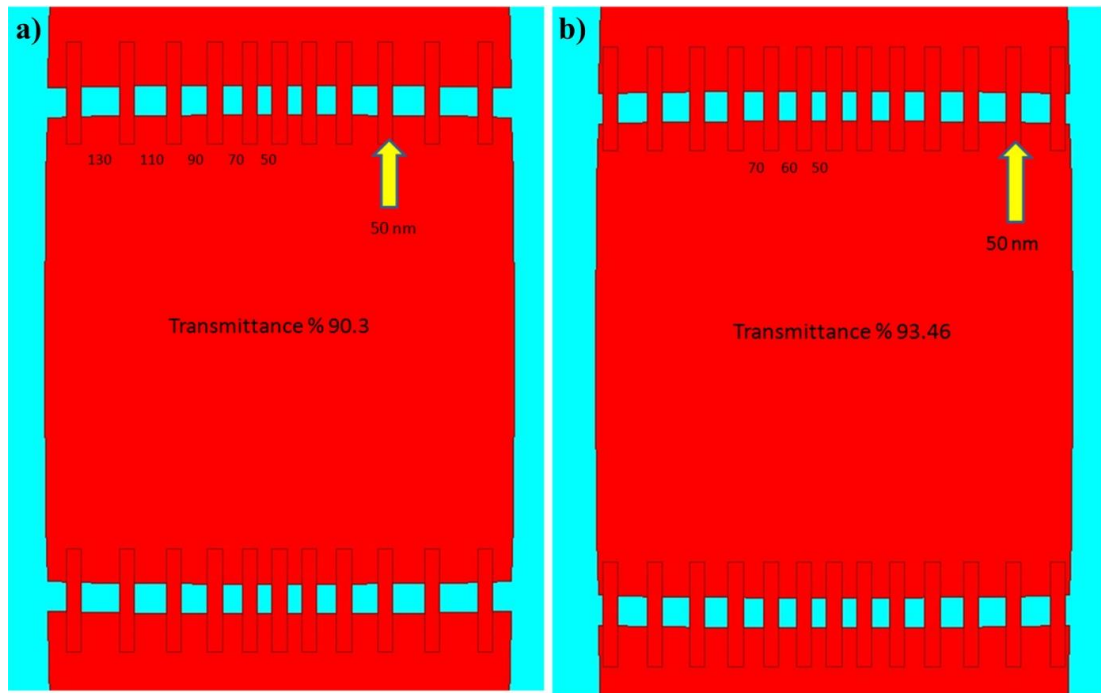
Figure 6.10: Schematic view of asymmetric models of intersections.

6.3.4 Effect in the two fold intersection

Two fold intersection optical performance 88.88% is reported. Bridge structure is employed to elliptical intersection. First, width of elliptical intersection is studied which are 5.2μm, 10.4μm and 15.6μm, as shown in Fig. 6.11 in order. The simulations are based on the large range of the width to find the optimum pick value in the diagram. The transmittances are 71.17%, 97.02% and 79.72% as shown in Fig. 6.11a through 6.11c, respectively. The pick value is near to 10.4μm elliptical width.

100nm waveguide air gap is simulated and transmittance is obtained 97%. Various waveguide air gap is studied to find optimum performance which are 50nm, 100nm, 150nm and 200nm considering the fabrication limits, as shown in Fig. 6.12. Waveguide air gap is increased from 100nm to 200nm due to easy of fabrication and see the bridges effects on the waveguide. Transmittance is decreased to 75.83%. Next, 100nm is used as a waveguide air gap and transmittance is powered up to 87.76%. Last, waveguide air gap is decreased to 50nm and performance is achieved 99.8%.
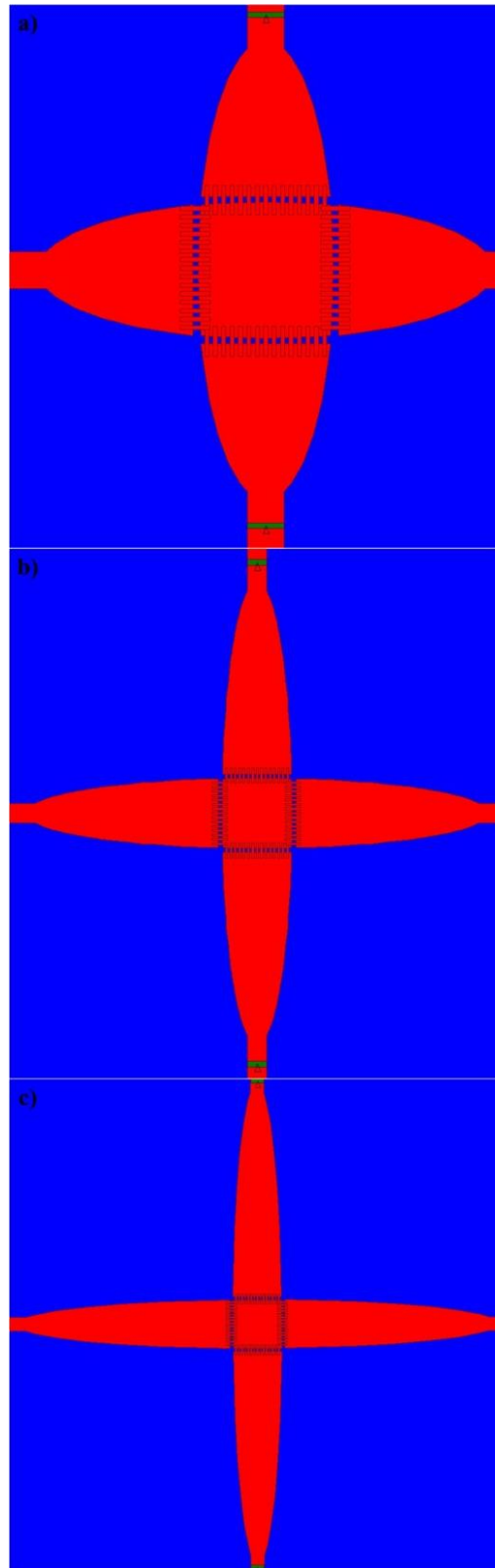
Figure 6.11: Two fold elliptical intersection as a function of width.
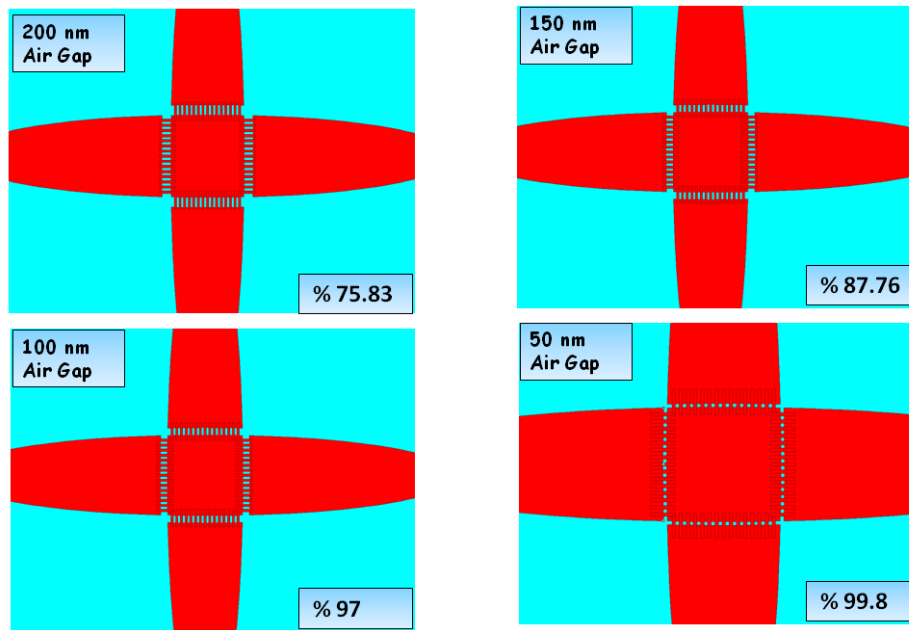
Figure 6.12: Two fold elliptical intersections as a function of waveguide air gaps.

Figure 6.13 illustrate the lightwave in the elliptical intersection. Normally light follows in the middle of the two fold intersection all way and optical loss increases. However, in the presented new method light shrinks to middle so optical loss minimize.
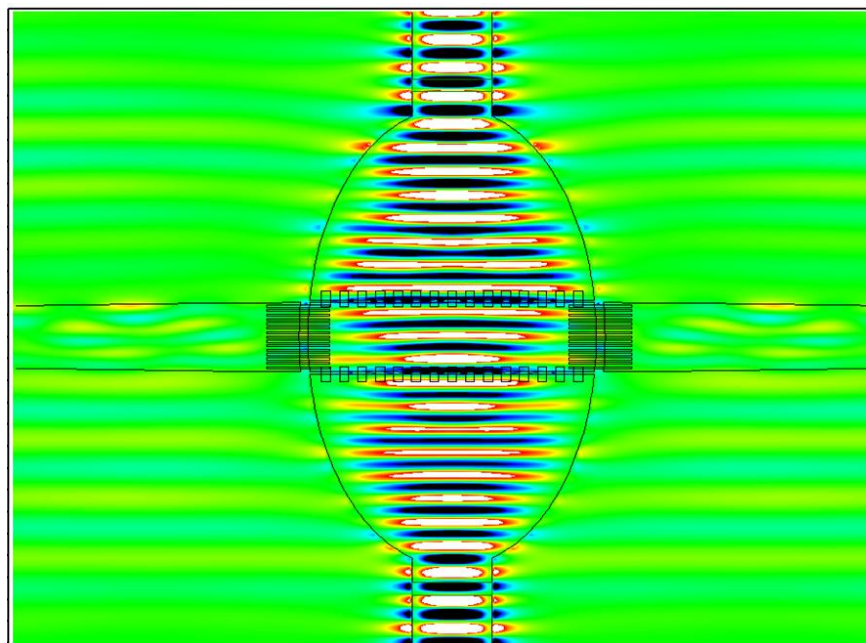
Figure 6.13: Lightwave in two fold elliptical intersection.

As a result, two elliptical intersection are selected to verify the numerical and experimental results. First one is single fold intersection parameters are 50nm bridge air gap, 50nm bridge width, 50nm waveguide air gap, 7.2μm elliptical length, 1.5μm elliptical width and 260nm thickness. Second one is two fold intersection parameters are same with the single fold.

6.4 Fabrication at UNAM

Diffraction grating elliptical intersection structures are fabricated on a SOI wafer with 340nm-thick device silicon and 1μm-thick SiO_2 layers. Fabrication process is shown in Fig. 6.14.
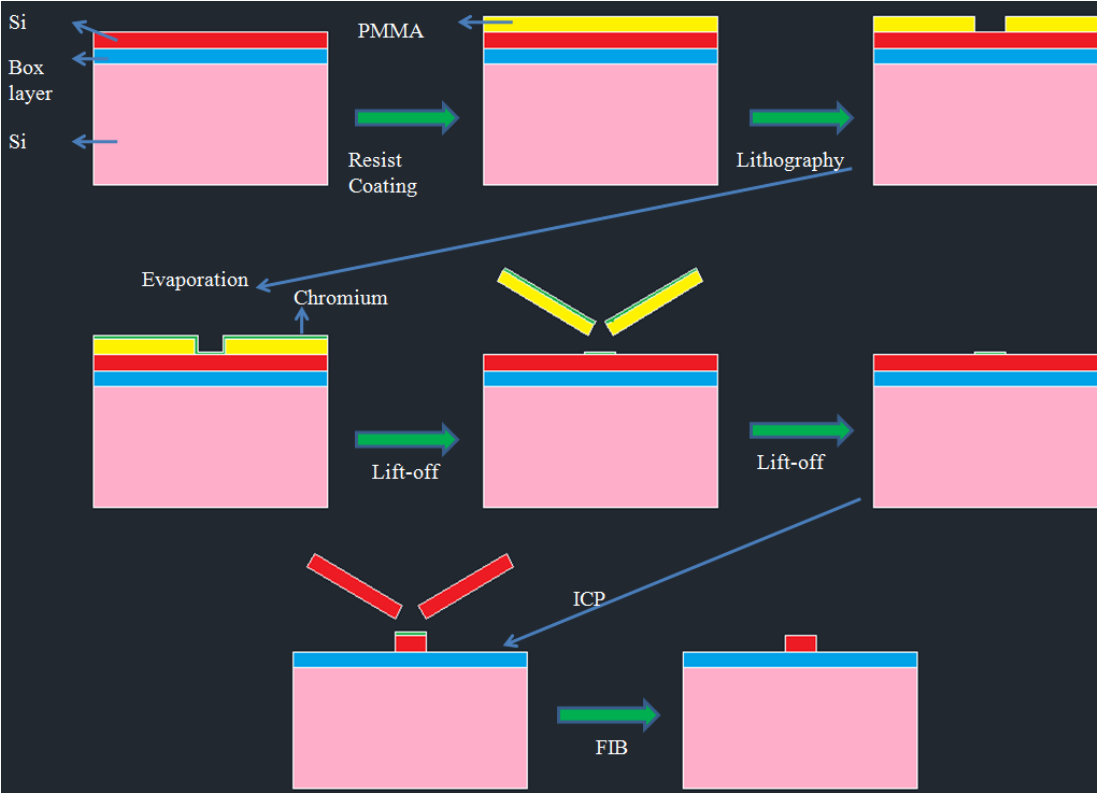
Figure 6.14: Fabrication process.

First, device silicon layer is spin-coated by 120nm-thick positive electron beam resist, PMMA. Then, structures geometries are patterned using EBL. Figure 6.15 depicts the patterned two fold and single fold features top of to PMMA in order.
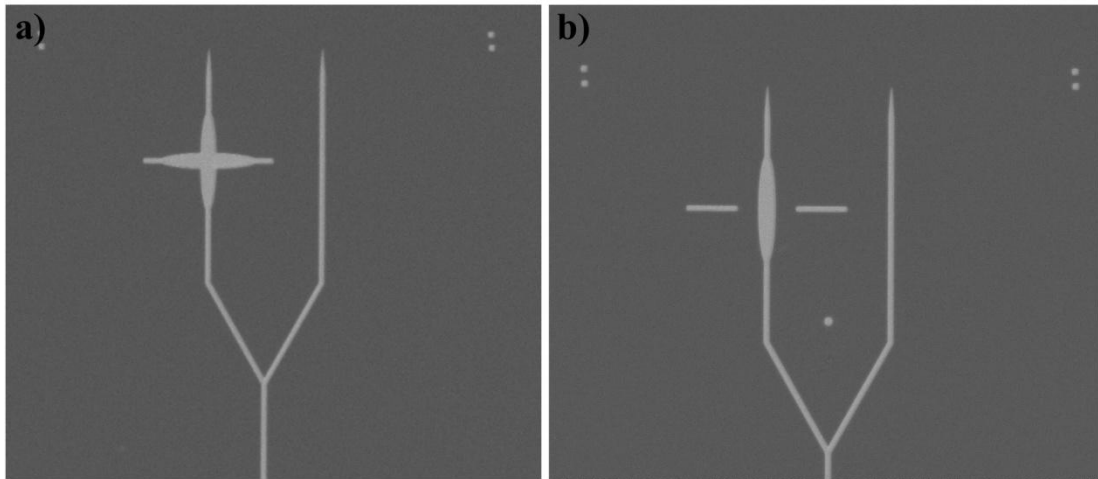
Figure 6.15: Exposed two and single fold intersection.

Next, 70nm-thick chromium layer is deposited at 2 nm/min deposition rate by Electron Beam Evaporation as a hard-mask protecting the structures. Then, lift-off process is realized to define windows to be etched, as shown in Fig. 6.16. Chromium layer as a hard mask is coated top of the device silicon layer. The thickness of chromium layer is measured after lift-off process under the surface profiler as a 66nm.
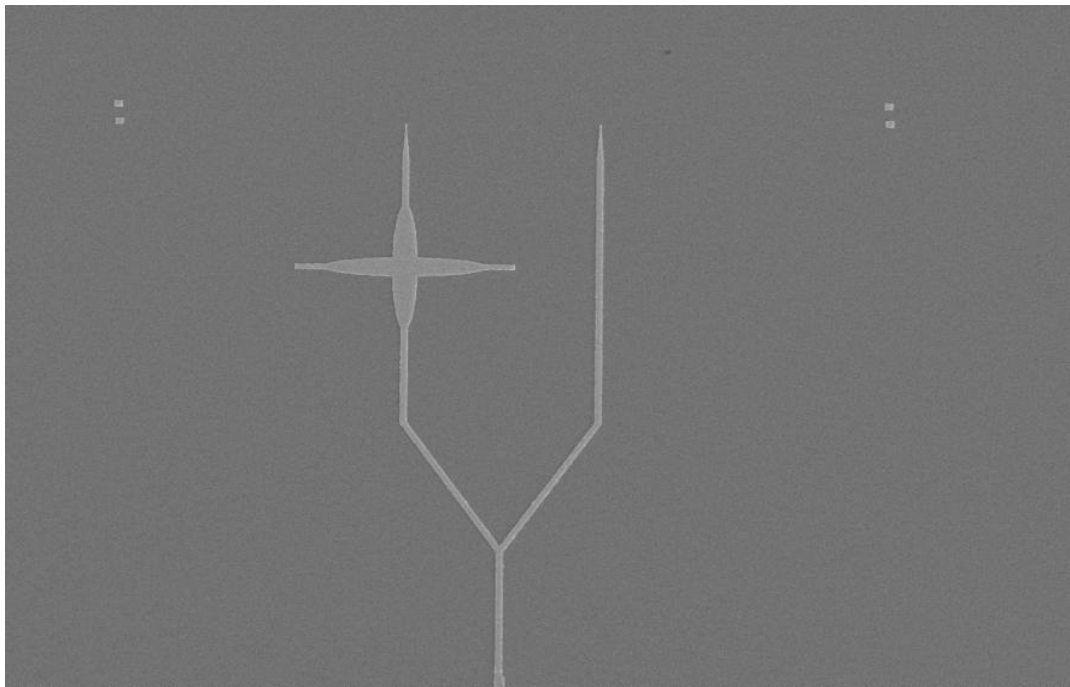
Figure 6.16: Chromium layer as a hard mask.

Later, 340nm-thick device silicon is dry etched via ICP-DRIE using SF_6 and O_2 gases as activation and passivation gases, respectively, at 34.34nm/min in order to keep the sidewall roughness of the sensing structures as low as possible. Figure 6.17 shows that result of the surface profiler. The sidewall of the waveguides and device silicon layer is proper smoothness.
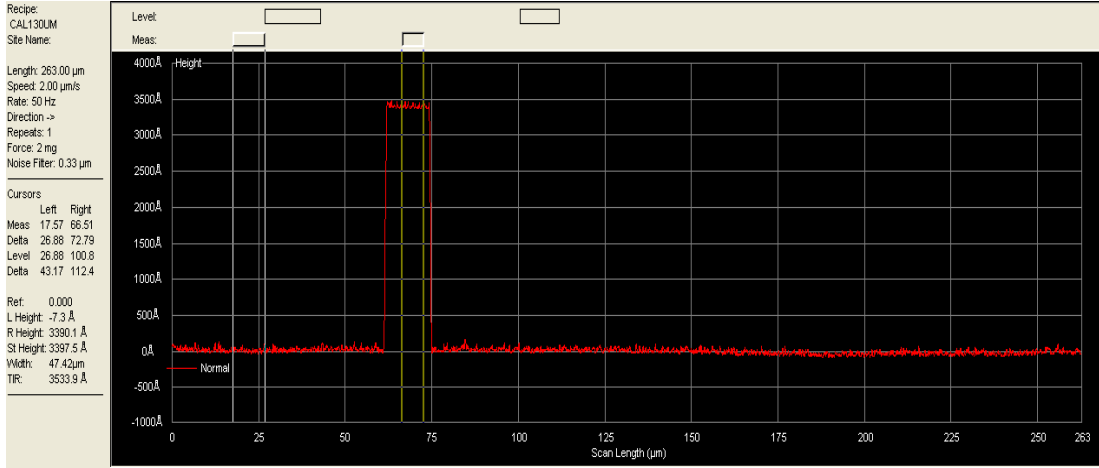
Figure 6.17: The thickness of device silicon after ICP process.
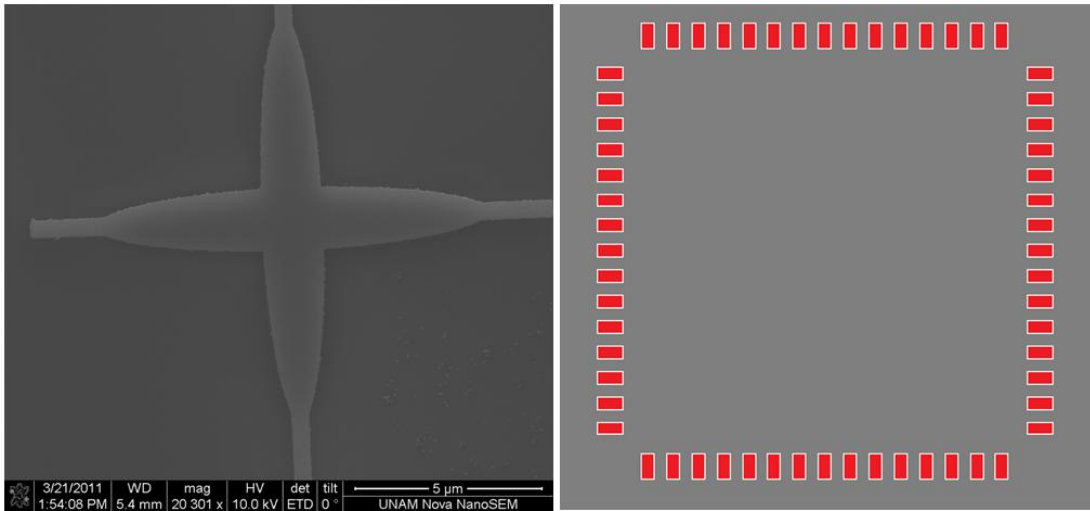
Figure 6.18: Fabricated intersection with designed bridge structure for FIB process.

Next, chromium layer is removed after etching process with etchant liquid. As the last step, 50nm bridge width and 50nm bridge air gap is open a holes top of the silicon. Figure 6.18 depicts the fabricated elliptical intersection and designed holes in Focused Ion Beam (FIB) process. When the bridge structure is created in the device layer, rectangle shape converted to circle and dimensions are changed from 50nm to 120nm as shown in Fig. 6.19.

Several recipes and parameters are utilized to exposure the features due to limitations of the equipment aren't achieved. The main problem is 50nm×100nm shape is under the limitations.
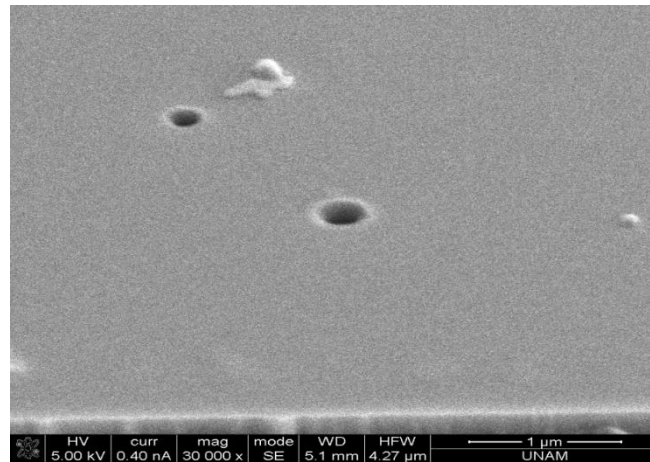
Figure 6.19: Exposed rectangle shape in FIB

6.5 Fabrication at SU-NUM

According to previous fabrication results, it is decided to change the fabrication location which is Sabancı University Nanotechnology Research and Application Center (SU-NUM). The critical dimension is 50nm for the diffraction grating models. First of all, the advantage to change the new facilities is enable to use 100kV to make more small features. The new EBL system has a 100kV electron source power which let us the fabricate around 50nm lines.
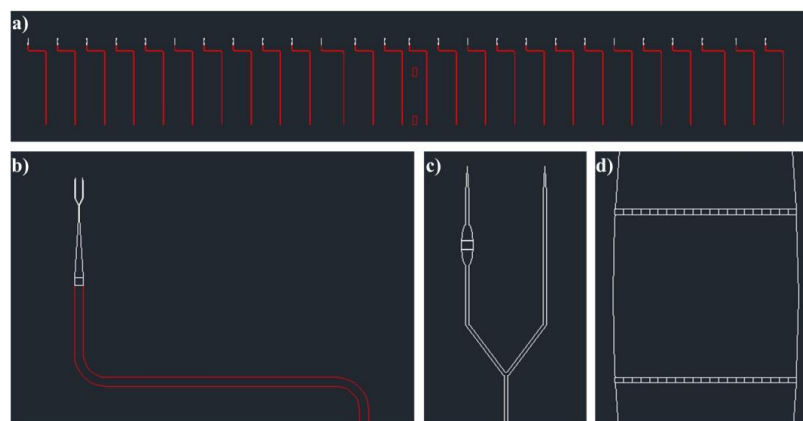
Figure 6.20: a) Single fold diffraction grating model. b) 30 µm radius. c) Diffraction grating and reference line. d) 50nm features inside the elliptical shape.
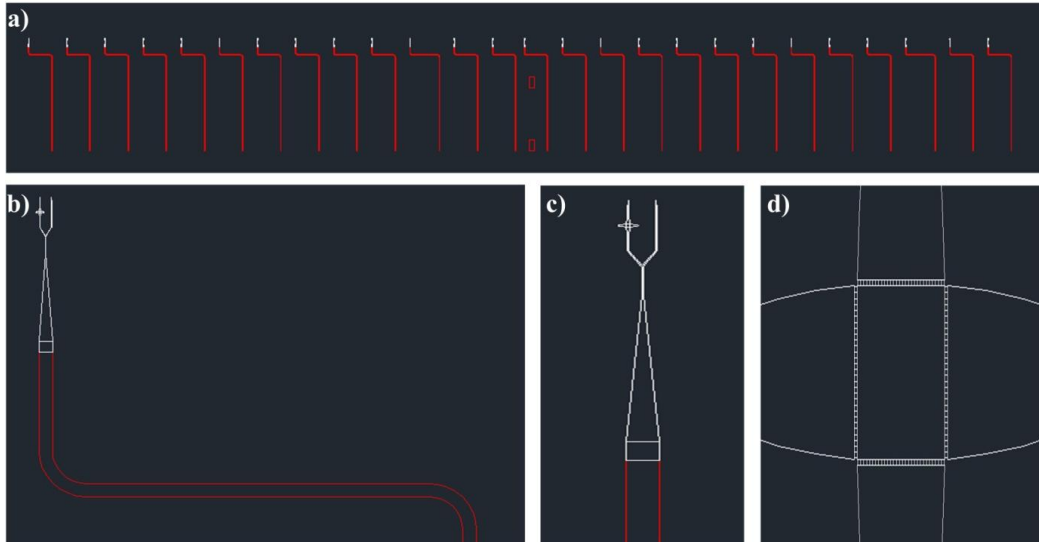
Figure 6.21: a) Two fold diffraction grating model. b) 30 μm radius. c) Two fold diffraction grating and reference line. d) 50nm features inside the elliptical shape.

Appropriate files for the diffraction grating models are designed as a 2D dxf file. Figures 6.20 and 6.21 illustrate the one fold and two fold diffraction grating models, respectively. All AutoCAD files is converted to suitable format for the EBL system interface software which name is Layout Beamer. In this software, all parameters are defining to effect the fabrication result. For the fabricate smallest feature in this system, you should use smallest beam current and highest acceleration voltage value. The resolution should small 10% of the critical dimension which give us in this design 5nm. However, desired feature have small squares and these are so close to each other with 50nm air gaps. When the electron source hit the first place, the other square are under the exposure. the proximity effect calculation is used to unable this problem. So the over dose and proximity effect can eliminate on the features top of the PMMA.

Table 6.1. Patterning recipe.

Patterning recipe			
PMMA C2	Prebake	180 °C	2 min
	Spin coating resist	1000rpm	2 secs
		4000rpm	45 secs
	Postbake	180°C	60 min
	Resist thickness	100nm	
Patterning in Vistec 2000	Voltage	100kv	
	Beam current	80pA	
	Step size x, y	2nm	
	Exposure Density	800μC/cm^2	
	Write Field	260x260μm^2	
Developing	Developing	25°C	40 secs
	Rinsing by IPA	25°C	20 secs
	Bake	120°C	5 min

In the second step of the fabrication, 30nm chromium is coated as a mask layer. The coating ratio is 0.3Å/s. This value should be below 1Å/s to keep the sidewall and roughness less. The unwanted resist/chromium layer is lifted off inside of acetone liquid solution under the ultrasonic cleaner. the diffracting grating features with only 30nm chromium layer is depicted Fig. 6.21. Table 6.2 shows the chromium deposition parameters.
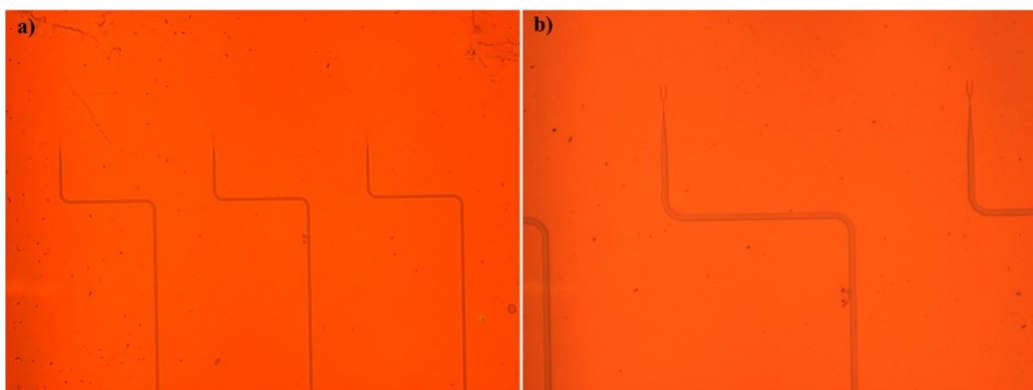
Figure 6.21: 30nm chromium mask layer on the SOI wafer.

Table 6.2. Chromium Deposition

Chromium Coating		
	Chamber Vacuum	4×10^{-6}Torr
	Chromium Density	7.19g.cm^{-3}
Chromium Aligment	K factor	127
	Energy of first ionisation	2987kJ.mol^{-1}
	Tempature	45°C
	Voltage	4.2V
	Beam Current	2.1A
Deposition	Rate	0.3nm/s
	Thickness	30nm
Drying	Dry N_2 gas	

340nm silicon is etched under the ICP-DRIE Oxford PlasmaLab System 100 ICP 300 Deep RIE. SF_6 and O_2 gases are used for etching. Figure 6.23 illustrate the silicon layer thickness is 340nm under the SEM. This system only etches from top to down in one direction and skip the cycle process. The table 6.3 gives the all parameters of the etching process.

Table 6.3. Silicon Etch Parameters.

Silicon Etch Parameters	
Temperature	-20°C
Etch Duration	56s
Pressure	10mTorr
SF_6	48sccm
O_2	24sccm
RF Platen Power	1000W
RF Generator Power	20W

The fabricated models are separated with dicing saw machine. The chromium layer top of the silicon is removed with chromium etchant solution under the ultrasonic cleaner. Figure 6.23 shows the SEM photographs of the fabricated diffraction grating models. However, the holes inside of the elliptical shapes are not fabricated because of the proximity effect. In the literature, there are some academic work fabricated 50nm line width and 50nm air gap during line which make easer compare to our design. Because Electron gun is shooting bigger area according to shoot one spot.
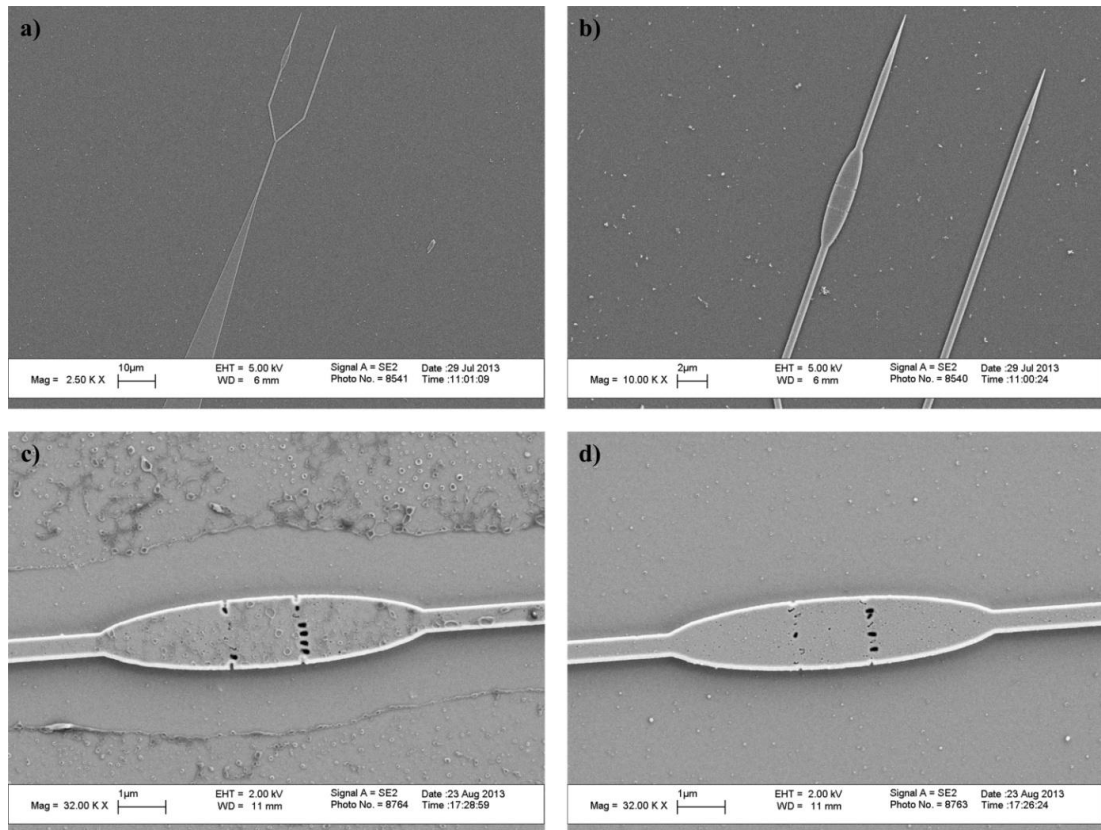
Figure 6.23: a) Elliptical shape with the shrunken waveguide. b) Zoom into elliptical intersection. c) 50nm holes only at half of the one side. d) Some random holes on the elliptical shape.

133

6.6 Summary

As a result, fabrication progress is failed because of the smallest features. The simulation results are very well but according to compare with experimental results are not possible.

In this chapter, low loss silicon elliptical intersection based on diffraction grating method is presented at the first time. Diffraction grating is demonstrated as a numerical at sub-nanometer for optical devices. The optical performance of silicon intersection for single fold is increased from 92.14% to 98.99% without extra fabrication cost and footprint. Also, for double fold intersections efficiency is powered up to 99.80%. Optical performance of optical NEMS/MEMS can be improve with presented elliptical intersections. Two new intersections could not fabricate due to used equipment.

7. CONCLUSION

Efforts towards integrated optical circuits have seen significant interest for combining microelectronics and photonics in order to bring compact device sizes and volume economics. Silicon nanowire waveguides and photonic crystals are among those heavily investigated. Photonic devices with embedded NEMS/MEMS such as an optical add-drop multiplexer deploying relative motion of silicon waveguides, nanowire waveguide ring and microdisk resonators demonstrated as narrow-band filters, optical switches utilizing silicon nanowire waveguide couplers, and an optical waveguide modulator have been reported.

Integrated photonic circuit devices with embedded NEMS/MEMS technology utilize either in-plane or out-of plane motion to accomplish their task. Characterization of such devices can be realized either under SEM or optical microscopes. Ultimate device characterization, therefore, depends on the quality and evaluation accuracy of the series of images taken consecutively under the corresponding microscope at various actuation levels. Hence, employment of images for device motion characterization causes measurement errors from several tens to hundreds of nanometers during evaluation stage for SEM and optical microscope uses, respectively. Without proper characterization of devices where precise motion or distance in the nano/micro-system level is critical, full understanding of the studied concept, or proper operation or control of the system becomes impossible. In addition, they are usually only for testing purposes and cannot be integrated into the device level.

Targeting the aforementioned need, embedded in-plane distance/displacement sensors utilizing Bragg reflectors within an optical Fabry-Pèrot microcavity, geometrical modulation-based interferometry are reported.

Performances in both approaches are highly dependent on the optical wavelengths employed, which, as a result, enforces highly accurate microfabrication or arises calibration need afterwards for proper functionality. In addition, while the former provides only 29nm measurement range, the latter requires large device footprint.

In this thesis, chapter 2 presents an embedded nanophotonic displacement sensing mechanism using end-to-end waveguide coupling in the near-field region is simulated, fabricated and characterized. The approach is capable of yielding high displacement-sensitivity, subwavelength measurement range, high wavelength-insensitivity and small footprint. Specifically, respective values of maximum 0.29% change of light intensity per nanometer, about 1000nm, and $85 \times 50 \mu m^2$ in area including the motion source are achieved both numerically and experimentally at 1.55μm wavelength. The studied mechanism has weak dependency on wavelength in the range of 1.52-1.60μm providing wide bandwidth. It is well-suited for real-time displacement and distance measurements in integrated optical circuits operating with the help of embedded NEMS/MEMS actuation. The mechanism is estimated to find use also in various nano-scale positioning and imaging applications.

In chapter 3, design, microfabrication and characterization of two mechanical tuning mechanisms for evanescent wave mode coupling in PLCs with sub-nanometer sensitivity values are completed. Since the presented mechanisms are embedded, they depicted improvements already in tunability and device footprint, and a future cost advantage is expected in case of their use in mass production. Numerical and experimental results in optical response are in good agreement with a maximum deviation of 9.12% and 4.23% in the first and the second mechanisms, respectively. Tunability of the mechanisms in the 75nm and 100nm excitation range at 1.55μm wavelength are 1.13nm and 1.19nm per percent of average light intensity change in order. The studied evanescent wave mode coupling mechanisms are well-suited for employment in PLCs where mechanical tuning with sub-nanometer or greater excitation is needed.

Chapter 4 presents 1x2 optical switch is designed and fabricated. The experimental results show that the optical contrast is around 39% well agreed with the theoretically results. The experimental results shows that the optical performance of the output is around 59% well agreed with the theoretically results. 12 extra springs are used to hold the waveguide and effects the performance but at least can present the concept

works very high sensitivity which is 0.078nm per percent of the light intensity. Experimental and numerical spectral response results of the 1x2 optical switch are studied. The optical switch has an optical peak around 1.58µm wavelength.

Chapter 5 presents two types of sensing mechanisms are introduced and fabricated. Short-range high-sensitivity in-plane optical sensor again, but at normally-on state are being investigated in order to clarify their initial state effects on the sensing characteristics. Towards this goal, two major types of sensor approaches are studied. All sensors utilized in Chapter 3 are based on EFM. Sensitivities achieved in this phase are from 0.84nm down to 0.06nm per percent of light intensity within sub-100nm distances. For the half-circled waveguide optical switch two different second waveguide is fabricated. The sensitivity is measured 0.045nm and 0.039nm per percent of the light intensity 1µm and 2µm radius, respectively. These values are very well in the mechanical tuning at the optical performance at switching in the literature. For the trigunlar waveguide optical switch two different second waveguide is fabricated which are 2µm and 3µm. The sensitivity is measured as a experimental 0.077 and 0.026nm per percent of the light intensity.

In chapter 6, low loss silicon elliptical intersection based on diffraction grating method is presented at the first time. Diffraction grating is demonstrated as a numerical at sub-nanometer for optical devices. The optical performance of silicon intersection for single fold is increased from 92.14% to 98.99% without extra fabrication cost and footprint. Also, for two fold intersections efficiency is powered up to 99.80%. Optical performance of optical NEMS/MEMS can be improve with presented elliptical intersections. Two new intersection could not fabricate due to used equipment.

As a result, embedded nanophotonic displacement sensing mechanism is designed, fabricated and tested. The displacement sensing mechanism has a maximum 0.29% change of light intensity per nanometer, about 1000nm, and $85{\times}50µm^2$ in area including the motion source are achieved both numerically and experimentally at 1.55µm wavelength. Design, microfabrication and characterization of two mechanical tuning mechanisms for evanescent wave mode coupling in PLCs with sub-nanometer sensitivity values are completed.

Tunability of the mechanisms in the 75nm and 100nm excitation range at 1.55µm wavelength are 1.13nm and 1.19nm per percent of average light intensity change in order. High-sensitivity 1x2 optical switch is fabricated $200 \times 150 \mu m^2$ in area including the motion source are achieved both numerically and experimentally at 1.55µm wavelength. Two different short-range high-sensitivity in-plane optical switch at normally-on is investigated with sensitivities from 0.84nm down to 0.06nm per percent of light intensity within sub-100nm distances. Diffraction grating is demonstrated as a numerical at sub-nanometer for optical devices. Optical performance of optical NEMS/MEMS can be improve with demonstrated silicon elliptical intersections.

REFERENCES

[1] **Jalali B., and Fathpour S.** (2006). Silicon photonics. *J. Lightwave Technol.*, Vol. 24, pp. 4600-4615.

[2] **Sakai A., Hara G., and Baba T.** (2001). Propagation Characteristics of Ultrahigh-Δ Optical Waveguide on Silicon-on-Insulator Substrate. *Jpn. J. Appl. Phys.*, Part 2 40, L383-385.

[3] **Koster A., Cassan E., Laval S., Vivien L., and Pascal D.** (2004). Ultracompact splitter for submicrometer silicon-on-insulator rib waveguides. *J. Opt. Soc. Am. A*, pp. 2180-2185.

[4] **Yamada H., Chu T., Ishida S., and Arakawa Y.** (2006). Si photonic wire waveguide devices. *IEEE J. Sel. Topics Quantum Electron.*, Vol. 12, no. 6, pp. 1371-1379.

[5] **Sasaki K., Ohno F., Motegi A., and Baba T.** (2005). Arrayed waveguide grating of $70 \times 60 \ \mu m^2$ size based on Si photonic wire waveguides. *Electron. Lett.*, Vol. 41, 801.

[6] **Takahashi K., Kanamori Y., Kokubun Y., and Hane K.** (2008). A wavelength-selective add-drop switch using silicon microring resonator with a submicron-comb electrostatic actuator. *Opt. Exp.*, Vol. 16, no. 19, pp. 14421-14428.

[7] **Iwamoto S.,** *et al.* (2006). Observation of micromechanically controlled tuning of photonic crystal line-defect waveguide. *Appl. Phys. Lett.*, Vol. 88, pp. 011104.

[8] **Umemori K., Kanamori Y., and Hane K.** (2006). Photonic crystal waveguide switch with a microelectromechanical actuator. *Appl. Phys. Lett.*, Vol. 89, pp. 021102.

[9] **Higo A.,** *et al.* (2007). Design and fabrication of photonic MEMS waveguide modulators. *Int. Conf. on Optical MEMS and Nanophotonics*, 173.

[10] **Bulgan E., Kanamori Y., and Hane K.** (2008). Submicron silicon waveguide optical switch driven by microelectromechanical actuator. *App. Phys. Lett.*, Vol. 92, pp. 101110.

[11] **Bulgan E., Kanamori Y., and Hane K.** (2008). Theoretical Analysis of Mechanical-Contact Based Submicron Si Waveguide Optical Microswitch at Telecommunication Wavelengths. *IEEJ Transactions on Sensors and Micromachines*, Vol. 128, no. 3, pp. 80-84.

[12] **Sandoz P., Friedt J., and Carry E.** (2007). In-plane displacement measurement with sub-pixel resolution: application to vibration characterization of a shear-force scanning probe. *Proc. SPIE* 6616.

[13]**Moon E.E.,** *et al.* (2004). Nanometer gap measurement and verification via the chirped-Talbot effect. *J. Vac. Sci. Technol*. B 22, 3378.

[14]**Dobbelaere P. D.** *et al.* (2000). Digital MEMS for Optical Switching," *IEEE Commun. Mag.*, Vol. 40, no. 3, pp. 88–95.

[15] **Ollier E.** (2002). Optical MEMS Devices Based on Moving Waveguides. *IEEE J. Sel. Topics Quantum Elect.*, Vol. 8, no. 1, pp. 155–162.

[16]**Sakata T., Togo H., Makihara M., Shimokawa F., and Kaneko K.** (2001). Improvement of Switching Time in a Thermocapillarity Optical Switch. *J. Lightwave Technol.*, Vol. 19, no. 7.

[17] **Zandi K., Wong B., Zou J., Kruzelecky R. V., Jamroz W. and Peter Y. A.** (2010). In-Plane Silicon-On-Insulator Optical MEMS Accelerometer Using Waveguide Fabry-Perot Microcavity with Silicon/Air Bragg Mirrors. *IEEE*, pp. 839-842.

[18]**Grutter K. E., Yeh A. M., Patra S. K., Wu M. C.** (2010). A New Fabrication Technique for Integrating Silica Optical Devices and MEMS. *Int. Conf. on Optical MEMS and Nanophotonics*, pp. 33-34.

[19]**Sugimoto Y., Abe M., Hirayama S., Oyabu N., Custance Ó., and Morita S.** (2005). Atom inlays performed at room temperature using atomic force microscopy. *Nature* 4, pp. 156-159.

[20]**Kim C. H., Jeong H. M., Jeon J. U., and Kim Y. K.** (2003). Silicon micro XY-stage with a large area shuttle and no-etching holes for SPM-based data storage. *J. Microelectromech. S.*, Vol. 12, no. 4.

[21]**Vettiger P., Cross G., Despont M., Drechsler U., Dürig U., Gotsmann B., Häberle W., Lantz M. A., Rothuizen H. E., Stutz R., and Binnig G. K.** (2002). The "millipede" - nanotechnology entering data storage. *IEEE T. Nanotechnol.*, Vol. 1, 39.

[22]**Sun L., Wang J., Rong W., Li X., and Bao H.** (2008). A silicon integrated micro nano-positioning XY-stage for nano-manipulation. *J. Micromech. Microeng.*, Vol. 18, pp. 125004.

[23]**Cuesta-Soto F., Martínez A., García J., Ramos F., Sanchis P., Blasco J., and Martí J.** (2004). All-optical switching structure based on a photonic crystal directional coupler. *Opt. Express,* Vol. 12, 161.

[24] **Lin C. J. and Tseng F. G.** (2004). A micro Fabry–Perot sensor for nano-lateral displacement sensing with enhanced sensitivity and pressure resistance. *Sensor Actuat. A-Phys.*, Vol. 114, 163

[25] **Xu Z., Cao L., Gu C., He Q., and Jin G.** (2006). Micro displacement sensor based on line-defect resonant cavity in photonic crystal. *Opt. Express*, Vol. 14, 298.

[26]**Hong C. and Andrew W.** (2010). Optical manipulation and transport of microparticles on silicon nitride microring-resonator-based add–drop devices. *Opt. Lett.*, Vol. 35, no. 17, pp. 2855-2857.

[27]**Yamada T. and Kokubun Y.** (2009). Hitless wavelength selective switch using vertically coupled microring resonator manipulated by micro-electro-

mechanical systems structure. *Appl. Phys. Exp.*, Vol. 2, no. 6, pp. 062402.

[28] **Akihama Y., Kanamori Y., and Hane K.** (2011). Ultra-small silicon waveguide coupler switch using gap-variable mechanism. *Opt. Exp.*, Vol. 19, no. 24, pp. 23658-23663.

[29] **Akihama Y. and Hane K.** (2012). Single and multiple optical switches that use freestanding silicon nanowire waveguide couplers. *Light: Sci. Appl.*, Vol. 1 no. e16.

[30] **Akio H., Hiroyuki F., Yoshiaki N., and Hiroshi T.** (2007). Design and fabrication of photonic MEMS waveguide modulators. *IEEE/LEOS Int. Conf. on Optical MEMS and Nanophotonics*, pp. 173-174.

[31] **Pruessner M. W., Stievater T. H., and Rabinovich W. S.** (2008). In-plane microelectromechanical resonator with integrated Fabry–Pérot cavity. *Appl. Phys. Lett.*, Vol. 92, no. 8, pp. 081101.

[32] **Haronian D.** (1998). Displacement sensing using geometrical modulation in reflection mode (GM-RM) of coupled optical waveguides. *J. Microelectromech. Sys.*, Vol. 8, no. 4, pp. 323-326.

[33] **Pruessner M. W., Siwak N., Amarnath K., Kanakaraju S., Chuang W. H., and Ghodssi R.** (2006). End-coupled optical waveguide MEMS devices in the indium phosphide material system. *J. Micromech. Microeng.*, Vol. 16, no. 4, pp. 832-842.

[34] **Hirano T., Furuhata T., Gabriel K. J., and Fujita H.** (1992). Design, fabrication and operation of sub-micron gap electrostatic comb-drive actuators. *J. Microelectromech. S.*, Vol. 1, pp.52-59.

[35] **Avelar-Batista J. C., Spain E., Housden J., Fuentes G. G., Rodriguez R., Montalá F., Carreras L. J., and Tate T. J.** (2005). Effect of coating thickness and deposition methods on the stripping rate of Cr–N coatings. *Surf. Coat. Tech.*, Vol. 200, no. 5-6, pp. 1842-18448.

[36] **Gogolides E., Boukouras C., Kokkoris G., Brani O., Tserepi A., and Constantoudis V.** (2004). Si etching in high-density SF6 plasmas for microfabrication: surface roughness formation. *Microelectron. Eng.*, Vol. 73-74, pp. 312-318.

[37] **Passi V., Sodervall U., Nilsson B., Petersson G., Hagberg M., Krzeminski C., Dubois E., Bois B. D., and Raskina J. P.** (2012). Anisotropic vapor HF etching of silicon dioxide for Si microstructure release. *Microelectron. Eng.*, Vol. 95, pp. 83-89.

[38] **Fukazawa T., Hirano T., Ohno F., and Baba T.** (2004). Low loss intersection of Si photonic wire waveguides. *Jpn. J. Appl. Phys.*, Vol. 43, no. 2, pp. 646-647, 2004.

[39] **Doerr C. R.** (2006). Advances in Silica Planar Lightwave Circuits (2006). J. Lightwave Technol., Vol. 24, no.12, pp. 4763-4789.

[40] **Takahashi R.** (2004). 40-Gbit/s label recognition and 1×4 self-routing using self-serial-to-parallel conversion. *IEEE Photonics Technol. Lett.*, Vol. 16, no. 2, pp. 692-694.

[41]**Kaykisiz M. and Bulgan E.** (2011). Low-loss Optical Switch using Brewster Angle. *Int. Conf. on Optical MEMS and Nanophotonics*, pp. 215-216.

[42]**Kaykisiz M. and Bulgan E.** (2013). Embedded Nanophotonic Displacement Sensing using End-to-End Waveguide Coupling. *J. Microelectromech. Sys*.

[43]**Zhang A.** *et al.* (2005). Integrated liquid crystal optical switch based on total internal reflection. *Appl. Phys. Lett.*, Vol. 86, pp. 211108.

[44]**Hoffman M., Kopka P., and Voges E.** (1998). Thermo optical digital switch arrays in silica on silicon with defined zero voltage state. *IEEE J. Lightwave Technol.*, Vol. 16, pp. 395–400.

[45]**Secundo L.** *et al.* (2006). Electro holographic tunable wavelength selective switch. *Conf. on Lasers and Electro-Optics/Quantum Electronics and Laser Science Conference and Photonic Applications Systems Technologies,* pp. CThZ3.

[46]**Smith D. A.** *et al.* (1996). Multi wavelength performance of an apodized acousto-optic switch. *IEEE J. Lightwave Technol.*, Vol. 14, pp. TuM5.

[47]**Dorgeuille F. et al.** (1996). Novel approach for simple fabrication of high performance In P-switch matrix based on laser-amplifier gates. *IEEE Photon. Technol. Lett.,* Vol.8, pp. 1178-1181.

[48]**Kwon S. H., Kamp M., Forchel A., Seo M. K., and Lee Y. H.** (2008). Elimination of cross-talk in waveguide intersections of triangular lattice photonic crystals. *Opt. Exp.,* Vol. 16, no. 15, pp. 11399-11404.

[49]**Chen H. and Poon A. W.** (2006). Low-Loss Multimode-Interference-Based Crossings for Silicon Wire Waveguides. *IEEE Photonic. Tech. Lett.*, Vol. 18, no. 21, pp. 2260-2262.

[50]**Bogaerts W., Dumon P., Thourhout D. V., and Baets R.** (2007). Low-loss, low-cross-talk crossings for silicon-on-insulator nanophotonic waveguides. *Opt. Lett.*, Vol. 32, no. 19, pp.2801-2803.

CURRICULUM VITAE

Name Surname: Muhammet Mustafa KAYKISIZ

Place and Date of Birth: Divrigi and 03/04/1988

Address: Moroglu Sitesi Lale Apt. No:31B/39 M.sinan/B.cekmece/Istanbul

E-Mail: mustafakaykisiz@gmail.com

B.Sc.: Eskisehir Osmangazi University/Mechanical Engineering

Professional Experience and Rewards:

Jan. 2012–Jan. 2013	Reasearch Asst.	Istanbul Technical University
Jun. 2010–Jan. 2012	Research Asst.	Ozyegin University
Jun. 2008–Sep. 2008	Intern Engineer	Hipak Inc.

List of Publications and Patents:

▪ Kaykisiz M. and Bulgan E., 2013: Embedded Nanophotonic Displacement Sensing using Enhanced End-to-End Waveguide Coupling. *Journal of Microelectromechanical Systems*. (in preparation)

▪ Kaykisiz M. and Bulgan E., 2013: Sub-nanometer Mechanical Tuning of Evanescent Wave Mode Coupling in Planar Lightwave Circuits. *IEEE Photonics Technology Letter.* (in preparation)

▪ Gorajoobi S. B., Kaykisiz M., and Bulgan E., 2013: Characterization of Strongly Coupled Si-Wire Waveguides for High-Density Optical WDM and Sensing Applications. *Journal of Lightwave Technology*, Vol:31, No:22, Dec 2013.

▪ Kaykisiz M., and Bulgan E., Low-Loss Optical Switch using Brewster Angle. *2011 International Conference on Optical MEMS & Nanophotonic,* August 8-11, 2011.

▪ Kaykisiz M., Bulgan E., Nano-scale Sensing in Integrated Micromechanical Devices via Photonic Coupling for High-resolution Positioning. *2013 Integrated Photonics Research, Silicon and Nano-Photonics IPR.*

▪ Kaykisiz M., Bulgan E., Nanoscale Mechanical Tuning of Optical Coupling in Planar Lightwave Circuits. *2013 Integrated Photonics Research, Silicon and Nano-Photonics IPR.*

▪ Kaykisiz M., Bulgan E., Nanoscale optical coupling in planar lightwave circuits. *2013 9th National Conference on Nanoscience and Nanotechnology NanoTR-9.*

▪ Kaykisiz M., Bulgan E., " NEMS-actuated silicon nanowire waveguide in-plane displacement sensor", *2013 9th National Conference on Nanoscience and Nanotechnology NanoTR-9.*

▪ Gorajoobi S. B, Kaykisiz M., Bulgan E., Nano-scale Tunability of Sub-wavelength Optical Couplers. *2013 9th National Conference on Nanoscience and Nanotechnology NanoTR-9.*